

# **Design, Evaluation and Implementation of a Multi-Carrier Transmission System for Aeronautical Communications**

Dem Fachbereich Energie-, Verfahrens- und Elektrotechnik der  
Universität-Gesamthochschule Essen  
zum Erwerb des Grades

**Doktor-Ingenieur**

vorgelegte Dissertation von

**Dipl.-Ing. Univ. Erik Haas**

München, Deutschland

Tag der mündlichen Prüfung: 10. Oktober 2002

Vorsitzender der Prüfungskommission: Prof. Dr.-Ing. E. von Lavante

1. Gutachter: Prof. Dr.-ir. A.J. Han Vinck

2. Gutachter: Prof. Dr.-Ing. Peter Höher



Verlagstitelblatt

IV

Impressumseite

# Vorwort

Die vorliegende Arbeit entstand während meiner Tätigkeit als wissenschaftlicher Mitarbeiter im Institut für Kommunikation und Navigation, Abteilung Nachrichtensysteme des Deutschen Zentrum für Luft- und Raumfahrt (DLR) e.V. in Oberpfaffenhofen.

Mein besonderer Dank gilt Herrn Prof. Dr.-ir. A.J. Han Vinck für die Betreuung dieser Arbeit, die damit verbundenen Diskussionen und Strukturierungsvorschläge und den gewährten Freiraum, um den Inhalt und Umfang nach eigenem Ermessen zu gestalten. Ferner danke ich Herrn Prof. Dr.-Ing. Peter Höher, der das Koreferat übernommen hat.

Weiterhin bedanken möchte ich mich bei allen Kollegen und Freunden im Institut für Nachrichtentechnik, dem späteren Institut für Kommunikation und Navigation des DLR und bei allen Mitarbeitern des Instituts für experimentelle Mathematik der Universität Essen. Das gute Arbeitsklima in der Gruppe und zahlreiche Diskussionen, Anregungen und daraus resultierende Ideen haben zum Gelingen dieser Arbeit beigetragen. Insbesondere bedanken möchte ich mich bei Herrn Dr.-Ing. Michael Schnell für das Korrekturlesen der Arbeit und die damit verbundene stets konstruktive Kritik. Weiterer Dank gilt meinem Abteilungsleiter Dr.-Ing. Uwe-Carsten Fiebig.

Die Arbeit ist in Englisch gehalten um sie einem möglichst breiten Publikum zugänglich zu machen. Der Leser soll einen praxisnahen Einblick in aktuelle Themen der Nachrichtentechnik und Übertragungskanalmodellierung bekommen. Theoretische Betrachtungen und Simulationen werden durch zahlreiche Abbildungen und den Aufbau eines realen Mehrträgerübertragungssystems in digitaler Signalprozessortechnologie vertieft. Ein besonderer Augenmerk gilt dabei den Problemen, die in solchen Systemen in der Wirklichkeit auftreten, und wie sie gelöst werden können. Ich wünsche allen Lesern und Leserinnen viel Freude beim Durchsehen.

München, im Oktober 2002

Erik Haas

**Für meine Eltern  
Rüdiger und Renate**

ohne deren Unterstützung vieles nicht möglich gewesen wäre.

*“Der Fortschritt geschieht heute so schnell, daß während jemand eine Sache für gänzlich undurchführbar erklärt, er von einem anderen unterbrochen wird, der sie schon realisiert hat.”*

ALBERT EINSTEIN (1879-1955), DEUTSCH-AMERIKANISCHER PHYSIKER

*“Der Wissende weiß, daß er glauben muß.”*

FRIEDRICH DÜRRENMATT (1921-90), SCHWEIZER DRAMATIKER

# Contents

<b>1</b>	<b>Introduction</b>	<b>1</b>
<b>2</b>	<b>Aeronautical Channel Modelling</b>	<b>7</b>
2.1	Technical Background . . . . .	7
2.2	Aeronautical Channel Models . . . . .	12
2.2.1	En-Route Scenario . . . . .	13
2.2.2	Arrival and Take-Off Scenario . . . . .	16
2.2.3	Taxi Scenario . . . . .	18
2.2.4	Parking Scenario . . . . .	19
2.2.5	Aircraft Flying Over Ground Station . . . . .	21
2.2.6	Summary of Channel Parameters . . . . .	22
2.3	Channel Emulation . . . . .	22
2.3.1	WSSUS Model . . . . .	22
2.3.2	Flat Fading . . . . .	23
2.3.3	Frequency-Selective Fading . . . . .	24
2.4	Implementation on Digital Signal Processing Systems . . . . .	24
2.4.1	Choice of Doppler, Delay and Phase . . . . .	24
2.4.2	Discrete Time Realization . . . . .	25
2.4.3	Discrete Frequency Realization . . . . .	27
<b>3</b>	<b>Multiple Access Techniques</b>	<b>29</b>
3.1	Multiplexing Techniques . . . . .	29
3.1.1	Frequency Division Multiple Access - FDMA . . . . .	30
3.1.2	Time Division Multiple Access - TDMA . . . . .	30
3.1.3	Code Division Multiple Access - CDMA . . . . .	30
3.2	Single-Carrier, Spread Spectrum and Multi-Carrier . . . . .	31
3.2.1	Single-Carrier Modulation . . . . .	32
3.2.2	Spread Spectrum Modulation . . . . .	34
3.2.3	Multi-Carrier Modulation . . . . .	36

<b>4</b>	<b>Modulation and Demodulation Techniques for OFDM</b>	<b>48</b>
4.1	Coherent Modulation/Demodulation . . . . .	48
4.2	Channel Estimation and Equalization . . . . .	49
4.2.1	Requirements for MC Channel Estimation . . . . .	49
4.2.2	Analysis of Interpolation Methods . . . . .	51
4.2.3	Channel Equalization . . . . .	57
4.3	Differential Coherent Modulation/Demodulation . . . . .	58
4.3.1	Differential MC-CDMA . . . . .	59
4.4	Two-Dimensional Differential Demodulation . . . . .	62
4.4.1	Basic Idea for Two-Dimensional Differential Demodulation . . . . .	63
4.4.2	Frame-Worm Algorithm for Detour Path Determination . . . . .	63
4.4.3	Mathematical Theory for Path Determination . . . . .	66
4.4.4	Minimum Phase Error Criteria . . . . .	71
4.4.5	Path Evaluation . . . . .	72
4.5	Synchronization . . . . .	73
4.5.1	Frame/Symbol Timing Synchronization . . . . .	74
4.5.2	Carrier Frequency Synchronization . . . . .	74
4.5.3	Sampling Rate Synchronization . . . . .	74
4.5.4	Synchronization Algorithms . . . . .	76
4.5.5	Improvements for Schmidl and Cox Algorithm . . . . .	80
<b>5</b>	<b>System Design and Evaluation</b>	<b>84</b>
5.1	General Considerations . . . . .	84
5.2	Performance Analysis for Coherent QPSK . . . . .	87
5.2.1	Results with Aeronautical Channel Models . . . . .	87
5.2.2	Results with Non-Linear Power-Amplifier . . . . .	93
5.2.3	Results with Frame/Symbol Timing Synchronization Offset . . . . .	96
5.2.4	Results with Carrier Frequency Synchronization Offset . . . . .	96
5.2.5	Results with Multi-User MC-CDMA . . . . .	97
5.2.6	Discussion of the Coherent Performance Results . . . . .	99
5.3	Performance Analysis for Differential Coherent DQPSK . . . . .	101
5.3.1	Results with AWGN Applying 2D-DD . . . . .	101
5.3.2	Results with Aeronautical Channel Models . . . . .	102
5.3.3	Results with Non-Linear Power-Amplifier . . . . .	105
5.3.4	Results with Frame/Symbol Timing Synchronization Offset . . . . .	105

5.3.5	Results with Carrier Frequency Synchronization Offset . . . . .	106
5.3.6	Results with Coded CDMA System . . . . .	110
5.3.7	Discussion of the Differential Coherent Performance Results . . . . .	110
5.4	Selection of System for Ground-Air and Air-Ground Link . . . . .	111
5.4.1	Coherent Ground-Air Link . . . . .	111
5.4.2	Differential Coherent Air-Ground Link . . . . .	114
<b>6</b>	<b>System Implementation</b>	<b>116</b>
6.1	Flexible and Adaptable Parameter Structure . . . . .	116
6.1.1	OFDM/TDMA Frame Parameters . . . . .	116
6.1.2	Estimation and Equalization Parameters . . . . .	118
6.1.3	Synchronization Parameters . . . . .	119
6.1.4	MC-CDMA Parameters . . . . .	119
6.1.5	Digital Programmable Filters . . . . .	119
6.1.6	RF Components . . . . .	120
6.1.7	Protocol Interface Structure . . . . .	120
6.2	DSP-System . . . . .	120
6.2.1	TARMAC ADL Demonstrator System Structure . . . . .	120
6.2.2	Multiprocessor System Structure . . . . .	122
6.2.3	I/Q Lowpass Area Adaptation . . . . .	127
6.2.4	IF Area Analysis . . . . .	143
6.2.5	RF Area Analysis . . . . .	149
6.2.6	Conclusions for the DSP-System Implementation . . . . .	156
<b>7</b>	<b>Summary</b>	<b>158</b>
<b>A</b>	<b>Maximum Doppler Rate Derivation</b>	<b>163</b>
<b>B</b>	<b>Shortened <math>\text{si}(x)</math>-Function Spectrum</b>	<b>164</b>
<b>C</b>	<b>Linear Interpolation Function Spectrum</b>	<b>165</b>
<b>D</b>	<b>SDR MC-CDMA Parameter Structure</b>	<b>166</b>
	<b>Notations</b>	<b>170</b>
	Symbols . . . . .	170
	Abbreviations . . . . .	175
	<b>Bibliography</b>	<b>178</b>
	<b>Publications</b>	<b>184</b>



# Chapter 1

## Introduction

Digital wireless communications systems are gaining more and more influence in state-of-the-art technologies, where performance, mobility and safety are important issues. Using the Discrete Fourier Transformation (DFT) in combination with data transmission systems has first been proposed in [Wei71]. With modern technologies, Orthogonal Frequency Division Multiplexing (OFDM) using the Fast Fourier Transformation (FFT) to modulate multiple subcarriers at the same time has become an interesting option.

Like with single-carrier signals, coherent and differential coherent modulation techniques [Pro95] are applicable to OFDM and according standards are already in use for Digital Audio Broadcasting (DAB) [DAB95], Terrestrial Digital Video Broadcasting (DVB-T) [DVB99] or HIPER-LAN/2 [HIP00] to name only a few.

The strong focus on OFDM-based communications systems is related to the fact that this Multi-Carrier (MC) transmission technique in conjunction with  $M$ -ary mapping, where  $M \gg 2$ , shows a high spectral efficiency due to optimum Nyquist criteria application for the subcarriers. As can be seen from the prices that are asked for the current frequency bands of the third generation Universal Mobile Telecommunications System (UMTS), such a spectral efficiency has a high priority for future fourth generation and beyond systems.

Nowadays aeronautical communications systems are suffering a similar nuisance in the Very High Frequency (VHF) band. The applied analog Amplitude Modulation (AM) technique is more than fifty years old and the assigned frequency band between 118 and 137 MHz with a channel spacing of 25 kHz can only occupy a maximum of 760 channels worldwide, of which certain channels are fixedly assigned to aircraft authorities and airlines. The introduction of a new AM modulation with 8.33 kHz channel spacing did not solve the problem, since no data transmission is possible with this technique. Furthermore, the safety of the radio messages is not guaranteed due to the fact that everybody can listen to or even interfere the communication. The lack of digital data exchange and safety has led the aircraft authorities to investigate digital transmission techniques that were intended to solve these problems. The respective data links are known as VHF Data Link (VDL) Mode 2 [DDR01], VDL Mode 3 and VDL

Mode 4 [HHL99]. The drawback of all these data links is that they still operate in the VHF band with only 25 kHz bandwidth and therefore have a very poor performance considering the achievable throughput. This situation is worsened by the fact that the aforementioned aircraft authorities and airlines are not willing to give up their owned channels as long as it is not clear whether the new system(s) will be a success or not.

For that reason, the investigations in this work concentrate on a different frequency band. Since the allocation of frequency bands to aeronautical communications is a difficult task and the proposed systems will only be a success if they can be applied world-wide, a frequency band is used that is already reserved for aeronautical applications. It is the 5 GHz band in which the so-called Microwave Landing System (MLS) operates. Since the MLS has, due to a minor commercial success, not been introduced in all countries, but has on the other hand world-wide reserved frequencies, this frequency band is an ideal candidate for an Advanced aeronautical Data Link (ADL). The ADL can either occupy the full bandwidth or operate in parallel to an existing MLS system. For the case that the MLS frequency band will not be available to the ADL, it can be guaranteed that the ADL will also work in lower frequency bands.

In aeronautical communications, two different directions for the data link exist. One is the so-called ground-air link, forward link or downlink. In this case, the base station, normally at an airport, transmits information to a mobile receiver, normally an aircraft or a different mobile user, e.g. a follow-me car. The other link is the so-called air-ground link, reverse link or uplink. In this case, the information is transmitted from a mobile user to the base station. For the ground-air link, information is transmitted from one base station to several mobile users, whereas for the air-ground link, several mobile users transmit information to one base station. Please note the confusing standardized meaning of down- and uplink here.

The investigations in this work will focus on two different transmission techniques both using OFDM. The first technique is based on coherent modulation and demodulation and is commonly known as Multi-Carrier Code Division Multiple Access (MC-CDMA) [FaP93][YLF93]. As the name already suggests, it offers the possibility to transmit multiplexed information for several users, known as Multiple Access (MA). The reason for choosing MC-CDMA instead of a different MA techniques is justified with the facts that it offers a high flexibility and the possibility to exchange users versus data rates. Furthermore, MC-CDMA can be made extremely stable against worst case transmission channel conditions [Kai98]. The second technique is based on differential coherent modulation and demodulation applying Differential Phase Shift Keying (DPSK) [Pro95] on subcarrier level. It benefits from the fact that it does not need an explicit transmission channel estimation and equalization, compared to coherent transmission methods, and therefore is an interesting option for the air-ground link, where the channel conditions for each mobile user transmitting to the ground station vary. Despite the fact that the investigations concentrate on aeronautical communications, the proposed algorithms and techniques are also applicable for other wireless or wired communications areas.

To prove the accurateness and operability of the proposed methods, a Digital Signal Processor (DSP) based demonstrator is built that features a wireless link in the 5 GHz band for outdoor

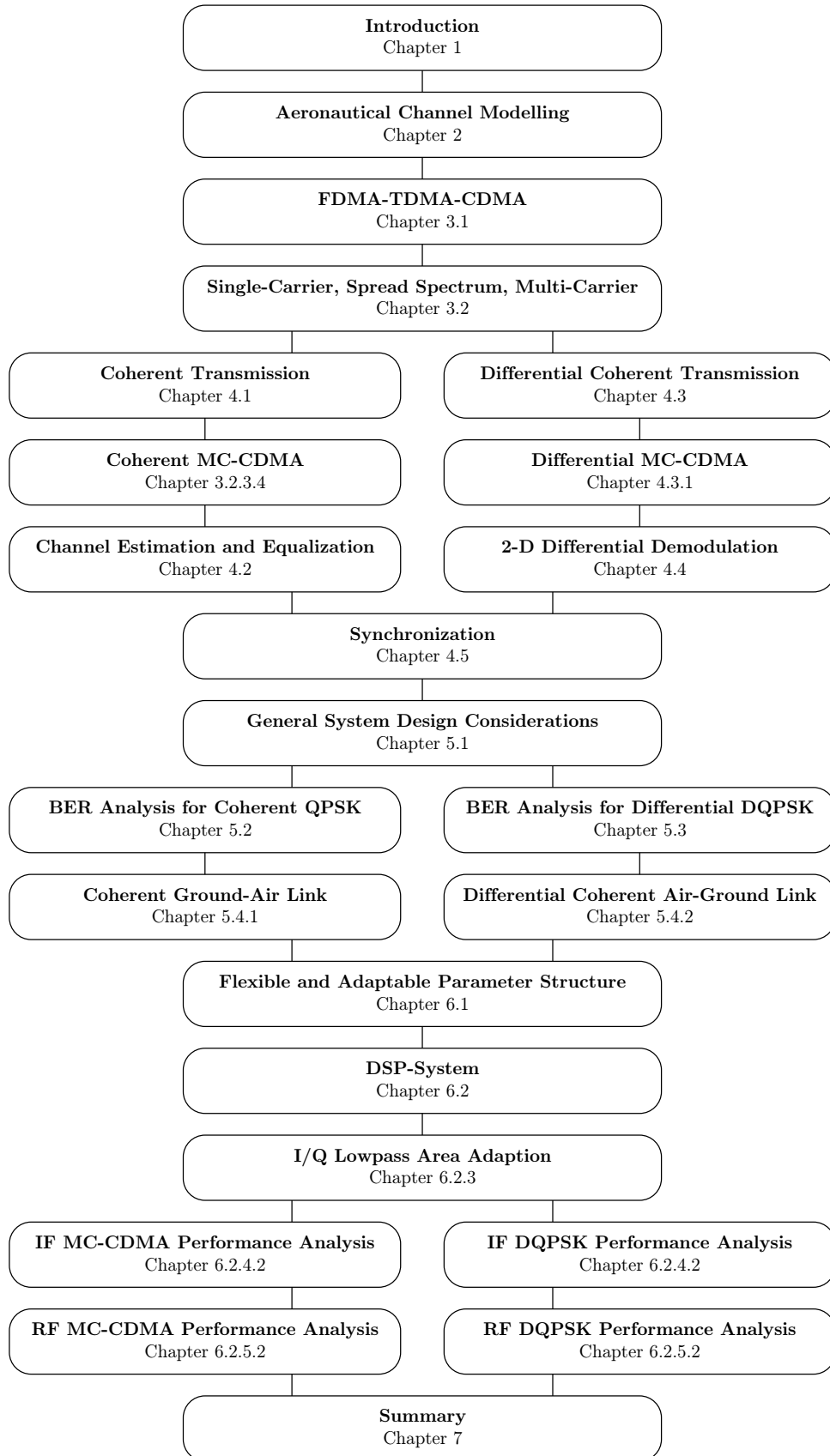


Figure 1.1: Synopsis

communications. It is the first known demonstrator world-wide that uses MC-CDMA transmission techniques. A benefit from this demonstrator is achieved by offering the possibility to investigate implementation aspects in a real-world system.

The outline of the contents of this work is shown in Fig. 1.1. The classification of the modulation technique into coherent and differential coherent aspects is reflected by the separation into a left- and right-hand side.

The introduction is followed in Chapter 2 by the presentation of a previously unknown class of aeronautical wideband channel models, featuring parking and taxi environments, take-off and landing situations, as well as en-route scenarios for ground-air and air-air links. Typical and worst case channel parameter sets, based on published measurement results and empirical data, are defined for the scenarios. They are used in conjunction with the system functions for a Wide Sense Stationary Uncorrelated Scattering (WSSUS) emulation of the aeronautical channel. Procedures are presented to implement the system functions on a digital signal processing system for simulation purposes in the time and frequency domain.

Chapter 3 first gives an overview about the differences between the available Frequency Division Multiple Access (FDMA), Time Division Multiple Access (TDMA) and Code Division Multiple Access (CDMA) multiplexing techniques. This is followed by a comparison of single-carrier, spread spectrum and multi-carrier modulation. Special attention is drawn onto the spectral identities of the transmitted signals with respect to the use of practical Digital-to-Analog (D/A) converter hardware of real-world systems. Measures for OFDM to overcome the resulting drawbacks related to real D/A-hardware are discussed and new hardware and software solutions are proposed. Finally, the basic MC-CDMA technique is explained and two modifications are presented to increase the maximum number of active users and the maximum data rate per user while keeping the complexity for each individual user low.

In Chapter 4, coherent modulation/demodulation in comparison to differential coherent modulation/demodulation is considered. Novel aspects for the interpolation and filtering process of the channel estimation for coherent demodulation are obtained. It is shown that linear interpolation is an option worth considering for several cases, compared to other far more complex interpolation methods. For differential demodulation, no explicit channel estimation and equalization exists. Since the algorithms for coherent MC-CDMA require an equalized signal, these methods are not applicable for differentially modulated systems. Therefore, different methods based on spreading the data with a code before DPSK mapping are proposed. To overcome the degrading effects of differential demodulation, a completely new and formerly unknown two-dimensional algorithm is proposed and investigated. It makes use of the fact that even though the transmitted information is only differentially modulated in one direction within an OFDM frame, neighbouring symbols belong to the same symbol alphabet and thus can be used for the demodulation process without changing the transmitter or existing standards. With a mathematical analysis it is proved that this two-dimensional algorithm improves the Bit Error Rate (BER) performance of the DPSK system. The set-up of an OFDM demonstrator system further necessitates a freerunning synchronization. The interference ratios resulting from a

synchronization mismatch are investigated and the most commonly used algorithms illustrated. Some improvements for the chosen algorithm, that is implemented in the demonstrator system, are given.

Having the aeronautical channel parameter sets from Chapter 2 available, some general considerations about the OFDM system design are done in Chapter 5. These are followed by simulations of the chosen parameters for coherent Quadrature Phase Shift Keying (QPSK) systems and Differential Quadrature Phase Shift Keying (DQPSK) systems. The simulation scenarios enclose the simulated aeronautical channel models as well as non-linear transmitter power amplification effects, synchronization mismatches and CDMA. For DQPSK, the benefits with two-dimensional differential demodulation are investigated as well. It is shown that coherent MC-CDMA applying PSK further improves the system performance compared to normal coherent PSK. Moreover, it is proved that two-dimensional differential demodulation cannot only overcome degrading effects from additive noise, but also from synchronization mismatches, non-linear amplifying effects and fading channels. With the simulation results, parameter sets for a coherent and differential coherent demonstrator set-up are derived.

Chapter 6 deals entirely with the system implementation aspects of the OFDM DSP multi-processor demonstrator. To keep the system as flexible and adaptable as possible, generalized parameter structures are defined which make it possible to change the functionality completely by changing only a few definitions in the parameter list. This makes it possible to have a Software-Defined Radio (SDR) at hand that can be easily adapted to changing demands and new ideas. A detailed description of the transmitter and receiver hardware and software architecture is given next, followed by a description how the different tasks are distributed among the available processors. The investigation of the analog signal identities is done in several steps. First, the In-phase/Quadrature (I/Q) lowpass area is adapted by choosing the correct lowpass filter type and bandwidth and compensating DC gain, DC offset, filter bandwidth and subcarrier attenuation mismatches. In the next step, the Intermediate Frequency (IF) area is considered, where additional subcarrier compensation is necessary. The system improvement through accurate compensation is illustrated with corresponding performance results for coherent and differential coherent modulation/demodulation techniques and additive noise. In a final step, the Radio Frequency (RF) hardware is connected and additional measurements are investigated. The performances with and without freerunning synchronization are opposed. Received equalized subcarrier constellation diagrams for MC-CDMA applying QPSK are presented with varying numbers of active user.

A summary of all investigated results can be found in Chapter 7 which concludes this work.

Since OFDM symbols are generated in the frequency domain, but the equivalent time domain signal is transmitted, corresponding signals of both domains have to be distinguished properly. Throughout this work, capital letters are used for the frequency domain representation and small letters are used for the time domain representation of signals. Furthermore, the equivalent lowpass representation for signals is applied [Pro95].

Performance results are in most cases compared by the BER  $P_b$  versus the Signal-to-Noise Ratio (SNR) per bit  $\gamma_b$ . The overall SNR is  $\gamma_c = C/N$ , where  $C$  is the average received signal power and  $N$  is the noise power. For the case that the equivalent signal bandwidth  $B$  and the noise bandwidth are the same,  $\gamma_c$  can be rewritten as  $\gamma_c = C/N = (E_s B)/(N_0 B) = E_s/N_0$ , where  $E_s$  is the energy per modulation symbol and  $N_0$  is the noise power density. Since modulation symbols can consist of several bits  $n$ , the SNR per bit  $\gamma_b = E_s/(nN_0) = E_b/N_0$  is defined, where  $E_b$  is the energy per bit.

Unless otherwise noted, all calculations were done by hand and verified with Mathematica [Wol94].

# Chapter 2

## Aeronautical Channel Modelling

### 2.1 Technical Background

The design of a digital communication link makes it necessary to assess its performance and reliability for the desired operational environments. This is done in simulations prior to implementation of the link in hardware. This chapter especially focuses on the environmental conditions that affect the transmission of a wireless digital signal during the different states of a flight of an aircraft including conditions on the ground and in the air. Channel models are suggested from these environmental conditions that serve for an analysis of the link based on communications theory.

In general, environmental influences on the transmitted signal and the resulting performance losses in a mobile communication system can be summarized to six main causes:

- **Reflection** occurs on a smooth object with large dimensions compared to the wavelength  $\lambda$ . The signal delay, caused by this effect, between the transmitter and the receiver can be described by Geometrical Optics (GO).
- **Scattering** is observed on diffuse surfaces where not just one ray is reflected, but a whole number of reflected rays from the same object arrives at the receiver. The dimension of the reflecting object can be in the dimension of the wavelength. A more general assumption is that the reflected rays from one scattering object have the same signal delay, but different phases. Again, the signal delay can be calculated by GO.
- **Diffraction** is an effect that occurs on edges and corners. The electromagnetic wave diffuses into the material and through the formation of secondary waves, the signal is diffracted. The diffraction can be assessed with the Uniform Theory of Diffraction (UTD) which also takes creeping rays into account. GO is also an option, but UTD is more accurate if it is possible to include all stationary rays arriving at the receiver.
- **Shadowing** results from objects that block the propagation path.

- **Path loss** results from the distance between the transmitter and receiver and depends on the propagation environment that induces reflection, scattering and/or diffraction. A simple estimation for the path loss is

$$P_{R_x}(d) = P_{R_x}(d_0) \left( \frac{d_0}{d} \right)^n, \quad (2.1)$$

where  $P_{R_x}(d)$  is the received power at distance  $d$ ,  $P_{R_x}(d_0)$  is the known received power at distance  $d_0$  and  $n$  is an environment-specific constant that varies from rural areas ( $n = 2$  for free space loss ... short distance  $n \rightarrow 4$ , where  $d > 1$  km) to urban areas ( $n = 3 \dots 5$ ). Equation (2.1) only gives the mean loss but not the fluctuation of the loss when the distance remains constant. This fluctuation can be modelled as the variance of a log-normal (Gaussian) distribution.

- **Thermal noise** is a stochastic signal that is added to the transmitted signal during the analog processing. It can be modelled by the noise power density  $N_0$  with

$$N_0 = k \cdot T_0, \quad (2.2)$$

where  $k$  is the Boltzmann constant and  $T_0$  is the equivalent noise temperature in Kelvin.  $N_0/2$  describes an average power density spectrum that is added to the signal power density spectrum.

The mentioned reflection, scattering, diffraction and shadowing effects together with a direct Line Of Sight (LOS) path are shown in Fig. 2.1. They are known as multipath propagation in mobile communications and result in fading of the received signal due to constructive and destructive superpositioning. In [Cha97], ducting effects and tropospheric propagation are considered for the Very High Frequency (VHF) band between 118 and 137 MHz. Ducting will be implicitly included in the channel models by reflection effects. Tropospheric propagation is not considered for digital communications here, since the possible range of delays and thus the signal attenuation in the 5 GHz band is too high to be included in the channel models. Furthermore, the occurrence of this effect is quite rare and only of importance for analog VHF radio communications.

Multipath propagation indicates that many different physic effects, that result in fading, are combined in the receiver. Since GO and UTD, which belong to the *causal methods*, require an accurate knowledge of all objects with their materials and geometry, predicting the signal at the receiver is a difficult task and often focuses on just one special environmental condition, see e.g. [Rot97]. Therefore *statistical methods* for describing the channel between the transmitter and the receiver that represent a more general view of the received signal are best for simulating the performance of a digital link. These statistical methods are specified in the following and are based on the so-called wideband stochastic multipath propagation channel models. They are characterized here by the Doppler power spectrum and the delay power spectrum, i.e. the scattering function  $P_s(\tau, f_D)$  [Bel63].

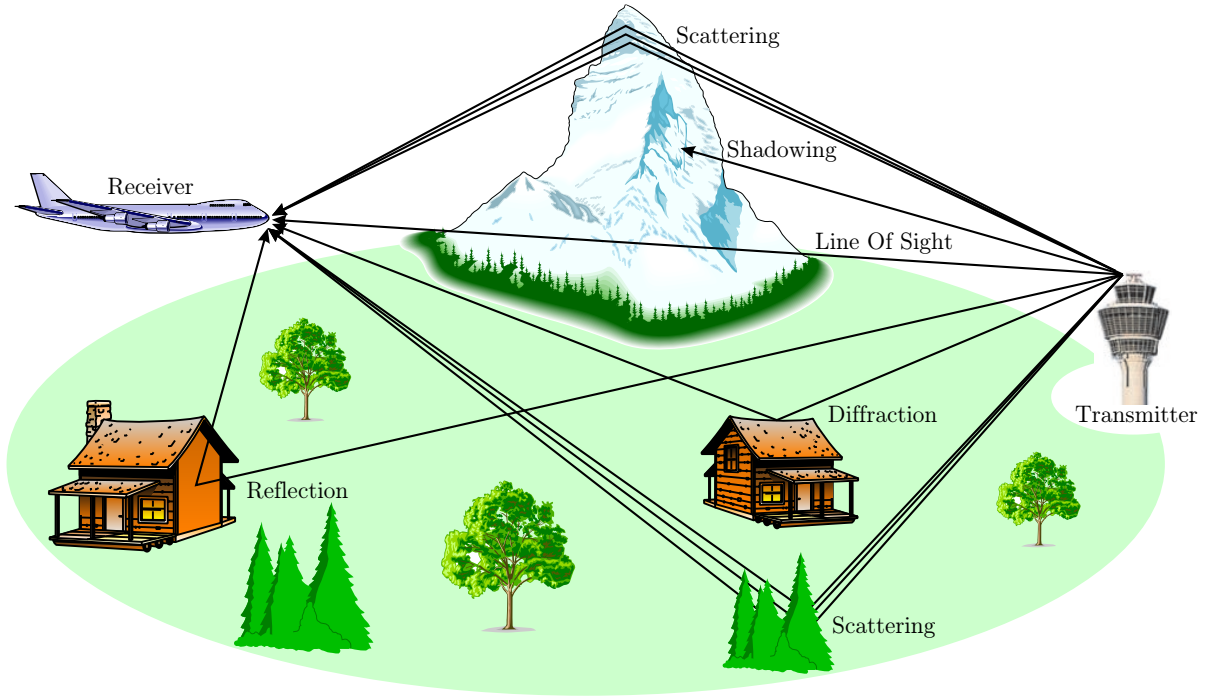


Figure 2.1: Multipath propagation in mobile communications systems

- The **Doppler power spectrum** describes the distribution of the signal power among the Doppler frequency offsets  $f_D$  that occur in the channel. The Doppler frequencies result from different relative velocities  $\Delta v$  between the receiver and the direction of the received paths. The Doppler frequency is related to the relative velocity  $\Delta v$  and carrier frequency  $f_c$  via  $f_D = \Delta v / \lambda = f_c \cdot \Delta v / c$ , where  $c \approx 3 \cdot 10^8$  m/s is the speed of light.
- The **delay power spectrum** describes the distribution of the signal power among the delays  $\tau$  that occur in the channel. The delays result from different path lengths of the multipath propagation. By definition,  $\tau = 0$  refers to the LOS path. This forces  $\tau \geq 0$ . Hence,  $\tau$  is called excess delay, which is related to the detour distance  $\Delta d$  via  $\tau = \Delta d / c$ .

In the following, the Doppler power spectrum is assumed to be independent from the delay power spectrum:  $P_s(\tau, f_D) = P_s(\tau) \cdot P_s(f_D)$ . Given this assumption, it is sufficient to specify the 1-D Doppler power spectrum,  $P_s(f_D)$ , and the 1-D delay power spectrum,  $P_s(\tau)$ , for the different environments. In [Hoe92] it has been shown that the scattering function is proportional to the 2-D probability density function (pdf)  $p(\tau, f_D)$  of the Doppler frequencies and the echo delays:  $P_s(\tau, f_D) \sim p(\tau, f_D)$ . Given these two requisites, it is sufficient to specify the 1-D probability density functions  $p(\tau)$  and  $p(f_D)$  to compile a stochastic model of the aeronautical channel.

Characterization of the aeronautical channel can further be divided into two different aspects:

- **Small-area models** are representative to evaluate, to validate and to compare transmission standards. By definition, they are valid within a few dozens of wavelengths and are

characterized by the scattering function. Small-area models can serve as a reference for simulations. Thus, the purpose of this chapter is to design a small-area characterization of the aeronautical channel, similar to the procedure that has been established in connection with the Global System for Mobile communication (GSM) work, where suitable channel models have been defined by COST-207 [COS88] for validation and comparison purposes.

- **Large-area models** already have been considered in other studies [Rot97]. In addition to multipath propagation, these models also take shadowing and other propagation path losses, like different dielectric ground conditions and creeping rays, into account. Such models can be useful for the link budget design, for the simulation of outage probabilities or may serve as a basis for traffic models, etc. However, they are generally not necessary for the design or validation of physical layer transmission techniques, that are considered here.

The time-variant, linear, causal mobile communications channel is completely described by the *time-variant channel weight function*  $h(\tau, t)$  [Hub96] often wrongly dubbed time-variant channel impulse response. The time-variant channel weight function is one of the four existing system functions [Bel63] and relates the output signal  $y(t)$  to the input signal  $x(t)$  through the convolution

$$y(t) = \int_{-\infty}^{+\infty} x(t - \tau) \cdot h(\tau, t) d\tau. \quad (2.3)$$

The signal in the time-variant system is observed at time  $t$ . The time dispersion at time  $t$  due to the echoes is described by  $\tau$ . The stochastic channel description, i.e. the delay density function  $p(\tau)$  and Doppler density function  $p(f_D)$ , is contained in  $h(\tau, t)$  as will be seen in Section 2.3.

In contrast to this, the time-variant channel impulse response  $h_0(\tau_A, t)$  relates the output signal  $y(t)$  to the input signal  $x(t)$  through

$$y(t) = \int_{-\infty}^{+\infty} x(\tau_A) \cdot h_0(\tau_A, t) d\tau_A, \quad (2.4)$$

where  $\tau_A$  is the excitation instance. The following relationships exist between the weight function and the impulse response:

$$h(\tau, t) = h_0(t - \tau, t) \quad ; \quad h_0(\tau_A, t) = h(t - \tau_A, t). \quad (2.5)$$

The difference between the impulse response  $h_0(\tau_A, t)$  and the weight function  $h(\tau, t)$  is explained with the simple example of Fig. 2.2. The received echoes are considered at time  $t_0 = 0 \mu\text{s}$ . First, the time-variant channel impulse response is observed, see Fig. 2.2(a). The signal at excitation instance  $\tau_{A1} = -6 \mu\text{s}$  generates an echo with delay  $\tau_e = 6 \mu\text{s}$ . At excitation instance  $\tau_{A2} = -4 \mu\text{s}$ , the echo delay changes to  $\tau_e = 4 \mu\text{s}$ . The resulting received signal at  $t_0 = 0 \mu\text{s}$  consist of a superpositioning of both echo parts. In contrast to this, the time-variant channel weight function uses the echo delay  $\tau_e = 2 \mu\text{s}$  at time  $t_0 = 0 \mu\text{s}$  to get the echo part of the received signal from time  $t_3 = t_0 - \tau_e = -2 \mu\text{s}$ , see Fig. 2.2(b). It becomes clear that

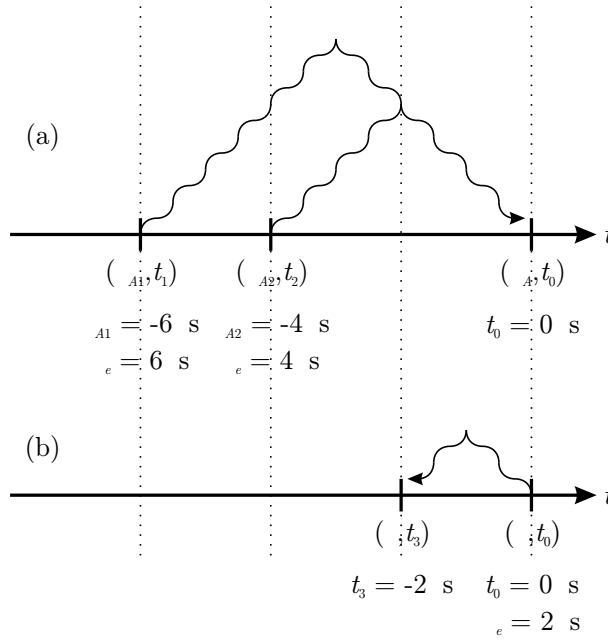


Figure 2.2: Impact of echo for time-variant channel impulse response  $h_0(\tau_A, t)$  (a) and time-variant channel weight function  $h(\tau, t)$  (b)

even though *only one echo path exists*, the received echo signal for the time-variant impulse response may consist of several signal parts, whereas the received echo signal for the time-variant weight function will always consist of just one signal part in this example. In the time-invariant case, the result of the channel impulse response is identical to the result of the channel weight function. A detailed description of the system theory bases can be found in [Hub96].

Another important system function is the *time-variant channel transfer function*  $T(f, t)$  that results from a Fourier transform of  $h(\tau, t)$  with regard to  $\tau$

$$T(f, t) = \mathcal{F}_\tau\{h(\tau, t)\} = \int_{-\infty}^{+\infty} h(\tau, t) \cdot e^{-j2\pi f\tau} d\tau. \quad (2.6)$$

The *delay-Doppler function*  $S(\tau, f_D)$  [Hub96] is obtained from a Fourier transform of  $h(\tau, t)$  with regard to  $t$

$$S(\tau, f_D) = \mathcal{F}_t\{h(\tau, t)\} = \int_{-\infty}^{+\infty} h(\tau, t) \cdot e^{-j2\pi f_D t} dt. \quad (2.7)$$

Finally, the *Doppler-variant channel transfer function*  $H(f, f_D)$  can either be obtained from a Fourier transform of  $T(f, t)$  regarding to  $t$  or from a Fourier transform of  $S(\tau, f_D)$  regarding to  $\tau$

$$H(f, f_D) = \mathcal{F}_t\{T(f, t)\} = \mathcal{F}_\tau\{S(\tau, f_D)\}. \quad (2.8)$$

An overview of the relationships between the four system functions is given in Fig. 2.3. The frequency domain representation  $Y(f)$  of the received signal is therefore related to the frequency domain representation of the transmitted signal  $X(f)$  by

$$Y(f) = \int_{-\infty}^{+\infty} X(f - f_D) \cdot H(f, f_D) df_D \quad \text{and} \quad (2.9)$$

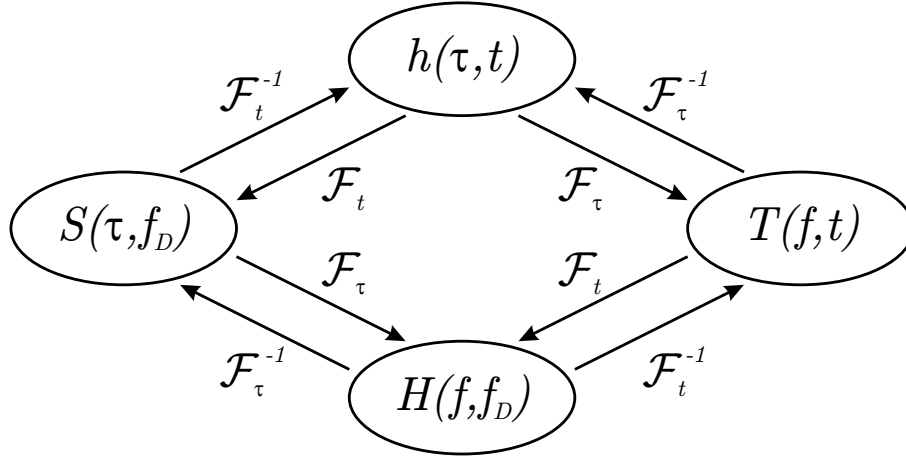


Figure 2.3: Relationships between the different system functions

$$Y(f) = \mathcal{F}_t \left\{ \int_{-\infty}^{+\infty} X(f) \cdot T(f, t) \cdot e^{j2\pi ft} df \right\}. \quad (2.10)$$

Up to now, computer simulations have been difficult to compare since no common aeronautical channel model is available. Most of the open literature on aeronautical channel models focuses on the satellite aircraft channel [Bel73][Pai73][Neu87]. Concerning VHF air-ground links, at least one stochastic model for the aeronautical radio channel exists [Eln92], but this model considers the Doppler power spectrum only, since the underlying measurement results are based on Continuous Wave (CW) signals. It features the en-route situation only and parameters representing typical or worst case conditions are entirely missing.

Published measurement results in [Dye97][RTC93] and empirical data are used in the following to specify the different aeronautical scenarios and to propose typical and worst-case parameter sets. The COST-207 models are utilized as a basis for airport scenarios that are similar to the ones specified for rural and urban areas [COS88].

## 2.2 Aeronautical Channel Models

The different conditions during the flight of an aircraft lead to different channel scenarios. These scenarios are characterized by the type of fading, the Doppler and the delays in the system, where the Doppler and the delay power spectra represent the diffuse scattered multipath components. A line-of-sight path must be separately taken into account. The power ratio between the LOS and the diffuse components is called Rice-factor

$$K_{Rice} = \frac{a^2}{c^2} \quad \text{or equivalently} \quad K_{Rice} = 10 \cdot \log_{10} \frac{a^2}{c^2} \text{ dB}, \quad (2.11)$$

where  $a \in \mathcal{R}$  is the amplitude of the LOS path and  $c^2 \in \mathcal{R}$  is the variance of the diffuse components with zero-mean quadrature components. A multipath channel without a LOS component is called *Rayleigh channel*. A multipath channel with a LOS component is called *Rician channel*. That way, the Rayleigh channel can be seen as a special case of the Rician channel with

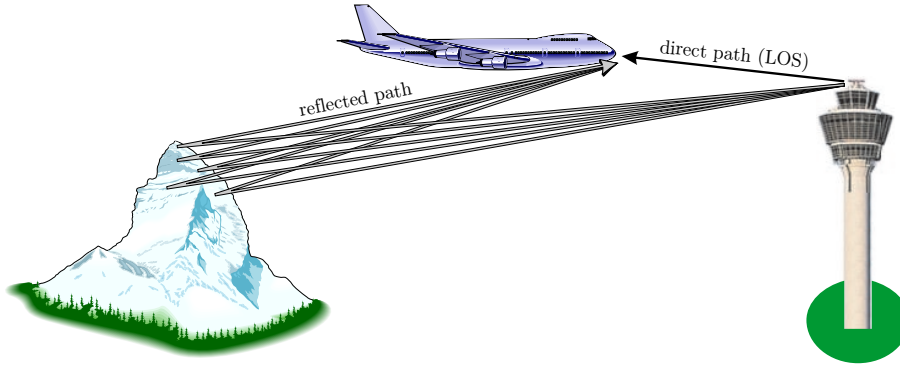


Figure 2.4: Multipath propagation for en-route scenarios

$K_{Rice} = 0 = -\infty$  dB. For a simple implementation of the multipath fading channel models, it is required that the mean throughput power remains unchanged, i.e.  $E\{|h(\tau, t)|^2\} = a^2 + c^2 = 1$ . Then the following normalization as a function of the Rice factor is obtained

$$a = \sqrt{\frac{K_{Rice}}{K_{Rice} + 1}}, \quad (2.12)$$

$$c = \sqrt{\frac{1}{K_{Rice} + 1}}. \quad (2.13)$$

In the limit for  $K_{Rice} \rightarrow 0$  (Rayleigh fading) one gets  $a = 0$  and  $c = 1$ , whereas in the limit  $K_{Rice} \rightarrow \infty$  (AWGN) one obtains  $a = 1$  and  $c = 0$ , respectively.

### 2.2.1 En-Route Scenario

The en-route scenario is applied when the aircraft is airborne and engaged in ground-air or air-air communication as shown in Fig. 2.4. Ground-air communication is considered to be the link between a base station on the ground and an aircraft. Air-air communication is considered to be the link between two airborne aircrafts.

Type of fading: Typically, this multipath channel consists of a LOS path as well as a cluster of reflected, delayed paths. Therefore, the scenario may be characterized by a two-ray model. Based on [Neu87] and [Eln92] and for simplicity, the direct path is proposed to be modelled as a constant process and the diffuse channel component as a Rayleigh process. In [Dye97] large varying Rice factors of  $K_{Rice} \approx 2 \dots 20$  dB were determined.  $K_{Rice} = 2$  dB is the worst case reported. Comparing these results with the measurements in [Eln92], it shows that the distance between the LOS peak and the peak of the diffuse components is 18 dB. Summing up the whole diffuse power, the distance further decreases by about 3 dB, leading to a typical Rice factor for this model of  $K_{Rice} = 15$  dB.

Doppler: The en-route scenario is characterized by fast fading. The conditions that occur are  $v_{max} = 440$  m/s for ground-air links and  $v_{max} = 620$  m/s for air-air links. The

minimum speed is assumed to be about  $v_{min} = 17$  m/s. The scattered components are typically not isotropically distributed, i.e. the beam width of the scattered components is less than  $360^\circ$ . In [Eln92], a beam width of about  $\beta = 3.5^\circ$  was computed and a corresponding Doppler spectrum was derived, assuming that the scatterers are uniformly distributed within the beam width, compare Fig. 2.5. The dithered area indicates the direction of arrival of the scattered components. This non-isotropical distribution results in a Doppler probability density function that is only a part of the classical 2-D isotropic Doppler density function derived by R.H. Clarke [Cla68][Gan72] and sometimes dubbed Jakes distribution

$$p_{f_D}(f_D) = \begin{cases} \frac{1}{\pi f_{Dmax} \sqrt{1-(f_D/f_{Dmax})^2}} & \text{if } |f_D| < f_{Dmax} \\ 0 & \text{else.} \end{cases} \quad (2.14)$$

If the scattering is 2-D uniform within a narrow beam width of, for example  $\varphi_{a_L} < \varphi_a < \varphi_{a_H}$ , where  $\varphi_{a_L}$  is the lowest angle and  $\varphi_{a_H}$  is the highest angle of arrival, compare Fig. 2.5, it has to be distinguished between the following cases:

(1) If  $0 \leq \varphi_{a_L} < \varphi_{a_H} \leq \pi$  [Eln92]

$$p_{f_D}(f_D) = \begin{cases} \frac{1}{(\varphi_{a_H} - \varphi_{a_L}) f_{Dmax} \sqrt{1-(f_D/f_{Dmax})^2}} & \text{if } f_{Dmax} \cos \varphi_{a_H} < f_D < f_{Dmax} \cos \varphi_{a_L} \\ 0 & \text{else,} \end{cases} \quad (2.15)$$

is obtained.

(2) If  $\pi \leq \varphi_{a_L} < \varphi_{a_H} \leq 2\pi$

$$p_{f_D}(f_D) = \begin{cases} \frac{1}{(\varphi_{a_H} - \varphi_{a_L}) f_{Dmax} \sqrt{1-(f_D/f_{Dmax})^2}} & \text{if } f_{Dmax} \cos \varphi_{a_L} < f_D < f_{Dmax} \cos \varphi_{a_H} \\ 0 & \text{else,} \end{cases} \quad (2.16)$$

is obtained.

(3) All other cases (i.e., if the beam width crosses 0 or  $\pi$ ) can be constructed by adding the probability density functions (2.15) and (2.16), where the terms of the sum have to be weighted according to their likelihood. Example: If the scatterers  $\{\varphi_{a_L}^{(1)} = 0, \varphi_{a_H}^{(1)} = \pi/4\}$  and  $\{\varphi_{a_L}^{(2)} = 3\pi/2, \varphi_{a_H}^{(2)} = 2\pi\}$  are received, then the first term of the sum must be weighted by 1/3 and the second term must be weighted by 2/3.

In the derivation of (2.15) and (2.16) the fact that  $\arcsin(\cos(x)) = \pi/2 - |x|$  for all  $|x| \leq \pi/2$  is used. The area under the probability density function is normalized to be one in (2.15) and (2.16). In the limit for  $\varphi_{a_L} = 0$  and  $\varphi_{a_H} = 2\pi$  (case 3), the classical Doppler spectrum is obtained. The same applies for  $\varphi_{a_L} = 0$  and  $\varphi_{a_H} = \pi$  (case 1) or for  $\varphi_{a_L} = \pi$  and  $\varphi_{a_H} = 2\pi$  (case 2).

The model may be improved by assuming 3-D scattering and by assuming Gaussian distributed angles. Also, the beam width depends on the distance between transmitter

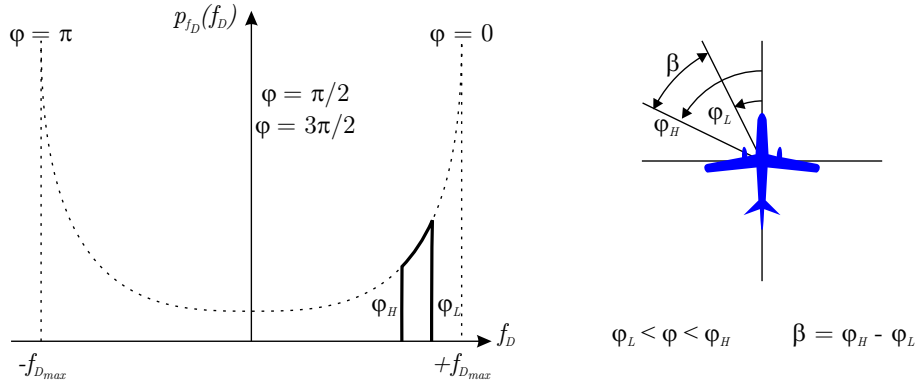


Figure 2.5: Doppler power spectrum for non-isotropic 2-D scattering

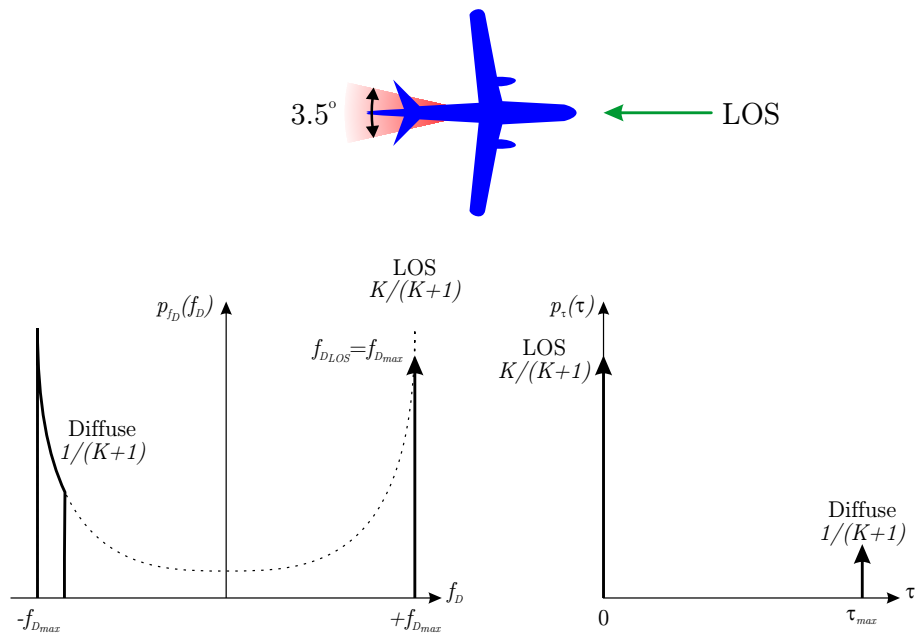


Figure 2.6: Doppler power spectrum and delay power spectrum for en-route scenarios

and receiver: the beam width is likely to decrease with increasing distance. As a worst case, the direction of the LOS path coincides with the heading of the aircraft resulting in a carrier shift of the LOS path of  $f_{D,LOS} = f_{D,max}$ , whereas the scattered components come from behind. This worst case is assumed in Fig. 2.6.

Delay: Worst-case echo delays of approximately  $200 \mu s$  ( $\Delta d = 60$  km) for ground-air links and up to  $1$  ms ( $\Delta d = 300$  km) and more for air-air links are reported in [RTC93]. In [Dye97], worst case echo delays of  $6 \dots 8 \mu s$  ( $\Delta d = 1.8 \dots 2.4$  km) are reported for ground-air links during take-off and landing approaches, where the maximum distance was  $19 - 37$  km from the airport. The latter numbers are considerably smaller.

A simple geometrical analysis reveals that  $\Delta d \approx h$  for ground-air links and  $\Delta d \approx 2h$  for air-air links, if one dominant reflector is present, where  $h$  is the altitude of the aircraft above ground. This geometrical analysis is based on the fact, that during the flight, the

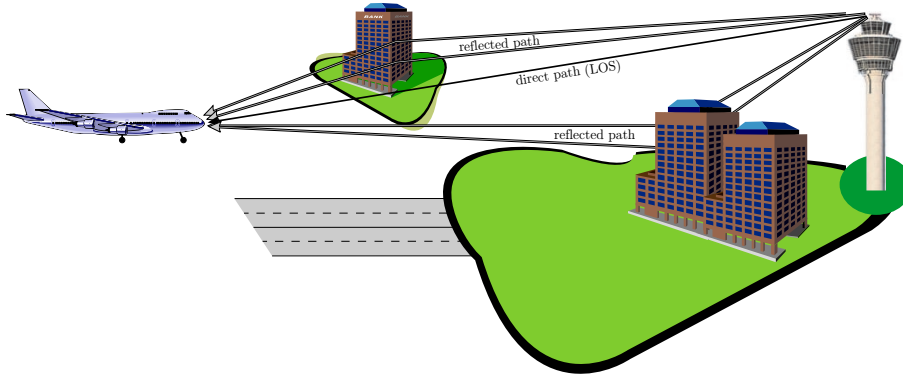


Figure 2.7: Multipath propagation for arrival scenarios

aircraft distance to the base station is large compared to its altitude, so that the projected distance on the ground is about the same as the real distance. If reflection, scattering or diffraction occurs on objects on the ground, the maximum detour distance can be estimated to be the aircraft altitude for ground-air communication and twice the altitude for air-air communication. Assuming a typical maximum altitude of 10 km, one obtains  $\tau_{max} \approx 33 \mu s$  for ground-air links and  $\tau_{max} \approx 66 \mu s$  for air-air links. These values are assumed in the following as typical values, if no ducting effects are taken into account.

Doppler and delay power spectra are plotted in Fig. 2.6. This scenario will result in fast fading, particularly for air-air links, as well as frequency-selective fading, particularly for small Rice factors, given the worst case parameters.

### 2.2.2 Arrival and Take-Off Scenario

The arrival/take-off scenario is applied when the aircraft is engaged in ground-air communication, already has left its cruising speed and altitude and is about to land and vice versa, compare Fig. 2.7. This scenario is likely to be a mixture of the en-route scenario and the taxi scenario described later. It is unlikely to be the worst case, but since the aeronautical datalink, that is investigated in this work, is particularly used during the arrival of an aircraft at the airport, a special arrival scenario is proposed here for this case. A take-off scenario would be similar with the difference of inverted Doppler frequencies.

Type of fading: It can be assumed that the LOS path is present during the arrival while the aircraft is still airborne. On the other hand, there will be also scattered path components, mainly from buildings at the airport itself, that can be modelled by a Rayleigh process. The result is again a Rician channel. The Rice factor is set to  $K_{Rice} = 15$  dB assuming a strong LOS component. This assumption is substantiated by measurements at different airports presented in [Dye97] where, neglecting some small outlier percentage, the calculated Rice factor was above 15 dB with the average Rice factor being even higher at 18 dB.

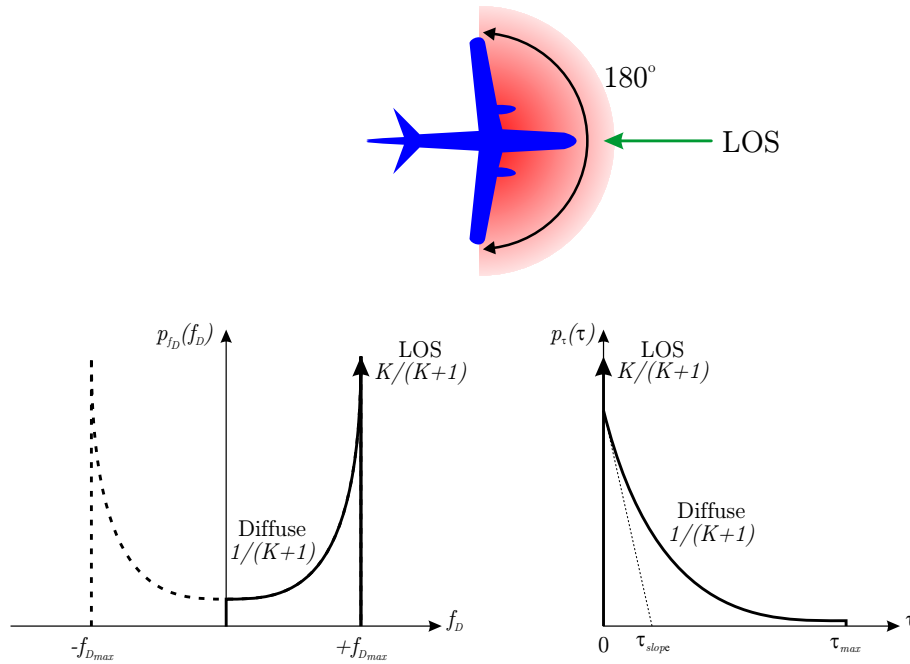


Figure 2.8: Doppler power spectrum and delay power spectrum for arrival scenarios

**Doppler:** The scenario is characterized by fast fading:  $v = 25 \dots 150$  m/s during the arrival of the aircraft. The scattered components are not isotropically distributed, but are assumed to arrive at the front of the aircraft. The beam width of the scattered components is broader than in the en-route environment but typically will be narrower than in the taxi environment. This can be justified by the fact that the base station will in general be located at the airport itself, so that the scattered components will result from reflections on buildings, aircrafts or other obstacles in the airport area. The beam width is assumed to be  $\beta = 180^\circ$  resulting in the Doppler spectrum of Fig. 2.8. The LOS path is assumed to arrive directly in front of the aircraft resulting in a carrier shift of the LOS path of  $f_{D_{LOS}} = f_{D_{max}}$ .

**Delay:** Since the aircraft is still some distance away from the airport, excess delays up to  $\tau_{max} = 7 \mu\text{s}$  are assumed in correspondence to [Dye97]. This is equal to  $\Delta d = 2100$  m. The limit stays below the value for en-route scenarios. The delay power spectrum is likely to switch from a two-ray scenario towards a rural area characteristic. This necessitates that the excess delays are assumed to be exponentially decreasing as shown in Fig. 2.8. The pdf of such a one-sided delay power spectrum is expressed by

$$p_{\tau}(\tau) = \begin{cases} \frac{1}{\tau_{slope}(1-e^{-\tau_{max}/\tau_{slope}})} e^{-\tau/\tau_{slope}} & \text{if } 0 < \tau \leq \tau_{max} \\ 0 & \text{else,} \end{cases} \quad (2.17)$$

where  $1/\tau_{slope}$  is the slope and  $\tau_{slope}$  is expected to be  $1 \mu\text{s}$  here.

This scenario should not give the worst case results, since a strong LOS path can always be expected due to the proximity to the base station at the airport. Still, the high Doppler shift of the LOS path should be noted.

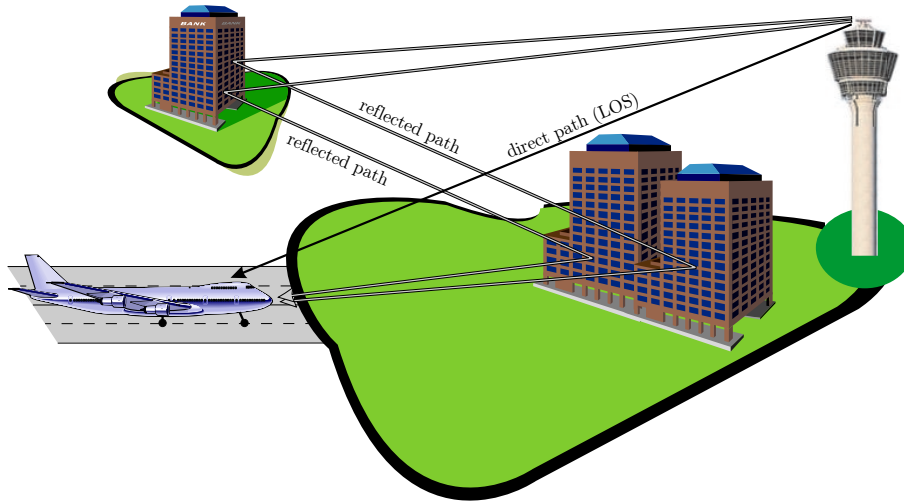


Figure 2.9: Multipath propagation for taxi scenarios

### 2.2.3 Taxi Scenario

The taxi scenario is applied when the aircraft is on the ground and traveling towards or from the terminal as shown in Fig. 2.9. The Doppler and delay power spectra and the Rice factor are based on the recommendations for rural (non-hilly) areas in [COS88].

Type of fading: Rician fading is assumed in the rural area environment according to [COS88].

The suggested Rice factor is calculated by

$$K_{Rice} = \frac{0.91^2}{0.41^2} = \frac{0.83}{0.17} = 4.9 = 6.9 \text{ dB}. \quad (2.18)$$

Doppler: This scenario is characterized by slow fading:  $v = 0 \dots 15$  m/s are typical speeds during taxi. The worst case speed during taxi is assumed to be 50 m/s. As a worst case, 2-D isotropic scattering can be assumed, i.e., the echoes are assumed to arrive equally distributed from all directions within a plane: the beam width of the scattered components is  $\beta = 360^\circ$ . In this case, the classical Doppler power spectrum (2.14) applies [COS88], see Fig. 2.10. The LOS path is assumed to come slantwise from the front resulting in a carrier shift of the LOS path of  $f_{D_{LOS}} = 0.7 \cdot f_{D_{max}}$ .

Delay: The rural area specified by [COS88] implies a maximum delay of  $\tau_{max} = 0.7 \mu\text{s}$  corresponding to  $\Delta d = 210$  m. The delay is exponentially decreasing with a suggested slope time of  $\tau_{slope} = 1/9.2 \mu\text{s}$ , compare Fig. 2.10. The COST-207 models assume UHF-frequencies around 900 MHz. A re-scaling of the delay profile from UHF frequencies may be done. However, since inflexion and reflection effects (as a function of frequency) are partly compensating each other, the power delay profile is expected to be similar at other mobile communications frequency bands.

Even though the maximum Doppler and the maximum delay have decreased, the decrease in the Rice factor of this scenario compared to the en-route and the arrival scenario will lead to more severe fading of the signal.

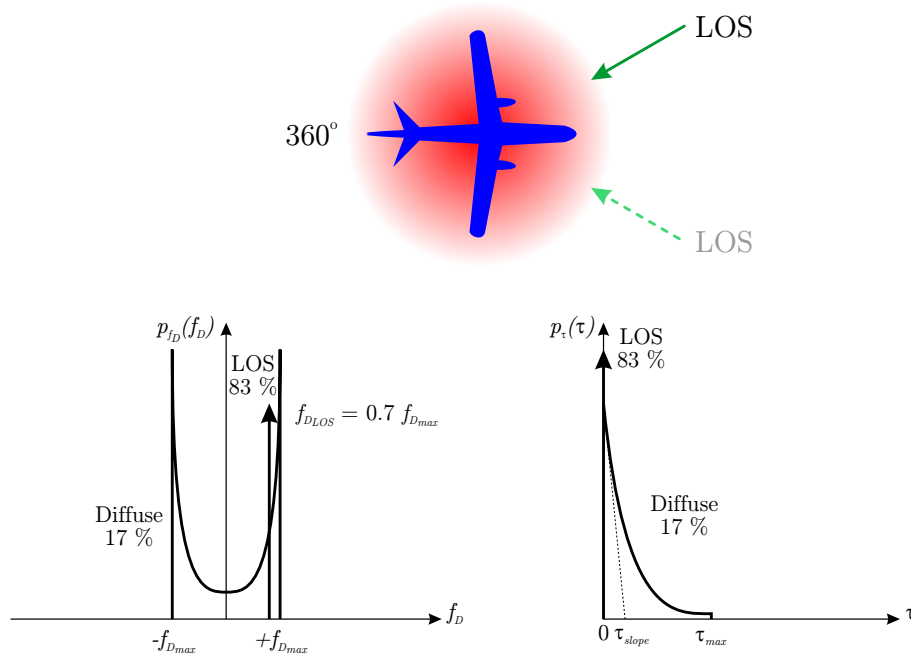


Figure 2.10: Doppler power spectrum and delay power spectrum for taxi scenarios

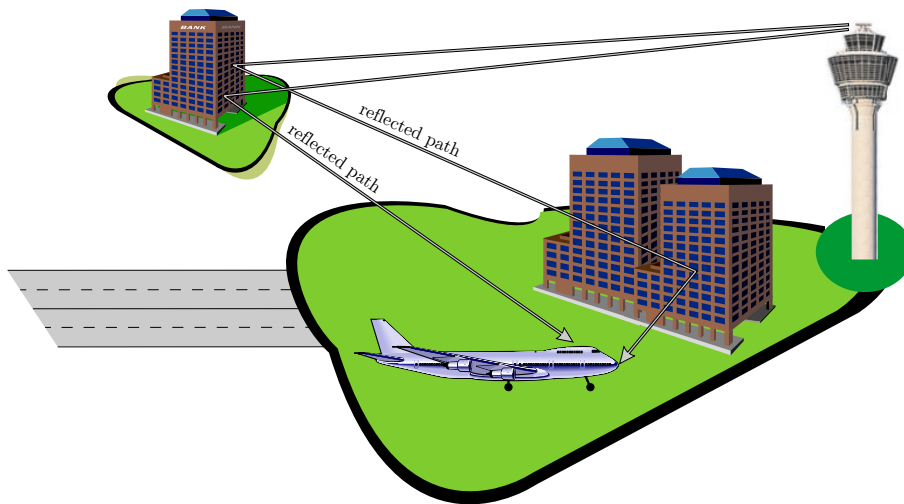


Figure 2.11: Multipath propagation for parking scenarios

### 2.2.4 Parking Scenario

The parking scenario is applied when the aircraft is on the ground and travelling at very slow speed close to the terminal or is parked at the terminal as shown in Fig. 2.11. The Doppler and delay power spectra are based on the recommendations for urban (non-hilly) areas in [COS88].

Type of fading: The LOS path is assumed to be blocked in this scenario which results in Rayleigh fading. This is the worst case assumption. The airport ground station should of course always be installed in a place where there is a line of sight to all aircrafts, taxiing

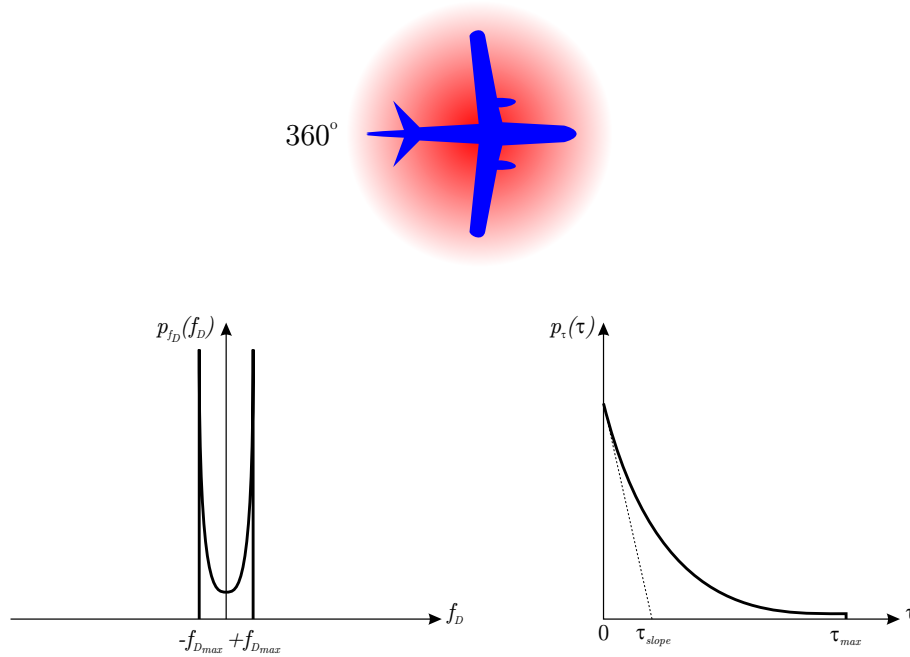


Figure 2.12: Doppler power spectrum and delay power spectrum for parking scenarios

or parking, which is, due to the high density on airports, not always possible.

**Doppler:** Due to the fact that the aircraft is parked at the terminal or travelling at very slow speed, the fading is even slower than in the taxi scenario:  $v = 0 \dots 5.5$  m/s is a typical range of velocities if the aircraft arrives at the terminal. Again, the classical Jakes distribution (2.14) can be assumed for the Doppler frequencies  $f_D$ , compare Fig. 2.12. Due to the low Doppler frequencies, the actual shape of the spectrum is only of minor influence. For 3-D isotropic scattering the Doppler power spectrum would be rectangular with  $|f_D| < f_{Dmax}$ , which is less critical.

**Delay:** A typical urban environment is proposed like specified in [COS88] with a maximum delay of  $\tau_{max} = 7 \mu\text{s}$  corresponding to  $\Delta d = 2100$  m. The distribution of the delays again is exponentially decreasing with a slope time of  $\tau_{slope} = 1 \mu\text{s}$ .

Since the LOS path is blocked, the information contained in the received signal has to be reconstructed from the echo paths alone. The fading will be frequency-selective with increasing bandwidth of the signal. The problem with this scenario for traditional narrowband systems with a single Tx and a single Rx antenna is the “red light effect”<sup>1</sup>. Wideband signal design with spreading and channel coding in conjunction with interleaving, as proposed in this work, are counteractions for compensating the fading effect.

<sup>1</sup>The “red light effect” is familiar in the context of VHF/FM mobile radio: The signal strength may fade within half a wave-length, i.e. depending where the mobile stops. The “red light effect” may be compensated by a measure known as Rx antenna diversity. Optimizing the transmitter position (given a single Tx antenna) may be not possible for all situations.

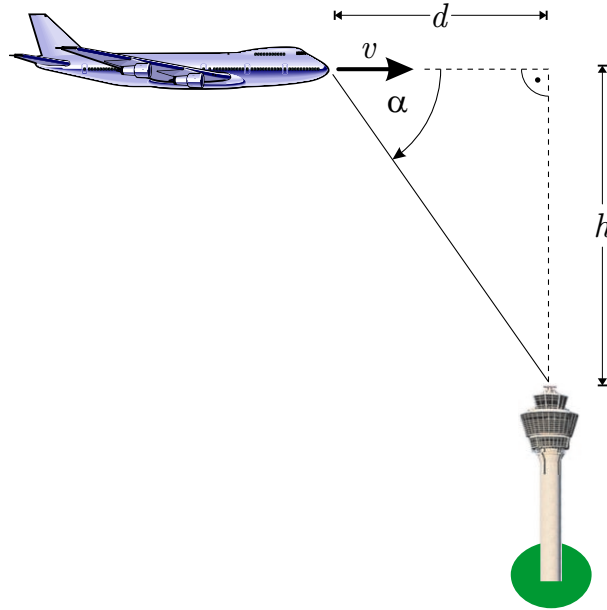


Figure 2.13: Aircraft flying over ground station

### 2.2.5 Aircraft Flying Over Ground Station

So far, the static conditions during the different states of a flight, by the means that the Doppler power spectrum and the delay power spectrum remains unchanged, have been presented. However, dedicated flight situations cannot be described by these models. If for example the aircraft passes a ground station during the flight, the sign of the Doppler changes. This situation is depicted in Fig. 2.13. The Doppler does not change its sign abruptly, but the Doppler frequency is continuously decreasing with decreasing projected distance  $d$  of an aircraft flying over the ground station in altitude  $h$ . The so-called maximum Doppler rate  $f'_{D_{max}}$ , which means the maximum Doppler frequency change per second, is obtained for this condition when the distance on the ground is  $d = 0$ . It gives an indication how fast the receiver for example has to adopt to a new Doppler shift of the LOS path.  $f'_{D_{max}}$  is derived as follows:

$$f_D(t) = f_{D_{max}} \cdot \cos(\alpha(t)) = f_{D_{max}} \cdot \frac{d(t)}{\sqrt{d^2(t) + h^2}} \quad (2.19)$$

is the current Doppler of the LOS path, where  $\alpha(t)$  is the angle between the heading of the aircraft and the ground station. With

$$d(t) = d_0 - vt, \quad (2.20)$$

where  $d_0$  is the distance at time  $t = 0$ ,

$$f'_{D_{max}} = \left. \frac{df_D(t)}{dt} \right|_{t=d_0/v} = f'_D \left( \frac{d_0}{v} \right) = -f_{D_{max}} \cdot \frac{v}{h} = -f_c \cdot \frac{v^2}{c \cdot h} \quad (2.21)$$

is obtained, see Appendix A. The expected maximum speed while the aircraft passes the ground station is  $v_{max} = 440$  m/s. For air-air communications, the scenario can be altered

to  $v_{max} = 620$  m/s and  $h$  is replaced by the distance between the heading paths of the two aircrafts.

Aircraft turns are another scenario that cause a Doppler rate, but in general lead to lower values of the frequency change, so that the aircraft flying over a ground station is supposed to be the worst case scenario for the Doppler rate.

## 2.2.6 Summary of Channel Parameters

To complete the list of possible aeronautical scenarios, Table 2.1 gives a set of parameters for the typical values that are proposed for simulations. Since most of the aeronautical transmission systems have to be available and reliable even in environment-critical conditions, expected worst case values are used for the parameters. The en-route scenario is divided into ground-air and air-air links. Note that only the aircraft velocity is given here since the maximum Doppler frequency  $f_{D_{max}} = f_c \cdot v/c$  depends on the chosen carrier frequency  $f_c$ . The second lines of the aircraft velocity, maximum delay and Rice factor indicate the range, where 'typ.' are typical values from a Boeing 747-400. For simulations, always the given maximum velocity should be chosen, since this is a long-term operating condition, whereas large maximum delays and small Rice factors in a specific scenario are only short-term effects and the chosen values represent typical conditions. The worst case assumptions of echoes from behind the aircraft for the en-route scenario can be altered to typically come from any direction with a  $\beta = 3.5^\circ$  beamwidth which would, due to the strong LOS path, not change the performance very much. It has to be mentioned though, that the presented typical values in the upper lines should be used for simulations to have a fixed set of simulation parameters. Choosing other values from the possible ranges would soften the scenarios and make simulation results from different sources difficult to compare.

## 2.3 Channel Emulation

In this section two channel emulators are presented; one for a flat fading channel and one for a frequency-selective fading channel.

### 2.3.1 WSSUS Model

According to Bello, the so called Wide-Sense Stationary Uncorrelated Scattering (WSSUS) channel model provides a useful *small-area* characterization of the diffuse components of multipath radio channels [Bel63]. The time-varying weight function of a WSSUS process can be approximated by [Hoe92]

$$h(\tau, t) = \lim_{N \rightarrow \infty} \frac{1}{\sqrt{N}} \sum_{n=1}^N \underbrace{e^{j\theta_n}}_{\text{phase}} \cdot \underbrace{e^{j2\pi f_{D_n} t}}_{\text{Doppler}} \cdot \underbrace{\delta(\tau - \tau_n)}_{\text{delay}}, \quad (2.22)$$

Table 2.1: Set of typical aeronautical scenarios for simulations

	Parking scenario	Taxi scenario	Arrival scenario	En-route scenario ground-air/air-air
Aircraft velocity $v$ [m/s]	5.5 0...5.5	15.0 0...15	150.0 25...150 typ. 85	440.0/620.0 17...440 typ. 250
Maximum delay $\tau_{max}$ [s]	$7.0 \cdot 10^{-6}$	$0.7 \cdot 10^{-6}$	$7.0 \cdot 10^{-6}$	$33 \cdot 10^{-6}/66 \cdot 10^{-6}$ $6 \cdot 10^{-6} \dots 200 \cdot 10^{-6}$
Number of echo paths $N$	20	20	20	20
Rice factor $K_{Rice}$ [dB]	-	6.9	15.0 9...20	15.0 2...20
$f_{D_{LOS}}/f_{D_{max}}$ factor	-	0.7	1.0	1.0
Start angle $\varphi_{a_L}$ of beam [°]	0.0	0.0	-90.0	178.25
End angle $\varphi_{a_H}$ of beam [°]	360.0	360.0	+90.0	181.75
Exponential or 2-ray delay	exp	exp	exp	two-ray
Slope time $\tau_{slope}$ [s]	$1.0 \cdot 10^{-6}$	$(1/9.2) \cdot 10^{-6}$	$1.0 \cdot 10^{-6}$	-

where  $t$  is the absolute time and  $\tau$  is the excess delay. In the time-invariant case the weight function is  $h(\tau) \forall t$ . The random numbers  $\theta_n$  ( $0 \leq \theta_n < 2\pi$ ),  $f_{D_n}$  ( $-f_{D_{max}} \leq f_{D_n} \leq f_{D_{max}}$ ) and  $\tau_n$  ( $0 \leq \tau_n \leq \tau_{max}$ ) have to be generated a-priorily, i.e., before the simulation run according to the chosen scenario, where  $p(\tau, f_D) \sim P_s(\tau, f_D)$  and  $p(\theta) = 1/(2\pi)$ . An intuitive interpretation of (2.22) is that  $h(\tau, t)$  is an incoherent superposition of  $N$  echoes, where each echo is characterized by a random phase,  $\theta_n$ , a random delay,  $\tau_n$ , and a random Doppler shift,  $f_{D_n}$ ,  $1 \leq n \leq N$ . The factor  $\sqrt{1/N}$  ensures that the average power is one; this factor is the same for all echoes and for all spectra. According to the central limit theorem (i.e., when  $N$  is large)  $h(\tau, t)$  is a complex Gaussian process, therefore its amplitude is Rayleigh distributed.

### 2.3.2 Flat Fading

The flat fading emulator is obtained from (2.22) by substituting  $\tau_n = 0 \forall n$ :

$$h(t) = \lim_{N \rightarrow \infty} \frac{1}{\sqrt{N}} \sum_{n=1}^N \underbrace{e^{j\theta_n}}_{\text{phase}} \cdot \underbrace{e^{j2\pi f_{D_n} t}}_{\text{Doppler}}, \quad (2.23)$$

with its corresponding frequency domain realization, compare Fig. 2.3,

$$T(t) = \mathcal{F}_\tau\{h(\tau, t)\} = \lim_{N \rightarrow \infty} \frac{1}{\sqrt{N}} \sum_{n=1}^N \underbrace{e^{j\theta_n}}_{\text{phase}} \cdot \underbrace{e^{j2\pi f_{D_n} t}}_{\text{Doppler}}. \quad (2.24)$$

It can be noted, that the time-variant weight function does not depend on  $\tau$ , so that the time-variant transfer function does not depend on  $f$  either and therefore is identical. Thus, all frequencies are influenced in the same way.

### 2.3.3 Frequency-Selective Fading

The time domain representation of a frequency-selective fading channel is already given by (2.22) with  $\tau_n \neq 0 \exists n$ . The time-variant channel transfer function is given by

$$T(f, t) = \mathcal{F}_\tau \{h(\tau, t)\} = \lim_{N \rightarrow \infty} \frac{1}{\sqrt{N}} \sum_{n=1}^N \underbrace{e^{j\theta_n}}_{\text{phase}} \cdot \underbrace{e^{j2\pi f D_n t}}_{\text{Doppler}} \cdot \underbrace{e^{-j2\pi f \tau_n}}_{\text{delay}}. \quad (2.25)$$

At least 25 echoes ( $N \geq 25$ ) have to be used in order to emulate the flat fading and frequency-selective fading channels well, if the parameter set  $\{\theta_n, f_{D_n}, \tau_n\}$  is generated once before the simulation starts. However, only about 7-10 echoes ( $N = 7-10$ ) are sufficient, if new parameter sets are generated from time to time, given the same statistics [Jak74, pp. 68-69][Hoe92]. That way, the real-time effort for a simulation can be reduced significantly.

## 2.4 Implementation on Digital Signal Processing Systems

Channel models are used in signal processing systems to simulate the different conditions of a transmission between the transmitter and the receiver. Most simulation tools are based on discrete time and/or discrete frequency domains. For that purpose, the time- and frequency-continuous models are transferred to the corresponding discrete realizations.

### 2.4.1 Choice of Doppler, Delay and Phase

As discussed in [Hoe92],  $\theta_n$ ,  $f_{D_n}$  and  $\tau_n$  may be generated by a functional transformation

$$v_n = g_v(u_n) = P_v^{-1}(u_n), \quad 1 \leq n \leq N, \quad (2.26)$$

where  $v_n$  is a substitute for  $\theta_n$ ,  $f_{D_n}$  and  $\tau_n$ , respectively,  $u_n \in (0, 1)$  is a random, uniformly distributed input variable produced by a random number generator and  $g_v(u_n)$  is a memoryless nonlinearity, which is the inverse of the desired cumulative distribution function  $P_v^{-1}(\cdot)$ .

The Doppler power spectra and the delay power spectra suggested in Section 2.2 can be generated as follows.

The classical Doppler spectrum (2.14) with application of (2.26) results in the nonlinearity

$$f_{D_n} = g_{f_D}(u_n) = f_{D_{max}} \cdot \cos(\pi \cdot u_n). \quad (2.27)$$

If the scattering is 2-D uniform non-isotropic

$$f_{D_n} = g_{f_D}(u_n) = f_{D_{max}} \cdot \cos(\varphi_{a_L} + (\varphi_{a_H} - \varphi_{a_L}) \cdot u_n). \quad (2.28)$$

is obtained for all three cases mentioned in Section 2.2.1. In the limit for  $\varphi_{a_L} = 0$  and  $\varphi_{a_H} = 2\pi$  (case 3), the classical Doppler spectrum is obtained. Note that the same applies for  $\varphi_{a_L} = 0$  and  $\varphi_{a_H} = \pi$  (case 1) or for  $\varphi_{a_L} = \pi$  and  $\varphi_{a_H} = 2\pi$  (case 2).

The nonlinearity for the one-sided exponentially decreasing delay power spectrum of (2.17) is

$$\begin{aligned}\tau_n = g_\tau(u_n) &= -\tau_{slope} \cdot \log_e \left( 1 - u_n (1 - e^{-\tau_{max}/\tau_{slope}}) \right) \\ &\approx -\tau_{slope} \cdot \log_e (1 - u_n) \text{ for } \tau_{max} \gg \tau_{slope}.\end{aligned}\quad (2.29)$$

It can be noted that for  $\tau_{max} \gg \tau_{slope}$  the slope,  $\tau_{slope}$ , is more important than the maximum excess delay,  $\tau_{max}$ .

These examples indicate that the parameters  $\tau_n$  and  $f_{D_n}$  (representing the excess delays respectively Doppler frequencies of  $N$  discrete echoes) can be quite easily generated by feeding a uniformly distributed random variable,  $u_k \in (0, 1)$ , into a simple nonlinearity (which may be implemented as a table look-up). Uniform random number generators are usually available on digital computers. Via (2.26), a frequency-modulated raster is generated inherently, i.e., most echoes are generated near positions where the probability density function has its maximum.

## 2.4.2 Discrete Time Realization

It is well established that the overall channel of a time-continuous linear transmission system, shown in Fig. 2.14a, can be exactly represented by the *equivalent discrete-time model* [Pro95] shown in Fig. 2.14b. The equivalent discrete-time model comprises pulse-shaping/filtering in transmitter and receiver, the physical channel, and sampling. All effects are represented by its complex-valued coefficients. Particularly, the Rx filter may be any linear filter, not necessarily a matched filter. The sampling rate is arbitrary. The equivalent discrete-time model is suitable for computer simulations. In order to model WSSUS channels, no excessive oversampling (in order to represent the delays) is necessary. The discrete noise process in Fig. 2.14b is obtained by filtering the continuous noise process in Fig. 2.14a with the Rx filter response, and sampling the result of the convolution. For ideal low-pass filters and square-root raised-cosine filters, for example, the discrete noise process is white within the signal bandwidth. In Fig. 2.14  $x_k$  are the complex-valued input samples and  $y_k$  the complex-valued output samples, respectively. The Tx filter  $g_{Tx}(\tau, t)$  is denoted as  $g_{Tx}(\tau)$ , since it is assumed to be time-invariant. The same applies for the Rx filter  $g_{Rx}(\tau)$ . The intention now is to model the coefficients of the discrete-time channel efficiently without introducing any further simplifications. It is assumed that echo-raster and sampling-raster do not agree, since a physical channel does not possess an echo-raster. Generally, this leads to correlations between the coefficients, which are inherently included in the formula. The assumption of uncorrelated coefficients, seen in many papers, is a simplification.

The coefficients of the *equivalent discrete-time model* are denoted by  $h_k(i)$ , where  $k$  is the time index  $t = k \cdot T_{sample}$  and  $i$  is the tap index,  $-L_- \leq i \leq L_+$ . The number of coefficients taken

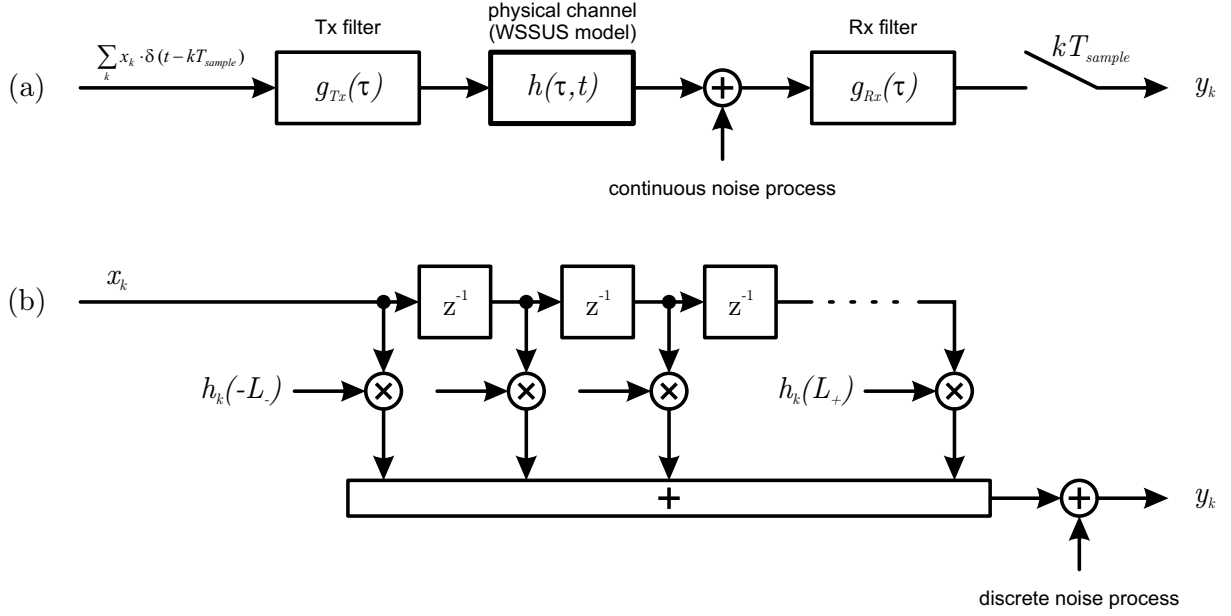


Figure 2.14: Time continuous linear transmission system (a) and its equivalent discrete-time model (b)

into account is  $1 + L_- + L_+$ . As a result, one obtains [Hoe92]

$$h_k(i) = \frac{1}{\sqrt{N}} \sum_{n=1}^N \underbrace{e^{j\theta_n}}_{\text{phase}} \cdot \underbrace{e^{j2\pi f_{Dn} k T_{\text{sample}}}}_{\text{Doppler}} \cdot \underbrace{g_{\text{total}}(iT_{\text{sample}} - \tau_n)}_{\text{delay}}, \quad -L_- \leq i \leq L_+, \quad (2.30)$$

where  $g_{\text{total}}(\tau) = g_{Tx}(\tau) * g_{Rx}(\tau)$  is the overall impulse response of the transmitter and the receiver. The flat fading case is a special case where  $\tau_n = 0$  (no delays) and  $i = 0$  (just one tap) resulting in

$$h_k = \frac{1}{\sqrt{N}} \sum_{n=1}^N \underbrace{e^{j\theta_n}}_{\text{phase}} \cdot \underbrace{e^{j2\pi f_{Dn} k T_{\text{sample}}}}_{\text{Doppler}} \cdot \underbrace{g_{\text{total}}(0)}_{\text{delay}}. \quad (2.31)$$

The average power of the coefficients,  $\rho_i = \mathbb{E}\{|h_k(i)|^2\}$ , is

$$\rho_i = \int_0^{\tau_{\text{max}}} p(\tau) |g_{\text{total}}(iT_{\text{sample}} - \tau)|^2 d\tau, \quad -L_- \leq i \leq L_+, \quad (2.32)$$

where  $p(\tau) = \int_{f_D} p(\tau, f_D) df_D$ . The overall pulse,  $g_{\text{total}}(\tau)$ , must be normalized so that  $\sum_i \rho_i = 1$ . To guarantee a compliance with the statistics, about ten to twenty echoes ( $N \approx 10 - 20$ ) are applied for aeronautical channel modelling for the case that new parameter sets are generated from time to time.

As an alternative, if  $g_{\text{total}}(\tau)$  is assumed to be unknown or if the filtering process is non-linear, the discrete output signal  $y_k$  of the physical channel  $h(\tau, t)$  may be modelled from the discrete input signal  $x_k$  as follows:

$$y_k = \frac{1}{\sqrt{N}} \sum_{n=1}^N e^{j(\theta_n + 2\pi f_{Dn} k T_{\text{sample}})} \cdot \sum_{i=\text{nint}(\tau_n/T_{\text{sample}}) - L/2}^{\text{nint}(\tau_n/T_{\text{sample}}) + L/2} x_{k-i} \cdot \text{si}\left(\pi(i - \tau_n/T_{\text{sample}})\right), \quad (2.33)$$

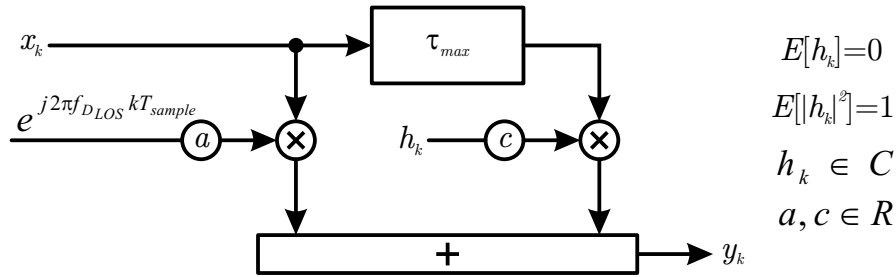


Figure 2.15: Two-ray model of the aeronautical channel for the en-route scenario

where  $\text{nint}(\cdot)$  denotes the nearest integer, and  $\text{si}(x) = \sin(x)/x$ , i.e.  $g_{\text{total}}(\tau)$  is replaced by an ideal low-pass filter restricted to length  $(L + 1)$ , (e.g.,  $L \approx 20$ ).

Since the discrete weight function,  $h_k$ , jumps when new parameters are generated, carrier and clock synchronization must be acquired in the latter case. This is certainly no problem for packet (or block-oriented) transmission. The statistics are best, if new parameter sets would be generated for every block of transmitted data, i.e. each transmission frame would have another channel realization approximating the same Doppler and delay power spectra.

A Rician channel can be modelled by adding a constant to the Rayleigh process. Let us denote the complex-valued direct (LOS) component by

$$h_{\text{LOS}_k} = a \cdot e^{j2\pi f_{D_{\text{LOS}}} k T_{\text{sample}}}, \quad (2.34)$$

where  $a \in \mathcal{R}$  is the amplitude of the LOS path and  $f_{D_{\text{LOS}}}$  is the Doppler frequency of the LOS path, and let us denote the complex-valued multipath component by  $\overline{c} \cdot h_k$ , where  $c \in \mathcal{R}$  is a constant weighting factor and  $E\{|h_k|^2\} = 1$  (due to the factor  $\sqrt{1/N}$ ). The resulting transmission model for the en-route channel, only maximum delay  $\tau_{\text{max}}$  for all echoes, (without additive noise) is shown in Fig. 2.15.

### 2.4.3 Discrete Frequency Realization

Modern modulation methods for digital communications systems, like OFDM that is used in the present work, sometimes use Multi-Carrier (MC) symbols with narrow-spaced carriers of distance  $F_s$  that are combined to fill a bandwidth  $B$  and are transmitted together during time  $T_s$ . For such a case, the time-variant channel transfer function  $T(f, t)$  is of special interest. If  $\vec{\mathbf{X}} = (X_1, X_2, \dots, X_{N_c})^T$  is the transmitted signal/symbol vector in the frequency domain consisting of the elements  $X_l$  with  $l = 1 \dots N_c$  and the channel can be assumed to be constant during one MC symbol duration  $T_s$ , then (2.25) can be simplified to

$$T_l(f_l, kT_s) = \lim_{N \rightarrow \infty} \frac{1}{\sqrt{N}} \sum_{n=1}^N \underbrace{e^{j\theta_n}}_{\text{phase}} \cdot \underbrace{e^{j2\pi f_{D_n} k T_s}}_{\text{Doppler}} \cdot \underbrace{e^{-j2\pi f_l \tau_n}}_{\text{delay}}, \quad (2.35)$$

where  $f_l$  are the elements of the subcarrier frequency vector  $\vec{\mathbf{f}} = (f_1, f_2, \dots, f_{N_c})^T$  and  $T_l$  are the elements of the channel transfer vector  $\vec{\mathbf{T}} = (T_1, T_2, \dots, T_{N_c})^T$  for the frequency domain with

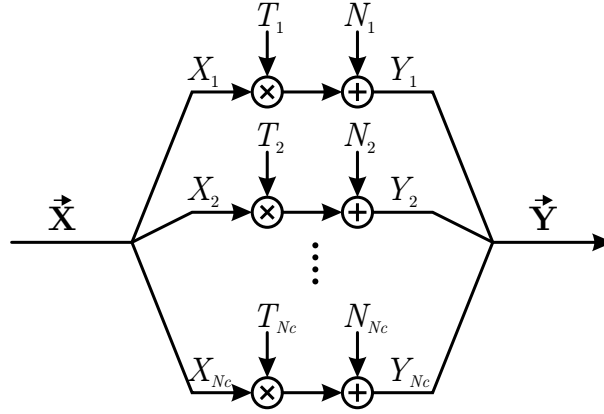


Figure 2.16: Frequency domain realization of WSSUS model

$l = 1 \dots N_c$ . The discrete time index  $k$  is used here for the chosen MC symbol. The resulting received signal vector  $\vec{Y} = (Y_1, Y_2, \dots, Y_{N_c})^T$  with additive noise  $\vec{N} = (N_1, N_2, \dots, N_{N_c})^T$  then can be written as the element-wise multiplication of

$$\vec{Y} = \vec{X} \cdot \vec{T} + \vec{N}. \quad (2.36)$$

This is a very simple representation, since it only necessitates the multiplication of each transmitted subchannel with its corresponding channel transfer function value and adding the corresponding noise, compare Fig. 2.16. On the other hand, since the channel is assumed to be constant during the duration  $T_s$  of the MC symbol, no IntersubCarrier Interferences (ICIs) are taken into account, which is an assumption that is not valid for all channel scenarios. In general, it should be assumed that the maximum Doppler  $f_{D_{max}}$  is less than 10% of the carrier spacing  $F_s$  for this case.

The aeronautical channel models that have been worked out in this chapter are applied in Sections 5.2.1 and 5.3.2 to determine the performance for coherent and differential coherent OFDM systems, respectively. The corresponding modulation and demodulation techniques are presented in Chapter 4, whereas in Chapter 3 first the different multiplexing techniques and their significance for single-carrier, spread spectrum and multi-carrier modulation are evaluated.

# Chapter 3

## Multiple Access Techniques

### 3.1 Multiplexing Techniques

Transmitting information from one entity to another entity in analog or digital communications systems has not only to comply with technical terms and restrictions, but also with the intended type of information that is exchanged.

The entities of a transmission system are in general transmitting and receiving stations. The transmission system can then be divided into two different types. The first type consists of one transmitter that transmits its information to one dedicated receiver, known as *Point-to-Point* communications. It is for example used in the up- and downlink from a mobile to the base station and vice versa in the GSM system. The second type consists of one transmitter that transmits its information to several independent receivers, known as *Point-to-Multipoint* communications or *Broadcast*. It is for example used in the Digital Audio Broadcasting (DAB) radio system.

The technical terms and restrictions that apply result from the fact that several different transmitters and receivers want to exchange different types of information in the same geographical region using point-to-point and point-to-multipoint communications. Rules have to be found for the different entities to make sure that the desired information can be separated from the undesired information in the receiver. In other words, the interference between the different entities has to be kept to a minimum.

In the following, rules are presented that outline the basis for such techniques, known as *multiplexing techniques*. These techniques are described and compared on the basis of equal energy consumption for all presented options. *Multiplexing* describes the process in which several signals are multiplexed, or combined, into a single signal domain. This signal is demultiplexed, or separated back, into the original signals on the receiving side. *Multiple Access* applies multiplexing techniques to separate the information of individual entities in one common signal domain. The multiplexing in that case does not necessarily have to take place in one transmit-

ter, but can happen implicitly through the combination of signals from different entities on the transmission channel.

### 3.1.1 Frequency Division Multiple Access - FDMA

The most commonly used multiplexing technique is known as Frequency Division Multiple Access (FDMA). In analog communications it is for example used in AM/FM radio broadcasting, where the different stations are separated by using different carrier frequencies  $f_c$  in different frequency bands. In digital communications, different entities, represented by different users here, transmit their individual data symbols of duration  $T_d$  in a bandwidth of approximately  $B_{FDMA} = 1/T_d$  at an assigned carrier frequency  $f_c$ . This situation is depicted in Fig. 3.1, where each entity is assumed to have the normalized power of one.

### 3.1.2 Time Division Multiple Access - TDMA

The second multiplexing technique is Time Division Multiple Access (TDMA). For analog communications, a radio station that has assigned time slots for the news, an entertainment program and advertisements can be considered. In digital communications, each entity again transmits its data symbol of duration  $T_d$ . Since the information of  $K$  entities has to be transmitted serially in a limited time-frame, the duration of  $T_d$  has to be decreased by  $1/K$  compared to FDMA. Therefore each entity uses an increased bandwidth of  $B_{TDMA} = 1/T_d$ , since  $1/T_d$  increases by  $K$ . This situation is shown in Fig. 3.1, where again each entity is assumed to have the normalized power of one.

### 3.1.3 Code Division Multiple Access - CDMA

Finally, there exists the possibility to separate the entities by different codes resulting in Code Division Multiple Access (CDMA). This situation in analog communications can be compared with many people in one room talking at the same time in different languages. If one dedicated language is known, it is possible to listen to the speaker with only minor distraction from other speakers. If more people would speak in the same language, it would be more complicated or even impossible to listen to one individual. In digital communications, CDMA can be achieved if every entity does not transmit its data symbol in one piece, but divides the symbol of duration  $T_d$  in  $L$  smaller parts of duration  $T_{chip}$ , known as chips. The generator rule for the  $L$  chips is known as the code of the entity. Since  $T_{chip}$  is smaller than  $T_d$ , again an increased bandwidth of  $B_{CDMA} = L \cdot 1/T_d = 1/T_{chip}$  has to be used. On the other hand, since the energy for the transmitted symbol has to remain the same, the normalized power is decreased to  $1/L$ . This situation is shown in Fig. 3.1.

The multiplexing techniques described above have all one thing in common. To regain the desired information, the receiver has to have a knowledge about how to find this information

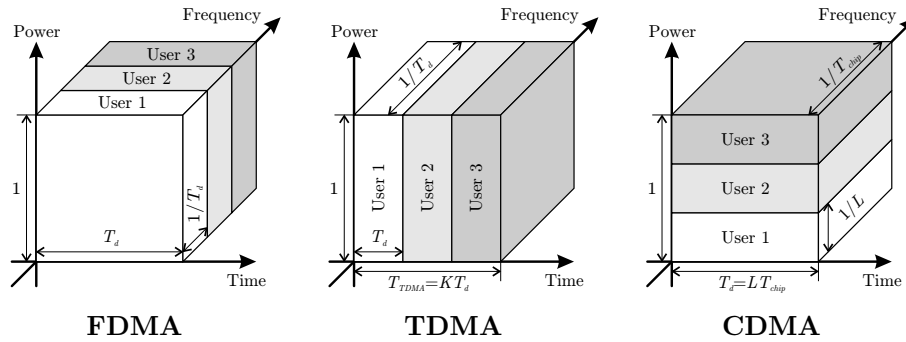


Figure 3.1: Comparison of FDMA, TDMA and CDMA multiplexing techniques assuming equal energy consumption

in the received signal and use this knowledge to synchronize on the received signal. All multiplexing techniques require the knowledge of the used carrier frequency of the transmitter entity in the receiver. For FDMA it is also necessary to regain the position of the data symbols in the received stream. For TDMA, it is necessary to regain the start of the TDMA-frame. With this and the knowledge of the position of the desired slot in the frame, it is possible to regain the position of the transmitted information. In CDMA it is necessary to know the code that was used for the generation of the chips of the desired information. Then the position of the symbols  $T_d$  can be regained in the receiver.

The different multiplexing techniques can be combined to make the transmission system more flexible to user needs. The complexity of regaining the information, that is necessary to synchronize the receiver on the transmitted data stream, not only depends on the used multiplexing technique(s), but also on the used modulation symbols. On the other hand, the synchronization complexity is not the main criteria for choosing a certain type of transmission. Even more important is the fact, how reliable the transmitted information can be regained in the receiver and how immune the transmitted signal is to effects that are implied by the physical transmission channel.

## 3.2 Differences of Single-Carrier, Spread Spectrum and Multi-Carrier Modulation

In the following, a closer look is taken on the physical structure of the transmitted digital modulated signals by means of the time and frequency domain representations for different modulation techniques. The figures used for the descriptions only symbolize the conditions and are not results of actual measurements.

### 3.2.1 Single-Carrier Modulation

According to [Pro95, Section 4-4], the power density spectrum  $\Phi_{xx}(f)$  of the equivalent lowpass representation  $x(t)$  of a transmitted digitally modulated signal is expressed by

$$\Phi_{xx}(f) = \frac{\sigma_I^2}{T_d} |G_{Tx}(f)|^2 + \frac{\mu_I^2}{T_d^2} \sum_{m=-\infty}^{\infty} \left| G_{Tx} \left( \frac{m}{T_d} \right) \right|^2 \delta \left( f - \frac{m}{T_d} \right), \quad (3.1)$$

where  $T_d$  is the duration of one complex-valued data symbol  $x_k$  of the sequence

$$x(t) = \sum_{k=-\infty}^{\infty} x_k \cdot g_{Tx}(t - kT_d), \quad (3.2)$$

$g_{Tx}(t)$  and  $G_{Tx}(f)$  are the time and frequency domain representations of the transmitter filter function and  $\mu_I$  and  $\sigma_I^2$  are the mean value and the variance of the data symbol sequence. If the data symbols are assumed to have zero mean, i.e.  $\mu_I = 0$ , the second term in (3.1) vanishes and the power density spectrum is shaped by the characteristics of the transmitter filter alone. This property is used in the following and the absolute value of the transmitted spectrum is approximated by

$$|X(f)| = |\mathcal{F}_t\{x(t)\}| \approx |G_{Tx}(f)|. \quad (3.3)$$

The basic technique for Single Carrier (SC) modulation uses rectangular pulses

$$\text{rect}(t) = \begin{cases} 1 & \text{for } |t| \leq 1/2 \\ 0 & \text{else} \end{cases} \quad (3.4)$$

and therefore the transmitter filter becomes

$$\begin{aligned} g_{Tx-rect}(t) &= \text{rect} \left( \frac{t}{T_d} \right), \\ G_{Tx-rect}(f) &= \mathcal{F}_t\{g_{Tx-rect}(t)\} = T_d \cdot \text{si}(\pi f T_d). \end{aligned} \quad (3.5)$$

The resulting absolute value of the spectrum  $|X_{SC-rect}(f)| \approx |G_{Tx-rect}(f)|$  is shown in Fig. 3.2(a), where  $F_d = 1/T_d$ . This spectrum is not limited in frequency,  $B = \infty$ , and therefore causes ICI to transmitters that use neighbouring carrier frequencies if no additional filtering is applied. For this reason, different transmitter filters are commonly used that have better spectral characteristics. For example, a Raised Cosine (RC) filter with the following characteristics can be considered

$$\begin{aligned} g_{Tx-RC}(t) &= \text{si} \left( \pi \frac{t}{T_d} \right) \cdot \frac{\cos(\alpha \pi \frac{t}{T_d})}{1 - 4 \left( \alpha \frac{t}{T_d} \right)^2} \\ G_{Tx-RC}(f) &= \begin{cases} T_d & \text{for } |f| \leq (1 - \alpha) \frac{1}{2T_d} \\ \frac{T_d}{2} \left( 1 - \sin \left( \frac{\pi T_d}{\alpha} \left( |f| - \frac{1}{2T_d} \right) \right) \right) & \text{for } (1 - \alpha) \frac{1}{2T_d} < |f| \leq (1 + \alpha) \frac{1}{2T_d} \\ 0 & \text{else} \end{cases}, \end{aligned} \quad (3.6)$$

where  $\alpha$  is the so-called roll-off factor. This filter is band-limited with the corresponding theoretical bandwidth  $B = (1 + \alpha) \cdot (1/T_d)$ . A visualization of the resulting transmitted signal

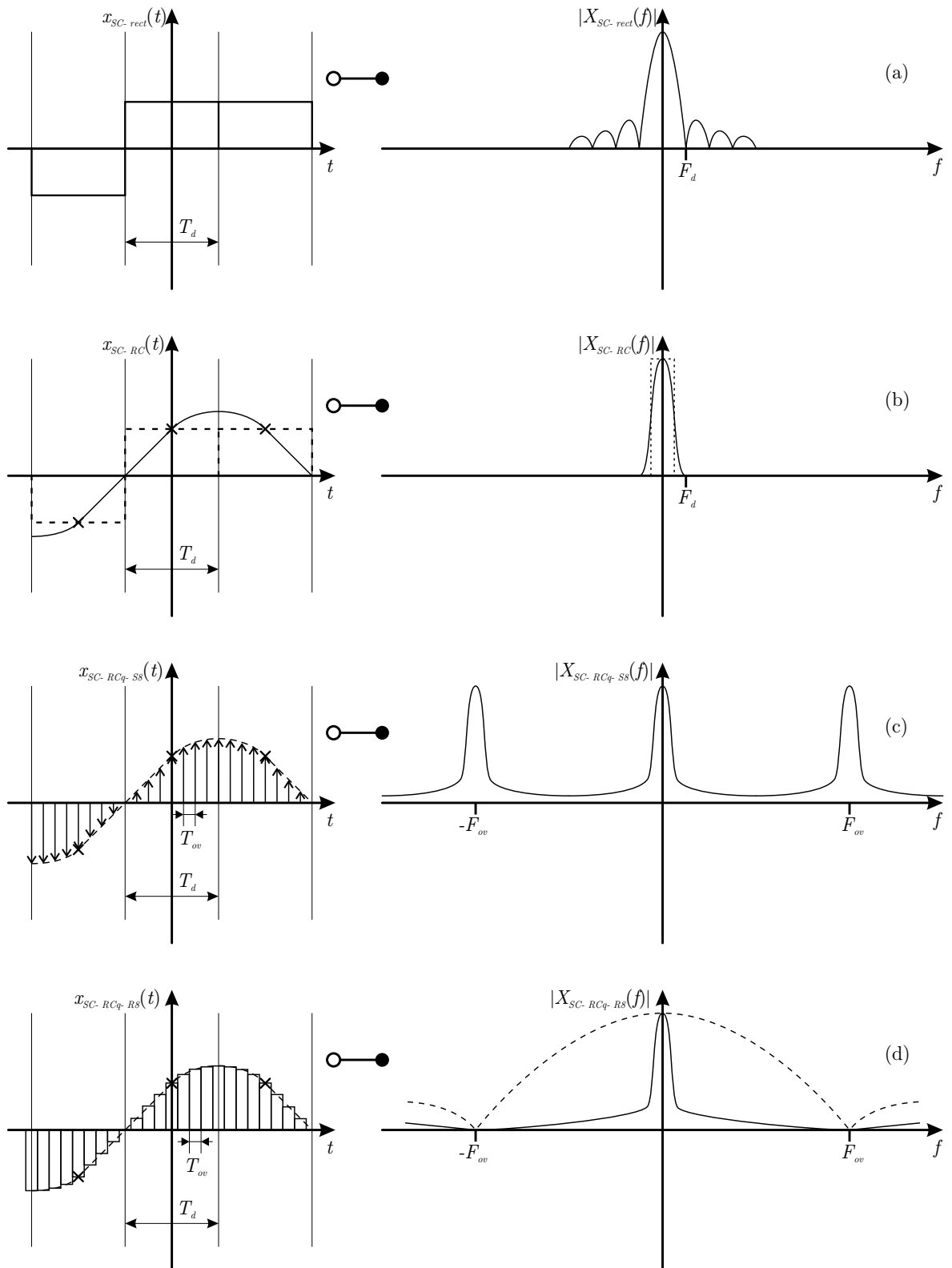


Figure 3.2: Single-carrier modulation with (a) rectangular pulse shaping, (b) raised cosine pulse shaping, (c) sampled time-limited raised cosine pulse shaping and (d) additional non-ideal rectangular sampling pulses

is shown in Fig. 3.2(b). The vertical dashed lines in the spectrum  $|X_{SC-RC}(f)|$  indicate the dot-symmetry of the edges. The crosses in the transmitted time domain signal  $|x_{SC-RC}(t)|$  mark the ideal ISI-free sampling times for the receiver. The dashed line indicates the original rectangular-shaped sequence. Now the time domain representation of the filter is unlimited. This cannot be implemented in real-world system, so that the duration of the filter response has to be limited to  $q$ -times the duration of the data symbol  $T_d$ . If the signal is generated with a digital signal processing system, the resulting signal is additionally sampled using  $n$ -times oversampling to have discrete values with distance

$$T_{ov} = \frac{T_d}{n}, \quad (3.7)$$

resulting in

$$\begin{aligned} x_{SC-RC_q-S_n}(t) &= \left[ x_{SC-RC}(t) \cdot \text{rect}\left(\frac{t}{qT_d}\right) \right] \cdot \sum_{i=-\infty}^{\infty} \delta(t - iT_{ov}) \\ X_{SC-RC_q-S_n}(f) &= q \cdot n \cdot [X_{SC-RC}(f) * \text{si}(\pi f q T_d)] * \sum_{i'=-\infty}^{\infty} \delta(f - i' F_{ov}), \end{aligned} \quad (3.8)$$

where  $F_{ov} = 1/T_{ov}$  is the oversampling rate. The outcome of these two steps can be seen in Fig. 3.2(c), using 8-times oversampling. The noise floor is the result of shortening the RC-function and the repeated spectra result from sampling. Since a real-world Digital-to-Analog (D/A) converter cannot produce Dirac samples  $\delta(t)$ , a further step is necessary where the D/A-samples are assumed to be non-ideal rectangular sampling pulses of duration  $T_{ov}$

$$\begin{aligned} x_{SC-RC_q-R_n}(t) &= x_{SC-RC_q-S_n}(t) * \text{rect}\left(\frac{t}{T_{ov}}\right) \\ X_{SC-RC_q-R_n}(f) &= X_{SC-RC_q-S_n}(f) \cdot [T_{ov} \cdot \text{si}(\pi f T_{ov})]. \end{aligned} \quad (3.9)$$

The si-function is zero at all integer multiples of  $F_{ov}$  besides  $f = 0$ . If the oversampling rate  $F_{ov}$  is large compared to the data symbol rate  $F_d$ , then all repeated spectra vanish. This is depicted in Fig. 3.2(d). The dotted line in the spectrum indicates the shape of the si-function.

The disadvantage of SC modulation when combined with FDMA or TDMA is obvious. If FDMA is used to separate the transmitting entities,  $F_d$  is chosen as small as possible. A small  $F_d$  makes the transmitted signal sensitive to fading and narrowband interferers, since the transmitted energy is concentrated in a small bandwidth of the spectrum. If fading or narrowband interference is implied on this bandwidth, the transmitted data cannot be regained from the received signal. If TDMA is used,  $F_d$  is increased to keep the amount of transmitting entities constant. Therefore, the used bandwidth increases as well and the signal becomes less sensitive to narrowband fading and interference in the frequency domain. But if time-selective fading due to a time-variant channel occurs, the information of one or several time slots and therefore the information of one or several transmitting entities gets lost.

### 3.2.2 Spread Spectrum Modulation

To overcome the disadvantages of FDMA and TDMA with SC modulation, CDMA can be used. The resulting modulation is called Spread Spectrum (SS) modulation. The basic signal

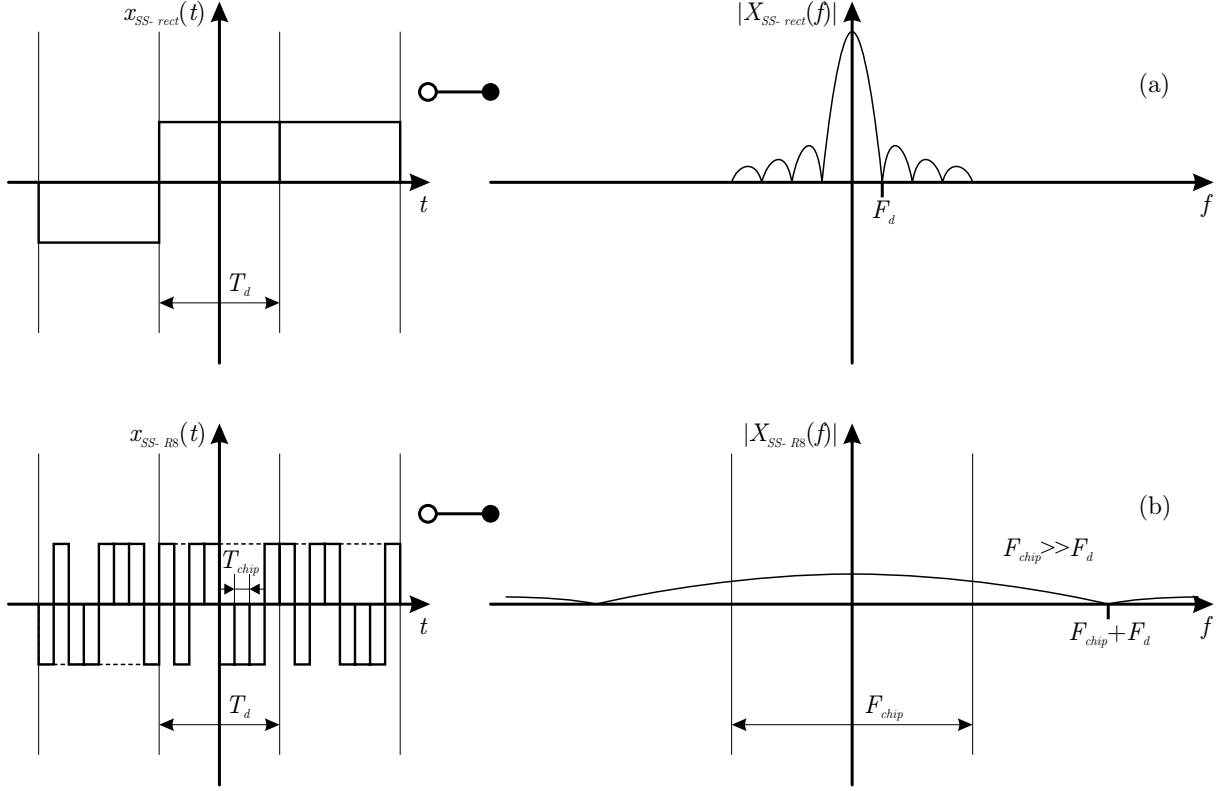


Figure 3.3: Spread spectrum modulation: (a) original signal and (b) spread spectrum signal using rectangular chips

$x_{SS-rect}(t)$ , shown in Fig. 3.3(a), again consists of zero-mean rectangular pulses with duration  $T_d$ , so that

$$x_{SS-rect}(t) = \sum_{k=-\infty}^{\infty} x_k \cdot \text{rect}\left(\frac{t-kT_d}{T_d}\right) \quad (3.10)$$

$$|X_{SS-rect}(f)| \approx |T_d \cdot \text{si}(\pi f T_d)| .$$

This signal is then multiplied with a wideband signal

$$c(t) = \sum_{i=-\infty}^{\infty} c_i \cdot p(t - iT_{chip}) , \quad (3.11)$$

where the rectangular pulse

$$p(t) = \text{rect}\left(\frac{t}{T_{chip}}\right) \quad (3.12)$$

is the simplest pulse shape for the chip sequence  $c(t)$ . The expectation of the random or pseudo-random values  $c_i \in \{-1, +1\}$  is in the ideal case

$$E\{c_i c_{i+j}\} = \begin{cases} 1 & j = 0 \\ 0 & j \neq 0 \end{cases} . \quad (3.13)$$

Since the chip sequence needs to be known in the receiver to recover the information contained in the received signal, pseudo-random sequences with period  $L$  are used, where it is convenient

to have  $T_d = L \cdot T_{chip}$  and the start of the chip sequence is aligned to the start of a symbol. The time-continuous ACF

$$\phi_{cc}(\tau) = \frac{1}{LT_{chip}} \int_0^{LT_{chip}} c(t) \cdot c(t + \tau) dt \quad (3.14)$$

is then also periodic with  $LT_{chip}$  and should have dominant Dirac-like peaks at  $\tau = n \cdot LT_{chip}$  and should be zero or close to zero otherwise. The Cross Correlation Function (CCF) of different sequences with the same duration  $L$  should ideally be zero all the time, so that different entities can use the same frequency band with their individual chip sequences without interfering each other. An example for a group of sequences with good ACF and CCF properties are Gold codes [Gol67], although they are not ideal in the sense that they provide zero CCF values.

The respective modulation technique is called Direct Sequence Spread Spectrum CDMA (DS-SS-CDMA), the SS signal is given by

$$\begin{aligned} x_{SS-R_L}(t) &= x_{SS-rect}(t) \cdot c(t), \\ X_{SS-R_L}(f) &= x_{SS-rect}(f) * C(f), \end{aligned} \quad (3.15)$$

shown in Fig. 3.3(b) with a period of  $L = 8$ . If  $T_{chip} \ll T_d$ , the spectrum  $C(f)$  dominates

$$|X_{SS-R_L}(f)| \approx |C(f)| \approx |T_{chip} \cdot \text{si}(\pi f T_{chip})| \quad (3.16)$$

and the bandwidth  $B$  of the signal is

$$B \approx B_{chip}, \quad (3.17)$$

where  $B_{chip}$  is the bandwidth of a chip sequence. Depending on the spectral properties of the chip sequence, the spectrum will have side lobes outside  $B_{chip}$  as shown here for the rectangular chip shaping. Spread spectrum modulation has many advantages especially in fading channels since the effective power density for one sequence is very small compared to non SS signals. Therefore, only a part of the transmitted energy will be cancelled if frequency-selective fading is present. Additionally, a narrowband interferer with power  $P_{disturb}$  is spread by the receiver sequence and has only an resulting effective power of

$$P_{disturb} \cdot \frac{B_d}{B_{chip}} = \frac{P_{disturb}}{G_{SS}}, \quad (3.18)$$

where  $B_d$  is the bandwidth of the original unsprung signal and  $G_{SS}$  is the so-called spread spectrum spreading gain. A narrowband interferer is therefore attenuated by  $10 \cdot \log(G_{SS})$  dB. If only wideband interference is present, e.g. white noise, this techniques does not bring any advantages compared to non SS signals.

### 3.2.3 Multi-Carrier Modulation

The DS-SS technique presented above offers a very simple way to generate a wideband signal. A more sophisticated solution for modern wideband communications systems with advantages

over DS-SS is presented in this section. It is based on the modulation of several narrowband signals that are combined to form a wideband signal. This kind of modulation is called Multi-Carrier (MC) modulation. The narrowband signals are not generated individually, but are combined by using the Discrete Fourier Transformation (DFT) [Wei71] or for faster processing the Fast Fourier Transformation (FFT), as assumed in the following. This technique has the advantage that only one carrier frequency  $f_c$  is needed for the RF wideband signal generation instead of individual carrier frequencies for each of the narrowband signals. Moreover, the spacing between the combined narrowband signals can be smaller due to the exploitation of some special signal identities. In the following, the theory of MC signal generation is described.

The narrowband subcarriers are assumed to have all the same bandwidth

$$B_s = \frac{1}{T_s}. \quad (3.19)$$

$N_c$  of these subcarriers with a subcarrier spacing of

$$F_s = B_s = \frac{1}{T_s} \quad (3.20)$$

are used for the wideband signal generation

$$\begin{aligned} x_{MC-\infty}(t) &= \sum_{l'=0}^{N_c-1} X_{l'} \cdot e^{j2\pi f_{l'} t}, \\ X_{MC-\infty}(f) &= \sum_{l'=0}^{N_c-1} X_{l'} \cdot \delta(f - f_{l'}), \end{aligned} \quad (3.21)$$

where

$$f_{l'} = \left( l' - \frac{N_c}{2} \right) \cdot F_s \quad (3.22)$$

are the subcarrier frequencies and  $X_{l'}$  are the complex-valued data symbols used for the subcarrier modulation. An example MC wideband signal with  $N_c = 8$  subcarriers is shown in Fig. 3.4(a). The signal  $x_{MC-\infty}(t)$  is periodic with  $T_s$ . That means that the whole information about the subcarriers is included in one interval  $T_s$ , the so-called multi-carrier symbol duration. This makes it possible to simply transmit a single interval resulting in

$$\begin{aligned} x_{MC-T_s}(t) &= x_{MC-\infty}(t) \cdot \text{rect}\left(\frac{t}{T_s}\right), \\ X_{MC-T_s}(f) &= X_{MC-\infty}(f) * [T_s \cdot \text{si}(\pi f T_s)] = T_s \cdot \sum_{l'=0}^{N_c-1} X_{l'} \cdot \text{si}(\pi(f - f_{l'})T_s). \end{aligned} \quad (3.23)$$

The according representation is shown in Fig. 3.4(b), where the solid line in the spectrum symbolizes the absolute value  $|X_{MC-T_s}(f)|$  of the envelope and the dotted lines symbolize the absolute values of the subcarrier envelopes.

Up to now, the signal is still time-continuous. To get discrete values,  $x_{MC-T_s}(t)$  is sampled

$$\begin{aligned} x_{MC-samp}(t) &= x_{MC-T_s}(t) \cdot \sum_{k'=-\infty}^{\infty} \delta(t - k'T_{sample}), \\ X_{MC-samp}(f) &= X_{MC-T_s}(f) * \left[ \frac{1}{T_{sample}} \sum_{l''=-\infty}^{\infty} \delta(f - l''F_{sample}) \right], \end{aligned} \quad (3.24)$$

where  $F_{sample} = 1/T_{sample}$  is the sampling rate. Resolving the equations one obtains

$$\begin{aligned} x_{MC-samp}(t) &= \sum_{k'=-\infty}^{\infty} \sum_{l'=0}^{N_c-1} X_{l'} \cdot e^{j2\pi f_{l'}(k'T_{sample})} \cdot \text{rect}\left(\frac{k'T_{sample}}{T_s}\right) \cdot \delta(t - k'T_{sample}) \\ &= \sum_{k'=\left[-\frac{T_s}{2T_{sample}}\right]}^{\left[\frac{T_s}{2T_{sample}}-0.5\right]} \sum_{l'=0}^{N_c-1} X_{l'} \cdot e^{j2\pi f_{l'}(k'T_{sample})} \cdot \delta(t - k'T_{sample}), \end{aligned} \quad (3.25)$$

$$X_{MC-samp}(f) = \frac{T_s}{T_{sample}} \cdot \sum_{l''=-\infty}^{\infty} \sum_{l'=0}^{N_c-1} X_{l'} \cdot \text{si}\left(\pi(f - l''F_{sample} - f_{l'})T_s\right).$$

According to the sampling theorem,  $F_{sample}$  has to be at least two times the maximum frequency occurring in the signal to avoid aliasing. For the presented system this means that

$$\begin{aligned} F_{sample} &= 2 \cdot \frac{N_c F_s}{2} = N_c F_s, \quad \text{or equivalently} \\ \frac{T_s}{T_{sample}} &= N_c. \end{aligned} \quad (3.26)$$

Insertion in the equations above results in

$$\begin{aligned} x_{MC-samp}(t) &= \sum_{k'=\lceil -N_c/2 \rceil}^{\lfloor N_c/2 - 0.5 \rfloor} \sum_{l'=0}^{N_c-1} X_{l'} \cdot e^{j2\pi \frac{f_{l'} k' T_s}{N_c}} \cdot \delta\left(t - \frac{k' T_s}{N_c}\right), \\ X_{MC-samp}(f) &= N_c \cdot \sum_{l''=-\infty}^{\infty} \sum_{l'=0}^{N_c-1} X_{l'} \cdot \text{si}\left(\pi(f - f_{l'})T_s - \pi l'' N_c\right). \end{aligned} \quad (3.27)$$

This signal and its according spectrum are shown in Fig. 3.4(c). Due to the convolution in the frequency domain, the spectrum of Fig. 3.4(b) is periodically repeated and, if all subcarriers use the same transmitter power, the envelope of the resulting spectrum is flat across the whole bandwidth. Since the time domain samples again have to be D/A-converted, the time-domain signal is convoluted with the non-ideal rectangular sampling pulse, so that

$$\begin{aligned} x_{MC-rect}(t) &= x_{MC-samp}(t) * \text{rect}\left(\frac{t}{T_{sample}}\right), \\ X_{MC-rect}(f) &= X_{MC-samp}(f) \cdot T_{sample} \cdot \text{si}\left(\pi f T_{sample}\right). \end{aligned} \quad (3.28)$$

The result is a reshaping of the spectrum envelope

$$\begin{aligned} x_{MC-rect}(t) &= \sum_{k'=\lceil -N_c/2 \rceil}^{\lfloor N_c/2 - 0.5 \rfloor} \sum_{l'=0}^{N_c-1} X_{l'} \cdot e^{j2\pi \frac{f_{l'} k' T_s}{N_c}} \cdot \text{rect}\left(t \frac{N_c}{T_s} - k'\right), \\ X_{MC-rect}(f) &= T_s \cdot \left[ \sum_{l''=-\infty}^{\infty} \sum_{l'=0}^{N_c-1} X_{l'} \cdot \text{si}\left(\pi(f - f_{l'})T_s - \pi l'' N_c\right) \right] \cdot \text{si}\left(\pi f \frac{T_s}{N_c}\right), \end{aligned} \quad (3.29)$$

as shown in Fig. 3.4(d), so that

$$|X_{MC-rect}(f)| \approx T_s \cdot \left| \text{si}\left(\pi f \frac{T_s}{N_c}\right) \right|, \quad \text{for } E\{|X_{l'}|\} = 1 \quad \forall l' \in \{0, 1, \dots, (N_c - 1)\}. \quad (3.30)$$

If the Inverse Fast Fourier Transform (IFFT) is used,  $N_c$  becomes

$$N_c = 2^m, \quad m \in \{1, 2, 3, \dots\}. \quad (3.31)$$

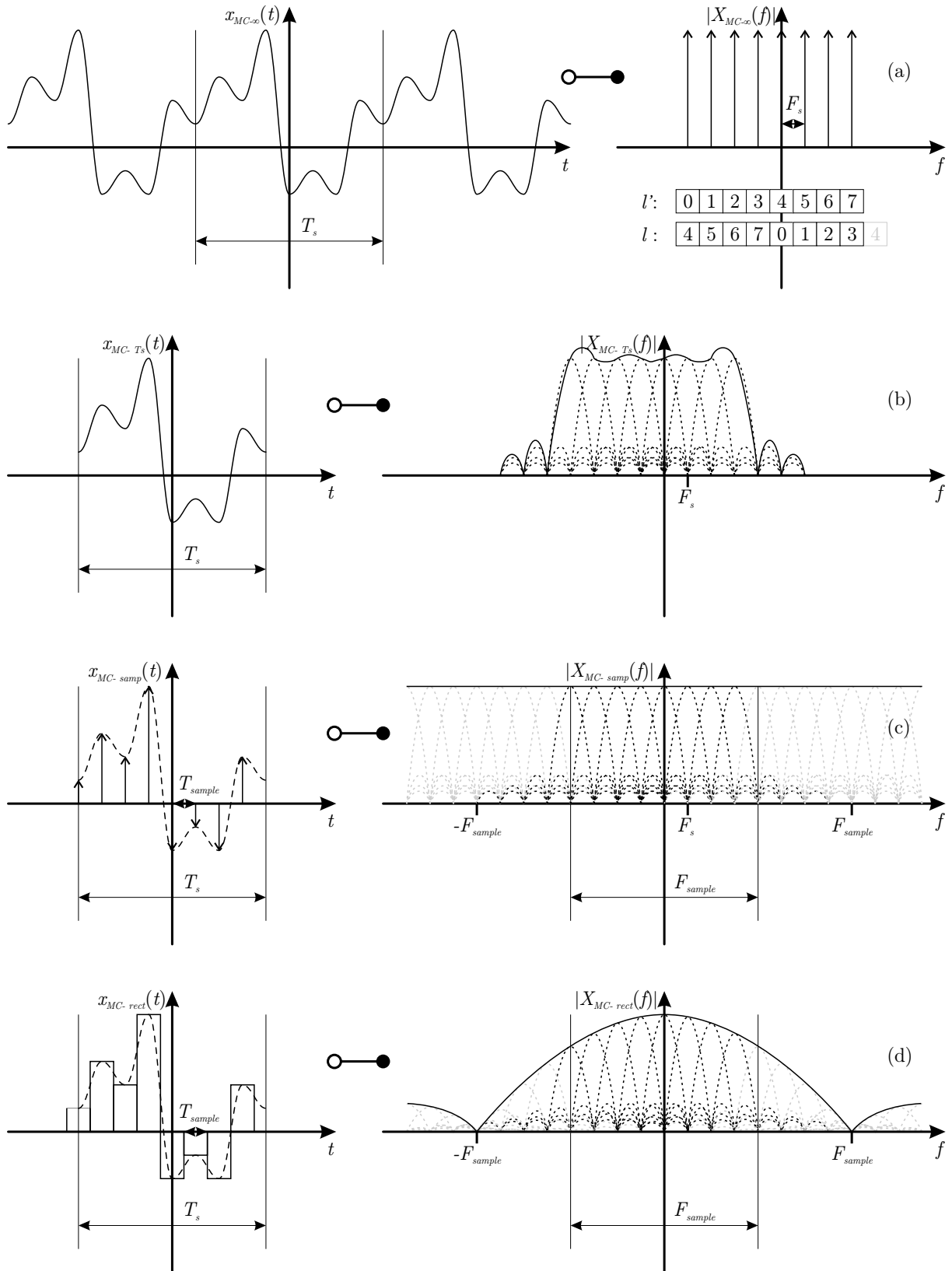


Figure 3.4: OFDM modulation: (a) Signal with modulated equal-spaced subcarriers, (b) time-limited representation, (c) using discrete samples and (d) non-ideal rectangular sampling pulses

The IFFT discrete time-domain samples are calculated by

$$x_k = \frac{1}{\sqrt{N_c}} \sum_{l=0}^{N_c-1} X_l \cdot e^{j2\pi \frac{kl}{N_c}}, \quad k \in \{0, 1, \dots, (N_c - 1)\}, \quad (3.32)$$

where

$$l' = \left( l + \frac{N_c}{2} \right) \bmod N_c \quad (3.33)$$

has to be reordered to comply with the transmitted spectral order that results from the IFFT. The resulting modulation using the IFFT on the transmitter side and the FFT

$$Y_l = \frac{1}{\sqrt{N_c}} \sum_{k=0}^{N_c-1} y_k \cdot e^{-j2\pi \frac{kl}{N_c}}, \quad l \in \{0, 1, \dots, (N_c - 1)\} \quad (3.34)$$

on the receiver side is called Orthogonal Frequency Division Multiplexing (OFDM).  $l'$  and  $l$  are shown in Fig. 3.4(a).  $l = N_c/2$  is shown two times since the corresponding frequency can be interpreted as a positive or negative subcarrier frequency if the FFT/IFFT is used.

In the following, the spectra of Fig. 3.4(b) and Fig. 3.4(d) are compared. Fig. 3.4(b) is the spectrum that is intended to be transmitted for OFDM, whereas due to the digital processing and the D/A-conversion, the transmitted spectrum looks like Fig. 3.4(d). Two main disadvantages are observed:

- The desired necessary signal information is contained in  $-F_{sample}/2 \leq f < F_{sample}/2$  as shown in Fig. 3.4(d), but the spectrum is unlimited in direction of frequency. Since the spectrum has to be cut off at  $|f| > F_{sample}/2$ , filtering is difficult because the spectrum is different to zero there. Using a filter with double-sided bandwidth  $B = F_{sample}$  will cause large self-distortion, due to non-ideal effects at the filter edges. On the other hand using a filter with a larger bandwidth will either make the frequency-range usage ineffective or will cause interference with neighbouring frequency bands.
- Additionally, the desired spectrum itself has a non-ideal shape, since due to the  $\text{si}(x)$ -shaping, the edges compared to the center of the spectrum are attenuated by

$$20 \cdot \log \left( \frac{|X_{MC-rect}(\pm F_{sample}/2)|}{|X_{MC-rect}(0)|} \right) \text{ dB} = 20 \cdot \log(\text{si}(\pi/2)) \text{ dB} = 20 \cdot \log(2/\pi) \approx -3.9 \text{ dB}. \quad (3.35)$$

For both disadvantages, different possible solutions are presented in the following subsections. Theoretically, the signal of Fig. 3.4(c) can be recovered in the receiver by ideal sampling of the signal in Fig. 3.4(d). This sampling results in a constructive superpositioning of the repeated spectrum. With an additional FFT or DFT step, the information  $X_l$  or  $X_{l'}$  of the modulated subcarriers then can be extracted accurately. However, in most practical cases the signal is additionally filtered in the transmitter and receiver and therefore part of the information needed for the constructive superpositioning is lost resulting in decreased symbol detection performance.

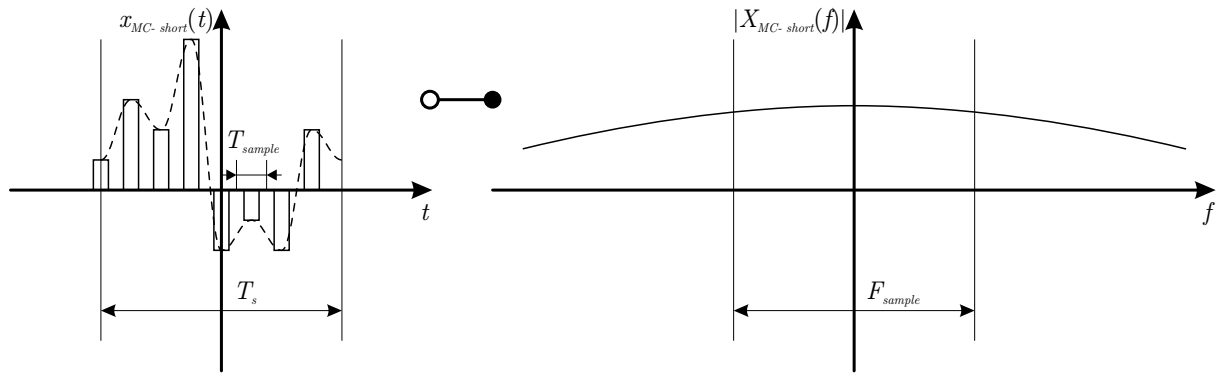


Figure 3.5: OFDM modulation with shortened sampling pulse

### 3.2.3.1 OFDM with shortened D/A-converter sampling pulse

To avoid the strong influence of the non-ideal D/A sampling pulse on the transmitted spectrum, first an attempt is made to have a more Dirac-like sampling pulse. Like shown in Fig. 3.5 this can be achieved by shortening the length of the rectangular D/A-conversion pulse to half of its previous length resulting in a stretched si-function in the frequency domain. Compared to (3.35), the attenuation of the edges is reduced to

$$20 \cdot \log(\text{si}(\pi/4)) \text{ dB} = 20 \cdot \log(2\sqrt{2}/\pi) \approx -0.9 \text{ dB}. \quad (3.36)$$

The drawback of this method is obvious. Since fifty percent of the time no signal is generated, the signal power is reduced by half as well and has to be regained by a good amplification process. Additionally, a good filtering process is necessary as well since the higher repeated versions of the spectrum are raised compared to the desired main spectrum. On the other hand, this method can be implemented in hardware quite easily. Since the D/A-sampling clock signal is in most cases generated externally or is at least available, the logical high level of the clock can be used to forward and the logical low level can be used to block the generated D/A-output, thus generating the signal described here. However the problem of filtering the close to one another lying repeated versions of the spectra still has to be solved. This is done in the next section.

### 3.2.3.2 OFDM with empty subcarriers

As mentioned above, the continuously repeated versions of the original spectrum make filtering difficult due to the high requirements on the filter quality. To reduce the requirements on the filter, subcarriers on both sides of the original spectrum can be left empty. Doing so, the system throughput is reduced. Therefore, it is better to double the number of subcarriers for the IFFT and set half of them to zero to comply with the needed amount of subcarriers. Since the subcarrier spacing  $F_s$  is bound to physical characteristics of the channel, it has to stay constant, so that the sampling rate  $F_{\text{sample}}$  has to be doubled as well if the number of FFT/IFFT subcarriers is doubled. This condition is shown in Fig. 3.6.

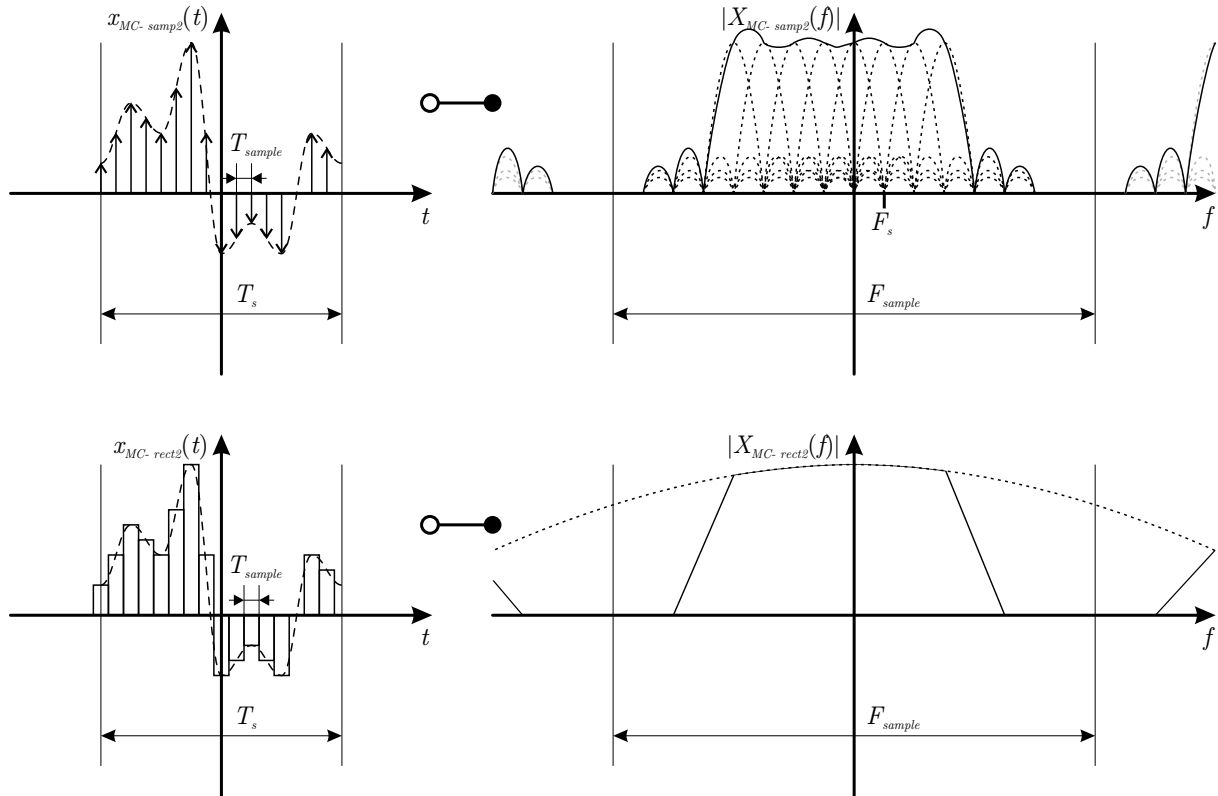


Figure 3.6: OFDM modulation with empty subcarriers

Due to the unused subcarriers, the repeated spectra have a gap. This makes filter-related signal distortion less critical. Additionally, since the duration of the rectangular sampling pulses is reduced by half, this method automatically incorporates the benefits mentioned in Section 3.2.3.1 without the loss in signal power. The time domain signal  $x_{MC-samp2}(t)$  can be compared to two-times oversampling. Because of the fact that the subcarriers of the signal are modulated in the frequency domain, it is of course also possible to leave less than half of the available subcarriers empty, making the FFT/IFFT process more efficient. It has to be mentioned though that doubling  $F_{sample}$  necessitates a faster D/A-conversion and doubling  $N_c$  necessitates a faster IFFT processing.

Another benefit is achieved by leaving the 0 Hz subcarrier  $X_{l=0}$ , i.e.  $X_{\nu=N_c/2}$ , empty. In practical implementations it is well possible that DC-offsets occur in the system that might affect this subcarrier. They even may vary with temperature and time and are sometimes difficult to compensate. By not using the 0 Hz subcarrier, it is possible to neglect the DC-offsets since no information is transmitted and recovered from this possibly defective subcarrier.

### 3.2.3.3 OFDM with pre-compensated subcarriers

The methods proposed in Sections 3.2.3.1 and 3.2.3.2 leave the problem of unequal spectrum amplitude distribution due to the D/A-converter si-function unsolved. The unequally distributed amplitudes result in an unequal protection against fading and interfering effects on the channel.

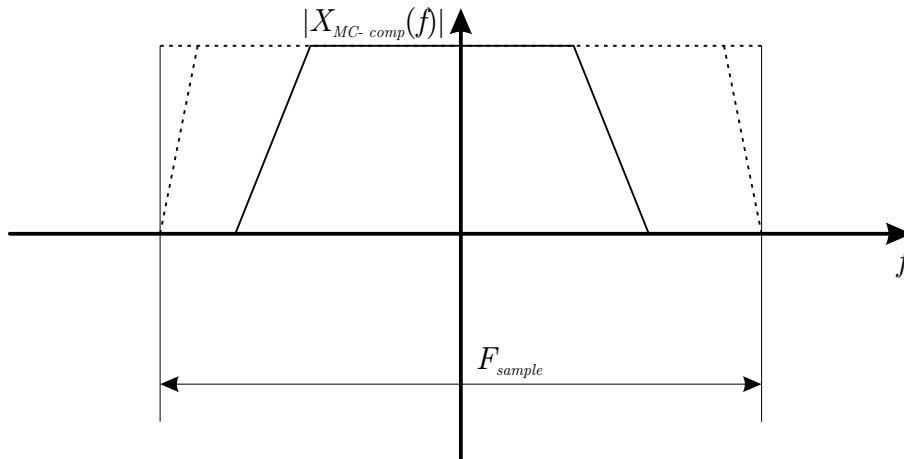


Figure 3.7: OFDM modulation with subcarrier pre-amplification

Since the signal is modulated in the frequency domain, possible amplitude and phase distortions, not only due to the transmitter D/A-converter si-function, can be pre-compensated on subcarrier level by multiplying each subcarrier with a corresponding complex correction factor. This does not influence the orthogonality of the subcarriers, e.g. for a compensation of the rectangular D/A-conversion sampling pulse, the subcarriers  $X_{l'}$  are transformed by

$$X_{l'_c} = X_{l'} \cdot \frac{1}{\text{si}\left(\frac{l' - N_c/2}{N_c} \cdot \pi\right)}, \quad (3.37)$$

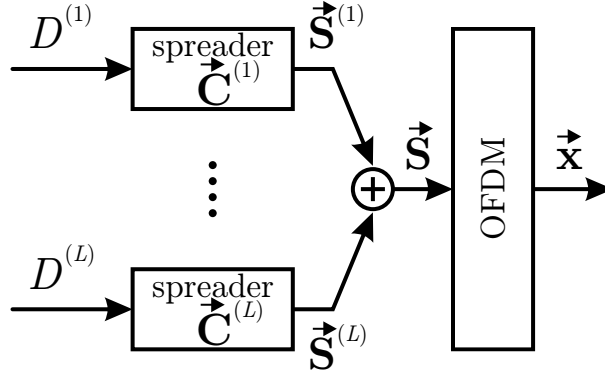
resulting in the new compensated subcarriers  $X_{l'_c}$ . The spectrum  $X_{MC-comp}(f)$  of such a compensated system using empty subcarriers is shown in Fig. 3.7. The horizontal dotted line indicates the range of subcarriers that can be compensated. The slanted dotted lines indicate the edges of a filter function that has been used to remove the repeated spectra.

#### 3.2.3.4 Multi-Carrier Code Division Multiple Access - MC-CDMA

In Section 3.2.2, the possibility to use different PN sequences to spread the information of several users for generating a CDMA signal has been discussed. Multi-carrier modulation offers an extremely good possibility to generate a CDMA scheme as well. The corresponding technique is called Multi-Carrier Code Division Multiple Access (MC-CDMA) [FaP93][YLF93].

Since the subcarrier bandwidth  $B_s$  in OFDM systems normally is quite small, the individual subcarriers are sensitive to narrowband fading and interference that might destroy the transmitted information. Combining several subcarriers to a group and distributing the information over the carriers in this group again spreads the information and thus increases its diversity. Spreading the information can be done by using a code chip-sequence or using a special binary encoder that combines the information of several users.

If the chip-sequence method is chosen and different codes are applied for the different users, the information of a dedicated user can be extracted from the received signal. A group of

Figure 3.8: OFDM MC-CDMA transmitter with spreading length  $L$ 

such codes, used for spreading and despreading, are the orthogonal, antipodal  $[-1; +1]$  Walsh-Hadamard codes [Pro95, Section 8-1-2][FaP93]. The  $k$ th user applies a spreading code of length  $L$  by multiplying a data symbol  $D^{(k)}$  with the corresponding MC-CDMA spreading code vector  $\vec{C}^{(l)}$ ,  $l = 1, \dots, L$ , resulting in the source vector  $\vec{S}^{(k)}$ . The source vectors of all users are added to generate the spread vector  $\vec{S}$ . This vector is then modulated on the  $L$  subcarriers of an OFDM system, resulting in the time domain vector  $\vec{x}$ , compare Fig. 3.8. Since it is convenient to transfer  $M$  data symbols per user at a time, reusing the same code, the index  $m$ ,  $m = 1, \dots, M$ , is added giving

$$\vec{S}_m^{(k)} = D_m^{(k)} \cdot \vec{C}^{(k)}, \quad k = 1, \dots, K, \quad K \leq L, \quad (3.38)$$

where

$$\vec{C}^{(l)} = (C_1^{(l)}, \dots, C_L^{(l)})^T \quad (3.39)$$

and

$$\vec{S}_m^{(k)} = (S_{1,m}^{(k)}, \dots, S_{L,m}^{(k)})^T. \quad (3.40)$$

There can only exist a maximum of  $L$  orthogonal codes. If a large number of active users  $K$  should be handled by the transmission system,  $L \geq K$  normally has to be quite high. Additionally the orthogonality of the codes is partially destroyed by distortions due to the transmission channel. In [Kai98] it has been shown that if adequate interleaving is applied, already short code length of  $L = 4, 8, 16$  achieve a large diversity gain. This makes the despreading and detection process in the receiver much easier, since the complexity increases with increasing  $L$ . This offers the opportunity to use the same short codes in several user groups  $Q$  instead of using only one group of long codes. The maximum number of users  $K_{max}$  each transmitting  $M$  data symbols then can be determined by

$$K_{max} = Q \cdot L. \quad (3.41)$$

The source vectors of the  $m$ th data symbol of up to  $L$  users in the  $q$ th group,  $q = 1, \dots, Q$ , are combined to the spread vector

$$\vec{S}_{m,q} = \sum_{l=1}^L \vec{S}_m^{((q-1) \cdot L + l)}, \quad (3.42)$$

where

$$\vec{\mathbf{S}}_{m,q} = (S_{1,m,q}, \dots, S_{L,m,q})^T. \quad (3.43)$$

Following this is a first stage where the components of the  $M$  spread vectors of the  $q$ th group are interleaved. This has to be done for each of the  $Q$  groups. Since all groups should be combined to one OFDM symbol consisting of  $N_c$  carriers, a second interleaving stage is necessary. The second interleaving stage can also be used to integrate additional information used for synchronization, demodulation or channel estimation. This is explained in the next chapter. Therefore and with the knowledge of Section 3.2.3.2, the number of subcarriers has to comply with

$$N_c \geq Q \cdot M \cdot L. \quad (3.44)$$

These  $N_c$  carriers forming the vector  $\vec{\mathbf{X}}$  are then IFFT processed resulting in the OFDM symbol time domain representation vector  $\vec{\mathbf{x}}$ , where the real part is the In-phase-part and the imaginary part is the Quadrature-part of the corresponding lowpass I/Q-representation. This signal is component-wise D/A-converted and transmitted. The whole transmitter system with  $Q$  groups,  $M$  data symbols for each user applying spreading codes of length  $L$  and interleaving is shown in Fig. 3.9.

The purpose of interleaving is to generate a signal where the frequency spacing of the components of each  $\vec{\mathbf{S}}_{m,q}$  vector is as large as possible, or at least larger than the coherence bandwidth of the channel to obtain a good diversity. Doing so, the components are affected nearly independently from each other by the channel and the probability that all components are eliminated in a deep fade can be reduced [Kai98].

### 3.2.3.5 Guard Interval

In Section 2.1, the time-dispersive behaviour of the mobile transmission channel has been characterized by the delay power spectrum with the maximum delay  $\tau_{max}$ . Since the transmission is not stopped after one OFDM symbol, but several independent time-domain representations of OFDM symbols  $\vec{\mathbf{x}}$  are transmitted in sequence, the result would be ISI of the OFDM symbols. Therefore, a guard interval, i.e. a cyclic prefix,

$$T_g \geq \tau_{max} \quad (3.45)$$

is added in front of the OFDM symbol resulting in the new symbol duration

$$T'_s = T_s + T_g. \quad (3.46)$$

The guard interval is a cyclic repetition of the last  $N_g$  components of the original symbol vector  $\vec{\mathbf{x}}$  resulting in the new signal vector

$$\vec{\mathbf{x}}_g = \begin{pmatrix} 0 & \vdots & \mathbf{I}_{N_g} \\ \dots & \dots & \dots \\ & & \mathbf{I}_{N_c} \end{pmatrix} \cdot \vec{\mathbf{x}}, \quad (3.47)$$

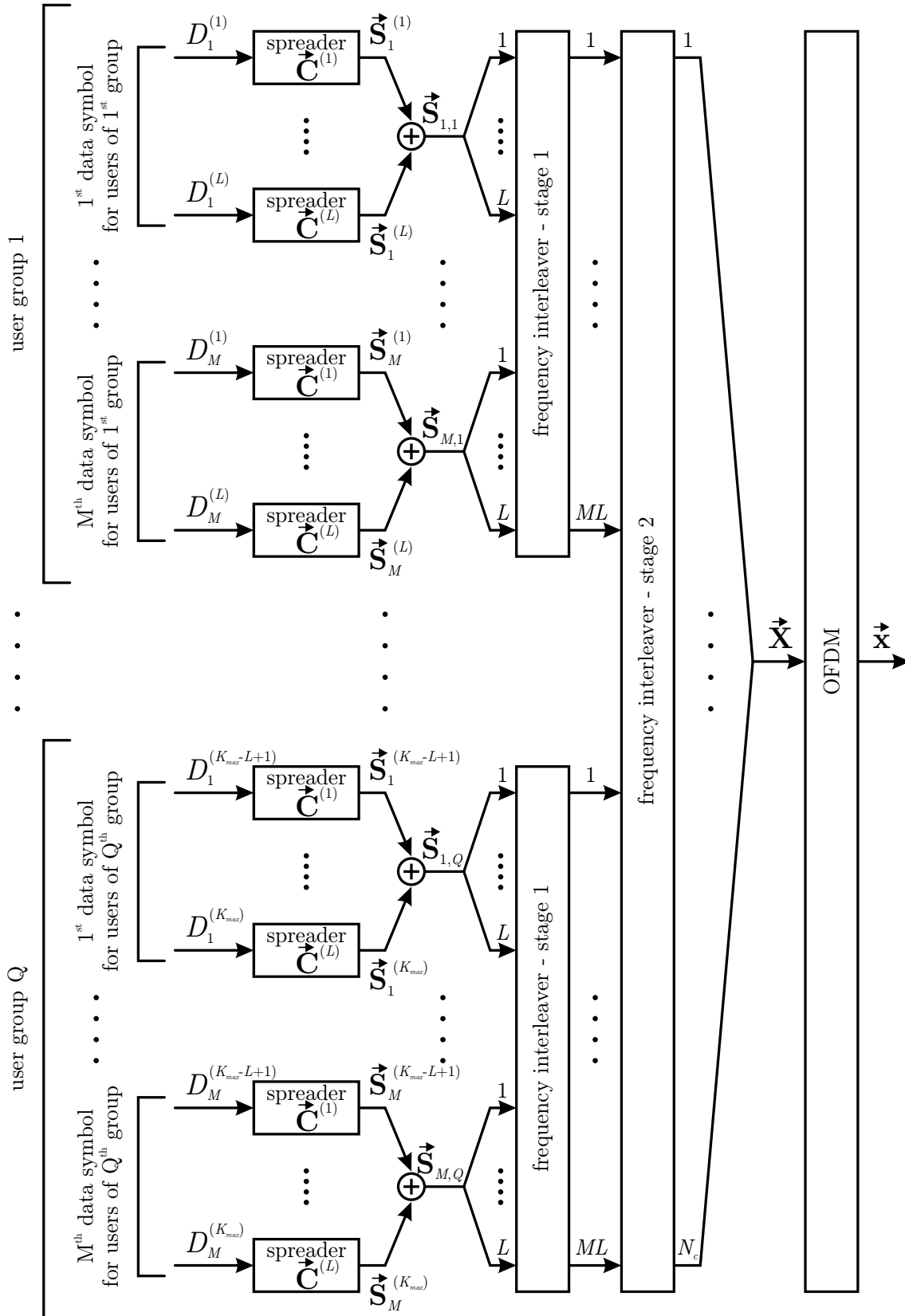


Figure 3.9: OFDM MC-CDMA transmitter with spreading length  $L$  and  $M$  data symbols for each user in  $Q$  user groups

where  $\mathbf{I}_n$  is the identity matrix of dimension  $n$  and

$$T_g = N_g \cdot T_{sample}. \quad (3.48)$$

The guard interval is removed in the receiver thus avoiding ISI without additional distortion of the signal. Nevertheless, there is a drawback for the use of a guard interval. Since the guard interval is transmitted as well, it consumes additional transmitter energy and degrades the power ratio by

$$10 \cdot \log \left( \frac{N_c + N_g}{N_c} \right) \text{ dB}. \quad (3.49)$$

Additionally, there is a loss in the data rate of  $N_g/(N_c + N_g) \cdot 100\%$ . To guarantee that the channel can be assumed to be time-invariant during the transmission of one OFDM symbol,  $T_s$  has to be smaller than the coherence time of the channel and therefore the duration of  $T_s$ , i.e. the size of  $M$ ,  $Q$  and  $L$  has to be restricted as well. A time-variant channel during  $T_s$  results in ICI of the subcarriers. This should be avoided since it decreases the system performance.

# Chapter 4

## Modulation and Demodulation Techniques for OFDM

It has been shown in Section 3.2.3 that OFDM/multi-carrier modulation can be compared to single-carrier modulation on  $N_c$  parallel subcarriers with bandwidth  $B_s$  each. Every subcarrier uses, for example, rectangular pulse shaping of duration  $T_s$  in the time domain. Therefore, any arbitrary phase and/or amplitude modulated signal, represented by complex-valued I/Q-symbols  $X_{k,l}$  can be applied on the subcarriers. In the sequel, the discrete frequency index  $l$ ,  $-N_c/2 \leq l < N_c/2$ , denotes the corresponding subcarrier frequency  $f_l = l \cdot F_s$ . Unlike the notation of the previous section, where due to the use of the FFT/IFFT the negative subcarrier frequencies were represented by positive numbers, the index now can also be negative. The overall bandwidth is  $B = N_c \cdot B_s$ . The number for the corresponding OFDM symbol in the OFDM frame is denoted by  $k$ ,  $0 \leq k < N_s$ , resulting in the overall OFDM frame duration

$$T_{fr} = N_s \cdot T'_s. \quad (4.1)$$

An example for such an OFDM frame consisting of  $N_s = 10$  OFDM symbols with  $N_c = 16$  subcarriers each is shown in Fig. 4.1. The black box indicates the first OFDM symbol of the frame. The reason for combining several OFDM symbols to a frame is related to equalization, synchronization and efficiency matters explained later on in this chapter.

### 4.1 Coherent Modulation/Demodulation

When coherent modulation and demodulation is considered, typically either Phase Shift Keying (PSK) or Quadrature Amplitude Modulation (QAM) is used [Pro95]. The modulation symbols can be applied directly to the I/Q-symbols  $X_{k,l}$  of the OFDM frame, compare Fig. 4.1, or the MC-CDMA technique of Section 3.2.3.4 can be used resulting in an OFDM symbol that contains the spread information of one or several users. Coherent modulation requires the recovery of the transmitted phase and amplitude in the receiver. Only in the special case of PSK without spreading, a recovery of the phase alone may be sufficient.

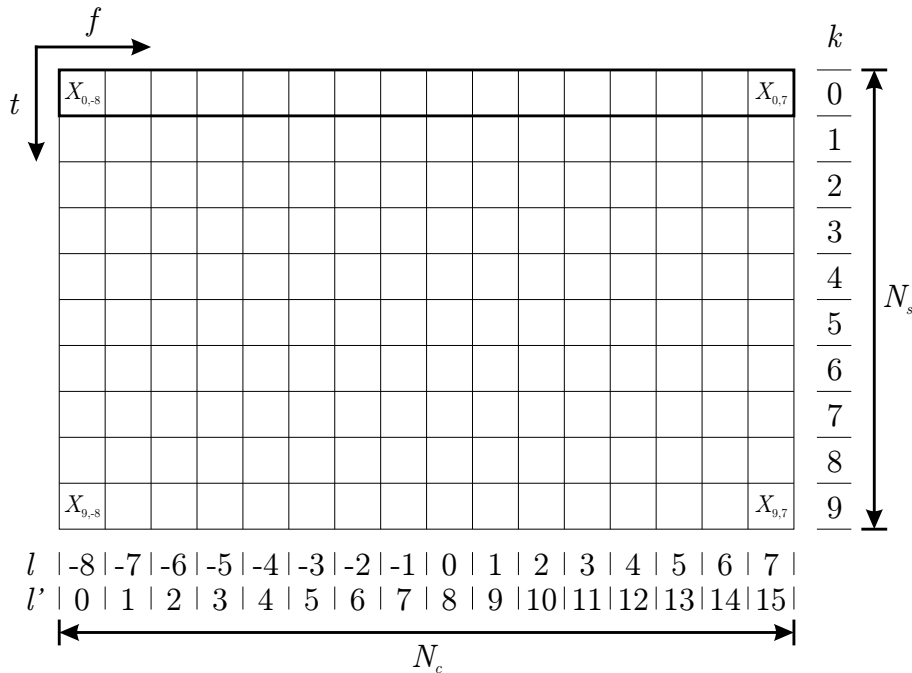


Figure 4.1: OFDM frame with  $N_s = 10$  OFDM symbols each having  $N_c = 16$  subcarriers

## 4.2 Channel Estimation and Equalization

### 4.2.1 Requirements for MC Channel Estimation

Channel estimation and equalization is essential for the reception of coherently modulated MC OFDM frames. During the transmission of the signal from the transmitter to the receiver, the transmission channel between these two entities imposes distortions on the signal. The distortions can be divided in random noise, like for example AWGN, and predictable disturbances, like fading. The distortions of the latter can be estimated and partly removed from the signal. For this purpose, pilot symbols have to be multiplexed into the data stream. Both the pilot symbol values and the positions in the data stream are known in the receiver. This knowledge is used to estimate the channel weight function  $h(\tau, t)$ . In MC transmission systems, it is possible to not only insert pilot symbols in direction of time  $t$ , but also in direction of frequency  $f$ . This facilitates the estimation of the time-variant channel transfer function  $T(f, t)$ . The gathered information about the channel at the positions of the pilot symbols has to be filtered to obtain estimates  $\hat{T}_{k,l}$  for  $T(f, t)$  at the positions of the data symbols, compare Fig. 4.2. The optimum filter coefficients are obtained applying the Minimum Mean Square Error (MMSE) criterion by 2-D Wiener filtering [Hay86][Pap91][HKR97][Kai98]. To avoid the resulting complexity of 2-D filtering, two-times 1-D filtering might be chosen. For the case that the Doppler power and the delay power spectra with their corresponding 1-D probability density functions  $p(f_D)$  and  $p(\tau)$  are independent from each other, this operation is loss-free.

For the channel estimation, due to a lack of the actual channel condition knowledge, it has to be assumed that the shapes of the density functions  $p(f_D)$  and  $p(\tau)$  are unknown besides

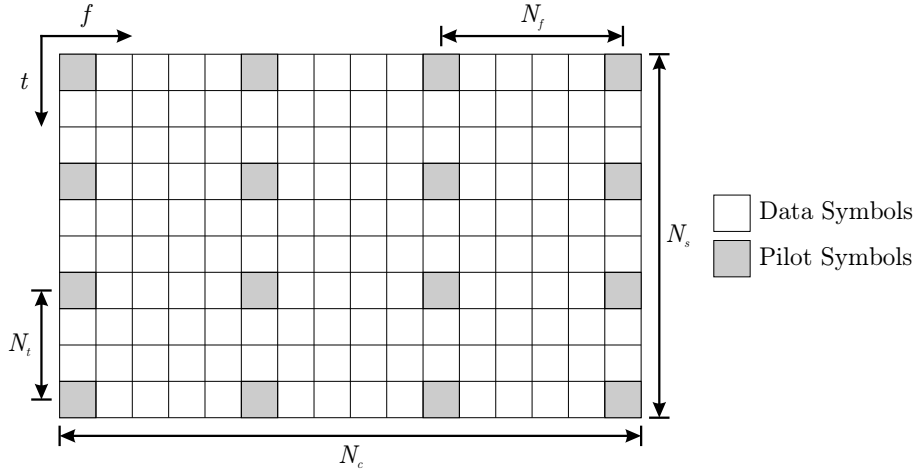


Figure 4.2: Pilot grid for two-times 1-D filtering

their maximum ranges  $f_{D_{max}}$  and  $\tau_{max}$ . To cover all possible cases as good as possible, equally distributed density functions are used,

$$p(f_D) = \begin{cases} \frac{1}{2 \cdot f_{D_{max}}} & |f_D| < f_{D_{max}} \\ 0 & \text{otherwise} \end{cases}, \quad (4.2)$$

$$p(\tau) = \begin{cases} \frac{1}{\tau_{max}} & 0 \leq \tau < \tau_{max} \\ 0 & \text{otherwise} \end{cases}. \quad (4.3)$$

For channel estimation and equalization this necessitates pilot symbols with distance  $N_f$  in frequency direction and distance  $N_t$  in time direction in the OFDM frame as shown in Fig. 4.2, where  $N_f$  and  $N_t$  are positive integer values. The structure in Fig. 4.2 is only one possible solution for a rectangular placement of the pilot symbols, with the advantage that pilot symbols will be placed on all edges and in all corners.

The maximum possible distances between pilot symbols depend on  $\tau_{max}$  and  $f_{D_{max}}$  respectively. The excess delay  $\tau_{max}$  leads to frequency selective fading between the different subcarriers with distance  $F_s$ , whereas the Doppler frequency  $f_{D_{max}}$  yields changes in the channel from one OFDM symbol to the next OFDM symbol with distance  $T'_s$  in time. The sampling theorem in combination with the normalized single sided filter bandwidth  $\tau_{max}/2 \cdot F_s$  and  $f_{D_{max}} \cdot T'_s$  therefore requires that the pilot symbol distances have to comply with

$$N_f \leq \left\lfloor \frac{1}{\tau_{max} \cdot F_s} \right\rfloor, \quad (4.4)$$

$$N_t \leq \left\lfloor \frac{1}{2 f_{D_{max}} \cdot T'_s} \right\rfloor. \quad (4.5)$$

The subsequent sections examine different interpolation methods for the gathered information of the received pilot symbols. The influence on the accuracy of the channel estimation is investigated and methods for a reduced interpolation complexity are compared.

## 4.2.2 Analysis of Interpolation Methods

The compliance with the sampling theorem ensures that a sampled signal will not show any aliasing effects and that the signal can be ideally reconstructed with the correct interpolation function. As mentioned before, two-times 1-D filtering is used, where first the pilots in frequency direction are interpolated and afterwards all pilots and the resulting calculated intermediate values from the previous step are interpolated in time direction [HKR97][Kai98]. Interpolation can be looked at in two different ways; either filtering the spectrum by means of multiplying the received spectrum with a *filter function* or interpolating the available pilot samples by means of convoluting the samples with an *interpolation function*. In the following, the filter functions are marked by capital letters and the corresponding interpolation functions are marked by small letters. The filter function is generated by a Fourier transform of the interpolation function.

### 4.2.2.1 $\text{si}(x)$ Interpolation

The Nyquist  $\text{si}(x)$  interpolation function is the commonly known method for theoretically ideal signal reconstruction of bandwidth-limited signals in the noise-free case, where

$$\text{si}(x) = \frac{\sin(x)}{x} \quad . \quad (4.6)$$

Due to the fact that the channel is not monitored continuously, but samples of the channel transfer-function  $T(f, t)$  are taken at the positions of the pilot symbols, the Doppler spectrum and the delay spectrum are cyclically repeated. To remove the cyclic repetitions, the spectra therefore have to be multiplied with the corresponding ideal filter functions for the Doppler spectrum

$$W_{\infty, f_D}(f_D) = \begin{cases} \frac{1}{2 \cdot f_{D_{filter}}} & |f_D| < f_{D_{filter}} \\ 0 & \text{otherwise} \end{cases} \quad (4.7)$$

and for the delay spectrum

$$W_{\infty, \tau}(\tau) = \begin{cases} \frac{1}{\tau_{filter}} & \frac{-\tau_{filter} + \tau_{max}}{2} < \tau < \frac{\tau_{filter} + \tau_{max}}{2} \\ 0 & \text{otherwise} \end{cases} \quad (4.8)$$

Note that  $f_{D_{filter}}$  is the maximum permitted Doppler frequency and  $\tau_{filter}$  is the maximum permitted delay for the filter design, resulting in the interpolation functions in direction of time  $t$

$$w_{\infty, f_D}(t) = \text{si}(\pi \cdot 2f_{D_{filter}} \cdot t) \quad (4.9)$$

and frequency  $f$

$$w_{\infty, \tau}(f) = \text{si}(\pi \cdot \tau_{filter} \cdot f) \cdot e^{j\pi\tau_{max}f} \quad (4.10)$$

The filter functions are shown in Fig. 4.3 for the cyclically repeated Doppler power spectrum (a) and delay power spectrum (b). Since only the time-discrete values  $t = k \cdot T'_s$  and the

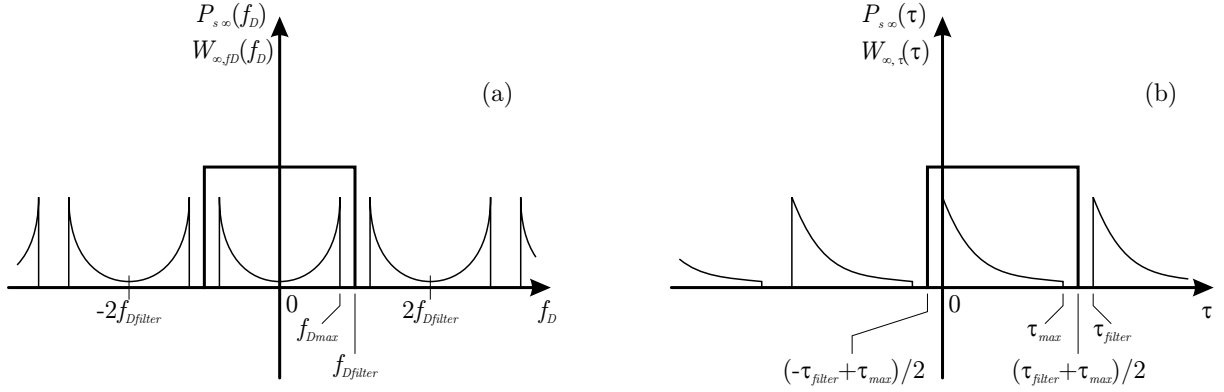


Figure 4.3: Ideal filter functions for the cyclically repeated Doppler power spectrum (a) and delay power spectrum (b)

frequency-discrete values  $f = l \cdot F_s$  are necessary for the interpolation, (4.9) and (4.10) can be rewritten as

$$w_{\infty,f_D}[k] = \text{si}\left(\frac{\pi \cdot k}{N_t}\right), \quad (4.11)$$

$$w_{\infty,\tau}[l] = \text{si}\left(\frac{\pi \cdot l}{N_f}\right) \cdot e^{j\frac{\pi \cdot l}{N_f} \cdot \frac{\tau_{\text{max}}}{\tau_{\text{filter}}}}, \quad (4.12)$$

where

$$N_t = \lfloor 1/(2f_{D\text{filter}}T'_s) \rfloor \quad (4.13)$$

is the distance of the pilots in direction of time and

$$N_f = \lfloor 1/(\tau_{\text{filter}}F_s) \rfloor \quad (4.14)$$

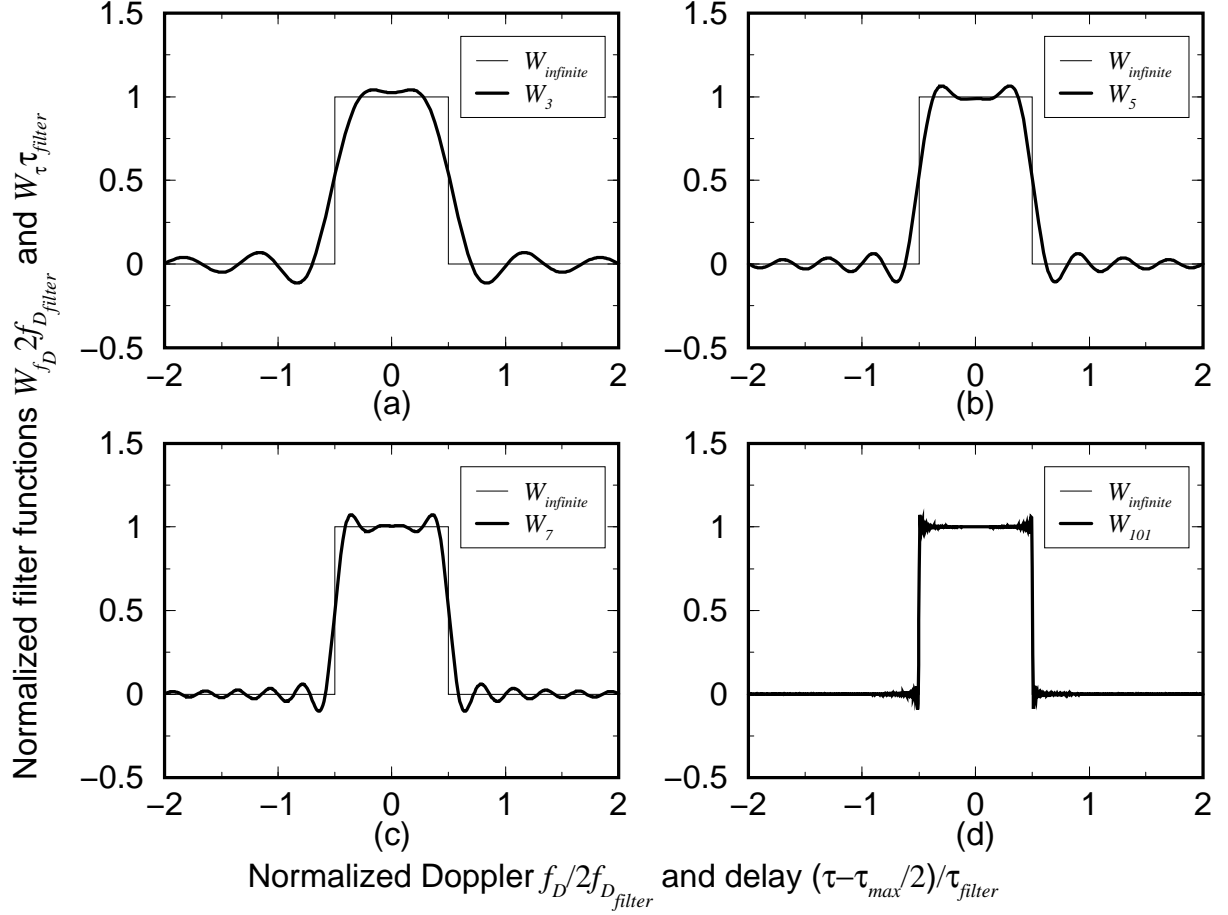
is the distance of the pilots in frequency direction. If  $f_{D\text{filter}} = f_{D\text{max}}$  and  $\tau_{\text{filter}} = \tau_{\text{max}}$  is chosen,  $N_t$  and  $N_f$  comply with the upper bound for the sampling theorem, compare (4.5) and (4.4).

**Shortened  $\text{si}(x)$  Function** The interpolation functions of (4.9) and (4.10) are not limited in direction of time  $t$ , respectively frequency  $f$ . For the implementation in practical systems they therefore have to be shortened to a finite length resulting in

$$w_{N_{\text{tap}},f_D}(t) = \begin{cases} w_{\infty,f_D}(t) & |t| < \frac{N_{\text{tap}}}{2} \cdot N_t T'_s \\ 0 & \text{otherwise} \end{cases}, \quad (4.15)$$

$$w_{N_{\text{tap}},\tau}(f) = \begin{cases} w_{\infty,\tau}(f) & |f| < \frac{N_{\text{tap}}}{2} \cdot N_f F_s \\ 0 & \text{otherwise} \end{cases}, \quad (4.16)$$

where  $N_{\text{tap}}$  is the number of filter taps that are used for the interpolated estimation of the channel transfer function  $T(f, t)$  at the position of a data symbol. For  $N_{\text{tap}}$ , different values can be chosen for the time and the frequency direction, even though the same value is applied here. Due to symmetric superposition effects in the interpolation process,  $N_{\text{tap}}$  should be an

Figure 4.4: Filter functions for  $\text{si}(x)$ -interpolated channel estimation

odd number. The shortening of the  $\text{si}(x)$  function affects the filter functions for the Doppler and the delay spectrum, see Appendix B, resulting in

$$W_{N_{tap}, f_D}(f_D) = \frac{1}{2\pi f_{D_{filter}}} \left[ \text{Si} \left( (f_D + f_{D_{filter}}) \cdot \frac{\pi N_{tap}}{2f_{D_{filter}}} \right) - \text{Si} \left( (f_D - f_{D_{filter}}) \cdot \frac{\pi N_{tap}}{2f_{D_{filter}}} \right) \right], \quad (4.17)$$

$$W_{N_{tap}, \tau}(\tau) = \frac{1}{\pi \tau_{filter}} \left[ \text{Si} \left( \left( \tau + \frac{\tau_{filter} - \tau_{max}}{2} \right) \cdot \frac{\pi N_{tap}}{\tau_{filter}} \right) - \text{Si} \left( \left( \tau - \frac{\tau_{filter} + \tau_{max}}{2} \right) \cdot \frac{\pi N_{tap}}{\tau_{filter}} \right) \right], \quad (4.18)$$

where  $\text{Si}(x)$  is the integral sine with

$$\text{Si}(x) = \int_0^x \text{si}(z) dz. \quad (4.19)$$

Since the interpolation functions in  $f$  and  $t$  are limited now, the filter functions in  $\tau$  and  $f_D$  are unlimited. The results of (4.17) and (4.18) are shown for some commonly used values of  $N_{tap} = \{3, 5, 7\}$  in Fig. 4.4. Additionally the results for  $N_{tap} = 101$  and  $N_{tap} = \infty$  are displayed. For large values of  $N_{tap}$ , the filter functions  $W_{N_{tap}}$  converge to  $W_{\infty}$ . Both filter functions  $W_{N_{tap}}$  are real-valued functions.

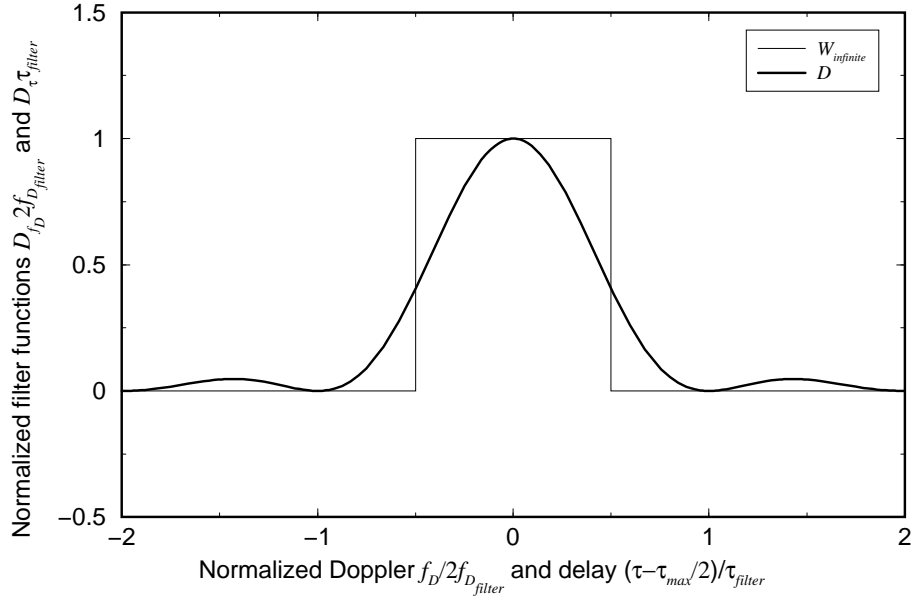


Figure 4.5: Filter functions for linear-interpolated channel estimation

#### 4.2.2.2 Linear Interpolation

Besides the  $\text{si}(x)$  interpolation, which in theory is optimal, there exists the possibility to use the simpler non-optimal linear interpolation method with the interpolation functions in direction of time  $t$

$$d_{f_D}(t) = \begin{cases} 1 - |t \cdot 2f_{D_{filter}}| & |t| < N_t T'_s \\ 0 & \text{otherwise} \end{cases}, \quad (4.20)$$

and frequency  $f$

$$d_{\tau}(f) = \begin{cases} (1 - |f \cdot \tau_{filter}|) \cdot e^{j\pi\tau_{max}f} & |f| < N_f F_s \\ 0 & \text{otherwise} \end{cases}. \quad (4.21)$$

The linear interpolation is simpler with respect to the fact that the number of used filter taps is always two, since only the two neighbour (pilot) samples are used for the interpolation. The corresponding filter functions, see Appendix C, are for the Doppler spectrum

$$D_{f_D}(f_D) = \frac{1}{2f_{D_{filter}}} \cdot \left[ \text{si} \left( \pi \frac{f_D}{2f_{D_{filter}}} \right) \right]^2, \quad (4.22)$$

and for the delay spectrum

$$D_{\tau}(\tau) = \frac{1}{\tau_{filter}} \cdot \left[ \text{si} \left( \pi \frac{\tau - \frac{\tau_{max}}{2}}{\tau_{filter}} \right) \right]^2. \quad (4.23)$$

The normalized representations of (4.22) and (4.23) are shown in Fig. 4.5. The filter functions  $D_{f_D}(f_D)$  and  $D_{\tau}(\tau)$  are real-valued functions.

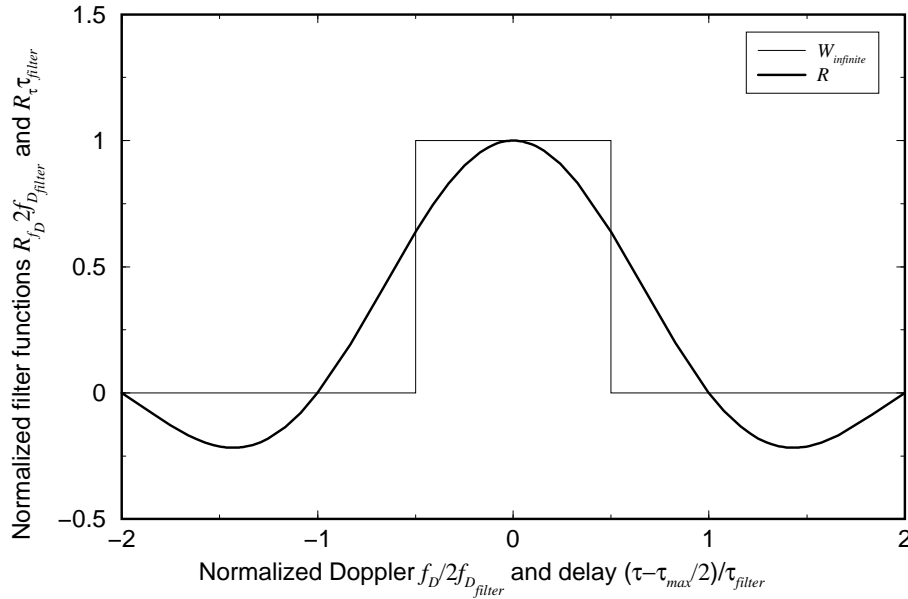


Figure 4.6: Filter functions for rectangular-interpolated channel estimation

#### 4.2.2.3 Rectangular Interpolation

The result of reducing the number of used filter taps to one is called rectangular interpolation. Actually this method doesn't really interpolate any more, but simply uses the estimated channel transfer function value of the closest pilot symbol. The resulting interpolation functions are in the direction of time  $t$

$$r_{f_D}(t) = \begin{cases} 1 & |t| < \frac{1}{2} \cdot N_t T'_s \\ 0 & \text{otherwise} \end{cases}, \quad (4.24)$$

and frequency  $f$

$$r_{\tau}(f) = \begin{cases} e^{j\pi\tau_{max}f} & |f| < \frac{1}{2} \cdot N_f F_s \\ 0 & \text{otherwise} \end{cases}. \quad (4.25)$$

The corresponding filter functions are for the Doppler spectrum

$$R_{f_D}(f_D) = \frac{1}{2f_{D_{filter}}} \cdot \text{si} \left( \pi \frac{f_D}{2f_{D_{filter}}} \right), \quad (4.26)$$

and for the delay spectrum

$$R_{\tau}(\tau) = \frac{1}{\tau_{filter}} \cdot \text{si} \left( \pi \frac{\tau - \frac{\tau_{max}}{2}}{\tau_{filter}} \right). \quad (4.27)$$

The normalized representations of (4.26) and (4.27) are shown in Fig. 4.6. The filter functions  $R_{f_D}(f_D)$  and  $R_{\tau}(\tau)$  are real-valued functions.

Besides si, linear and rectangular interpolation, there also exists the possibility to use splines as interpolation functions [Sch92]. In that case, the interpolation functions are built piece

by piece from cubic parabolas between two pilot symbols. Since new parameter sets have to be calculated individually for each parabola, the interpolation gets far too complicated and time-inefficient for the channel estimation process. Therefore, splines are not considered here.

#### 4.2.2.4 Comparison of the Different Interpolation Methods

To be able to compare the effectiveness of the different interpolation methods, one has to look at the different aspects that might influence the channel estimation performance:

- The **complexity** of the interpolation has to be considered. While rectangular and linear interpolation only use one or two neighbouring pilot symbols to estimate the channel transfer function at the current position, si-interpolation uses from three up to an unlimited number of filter taps. This makes the interpolation routine more time and energy consuming.
- In contrast to the theoretical assumption that there is an unlimited number of pilot symbols with distance  $N_f$  or  $N_t$  respectively, the **number of pilot symbols is limited** in a practical system at least in the frequency direction. This results in distortions of the estimated channel transfer function in positions close to the border of the pilot symbol frame, where more pilot symbols are needed than there are available to comply with the selected  $N_{tap}$ . Only the interpolation with the  $\text{si}(x)$  function is affected by this, since for linear and rectangular interpolation the two or one neighbouring pilot symbols are sufficient.
- It has been shown in the previous sections that the filter functions are always real-valued and therefore cause no phase distortions. On the other hand, all filter functions, besides the theoretical ideal filter, have out-of-band side-lobes which add high-frequency noise from repeated spectra. For si and rectangular interpolation these side-lobes are undergoing an additional **out-of-band phase-shift of the filter function**, which means that they are negated (phase-shifted by  $180^\circ$ ) in some areas and may cause complex noise by constructive superpositioning.
- As already mentioned in the previous item, non-ideal filter functions cause **out-of-band filtering noise** as well as **in-band filtering noise**. This can be expressed by the *in-band-signal to in-band-noise ratio* for the Doppler filter function

$$ISINR = 10 \cdot \log \left( \frac{\int_0^{f_{D_{filter}}} |F(f_D)|^2 df_D}{\int_0^{f_{D_{filter}}} |1/(2f_{D_{filter}}) - F(f_D)|^2 df_D} \right) dB \quad (4.28)$$

and the *in-band-signal to out-of-band-noise ratio*

$$ISONR = 10 \cdot \log \left( \frac{\int_0^{f_{D_{filter}}} |F(f_D)|^2 df_D}{\int_{f_{D_{filter}}}^{\infty} |F(f_D)|^2 df_D} \right) dB, \quad (4.29)$$

where  $F(f_D)$  is one of the possible filter functions  $W_{N_{tap}, f_D}(f_D)$ ,  $D_{f_D}(f_D)$  or  $R_{f_D}(f_D)$ . The same ratios apply for the delay filter functions respectively. The in-band filter noise disturbs the signal by not providing the full energy for the desired spectrum and the out-of-band filter noise disturbs the signal by adding undesired energy from repeated spectra.

The *ISINRs* and the *ISONRs* for the different filters are shown in Table 4.1. It appears that

Table 4.1: In-band and out-of-band noise-ratios for the different interpolation methods

	Ideal filter	si interpolation				linear	rect
						interpolation	
Filter taps $N_{tap}$	$\infty$	101	7	5	3	(2)	(1)
In-band ratio <i>ISINR</i>	$\infty$ dB	30.0 dB	18.8 dB	17.5 dB	15.4 dB	8.68 dB	14.4 dB
Out-of-band ratio <i>ISONR</i>	$\infty$ dB	29.9 dB	17.6 dB	15.9 dB	13.1 dB	12.8 dB	5.34 dB

the *ISINRs* and *ISONRs* of the si-interpolation are outperforming the linear and rectangular interpolation even for small tap sizes. Especially the rectangular interpolation has due to its large side-lobes a very poor *ISONR* and is therefore not considered for the interpolation of the estimated channel transfer function values. The *ISONRs* for the linear interpolation and si-interpolation with  $N_{tap} = 3$  are quite close, whereas the *ISINR* of the si-interpolation outperforms the linear one. Considering the border effects, the out-of-band phase shifts and the in-band overshooting of the si-function, linear interpolation is an appropriate option for a low complexity implementation of the channel estimation. Corresponding results are shown in Section 5.2.1.

### 4.2.3 Channel Equalization

The final equalization of the received subcarrier symbols in the OFDM frame is done by multiplying the matrix of the received OFDM frame  $\mathbf{Y}$  element-wise with the equalization matrix  $\mathbf{G}$  for all positions different to the pilot symbol positions. The elements  $G_{k,l}$  of  $\mathbf{G}$  on the other hand are calculated from the interpolated estimated channel transfer function matrix  $\hat{\mathbf{T}}$  for all  $l$ ,  $-N_c/2 \leq l < N_c/2$ , and  $k$ ,  $0 \leq k < N_s$ , depending on one of the following equalization methods [Kai98]:

- **Maximum Ratio Combining (MRC):**

$$G_{k,l} = \hat{T}_{k,l}^*, \quad (4.30)$$

- **Equal Gain Combining (EGC):**

$$G_{k,l} = \frac{\hat{T}_{k,l}^*}{|\hat{T}_{k,l}|}, \quad (4.31)$$

- **Zero-Forcing (ZF) Equalization:**

$$G_{k,l} = \frac{1}{\hat{T}_{k,l}} = \frac{\hat{T}_{k,l}^*}{|\hat{T}_{k,l}|^2}, \quad (4.32)$$

- **Minimum Mean Square Error (MMSE) Equalization:**

$$G_{k,l} = \frac{\hat{T}_{k,l}^*}{|\hat{T}_{k,l}|^2 + 1/\gamma_c}, \quad (4.33)$$

where  $\gamma_c$  is the average SNR per subcarrier at the input of the data detector.

### 4.3 Differential Coherent Modulation/Demodulation

The necessity of channel estimation and equalization is a large disadvantage of coherent demodulation. First, it is time and energy consuming in the receiver and second, there always remains the possibility to do a wrong estimation. Furthermore, the insertion of the necessary pilot symbols leads to a reduction of the available data rate. These disadvantages can be circumvented by choosing differential coherent modulation and demodulation, where the information is enclosed in the differential phase between two transmitted symbols and no additional channel estimation and equalization is needed. For that purpose Differential Phase Shift Keying (DPSK) with Gray encoding is used [Pro95]. The standard method for differential modulation in direction of time is

$$X_{k,l} = D_{k,l} \cdot X_{k-1,l}, \quad (4.34)$$

where  $D_{k,l}$  is the source symbol that contains the user information with  $|D_{k,l}| = 1$ . For  $M$ -ary DPSK the data symbols come from the set

$$D_{k,l} \in \left\{ 1, e^{j2\pi\frac{1}{M}}, \dots, e^{j2\pi\frac{M-1}{M}} \right\}. \quad (4.35)$$

Differential demodulation on the receiver side is done by calculating

$$\hat{D}_{k,l} = Y_{k,l} \cdot Y_{k-1,l}^*, \quad (4.36)$$

where  $\hat{D}_{k,l}$  is the estimation for the source symbol that has been transmitted. The same rules apply for differential modulation and demodulation in direction of frequency respectively. From

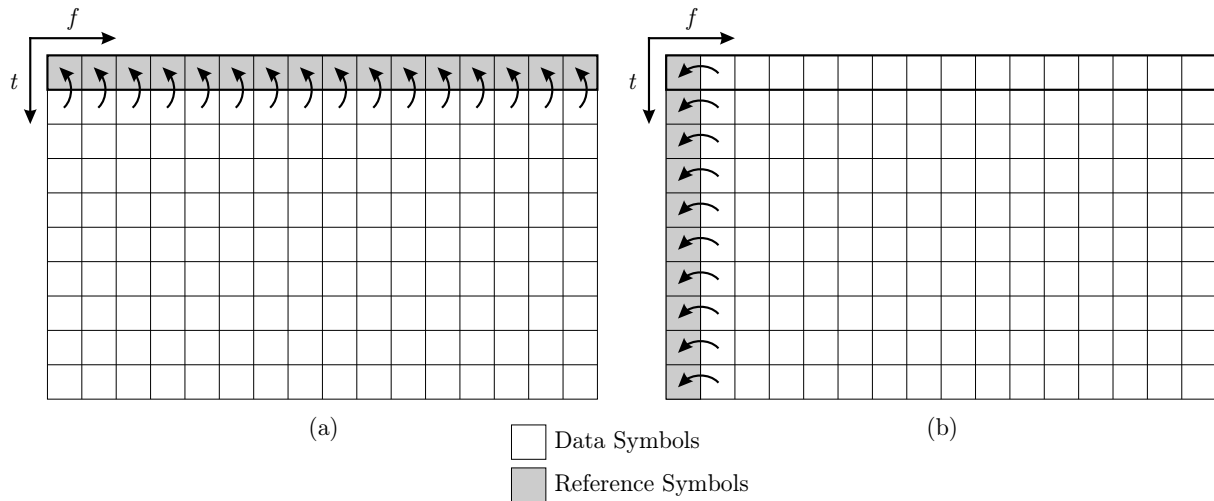


Figure 4.7: OFDM differential (de)modulation in direction of time (a) and frequency (b)

(4.34) and (4.36) it can be seen that a reference symbol is always needed in negative time or negative frequency direction. For the time direction, an initial OFDM reference symbol at the beginning of an OFDM frame, and for the frequency direction, an initial reference subcarrier in each OFDM symbol is needed that doesn't contain any user information, compare Fig. 4.7(a) and Fig. 4.7(b).

The missing (estimated) absolute reference in conjunction with a differential combination of the received symbols leads to a degradation of the performance compared to the coherent system. Furthermore, systems where  $M > 8$  or  $M > 16$  are not practical due to the decreasing phase differences between neighbouring data symbols from the corresponding set.

Therefore, in [RoB97], a 64 Differential Amplitude and Phase Shift Keying (DAPSK) modulation scheme is considered that uses a special amplitude mapping besides the phase mapping to increase the number of transmitted bits per symbol and thus the throughput. It can be incoherently or quasi-coherently demodulated. In conjunction with convolutional channel codes, a new metric is used for the Viterbi decoder and the results are compared to coherent 64 QAM. The lack of this modulation scheme is that the constellation points are not equally spaced and thus the BER of the amplitude bits is different to the BER of the phase bits. The corresponding amplitude mapping factor depends on the demodulation method and the SNR. Furthermore, for quasi-coherent demodulation the channel influence has to be eliminated with an estimation that requires knowledge about the time-variant channel for an optimum result.

### 4.3.1 Differential MC-CDMA

It now also becomes clear why normal MC-CDMA spreading with Walsh-Hadamard sequences, as introduced in Section 3.2.3.4, is not possible for differentially modulated signals. Since multiple access causes symbol constellations with high amplitudes on some subcarriers while at the same time the amplitude on other subcarriers can be zero, this is a fatal situation

for differential modulation. Due to the memory effect of the reference symbols, the symbol amplitude of consecutive symbols cannot be reconstructed correctly in the receiver, especially for the case that the transmitted symbol amplitude of the previous symbol was equal to zero.

Other differential modulation methods for MA, like for example chip-level differential encoding, have been proposed. This method is based on a post-detection antenna diversity scheme to reduce the MAI and only delivers good results if the number of active users is less than 10% of the number of possible users in the system [ToK98].

The techniques mentioned before are all based on MA on modulation symbol level that causes problems and a large performance loss on the receiver side for differential demodulation. Therefore, a different new method is introduced here that implements MA on data level. Two main goals are considered for such a system. First, the information of a single user should be spread over several subcarriers to benefit from the corresponding spreading gain. Second, several data elements or users should be able to use the same set of subcarriers to increase the throughput.

Spreading can not only be applied by using a chip sequence as introduced in Section 3.2.3.4, but also by using a block code. Fig. 4.8(a) shows the structure of a MC-CDMA system with differential modulation that uses a binary block code for spreading the binary data  $D^{(k)}$  of  $K$  users on  $L$  binary sub-symbols  $S_l$  resulting in the spread vector  $\vec{\mathbf{S}}$ . Groups of  $\log_2(M)$  bits of this vector are combined to one source symbol which is then  $M$ -DPSK modulated on subcarrier-level, requiring a total of  $\lceil L/\log_2(M) \rceil$  subcarriers, followed by an OFDM modulation. Possible codes that can be used for spreading are the Bose, Chaudhuri and Hocquenghem (BCH) codes in the Galois Field (GF)  $\text{GF}(2)$ . [ShC83, Chapter 6].

Since the  $\log_2(M)$  bits of a received symbol are similarly affected by the channel fading, it makes sense to use a code that can correct symbol errors in  $\text{GF}(M)$ . While in the previous case one received symbol error might affect up to  $\log_2(M)$  bits that are treated as individual errors by the decoder, now the received symbol is treated as one unit, no matter how many bits of the symbol are wrong. The corresponding spreading system is shown in Fig. 4.8(b). Another advantage of this technique is that every user can transmit  $\log_2(M)$  bits at the same time. For this implementation  $L$  subcarriers are needed. Possible candidates for the spreading codes are Reed-Solomon (RS) codes, any linear block codes that can operate in a  $\text{GF}(M)$  different to  $\text{GF}(2)$  [ShC83] or the block coding scheme based on complementary sequences for multi-carrier signals that has been investigated in [OcI00]. The latter has the advantage that it reduces the Peak-to-Average Power Ratio (PAPR) to 3 dB for code rate  $R = 5/16$  or 6 dB for code rate  $R = 4/8$  and can be implemented for any  $M$ -DPSK demodulated signal. One drawback that applies is that the code rate is fixed to  $R = K/2^{K-1}$ , i.e.  $L = 2^{K-1}$ .

For the case that RS-codes are used, there is a strict relation between the maximum codeword length, thus the size of the spread vector  $\vec{\mathbf{S}}$ , and the applied Galois field  $\text{GF}(2^m)$

$$L \leq 2^m - 1. \quad (4.37)$$

If the scheme of Fig. 4.8(b) is applied, this would require a high level  $M$ -DPSK mapping, since  $M = 2^m$ , so that if a sufficiently high number of users should be able to use the system, the

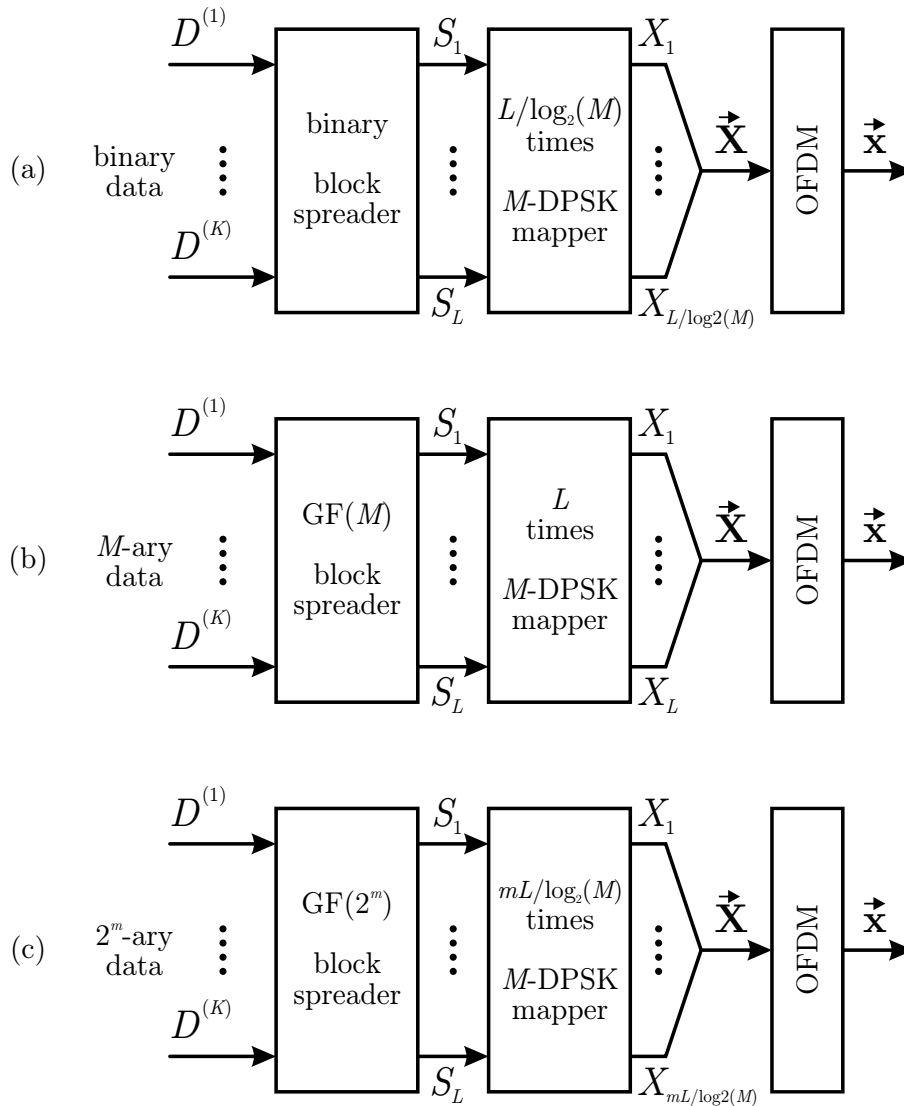


Figure 4.8: OFDM MC-CDMA transmitter for  $K$  users with differential modulation; binary spreader (a),  $\text{GF}(M)$  spreader (b) and  $\text{GF}(2^m)$  spreader (c)

filling of the I/Q constellation diagram would be inefficient due to the corresponding crammed  $M$ -DPSK scheme. Therefore, it makes sense to distribute one  $\text{GF}(2^m)$  symbol on several  $\text{GF}(M)$  symbols. For example, if a  $\text{GF}(2^8)$  (8 bit symbols) RS-code is used in conjunction with 4DPSK (DQPSK) modulation (2 bit symbols), one symbol of the codeword is distributed on four ( $=8/2$ ) DQPSK-modulated subcarriers. The total number of subcarriers needed is equal to  $\lceil (m \cdot L) / \log_2(M) \rceil$ . This scheme is shown in Fig. 4.8(c).

For all codes above used for spreading, the code rate is

$$R = \frac{K}{L}, \quad K \leq L. \quad (4.38)$$

For the special case  $K = L$ , the code rate is  $R = 1$ , which would not bring any benefit, since a received error would possibly influence the decoded information of all  $K$  users. On the other hand for  $K < L$ , two advantages result from the implementation. First, the code offers an

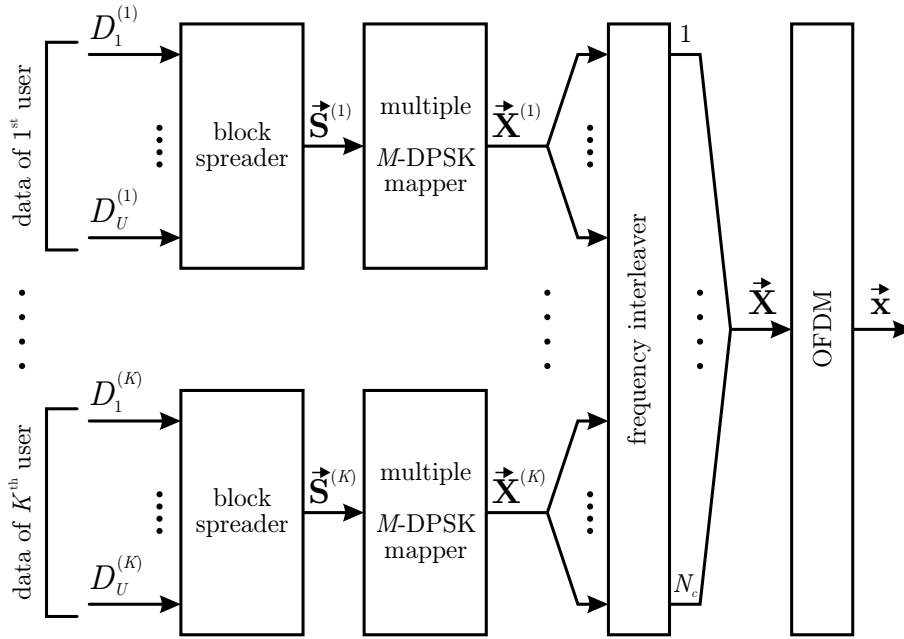


Figure 4.9: OFDM MC-CDMA transmitter for  $K$  users with differential modulation and  $U$  data symbols for each user

additional error protection besides its use for spreading. Second, differential modulation can be applied with this spreading method. Unfortunately, there is also a disadvantage for large codeword lengths  $L$ ; to extract the information-carrying data symbol of one user, normally the whole codeword has to be decoded.

Long codewords can be avoided by applying a variation of the spreading scheme from Fig. 4.8. An identically shorter block spreader is used for each individual user while the number of data symbols for each user is increased to  $U$ . The modulated vectors  $\vec{\mathbf{X}}^{(k)}$  of the users are afterwards combined in an additional frequency interleaver stage. The corresponding transmitter scheme is shown in Fig. 4.9. If a closer look is taken at this scheme, it becomes clear that it is similar to conventional coded OFDM with a frequency interleaver on top which gives an additional diversity gain. This scheme on the other hand is of special interest, since the use of differential modulation is promising in the uplink from a mobile entity to the base station. The channel estimation and equalization in the receiver for each transmitting mobile entity, as necessary for the coherent case, can be circumvented. For this purpose, each mobile entity is implemented as a separate user while the inputs of the other users in the frequency interleaver stage are left empty, so that the mobile entity only transmits its own information. Combination of the synchronized users takes place in the receiver entity.

## 4.4 Two-Dimensional Differential Demodulation

To overcome the degrading effects of differential demodulation, a variety of differential detection techniques has been discussed in the literature [DiS90] [AdS95] [RoB97] [HoL99]. One

of these algorithms is based on multiple-symbol detection [DiS90], while another algorithm applies an additional decision feedback from several multiple-symbol detectors [AdS95]. The third algorithm uses multiple differentially encoded amplitude levels in conjunction with decision feedback and filtering in the receiver [RoB97]. Another algorithm applies “turbo-decoding” by using the differential modulation scheme as an inner code with rate one [HoL99]. While [AdS95] and [HoL99] focus on single-carrier modulation, [RoB97] applies OFDM but also performs the differential demodulation in only one direction.

In this section, a new algorithm for differential demodulation is proposed that makes use of the two-dimensional structure of OFDM frames.

#### 4.4.1 Basic Idea for Two-Dimensional Differential Demodulation

In the European Digital Audio Broadcasting (DAB) standard [DAB95], differential modulation and demodulation is intended to be performed in only one direction, here by OFDM symbols in time  $t$ , see Fig. 4.10(b), with the help of one OFDM reference symbol at the beginning of the frame. This means that only the closest neighbour in negative direction of time is used for demodulation. It is obvious that there are additionally seven other closest neighbours, see Fig. 4.11. It is shown that these neighbours can also be used for differential demodulation without changing the transmitter. The distance to all eight neighbours is defined to be one.

Two-Dimensional Differential Demodulation (2D-DD) is done by not necessarily choosing the closest path with distance one, here in negative direction of time  $t$ , but by using a detour path. A detour path has the same origin  $A$  and destination  $B$  as the direct path, but with distance larger than one resulting from the combination of several differential demodulation steps. The detour path is obtained from hopping to one or several intermediate neighbours. The additional steps are chosen according to an algorithm that assures that the possibility of a bit error is decreased by choosing the detour path rather than the direct path. Differential demodulation between two arbitrary symbols within the frame is possible since all transmitted differentially modulated symbols in general come from the same transmission symbol alphabet, see Fig. 4.10(a). Thus, the demodulation between two arbitrary symbols again delivers a symbol from the source alphabet, see Fig. 4.10(c).

#### 4.4.2 Frame-Worm Algorithm for Detour Path Determination

An OFDM frame can be interpreted as a two-dimensional structure consisting of complex-valued symbols in direction of frequency  $f$  and time  $t$ . The used modulation scheme can be chosen to be DQPSK [Pro95] in time direction, for example. Like discussed above, all transmitted symbols themselves come from the same alphabet, here QPSK symbols, and differential demodulation can theoretically be performed on every selected pair of received symbols. Due to stronger statistical correlations, especially in fading channel environments, only the eight surrounding

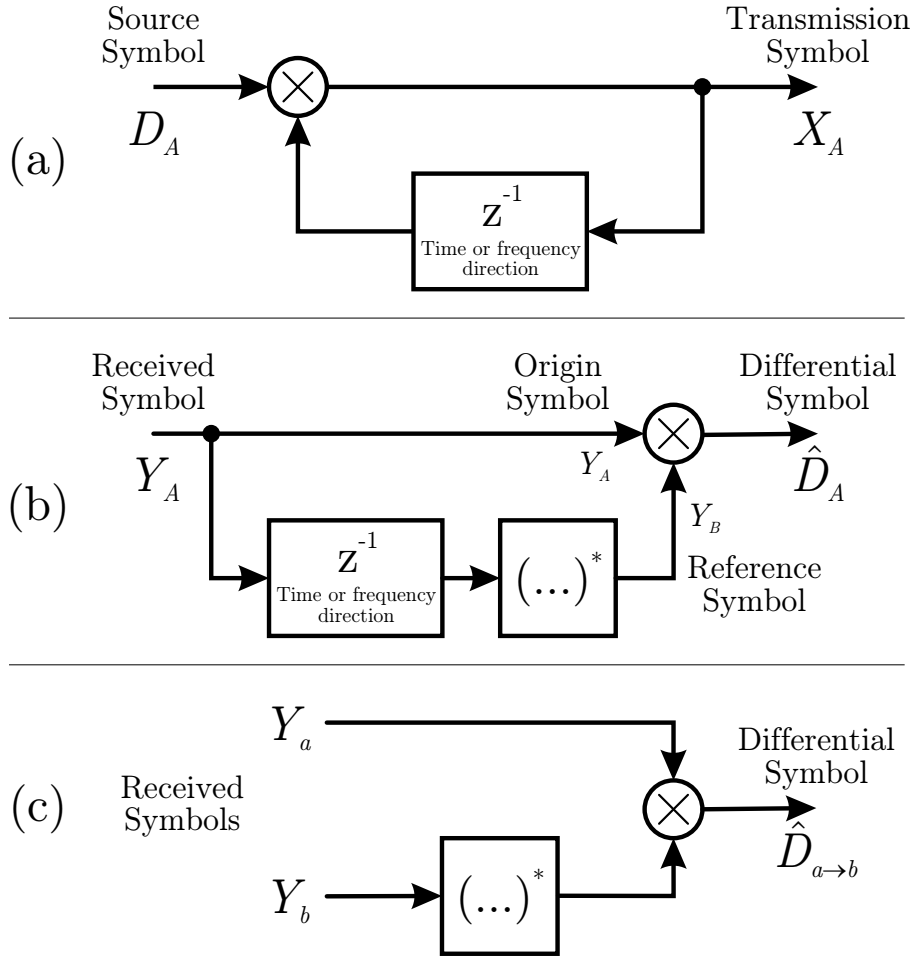


Figure 4.10: (a) One-dimensional differential modulation, (b) Conventional one-dimensional differential demodulation, (c) Differential demodulation between two arbitrary received symbols

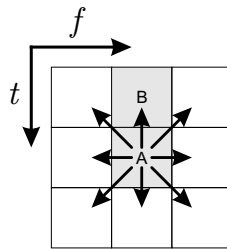


Figure 4.11: Differential neighbourhood demodulation of one OFDM subcarrier

symbols are regarded as relevant here. For each of the eight neighbours of one symbol in the center, now a differential demodulation step as shown in Fig. 4.11 and Fig. 4.10(c) is performed according to:

$$\hat{D}_{a \rightarrow b} = Y_a \cdot Y_b^* = a_a \cdot a_b \cdot e^{j(\varphi_a - \varphi_b)}, \quad (4.39)$$

where  $Y_a$  is the current symbol under investigation,  $Y_b$  is one of the eight neighbour symbols,  $\hat{D}_{a \rightarrow b}$  is the symbol after the differential demodulation,  $a_a, a_b$  are the amplitudes and  $\varphi_a, \varphi_b$  the arguments of the symbols.

If M-DPSK is considered, the information is included in the differential phase

$$\Delta\varphi_{a,b} = \varphi_a - \varphi_b. \quad (4.40)$$

This means that the information-carrying phase of the original one-dimensional differential demodulation is

$$\Delta\varphi_{A,B} = \varphi_A - \varphi_B. \quad (4.41)$$

If now instead of the direct path, a path with several intermediate steps is chosen, the result are differential phases  $\Delta\varphi_{A,1}, \Delta\varphi_{1,2}, \dots, \Delta\varphi_{(\mathcal{L}-1),B}$  for each step, where  $\mathcal{L}$  is the current investigated iteration path length, here  $\mathcal{L} \geq 2$ . If those differential intermediate phases would be summed up, the result would be

$$\begin{aligned} & \Delta\varphi_{A,1} + \left[ \sum_{i=1}^{\mathcal{L}-2} \Delta\varphi_{i,i+1} \right]_{\mathcal{L}>2} + \Delta\varphi_{(\mathcal{L}-1),B} = \\ & = (\varphi_A - \varphi_1) + (\varphi_1 - \varphi_2) + \dots + (\varphi_{\mathcal{L}-1} - \varphi_B) = \\ & = \varphi_A - \varphi_B = \Delta\varphi_{A,B}, \end{aligned} \quad (4.42)$$

which means that the phase difference  $\Delta\varphi_{A,B}$  remains unchanged and a simple adding of the intermediate phases would not bring any advantage, but on the other hand also would not influence the phase of the original path  $A \rightarrow B$ . This offers the possibility to take a closer look on the intermediate steps individually. Each received differential phase can be divided into a valid phase  $\varphi_{source\_a,b}$  and a phase error  $\varphi_{error\_a,b}$ , that corresponds to the phase offset of the closest matching source-symbol phase:

$$\Delta\varphi_{a,b} = \varphi_{source\_a,b} + \varphi_{error\_a,b}. \quad (4.43)$$

The common one-dimensional differential demodulation directly concludes from  $\Delta\varphi_{A,B}$  to the phase of the source-symbol  $\varphi_{source\_A,B}$ .

In contrast to this, the new 2D-DD algorithm proposed here decides for every individual intermediate phase  $\Delta\varphi_{A,1}, \Delta\varphi_{1,2}, \dots, \Delta\varphi_{(\mathcal{L}-1),B}$  on a possible phase of the source-alphabet  $\varphi_{source\_A,1}, \varphi_{source\_1,2}, \dots, \varphi_{source\_(\mathcal{L}-1),B}$ . Additionally, the phase errors  $\varphi_{error\_A,1}, \varphi_{error\_1,2}, \dots, \varphi_{error\_(\mathcal{L}-1),B}$  and the amplitudes  $a_A a_1, a_1 a_2, \dots, a_{(\mathcal{L}-1)} a_B$  can be used for the path criteria and the resulting estimation.

Whenever a decision is made about a possible symbol of the source alphabet, it cannot be guaranteed that this is the true source symbol. For this reason, the path criteria has to make sure that choosing a detour path rather than the direct path is more reliable even for the fact that the detour path with its intermediate steps is “longer”. Therefore, at first the direct path is considered the most reliable and chosen as the reference path; iteration length  $\mathcal{L} = 1$ . For a certain criteria now all paths or a subgroup of all possible paths up to a definable iteration path depth  $\mathcal{N}$  that reach the destination symbol  $B$  are investigated. If, considering the criteria, one of the alternative paths is more reliable than the reference path, this alternative path becomes the new reference path and so on.

Considering the criteria, the most reliable path therefore has a length  $\mathcal{L}$  of  $1 \leq \mathcal{L} \leq \mathcal{N}$ . For the final decision about the possible phase of the source symbol, now the differential phase sum  $\Delta\varphi'_{A,B}$  of the chosen path is calculated as follows:

$$\Delta\varphi'_{A,B} = \begin{cases} \varphi_{source\_A,B} & \text{for } \mathcal{L} = 1 \\ \varphi_{source\_A,1} + \varphi_{source\_1,B} & \text{for } \mathcal{L} = 2 \\ \varphi_{source\_A,1} + \sum_{i=1}^{\mathcal{L}-2} \varphi_{source\_i,(i+1)} + \varphi_{source\_(\mathcal{L}-1),B} & \text{otherwise} \end{cases} \quad (4.44)$$

To get the final corresponding bit sequence of the demodulation, the information from the obtained path has to be extracted. Therefore the phase sum  $\Delta\varphi'_{A,B}$  is DQPSK-demodulated.

### 4.4.3 Mathematical Theory for Path Determination

It has already been mentioned that when a detour path is chosen, one has to make sure that this path is more reliable than the direct path. To clarify what is meant by a more reliable path, a closer look on the mathematical theory of DPSK is taken. Since the information is included in the phase alone, minimum distance in the receiver is equal to minimum phase distance to one of the possible transmitted symbols. Therefore, first the two-dimensional density function for Additive White Gaussian Noise (AWGN)

$$f_{xy}(x, y) = \frac{1}{2\pi\sigma^2} e^{-\frac{(x-m_x)^2+(y-m_y)^2}{2\sigma^2}}, \quad (4.45)$$

in the I/Q Cartesian coordinate system  $(x, y)$  is transformed to the polar coordinate system  $(r, \varphi)$ :

$$f_{r\varphi}(r, \varphi) = \frac{r}{2\pi\sigma^2} e^{-\frac{r^2-2r(m_x \cos(\varphi)+m_y \sin(\varphi))+(m_x^2+m_y^2)}{2\sigma^2}} \quad (4.46)$$

where  $0 < r < \infty$  is the radius,  $-\pi < \varphi \leq \pi$  is the angle,  $\sigma$  is the standard deviation of the noise and  $(m_x, m_y)$  is the mean value of the signal in Cartesian coordinates. Without loss of generality, one possible transmitted symbol  $X_{(0)}$  can assumed to be  $(m_{x_{X(0)}}, m_{y_{X(0)}}) = (\sqrt{E_S}, 0)$ . By substituting

$$\sigma = \sqrt{\frac{N_0}{2}}, \quad m_{x_{X(0)}} = \sqrt{E_S}, \quad m_{y_{X(0)}} = 0, \quad (4.47)$$

the two-dimensional probability density function [Pap91][Pro95]

$$f_{r\varphi_{Y(0)}}(r, \varphi) = \frac{r}{\pi N_0} e^{-\frac{r^2-2r\sqrt{E_S} \cos(\varphi)+E_S}{N_0}} \quad (4.48)$$

is obtained for the received symbol  $Y_{(0)}$ .  $E_S$  is the transmitted signal energy per subcarrier and  $N_0/2$  is the AWGN variance. This function is displayed in Fig. 4.12.

So far only the received symbols have been investigated. From (4.39) it can be seen that during the differential demodulation process, two of these symbols are multiplied with each other, so

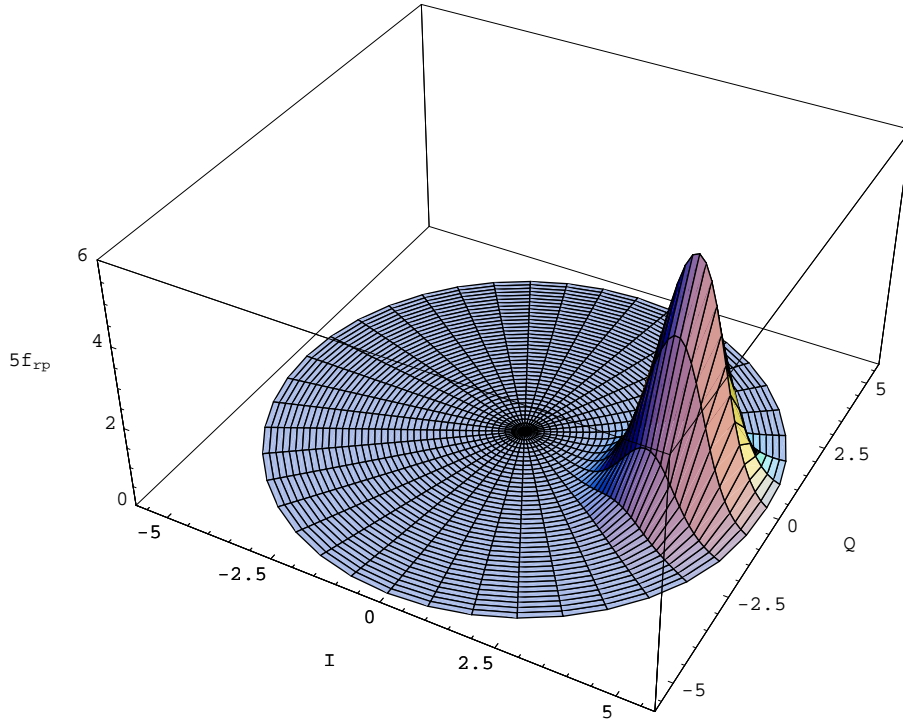


Figure 4.12: 2-D probability density function  $5 \cdot f_{r\varphi_{Y(0)}}(r, \varphi)$  for  $\gamma_c = 11$  dB

that the information carrying phase difference  $\varphi_a - \varphi_b$  arises. Since the amplitudes  $a_a$  and  $a_b$  play no role in the decision process, they can be eliminated by integrating (4.48) over  $r$ ,

$$f_{\varphi_{Y(0)}}(\varphi) = \int_0^{\infty} f_{r\varphi_{Y(0)}}(r, \varphi) dr, \quad (4.49)$$

resulting in

$$f_{\varphi_{Y(0)}}(\varphi) = \frac{e^{-\frac{E_S}{N_0}}}{2\pi\sqrt{N_0}} \left[ \sqrt{N_0} + e^{\frac{E_S \cos^2(\varphi)}{N_0}} \sqrt{\pi E_S} \cos(\varphi) \cdot \left( 1 + \operatorname{erf} \left( \frac{\sqrt{E_S} \cos(\varphi)}{\sqrt{N_0}} \right) \right) \right], \quad (4.50)$$

where  $\operatorname{erf}(x)$  is the error function  $\operatorname{erf}(x) = \frac{2}{\sqrt{\pi}} \int_0^x e^{-t^2} dt$ . Since the result of (4.50) cannot be analytically integrated in further steps, the following simplification is introduced

$$\tilde{f}_{\varphi_{Y(0)}}(\varphi) = \frac{f_{r\varphi_{Y(0)}}(\sqrt{E_S}, \varphi)}{\int_{-\pi}^{+\pi} f_{r\varphi_{Y(0)}}(\sqrt{E_S}, \varphi) d\varphi} = \frac{e^{2\gamma_c \cdot \cos(\varphi)}}{2\pi \cdot I_0(2\gamma_c)}, \quad (4.51)$$

where

$$\gamma_c = \frac{E_S}{N_0} \quad (4.52)$$

and  $I_0(\cdot)$  is the zero-order modified Bessel function of the first kind. The use of  $r = \sqrt{E_S}$  is chosen since most of the distributed energy can be found in this distance due to  $m_{x_{Y(0)}}$ .

The distributions of  $\varphi_a$  and  $\varphi_b$  can be considered independent, so that  $\Delta\varphi_{a,b}$  of (4.40) is the subtraction of two independent random variables. Again without loss of generality it can be assumed that the reference symbol  $Y_b$  has been the transmitted symbol  $X_{(0)}$  as well, so that the joint distribution for  $\hat{D}_{(0),a \rightarrow b} = Y_{(0),a} \cdot Y_{(0),b}^*$  (this is only one of  $M$  possible solutions for  $\hat{D}_{(0),a \rightarrow b}$  with M-DPSK) can be written as the Auto Correlation Function (ACF)

$$f_{\Delta\varphi \text{ ACF}}(\Delta\varphi) = f_{\Delta\varphi_{\hat{D}_{(0)}}}(\Delta\varphi) = \int_{-\pi}^{+\pi} f_{(\Delta\varphi+p)Y_{(0)}}(\Delta\varphi+p) \cdot f_{\Delta\varphi Y_{(0)}}(\Delta\varphi) dp, \quad (4.53)$$

with  $-\pi < \Delta\varphi \leq \pi$ . The result for the approximation of (4.51) is

$$\check{f}_{\Delta\varphi \text{ ACF}}(\Delta\varphi) = \int_{-\pi}^{+\pi} \check{f}_{(\Delta\varphi+p)Y_{(0)}}(\Delta\varphi+p) \cdot \check{f}_{\Delta\varphi Y_{(0)}}(\Delta\varphi) dp = \frac{\int_{-\pi}^{+\pi} e^{2\gamma_c \cdot (\cos(\Delta\varphi+\xi) + \cos(\Delta\varphi))} d\xi}{4\pi^2 \cdot [I_0(2\gamma_c)]^2}. \quad (4.54)$$

A further simplification step with

$$\cos(x) \approx 1 - \frac{x^2}{2} \quad (4.55)$$

for small  $x$  delivers the closed form solution

$$\check{f}_{\Delta\varphi \text{ ACF}}(\Delta\varphi) = \frac{e^{\gamma_c \left(4 - \frac{\Delta\varphi^2}{2}\right)} \left[ \operatorname{erf}\left(\left(2\pi - \Delta\varphi\right)\sqrt{\frac{\gamma_c}{2}}\right) + \operatorname{erf}\left(\left(2\pi + \Delta\varphi\right)\sqrt{\frac{\gamma_c}{2}}\right) \right]}{8\sqrt{2\pi^3\gamma_c} \cdot [I_0(2\gamma_c)]^2}. \quad (4.56)$$

Numerical integration of (4.53) and the approximation (4.56) result in the graph shown in Fig. 4.13.

Another numerical integration step delivers the commonly known values for the symbol error rate  $P_E(M)$  of  $M$ -ary DPSK [PRR82]

$$P_E(M) = 2 \int_{\pi/M}^{\pi} f_{\Delta\varphi \text{ ACF}}(\Delta\varphi) d\Delta\varphi. \quad (4.57)$$

In the following, DQPSK modulation is chosen. Using  $P_E(M)$  from [PRR82] and (4.57) with the approximation  $\check{f}_{\Delta\varphi \text{ ACF}}(\Delta\varphi)$  gives the standard one-dimensional exact and approximated representations of the Bit Error Rate (BER) for DQPSK-modulated signals with the AWGN channel shown in Fig. 4.14.

Investigation of all possible symbol combinations that result in a transmitted symbol  $X_{(\xi)}$ ,  $\forall \xi \in \{0, 1, 2, 3\}$  delivers the PDFs  $p(\hat{d}|D_{(\xi)})$  shown in Fig. 4.15 for the received differential symbol  $\hat{D}_{(\xi)}$ , where  $D_{(\xi)}$  are the source symbols before differential modulation.

The logarithmic pdf likelihood ratio  $\Lambda(\Delta\varphi)$  for making the correct decision for a differential symbol in spite of a wrong decision for the symbol in general can be expressed by

$$\Lambda(\Delta\varphi) = \log\left(\frac{p_{\text{correct}}}{p_{\text{error}}}\right) = \log\left(\frac{f_{\Delta\varphi \text{ ACF}}(\Delta\varphi)}{f_{\Delta\varphi \text{ ACF}}(\Delta\varphi - \frac{\pi}{2}) + f_{\Delta\varphi \text{ ACF}}(\Delta\varphi + \frac{\pi}{2}) + f_{\Delta\varphi \text{ ACF}}(\Delta\varphi + \pi)}\right) \quad (4.58)$$

$$\forall \Delta\varphi \in [-\pi/4, +\pi/4]$$

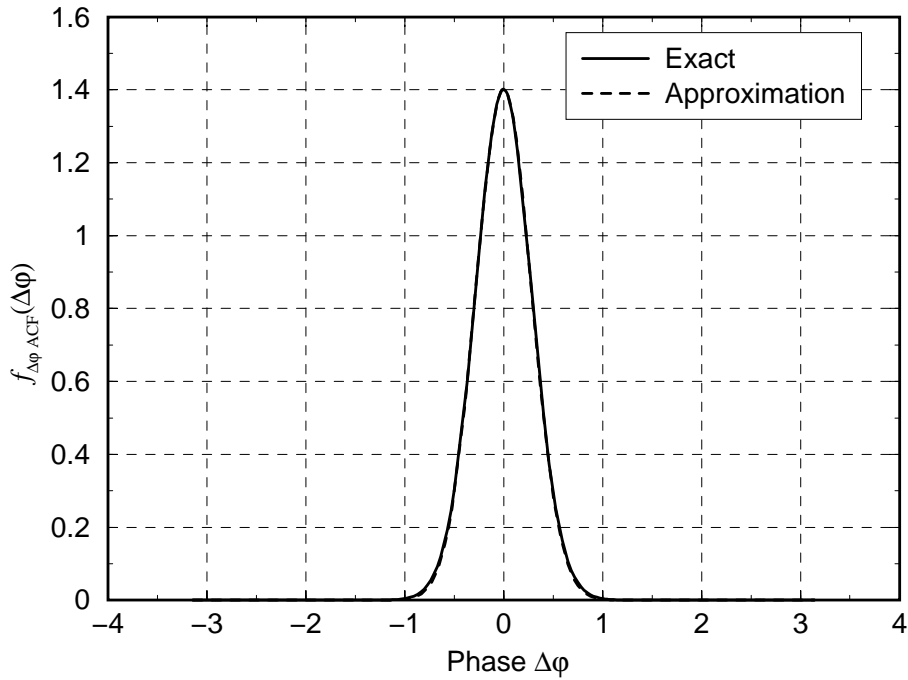


Figure 4.13: Probability density function  $f_{\Delta\varphi_{ACF}}(\Delta\varphi)$  for  $\gamma_c = 11$  dB

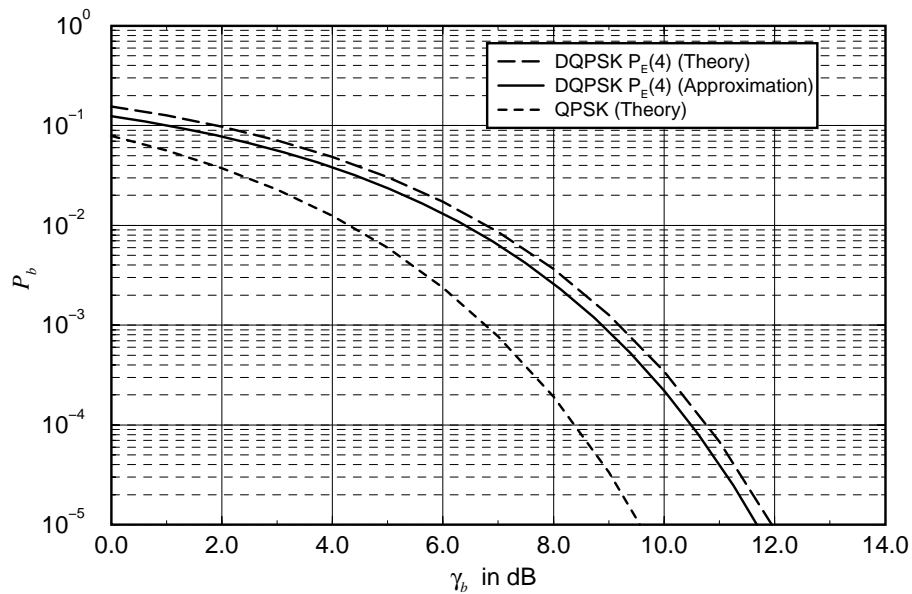


Figure 4.14: Exact and approximated results for DQPSK BER

The exact representation and the closed form log-likelihood ratio using the approximation (4.56) are shown in Fig. 4.16.

First, a look is taken at the differential phase  $\Delta\varphi_{(I)}$  of one possible differentially demodulated symbol  $\hat{D}_{(I)}$  in Fig. 4.15. A second symbol  $\hat{D}_{(II)}$  is shown as well. If now the two log-likelihoods for the phases of these symbols are compared, it can be seen that the likelihood of a correct decision is larger for (II) than for (I). If it is assumed that (I) would be the result of the direct path differential demodulation and if it is possible to find a detour path with a criteria that

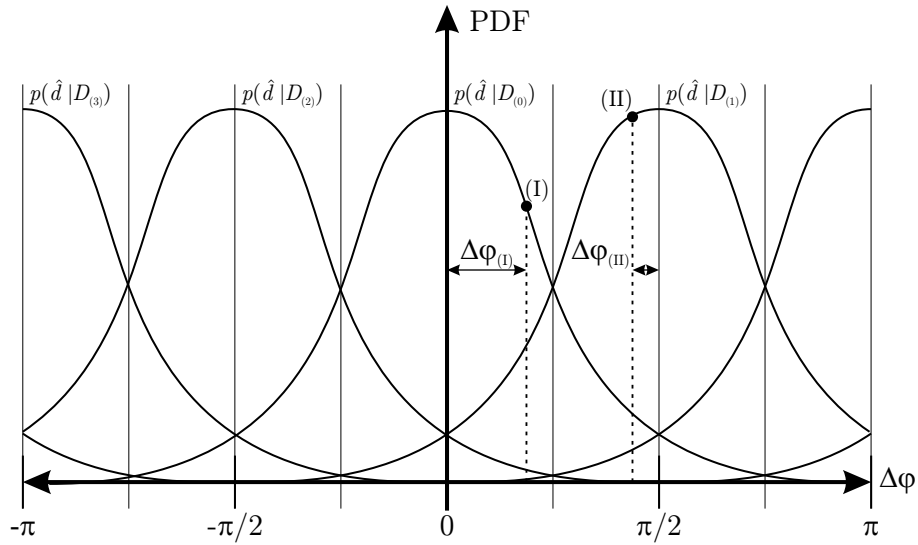


Figure 4.15: Conditional PDFs for DQPSK reception

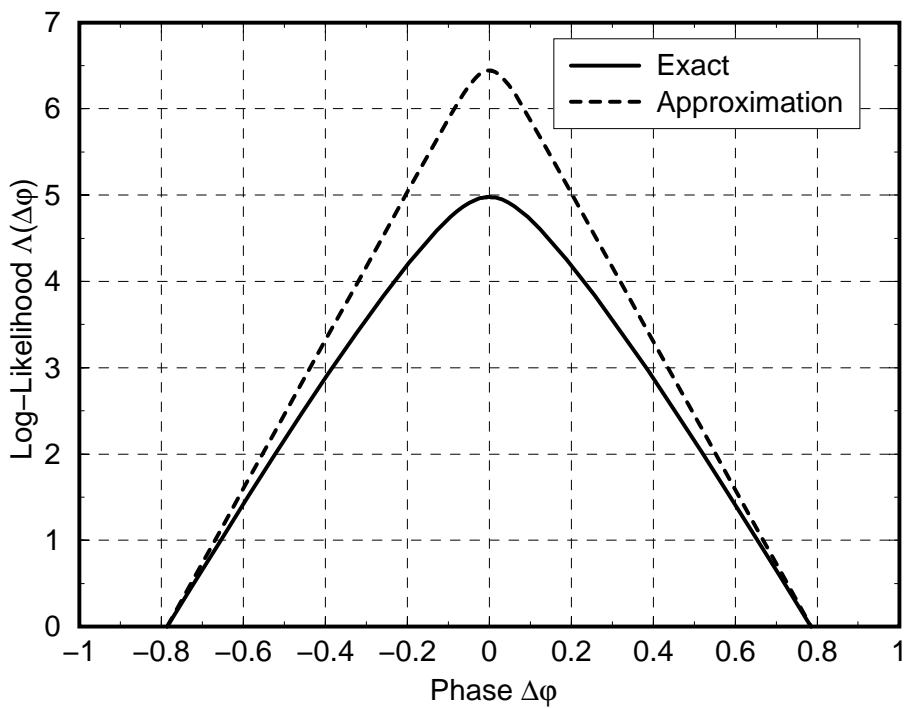


Figure 4.16: Log-likelihood ratio  $\Lambda(\Delta\varphi)$  for  $\gamma_c = 11$  dB

matches the requisite and delivers a possible solution (II), one can assume that the probability of making a wrong decision can be decreased and thus the bit error rate will decrease as well. This attempt is made in the following section.

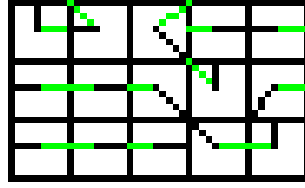


Figure 4.17: Detail of an OFDM-frame with marked neighbours that show the smallest differential phase error

#### 4.4.4 Minimum Phase Error Criteria

The phase error  $\varphi_{error_{a,b}}$  of the intermediate steps is used as a decision variable for the criteria of the presumed optimum path. First of all, the absolute value of the phase error  $\varphi_{error_{A,B}}$  for the direct path is calculated. This value is used as the reference value. All possible paths up to the chosen maximum iteration depth  $\mathcal{N}$  that lead to the destination symbol  $B$  are investigated. For each intermediate step of the current alternative path under investigation, the phase error  $\varphi_{error_{a,b}}$  is determined. If the absolute value of one of these phase errors is larger than the reference value, this alternative path is rejected. If on the other hand all individual absolute phase errors in the alternative path are smaller than the reference value, the maximum absolute value of the phase errors in this alternative path becomes the new reference value and this path becomes the new optimum path.

For an easier explanation of the algorithm, Fig. 4.17 shows a detail of an OFDM-frame. The frequency axis is the horizontal direction and the time axis is the vertical direction. Lines within one symbol point into the direction of the two neighbours with the smallest phase errors ( $1^{st}$ :black,  $2^{nd}$ :grey) with respect to the closest source symbol for differential demodulation. The channel that is used for this example transmission is Rician. Horizontal lines through several symbols indicate a high correlation of the fading in frequency direction during the transmission of the corresponding OFDM symbol. Vertical lines through several symbols indicate that the phase offset on the corresponding subcarrier has not changed very much throughout these symbols.

First, a look at the symbol in the right bottom corner is taken. The black line to the symbol above indicates that the best neighbour is the desired reference symbol for the DQPSK demodulation, so that it is likely that the differential demodulation can be performed in the common way.

Now the symbol in the center of the bottom line of Fig. 4.17 is investigated. Here the second best neighbour is to the left and the best neighbour is to the right of this symbol. This means that a decision in one of these directions is less likely to be wrong than making a decision to the top. If now the path to the right hand side is followed, it can be seen that again the best neighbour is the symbol to the top left corner. This symbol on the other hand is the needed reference symbol for the regular differential demodulation path. The resulting detour path therefore can be written as *right-topleft*. This detour path is only one and not necessarily the

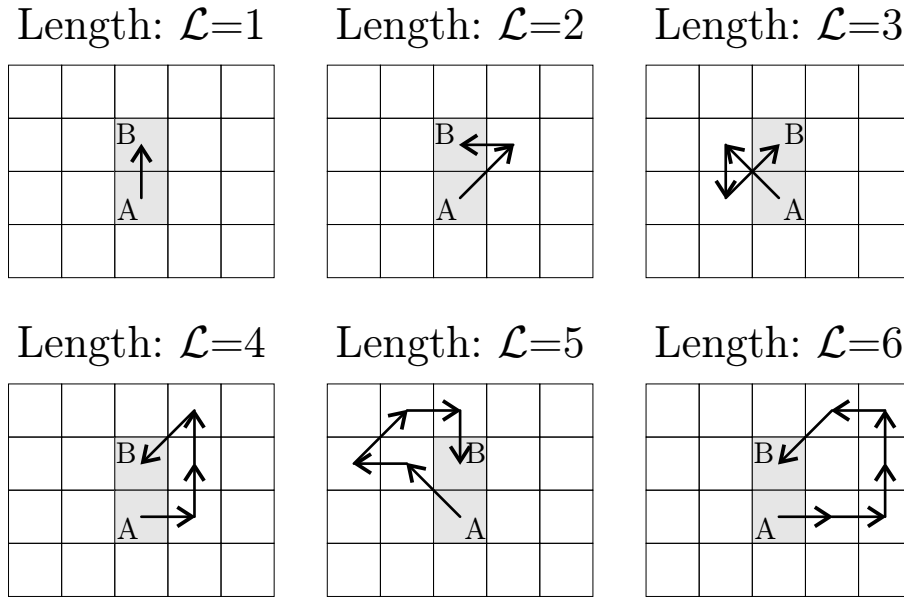


Figure 4.18: Examples of brute force method detour paths

best of all possible detour paths of a maximum depth  $\mathcal{N}$ .

#### 4.4.5 Path Evaluation

Theoretically, the amount of possible paths that can be evaluated is only limited by the frame size. Due to the fact that for each step differential demodulation can be performed for all eight neighbours, the complexity increases exponentially with  $8^{\mathcal{N}}$ . Measures have to be taken to reduce the amount of investigated paths to reasonable ones.

##### 4.4.5.1 Brute Force Method

The Brute Force Method (BFM) examines all possible paths up to the maximum pre-defined iteration path depth  $\mathcal{N}$ . Doing so, all impossible paths, i.e. paths that use a symbol of the frame that already has been used in this path before, are excluded from the search algorithm. A variety of possible paths is shown in Fig. 4.18. The complexity of this evaluation still increases exponentially with  $\mathcal{N}$ . Since all paths of length  $1 \leq \mathcal{L} \leq \mathcal{N}$  are investigated, the original one-dimensional direct path with iteration length  $\mathcal{L} = 1$  is included as well. Therefore, the result for iteration depth  $\mathcal{N} = 1$  is the common one-dimensional differential demodulation.

##### 4.4.5.2 Stream Method

In order to reduce the exponentially increasing complexity of the brute force path evaluation, it is desirable to reduce the amount of investigated paths to the most likely ones. Doing so, the investigated lengths of the most likely paths can be increased. One way to achieve this is to

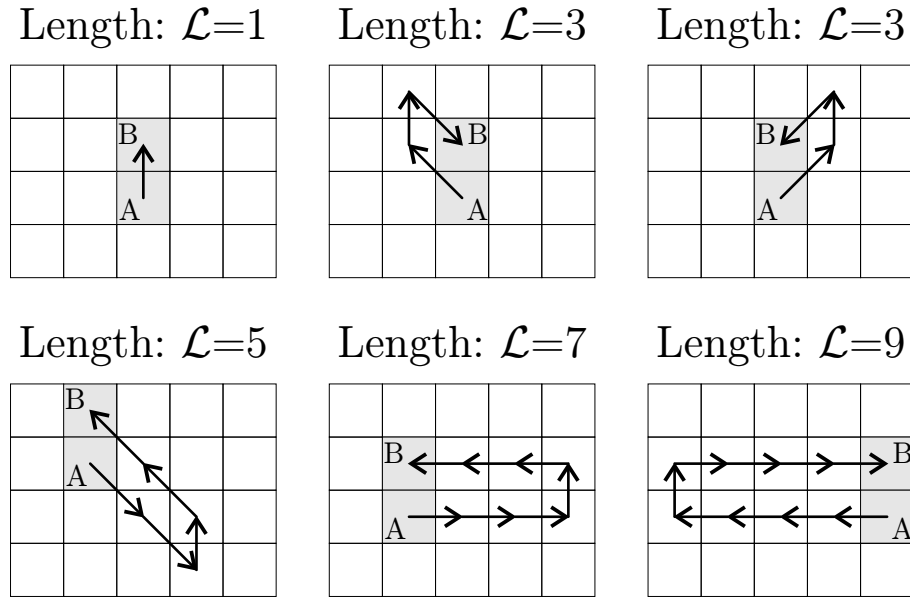


Figure 4.19: Examples of stream method detour paths

follow the streams within an OFDM frame. If a look is taken at the four received symbols in the bottom left corner of Fig. 4.17, one can observe that differential demodulation in direction of frequency seems to have the smallest phase errors. This preferred direction indicates the heading of the stream and is a result of frequency and/or time correlation due to fading. Following this heading is not sufficient; it is also necessary at some point to close the detour path by connecting two elements of parallel streams. There exist six simple solutions for the headings of a stream, two horizontal ones and four diagonal ones. Possible solutions for such detour paths are shown in Fig. 4.19. The original one-dimensional direct path is calculated as a reference first before the alternative paths are evaluated.

Performance results for the 2D-DD algorithm compared to conventional one-dimensional DPSK demodulation are given in Section 5.3.

## 4.5 Synchronization

Synchronization is a crucial task in digital communications systems. According to [Sti71], a communications system can be classified as *synchronous* if the existence of the time and frequency reference is a necessary condition for its satisfactory operation. For OFDM systems it can be distinguished between three synchronization issues:

- *OFDM-frame synchronization, i.e. OFDM-symbol synchronization*
- *Carrier frequency synchronization*
- *Sampling rate synchronization*

OFDM-based communications systems are highly sensitive to synchronization mismatches. The effects of such mismatches on the interference-to-signal power ratio are presented first, followed by measures that are taken by different algorithms to achieve and retain a synchronous state.

### 4.5.1 Frame/Symbol Timing Synchronization

The first step that needs to be achieved is correct frame timing synchronization. It is necessary to determine the start of an OFDM-frame to be able to remove the guard interval from each OFDM-symbol and thus isolate the consecutive OFDM-symbols from each other. The continuous I/Q-samples stream from the A/D-converter is therefore monitored until the start of a new OFDM-frame has been detected. If the detected start lies within the part of the guard interval that is currently not affected by the time diversity of the channel, ISI can be avoided. Possible linearly increasing phase shifts of the subcarriers due to a remaining time offset can either be removed by channel estimation or differential demodulation of the frequency domain representation of the OFDM-symbols.

Performance results for frame timing synchronization mismatch are given in Section 5.2.3 for coherent modulation and in Section 5.3.4 for differential coherent modulation.

### 4.5.2 Carrier Frequency Synchronization

The second important step for OFDM synchronization is to determine and correct the carrier frequency offset  $\Delta f_c$ . The carrier frequency offset is the result of Intermediate Frequency (IF) and/or Radio Frequency (RF) oscillator offsets between the transmitter and the receiver or possible Doppler shifts on the channel. It needs to be corrected since otherwise the orthogonality between the subcarriers is destroyed. As shown in Section 3.2.3, the si-function of a particular subcarrier is zero at the positions of the other subcarriers, thus avoiding ICI. Due to a possible carrier frequency offset  $\Delta f_c$ , the subcarriers are shifted and no longer sampled at the peak of their si( $x$ )-function, resulting in a lower subcarrier power  $P_{subcarrier}$  and additional ICI noise power  $P_{ICI}$  from neighbouring subcarriers. The corresponding intersubcarrier-interference-power-to-subcarrier-power ratios  $P_{ICI}/P_{subcarrier}$  for different carrier frequency offsets proportional to the subcarrier spacing  $\Delta f_c/F_s$  are shown in Fig. 4.20 for  $N_c = 128$  subcarriers.

Performance results with carrier frequency offset are given in Section 5.2.4 for coherent modulation and in Section 5.3.5 for differential coherent modulation.

### 4.5.3 Sampling Rate Synchronization

The third synchronization issue consists of correcting the receiver to transmitter sampling rate offset

$$\Delta f_{clk} = F_{sample_{Rx}} - F_{sample_{Tx}}, \quad (4.59)$$

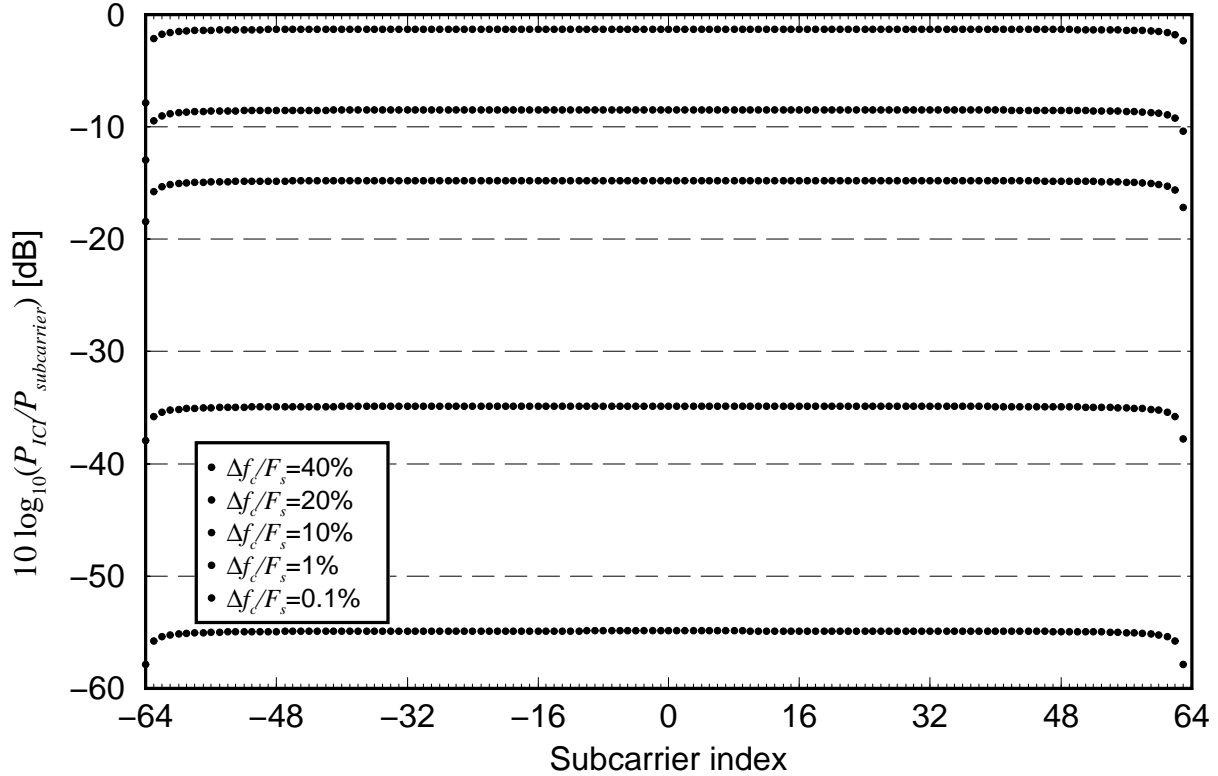


Figure 4.20: Intersubcarrier-interference-power-to-subcarrier-power ratios  $P_{ICI}/P_{subcarrier}$  for different carrier frequency offsets  $\Delta f_c$  with  $N_c = 128$  subcarriers

where  $F_{sample_{Rx}}$  is the receiver sampling clock rate and  $F_{sample_{Tx}}$  is the transmitter sampling clock rate. Non-zero  $\Delta f_{clk}$  have two effects on the received signal. First, there is a subcarrier-dependent increasing ICI noise power  $P_{ICI}$  for increasing subcarrier-index  $l$ . This results from the fact that the subcarrier spacing  $F_s$  depends on the sampling rate. The corresponding  $P_{ICI}/P_{subcarrier}$  ratios for different sampling rate offsets proportional to the transmitter sampling rate  $\Delta f_{clk}/F_{sample_{Tx}}$  are shown in Fig. 4.21 for  $N_c = 128$  subcarriers. Even inexpensive sampling circuits achieve maximum offsets below  $|\Delta f_{clk}/F_{sample_{Tx}}| = 10^{-5}$ .

The second effect results from the accumulative shift

$$\Delta t = T'_s \cdot \frac{\Delta f_{clk}}{F_{sample_{Tx}}} \quad (4.60)$$

in the sampling instant from one OFDM-symbol to the next OFDM-symbol. This results in a phase rotation

$$\Delta \varphi_l = 2\pi \cdot l \cdot \frac{\Delta t}{T_s} = 2\pi \cdot l \cdot \frac{\Delta f_{clk}}{F_{sample_{Tx}}} \cdot \frac{T'_s}{T_s} \quad (4.61)$$

of the subcarrier with index  $l$  from one OFDM-symbol to the next OFDM-symbol with the constellation points at higher subcarrier frequencies rotating faster. Both effects assume that sampling on the receiver side still takes place within the valid guard interval. From Fig. 4.21 and (4.61) it can be derived that sampling rate offsets up to  $10^{-5}$  have a minor effect on the received signal and can in most cases be neglected.

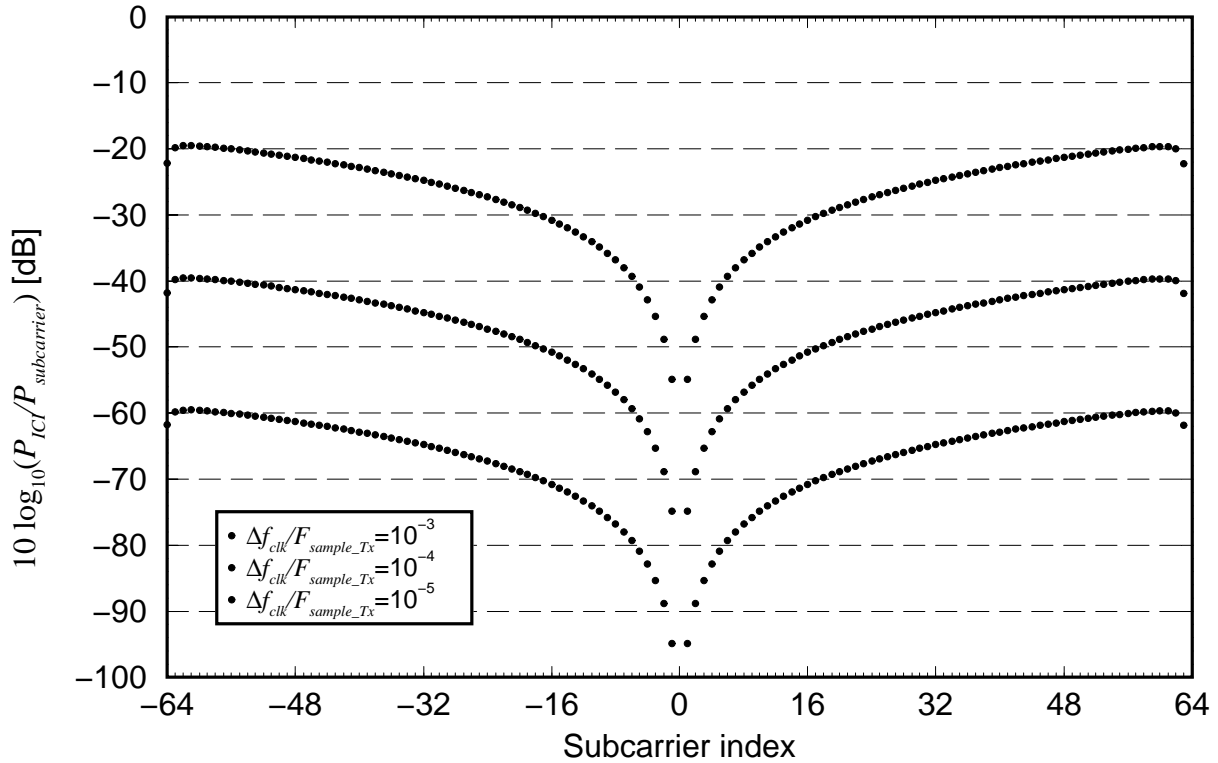


Figure 4.21: Intersubcarrier-interference-power-to-subcarrier-power ratios  $P_{ICI}/P_{subcarrier}$  for different sampling rate offsets  $\Delta f_{clk}$  with  $N_c = 128$  subcarriers

#### 4.5.4 Synchronization Algorithms

Many algorithms have been proposed in literature to handle one or several of the above mentioned synchronization issues for OFDM. Especially the ones discussed in patents often focus on the existing DAB standard to achieve frame [NoS99][LaW98], carrier frequency [TsS99] or sampling rate synchronization [BeB98]. A more general view is taken in [WaL93][WaL95] for frame timing synchronization, in [Moo94][TLZ00][SYP00][Rob97][CIM94] for carrier frequency synchronization, in [ScC97][SBB95][HuM99][PoM95][WeS95] for combined frame timing and carrier frequency synchronization and finally in [ScC98][GAA94] for combined frame timing, carrier frequency and sampling rate synchronization. There exists a variety of other sources for OFDM synchronization or digital receiver synchronization techniques in general [MeD97]. To reduce the number of possible OFDM synchronization techniques to the most reasonable ones, a closer look is taken in the following at the algorithms which are most commonly referred to.

##### 4.5.4.1 Schmidl and Cox Algorithm

This algorithm covers the search for the frame start and carrier frequency offset correction [ScC97] and can be extended for sampling rate adjustment [ScC98].

The algorithm needs up to two OFDM training symbols to achieve full synchronization. The

first OFDM training symbol consists of only even-numbered subcarriers applying a PN sequence. The result are two consecutive identical half-symbols in the time domain, consisting of  $N_c/2$  samples each. The second OFDM training symbol consists of even-numbered subcarriers that are differentially modulated to the even-numbered subcarriers of the first OFDM training symbol. The differential modulation is done with a PN sequence. The odd-numbered subcarriers of the second training symbol can be individually used for data, pilot or reference symbols.

Synchronization is achieved in several steps by computing metrics that utilize the unique properties of the two OFDM training symbols.

**Step 1:** Since the time domain representation of the first OFDM synchronization training symbol is identical for the first and the second half-symbol, complex-valued samples  $y_k$  and  $y_{k+N_c/2}$  of the I/Q-samples stream from the A/D-converter are ideally the same in that part and facilitate the set up of the vector sum

$$\mathcal{P}(d) = \sum_{k=0}^{N_c/2-1} y_{d+k}^* \cdot y_{d+k+N_c/2} = \mathcal{P}(d-1) + (y_{d+N_c/2-1}^* \cdot y_{d+N_c-1}) - (y_{d-1}^* \cdot y_{d-1+N_c/2}), \quad (4.62)$$

where  $d$  is the timing point index. This sum will be maximized for  $d = d_{opt}$  corresponding to the first sample of the first OFDM training symbol since all elements will line up in-phase. If there exists a guard interval, it will also be maximized for all positions within the guard interval that are not affected by the time diversity of the channel. The received energy  $\mathcal{R}(d)$  for the second half-symbol is also calculated

$$\mathcal{R}(d) = \sum_{k=0}^{N_c/2-1} |y_{d+k+N_c/2}|^2 = \mathcal{R}(d-1) + |y_{d+N_c-1}|^2 - |y_{d-1+N_c/2}|^2. \quad (4.63)$$

By maximizing the frame timing metric

$$\mathcal{M}(d) = \frac{|\mathcal{P}(d)|^2}{(\mathcal{R}(d))^2}, \quad (4.64)$$

the optimum estimate for frame and symbol timing  $d_{opt}$  can be found. If the received power can assumed to be almost constant, the  $\mathcal{R}(d)$  term can be neglected.

**Step 2:** At the optimal timing point  $d_{opt}$ , the vector sum  $\mathcal{P}(d_{opt})$  may have a phase shift

$$\phi = \angle(\mathcal{P}(d_{opt})) = \pi \cdot T_s \cdot \Delta f_c \quad (4.65)$$

due to a possible carrier frequency offset  $\Delta f_c$ , from which due to the limited range  $-\pi < \phi \leq \pi$  only the fractional part of the carrier frequency offset

$$(\widehat{\Delta f_c})_{frac} = \frac{\hat{\phi}}{\pi \cdot T_s}, \quad (4.66)$$

can be estimated in the range  $-F_s < (\Delta f_c)_{frac} < F_s$ .

**Step 3:** To be able to also calculate a possible integer part

$$(\Delta f_c)_{int} = \frac{2g}{T_s} \quad (4.67)$$

of the frequency offset, where  $g \in \mathcal{G} = \{-W, -W + 1, \dots, -1, 0, 1, \dots, W - 2, W - 1\}$  with  $W_{max} = N_c/4$ , both OFDM training symbols first need to be corrected with the fractional part before calculating the FFT of both symbols resulting in the frequency domain representations  $\vec{Y}_1$  and  $\vec{Y}_2$ . The even subcarriers of the OFDM symbols  $\vec{Y}_1$  and  $\vec{Y}_2$  are then element-wise differentially demodulated. The result is compared to the pre-calculated PN sequence

$$V_l = \sqrt{2} \cdot \frac{X_{2,l}}{X_{1,l}}, \quad \forall l \in \{-N_c/2, -N_c/2 + 2, \dots, -2, 2, \dots, N_c/2 - 4, N_c/2 - 2\}, \quad (4.68)$$

resulting from the corresponding transmitted symbols  $\vec{X}_1$  and  $\vec{X}_2$ . From these values a new correlation metric

$$\mathcal{B}(g) = \frac{\left| \sum_l Y_{1,l+2g}^* \cdot V_l^* \cdot Y_{2,l+2g} \right|^2}{2 \left( \sum_l |Y_{2,l}|^2 \right)^2}, \quad (4.69)$$

that also partially eliminates possible influences from the transmission channel, is calculated. The  $\hat{g}$  that maximizes  $\mathcal{B}(g)$  delivers the integer frequency offset, so that the total estimated frequency offset is

$$\widehat{\Delta f_c} = (\widehat{\Delta f_c})_{frac} + (\widehat{\Delta f_c})_{int} = \frac{\hat{\phi}}{\pi \cdot T_s} + \frac{2\hat{g}}{T_s}. \quad (4.70)$$

**Step 4:** With (4.61) the sampling rate offset  $\Delta f_{clk}$  can be calculated by

$$\Delta f_{clk} = \frac{\Phi}{2\pi} \cdot F_{sampleTx} \cdot \frac{T_s}{T_s'}, \quad (4.71)$$

where  $\Phi$  is estimated through

$$\Phi = \frac{\sum_l \angle(Y_{1,l}^* \cdot Y_{2,l} \cdot V_l^*) \cdot |Y_{1,l}^* \cdot Y_{2,l} \cdot V_l^*|^2 \cdot l}{\sum_l |Y_{1,l}^* \cdot Y_{2,l} \cdot V_l^*|^2 \cdot l^2}. \quad (4.72)$$

This equation performs linear MMSE estimation if the expected values of both the OFDM frequency domain sub-symbols indices and the phase differences are zero when weighted by the squares of the magnitudes of the sub-channels [ScC98].

Performance results for the algorithm are given in Section 6.2.5.2.

#### 4.5.4.2 Sandell, Beek and Börjessen Algorithm

The algorithm covers the search for the frame start and carrier frequency offset correction [SBB95].

It uses the difference of time domain samples  $y_k$  and  $y_{(k+N_c)}$  that are spaced  $N_c$  samples apart. If the received sample  $y_k$  belongs to the guard interval and  $y_{(k+N_c)}$  belongs to the OFDM symbol from which it was copied, the difference should be small. Otherwise the two samples can be regarded as uncorrelated random variables and the power of the difference will on average be twice their power, i.e. larger. By windowing several differences with the same length as the guard interval, the output of this function will have a minimum at the start  $\theta$  of the guard interval.

The start of the guard interval is estimated by

$$\hat{\theta} = \arg \max_{\theta} (|\gamma(\theta)| - \rho \cdot \mathcal{S}(\theta)), \quad (4.73)$$

where

$$\gamma(\theta) = \sum_{k=\theta}^{\theta+N_g-1} y_k \cdot y_{(k+N_c)}^*, \quad (4.74)$$

is the weighted magnitude of the sum of the correlation between  $N_g$  consecutive pairs of samples,

$$\mathcal{S}(\theta) = \frac{1}{2} \sum_{k=\theta}^{\theta+N_g-1} |y_k|^2 + |y_{(k+N_c)}|^2, \quad (4.75)$$

is the energy term and

$$\rho = \frac{\gamma_c}{\gamma_c + 1}, \quad (4.76)$$

is the magnitude of the correlation coefficient between  $y_k$  and  $y_{(k+N_c)}$  and can be calculated with the knowledge of the SNR  $\gamma_c$ . With  $\hat{\theta}$ , the estimate for the carrier frequency offset

$$\widehat{\Delta f_c} = -\frac{F_s}{2\pi} \cdot \angle (\gamma(\hat{\theta})) \quad (4.77)$$

can be calculated in the range  $-F_s/2 < \Delta f_c < F_s/2$ .

The main advantage of this algorithm is that it needs no additional OFDM training symbols. On the other hand it is sensitive to the time dispersive channel that generates correlations outside the guard interval and the algorithm requires a guard interval that is in the best case not influenced by the channel at all. Due to the limited size of the guard interval, averaging over several estimates is considerably increasing the performance.

#### 4.5.4.3 Moose Algorithm

The algorithm covers only the carrier frequency offset correction [Moo94].

A Maximum Likelihood Estimation (MLE) algorithm is derived that calculates the carrier frequency offset in the frequency domain after the FFT from demodulated data signals. The algorithm proposes to send two identical symbols. It is based on the fact that corresponding samples from the two symbols at the different times differ only by a rotated phase due to

the frequency offset and the influence of additional noise. The MLE function averages the differences over all subcarriers to calculate the carrier frequency offset.

It is necessary to repeat at least one symbol within the OFDM frame and the acquisition range of the carrier frequency offset is limited to  $-F_s/2 < \Delta f_c < F_s/2$ . Furthermore, the algorithm requires the prior knowledge of the frame/symbol timing.

#### 4.5.4.4 Warner and Leung Algorithm

The algorithm covers only the search for the frame start [WaL93][WaL95].

The synchronization information is represented by tones, centered in certain reserved subcarriers of the OFDM signal. The receiver uses a correlation detector, implemented in the frequency domain, to acquire synchronization. Synchronization takes place in three steps.

**Step 1:** The presence or the absence of the OFDM signal is detected by monitoring the received power and comparing it to a threshold. If the OFDM signal is present, the power increases.

**Step 2:** Coarse timing estimation within  $\pm T_{sample}/2$  is achieved with the correlation detector that only requires the spectral information of the synchronization tones. The phases from the synchronization tones are correlated with the known reference signal to obtain the timing estimate. The algorithm makes use of the fact that the information for the synchronization tones will be the same in the time domain for adjacent OFDM-symbols spaced  $(N_c + N_g)$  samples apart. The peak of the correlation is located by using an interpolation filter at four times the original data rate.

**Step 3:** Fine tuning is performed by equalizing phase and magnitude distortions due to the transmission channel. The channel estimation is done by using an update of the DFT/FFT.

#### 4.5.5 Improvements for Schmidl and Cox Algorithm

In the following, the use of the Schmidl and Cox algorithm is assumed and some improvements are proposed. They consider decreasing the receiver-side noise introduced by a non-ideal sampling instant and the correct detection and removal of the guard interval.

##### 4.5.5.1 Receiver-Side Oversampling

From the theory, a single time-continuous OFDM-symbol generated from  $N_c$  samples can be sampled and A/D-converted on the receiver side anywhere within the valid guard interval that is not affected by the time diversity of the channel. The theory assumes in that case, that the D/A-converter on the transmitter side generates ideal Dirac pulses spaced  $T_{sample}$  apart that are afterwards sent through an ideal low-pass filter with cut-off frequency  $F_{sample}/2$ .

In practical implementations, the low-pass filtering process is non-ideal. This results in remaining high-frequency noise terms especially on the edges of the non-ideal rectangular D/A sampling pulse shape. As long as the A/D-converter of the receiver takes its samples from the center of a previously rectangular pulse, the effects are relatively small and can be neglected. But since sampling rate offsets up to  $\Delta f_{clk}/F_{sampleT_x} = 10^{-5}$  may occur as shown in Section 4.5.3, it happens that the samples on the receiver side drift into the noisy area between two transmitter side samples, i.e. the sampling time offset is  $\pm T_{sample}/2$ .

To avoid this, two-times oversampling can be used on the receiver side, resulting in two groups of samples, where the first pair of I/Q-samples is put into the first group and the second pair of I/Q-samples is put into the second group and so on. These groups are processed independently from each other with the algorithm to determine the frame start. If now one group consists of the above mentioned noisy samples, the peak of the frame timing metric will be less dominant than the peak from the other group. Hereby, the best of the two groups can be selected for the OFDM-frame that is currently processed. Since the sampling rate offset is small, it can be assumed that the selected group is valid for the processing of the whole frame. With this method it is possible to reduce the sampling time offset to the range  $\pm T_{sample}/4$ . By further processing the difference of the two peaks, it is possible to adjust the sampling time even more exactly, since the two peaks can be regarded as early and late estimates of the ideal sampling time.

Performance results for this improved solution are given in Section 6.2.5.2.

#### 4.5.5.2 Guard Interval Detection

The algorithm from Section 4.5.4.2 makes use of the guard interval for frame start estimation by using the cyclic repeated part (cyclic prefix) of the OFDM symbol. As already mentioned in Section 4.5.4.1, the Schmidl and Cox algorithm has problems in detecting the exact frame start position since the timing metric produces in the noise-free case a plateau of  $(N_g + 1)$  almost equal-valued peaks. This has been already observed by Schmidl and Cox themselves. There exist different methods that can circumvent this inexact frame start estimation.

**Schmidl and Cox 90% method:** In [ScC97] it is proposed to first detect the peak of the timing metric  $\mathcal{M}(d)$  and then find the points to the left and to the right that only have 90% of the amplitude of this maximum peak. By averaging the two obtained positions it is possible to locate the center of the plateau. Adding an offset, of normally  $N_g/2$ , to the center position delivers the start of the frame.

The problem that occurs now in time-dispersive channels is that the plateau consists of less than  $(N_g + 1)$  samples, so that adding an offset to the obtained center position is critical. It may lead to a wrong estimated start of the frame resulting in ISI.

**Averaging method:** A different method of estimating the frame start is proposed in [MZB00]. The timing metric is changed to

$$\mathcal{M}_1(d) = \frac{1}{N_g + 1} \sum_{k=-N_g}^0 \mathcal{M}_f(d + k) , \quad (4.78)$$

averaging over  $(N_g + 1)$  metrics  $\mathcal{M}_f(d)$  that can be calculated by

$$\mathcal{M}_f(d) = \frac{|\mathcal{P}(d)|^2}{(\mathcal{R}_f(d))^2} , \quad (4.79)$$

where

$$\mathcal{R}_f(d) = \frac{1}{2} \sum_{k=0}^{N_c-1} |y_{d+k}|^2 \quad (4.80)$$

uses all samples over one symbol period to calculate the half-symbol energy.

Again the problem that occurs in time-dispersive channels is that there might be a misestimation of the frame start that results in ISI, due to the assumption of a plateau with  $(N_g + 1)$  values.

**Timing metric training symbol re-design:** There is also a second more promising method given in [MZB00]. It avoids the plateau completely by changing the time-domain representation of the first OFDM training symbol without guard interval to

$$\vec{\mathbf{x}}_1^T = [ +A \quad +A \quad -A \quad -A ] , \quad (4.81)$$

where  $A$  represents a sequence of length  $N_c/4$ . This requires the new timing metric

$$\mathcal{M}_2(d) = \frac{|\mathcal{P}_2(d)|^2}{(\mathcal{R}_2(d))^2} , \quad (4.82)$$

where

$$\mathcal{P}_2(d) = \sum_{i=0}^1 \sum_{k=0}^{N_c/4-1} y_{d+iN_c/2+k}^* \cdot y_{d+iN_c/2+k+N_c/4} , \quad (4.83)$$

and

$$\mathcal{R}_2(d) = \sum_{i=0}^1 \sum_{k=0}^{N_c/4-1} |y_{d+iN_c/2+k+N_c/4}|^2 . \quad (4.84)$$

Due the structure of the training symbol there will be only one prominent peak even with a guard interval. Additionally, instead of  $\mathcal{R}_2(d)$ ,  $\mathcal{R}_f(d)$  can be used resulting in a slight performance improvement.

The open question that remains is how to generate a training symbol with such a special structure. The sequence  $[ +A ]$  can be generated by a  $N_c/4$  IFFT with arbitrary subcarriers. This is proposed in [MZB00]. Here, the new proposal is to generate the sequence  $[ +A \quad +A ]$  by a  $N_c/2$  IFFT, where again only the even-numbered subcarriers are used. Both require a smaller IFFT/FFT than the normal one with  $N_c$  subcarriers/samples. This can cause some implementation problems especially in practical hardware realizations. A direct generation of

[ +A +A -A -A ] with a special subcarrier structure is unknown. The fractional carrier frequency offset that can be estimated from  $\mathcal{P}_2(d)$  is

$$(\widehat{\Delta f_c})_{frac2} = \frac{2 \cdot \angle(\mathcal{P}_2(d))}{\pi \cdot T_s}, \quad (4.85)$$

within the range  $-2F_s < (\Delta f_c)_{frac2} < 2F_s$ .

The [ +A +A ]  $N_c/2$  sequence with only even subcarriers and the respective [ -A -A ] sequence that generate (4.81) seem to be most promising since they enable using the frequency domain PN correlation from Schmidl and Cox to estimate a possible integer carrier frequency offset.

# Chapter 5

## System Design and Evaluation

The previous sections have shown that many details have to be considered for the design of a mobile communications system. They result from the influences of the physical transmission channel as well as user and throughput requirements. This knowledge is used in the following to determine parameters for the ground-air and air-ground link of an aeronautical demonstrator transmission system that is to be partially implemented in Digital Signal Processing (DSP) hardware for testing, optimization and evaluation purposes.

### 5.1 General Considerations

The carrier frequency of the aeronautical MC demonstrator system is in the 5 GHz band at

$$f_c = 5.1465 \text{ GHz.} \quad (5.1)$$

Using 5.0 GHz as the reference carrier frequency, the maximum Doppler frequencies for the different aeronautical channel scenarios can be calculated by applying  $f_{D_{max}} = f_c \cdot v/c$  and Table 2.1.

Table 5.1: Maximum Doppler frequencies

	<b>Parking scenario</b>	<b>Taxi scenario</b>	<b>Arrival scenario</b>	<b>En-Route scenario ground-air / air-air</b>
$f_{D_{max}}$ [Hz]	91.7	250.0	2500.0	7333.3 / 10333.3

The maximum Doppler rate of an aircraft flying over a ground station in an altitude of  $h = 1000$  m and at a speed of  $v = 440$  m/s is evaluated with (2.21) to

$$f'_{D_{max}} = -3227 \frac{\text{Hz}}{\text{s}}. \quad (5.2)$$

The bandwidth of the MC signal shall, due to hardware restrictions, not exceed 500 kHz. Thus, the transmitter sampling rate applying an internal divisible 25.6 MHz clock is fixed to

$$F_{sampleTx} = \frac{25.6 \text{ MHz}}{52} = 492.308 \text{ kHz}. \quad (5.3)$$

To be able to neglect ICI due to the channel Doppler spectrum, the maximum relevant Doppler frequency has to be less than 10% of the subcarrier spacing  $F_s$ . This condition can be fulfilled for the parking and taxi scenarios with an FFT/IFFT consisting of

$$N_c = 128 \quad (5.4)$$

carriers, resulting in a subcarrier spacing of

$$F_s = \frac{F_{sampleTx}}{N_c} = 3.85 \text{ kHz}. \quad (5.5)$$

The arrival and en-route scenarios are not considered for the choice of  $F_s$  here, since due to their strong LOS path, the resulting ICI from the echoes is accounted as an additive stochastic noise. The resulting OFDM symbol duration without a guard interval is

$$T_s = \frac{1}{F_s} = 260.0 \text{ } \mu\text{s}. \quad (5.6)$$

In accordance with the maximum delays of the parking and taxi scenarios, the guard interval is chosen to be

$$T_g = 5 \cdot \frac{1}{F_{sampleTx}} = 10.2 \text{ } \mu\text{s}, \quad (5.7)$$

giving the OFDM symbol duration including the guard interval of

$$T'_s = T_s + T_g = 270.2 \text{ } \mu\text{s}. \quad (5.8)$$

This guard interval is also valid for the arrival scenario. The resulting ISI for the en-route scenario due to an insufficient length of the guard interval again is considered as an additive stochastic noise.

With (4.4) and (4.5), the maximum distances for the pilot symbols, which still guarantee proper channel estimation, in frequency and time direction can be evaluated. They are shown in Table 5.2.

Table 5.2: Maximum pilot symbol distances

Parking		Taxi		Arrival		En-route (g-a)		En-route (a-a)	
$N_f \leq$	$N_t \leq$	$N_f \leq$	$N_t \leq$	$N_f \leq$	$N_t \leq$	$N_f \leq$	$N_t \leq$	$N_f \leq$	$N_t \leq$
37	20	371	7	37	0.74	7	0.25	3	0.18
(18)	(10)	(185)	(3)	(18)	(0.37)	(3)	(0.13)	(1)	(0.09)

The numbers in the brackets assume two-times oversampling for the pilot symbols; that means that twice as many pilot symbols are used than are necessary according to the sampling theorem.

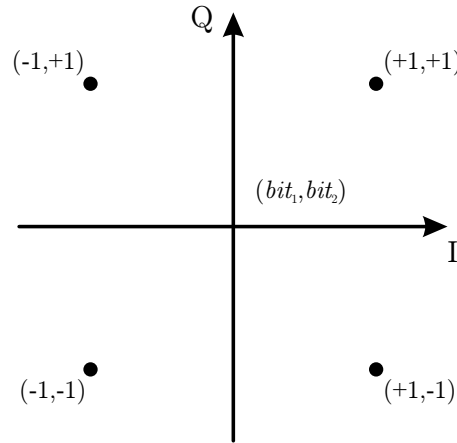


Figure 5.1: QPSK/DQPSK constellation diagram

Fractional numbers smaller than one indicate that the sampling theorem requires pilot symbol spacing that is smaller than the distance of two neighbouring subcarriers or two consecutive OFDM symbols, respectively. Since estimating the channel transfer function is only necessary at the position of data symbols and not between them, it is sufficient to set the corresponding pilot symbol distance to one in that direction. It has to be noted though that the channel changes significantly during one OFDM symbol in this case, resulting in a performance degradation due to ICI/noise.

The modulation scheme that is chosen for the coherent modulation is QPSK. For the differential coherent modulation, DQPSK in direction of time is applied. The datalink that is considered has to be very reliable and operate in all aeronautical channel conditions. High-order modulation schemes like  $M$ -PSK,  $M$ -DPSK ( $M \geq 8$ ) or 16-QAM, 64-QAM are too unreliable under these conditions since they require a very reliable channel estimation in conjunction with highly efficient channel coding that both would add additional delays in the signal processing. Since the information exchange is time-critical, such delays should be prevented.

But choosing QPSK and DQPSK brings also some other advantages. First, by choosing a Gray-encoded I/Q-constellation, the two bits included in each modulation symbol can be treated independently from each other in the receiver. Doing so, soft information for a possible channel decoder can be extracted simply by choosing  $softbit_1 = \text{Re}\{\hat{D}\}$  and  $softbit_2 = \text{Im}\{\hat{D}\}$  from a received data symbol  $\hat{D}$  that originally resulted from a transmitted data symbol  $D$  chosen from the constellation diagram shown in Fig. 5.1. Second, the similarity between these two schemes makes it simple to compare the performance of the coherent modulation to the performance of the differential coherent modulation.

The number of OFDM symbols in an OFDM frame, excluding the necessary synchronization symbols, is set to

$$N_s = 25 \tag{5.9}$$

in the simulations.

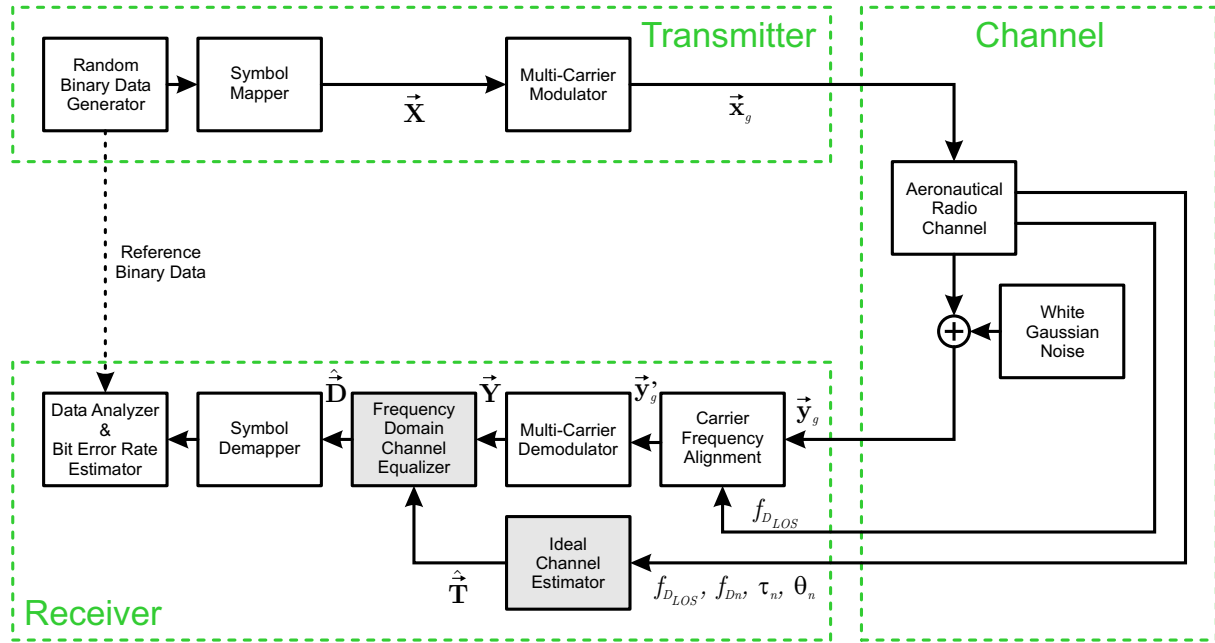


Figure 5.2: Simulator for OFDM transmission with aeronautical channel models

## 5.2 Performance Analysis for Coherent QPSK

### 5.2.1 Results with Aeronautical Channel Models

Knowing the conditions that occur on the aeronautical transmission channel, simulations can be conducted to determine the Bit Error Rate (BER) performances. For this purpose, a simulator with the implementation of the WSSUS aeronautical channel model, as shown in Fig. 5.2, is used. It consists of a random binary data generator that delivers a bitstream for the QPSK symbol mapper, where the bits are mapped according to the constellation diagram of Fig. 5.1. Additional pilot symbols with distance  $N_f$  and  $N_t$  are added for the receiver-side channel estimation, resulting in output symbol vectors  $\vec{\mathbf{X}}$  consisting of  $N_c$  carriers each. If, due to the pilot symbol spacing in the frequency domain, not all carriers can be used, the remaining subcarriers are left empty and the number of used subcarriers is reduced to  $N'_c$ . The pilot symbols increase the necessary data symbol energy, or bit energy respectively, by

$$10 \cdot \log \left( \frac{N'_c N_s}{N'_c N_s - \lceil N'_c / N_f \rceil \lceil N_s / N_t \rceil} \right) \text{ dB}, \quad (5.10)$$

assuming that the pilot symbols have the same power than the data symbols. In the worst relevant case, i.e.  $N_f = 18$ ,  $N_t = 1$ , this loss is 0.28 dB. The subsequent multi-carrier modulator, represented by an IFFT, uses two-times oversampling, i.e. twice as many subcarriers  $2 \cdot N_c$  are used and as a result  $N_c/2$  subcarriers on each side of the frequency domain representation of this new OFDM-symbol are left empty. This is done to avoid aliasing on the simulated channel. The drawback of this is that the time-domain signal vector  $\vec{\mathbf{x}}_g$  including the guard interval consists of twice as many values  $2(N_c + N_g)$  as necessary, which all have to be processed by the channel model, see Section 2.4.2.

As already mentioned in Section 2.3.3, new parameter sets have to be generated for the WSSUS channel model from time to time. This is done here for each new OFDM frame, i.e. the simulated scenario stays constant, whereas a new parameter set representing this scenario is generated. Furthermore, white Gaussian noise is added according to the chosen SNR  $\gamma_b$  per bit

$$\gamma_b = \gamma_c - 10 \cdot \log(\log_2(M)) \text{ dB}, \quad (5.11)$$

where  $M$  is the level of the  $M$ -PSK or  $M$ -DPSK modulation scheme, e.g.  $M = 4$  for QPSK and DQPSK, i.e.  $\gamma_b \approx \gamma_c - 3.0$  dB.

On the receiver side, first the carrier frequency is aligned to the Doppler shift of the LOS path by evaluating

$$y'_g(t) = y_g(t) \cdot e^{-j2\pi f_{D_{LOS}}t} \quad (5.12)$$

for all elements of the received time-domain vector  $\vec{y}_g$ . This assumes an ideal carrier frequency and carrier phase synchronization that locks on the LOS path. For the case that there is no LOS path, locking on the transmitter carrier frequency  $f_c$  is assumed, i.e.  $f_{D_{LOS}} = 0$  Hz. The resulting signal is fed through the multi-carrier demodulator, where the complete guard interval is removed and the frequency domain representation  $\vec{Y}$  of the received OFDM symbol is calculated with the FFT.

The subsequent frequency domain channel equalizer either uses ideal channel estimate vectors  $\hat{\vec{T}}$  resulting from known parameter sets of the current channel or interpolated estimates resulting from channel information obtained from the received pilot symbols, both consisting of  $N_c$  elements. For the first case, the time-variant channel transfer vector is estimated by

$$\hat{T}_{k,l} = \frac{1}{\sqrt{N}} \sum_{n=1}^N e^{j(\theta_n + 2\pi(f_{D_n} - f_{D_{LOS}})(k+0.5)T'_s - 2\pi l F_s \tau_n)}, \quad -\frac{N_c}{2} \leq l < \frac{N_c}{2}, \quad (5.13)$$

where  $k$  is the time index of the current OFDM symbol under investigation. This estimation is ideal with respect to the fact that the phases, Doppler frequencies and delays of the channel are known. It is not ideal considering the fact that the channel is assumed to be time-invariant during the transmission of one OFDM symbol, expressed by  $t = (k + 0.5)T'_s$ , and possible ICI is not taken into account for channel estimation. The final equalization is done with one of the methods described in Section 4.2.3 resulting in the estimated received symbol vector  $\hat{\vec{D}}$ . Which of the MRC, EGC, ZF or MMSE methods is used does not matter for OFDM PSK, since only the phase of the received symbol is important in this case. The symbol demapper extracts the binary information that is compared in the data analyzer to the reference binary data that originally has been transmitted. From the gathered information, the BER is calculated.

Fig. 5.3 shows performance results for the **en-route channel** (ground-air) using the simulation system with 64 bit floating point arithmetic and using the DSP system, where due to the A/D-converter an accuracy of only 16 bit integer values is available in the final implementation. The 16 bit accuracy is used for  $\vec{x}_g$  and  $\vec{y}_g$  only, whereas all other parts, also the channel, operate with 32 bit floating point arithmetic. No equalization is used for the results, i.e. the

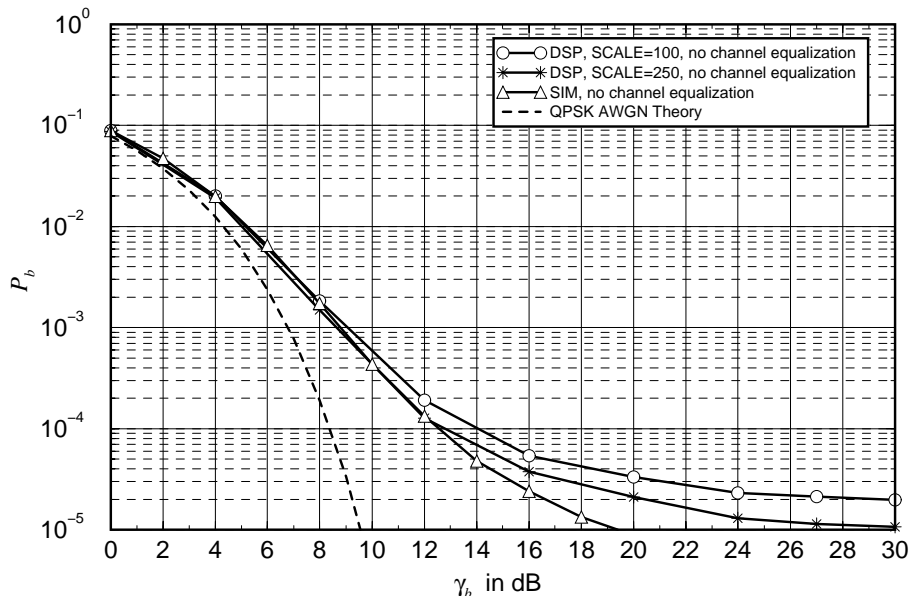


Figure 5.3: Difference of average BER for OFDM QPSK with aeronautical en-route channel using simulation system and DSP system for evaluation

receiver is assumed to be locked on the carrier frequency and carrier phase only. It shows that the DSP results have a higher error floor compared to the simulation system results and the performance gets worse with decreasing DSP scale size. The DSP scale size indicates which amplitude the QPSK symbols on each subcarrier have. A value of 250.0 approximates the theoretically highest value for 16 bit 2's complement the best, i.e.  $\pm 32767$ , since the maximum value after the IFFT is  $128 \cdot 250.0 = 32000.0$  in that case. Smaller DSP scale values show a degrading BER performance due to an increasing quantization noise. Simulation results from the DSP system using the amplitude scale 250.0 are marked with *DSP* and simulation results with the simulation system are marked with *SIM* in the following figures.

Next, the performance results for the en-route ground-air channel with the ideal channel equalization method and with estimated and interpolated channel equalization are presented, see Fig. 5.4.

The results are marked as follows: *Triangle right* for equalization without pilot-symbol oversampling (DSP), *square* for equalization with two-times pilot-symbol oversampling (DSP), *circle* for equalization with  $N_f = 7, N_t = 3$  (DSP), *triangle down* for the mentioned ideal channel equalization (SIM), *diamond* for results with aliasing due to an insufficient (too large) pilot symbol spacing (DSP), *star* without equalization on the DSP system and *triangle up* without equalization on the simulation system. *Solid line* equalization curves use linear interpolation and *dot-dashed line* equalization curves use  $\text{si}(x)$  interpolation with  $N_{\text{tap}} = 5$ .

Even though the pilot symbol spacings comply with the sampling theorem, the simulation results with equalization are worse than without equalization. This is explained by the fact that due to the high Doppler frequencies, the channel cannot be considered ICI free. Additionally, the LOS path is spaced about  $2f_{D_{\text{max}}} \approx 3.82 \cdot F_s$  apart from the echoes. This means that the

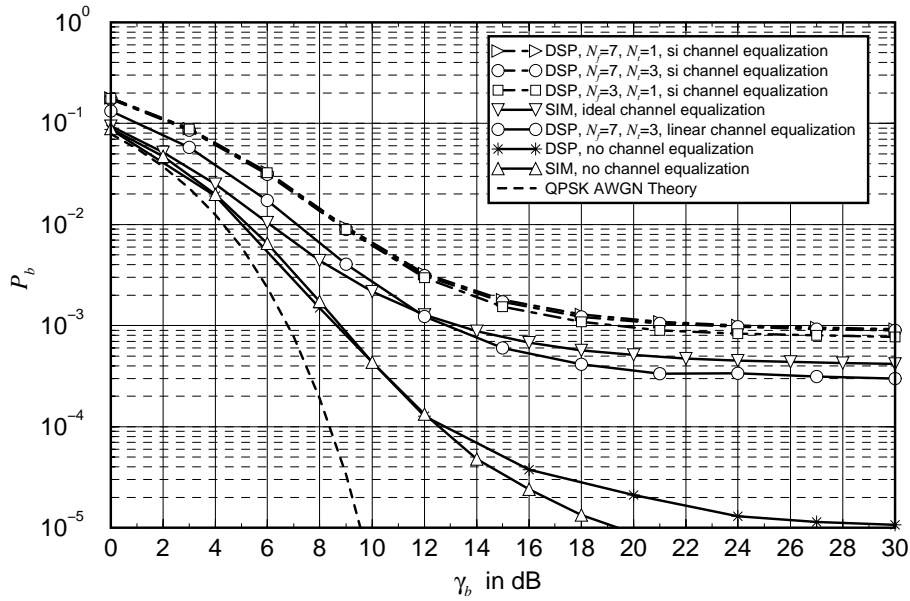


Figure 5.4: Average BER for OFDM QPSK with aeronautical en-route channel and different equalization settings

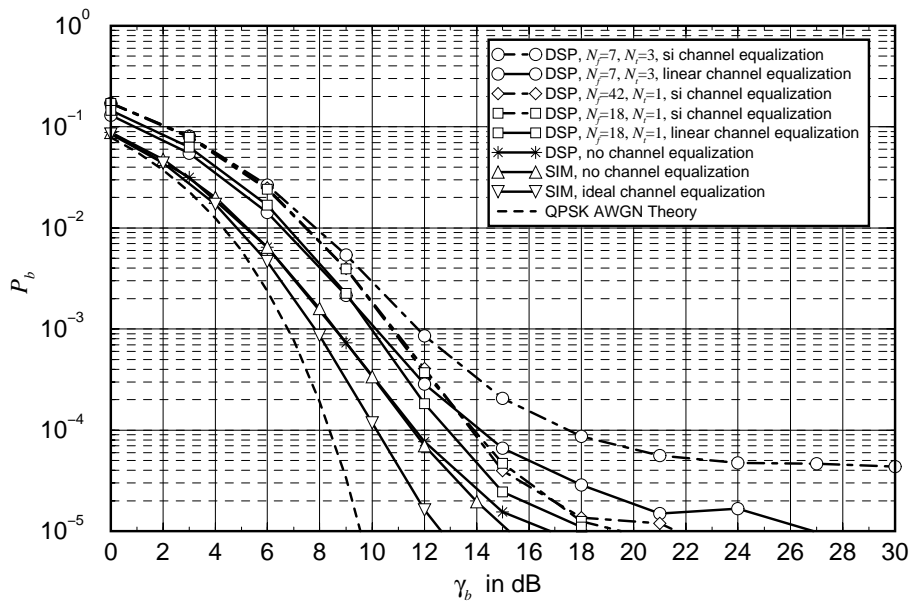


Figure 5.5: Average BER for OFDM QPSK with aeronautical arrival channel and different equalization settings

echoes influence subcarriers with distance  $\sim 4F_s$  and lead to a wrong channel estimation resulting in an increased BER floor. The equalization using linear estimation with  $N_f = 7$ ,  $N_t = 3$  has the least degradation of the investigated performances.

Considering the **arrival channel**, the BER performance improves, compare Fig. 5.5. This is the result of lower Doppler frequencies and a decreased delay spread. The high Rice factor again gives good results even without equalization. Assuming ideal knowledge about the fading characteristics of the channel and with much lower ICI, the ideal channel equalization is

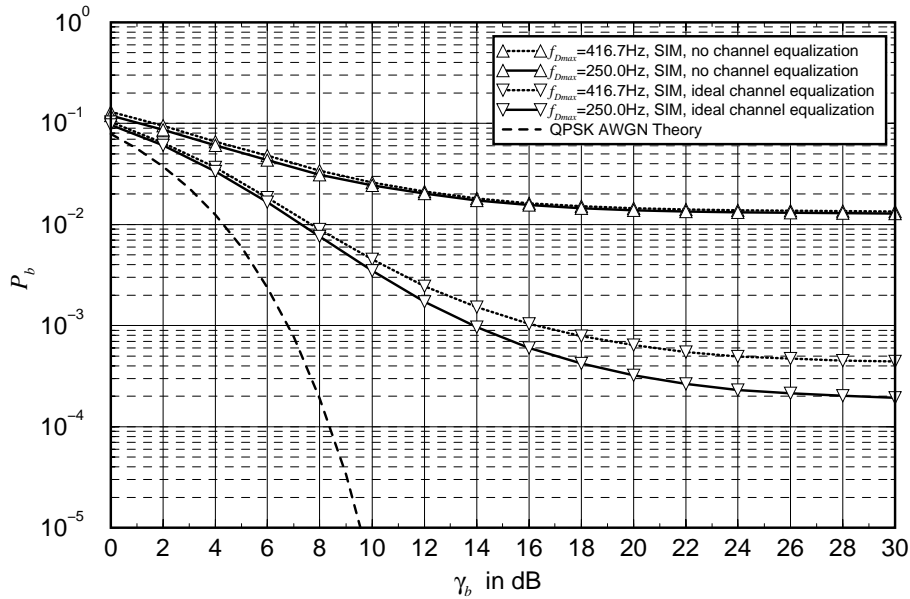


Figure 5.6: Average BER for OFDM QPSK with aeronautical taxi channel and different maximum Doppler frequencies

able to further improve the performance results by  $\sim 1 \dots 2$  dB compared to the simulation results without equalization. Using real channel equalization, the performance decreases, even compared to the case without equalization. The loss for  $N_f = 7$ ,  $N_t = 3$  is high, but decreases as the pilot spacing comes close to the case without oversampling and two-times oversampling. This effect originates from the fact that with decreasing pilot spacing, the allowed bandwidth for the Doppler and delay power spectra increases. Since this additional bandwidth is not necessary, high frequency noise from the AWGN is present within this bandwidth and delivers wrong channel estimates.

The DSP system performance results for the subsequent taxi and parking channels use the frequency domain representation of the WSSUS channel model, see Section 2.4.3, and thus make the multi-carrier modulator and demodulator redundant. The carrier frequency offset is already taken into account in the channel model.

The **taxi channel** with different maximum Doppler frequencies  $f_{D_{max}}$  is considered first, see Fig. 5.6. Due to the decreased Rice factor compared to the en-route and arrival scenarios, the poor performance for the two maximum Doppler frequencies without equalization is about the same. This changes with ideal channel equalization. The performance for  $f_{D_{max}} = 250.0$  Hz improves by almost two decades in the resulting BER. The improvement for  $f_{D_{max}} = 416.7$  Hz is less, due to the remaining larger ICI.

In Fig. 5.7, the maximum Doppler frequency is fixed to  $f_{D_{max}} = 250.0$  Hz and the performance results using the DSP system are appended. The  $\text{si}(x)$  interpolation with  $N_f = 7$ ,  $N_t = 3$  again delivers the lowest gain, whereas the same pilot distances with linear interpolation deliver the best result. This can be explained by looking at the filter functions for  $\text{si}(x)$  interpolation, compare Fig. 4.4, linear interpolation, compare Fig. 4.5, and the necessary pilot distances for

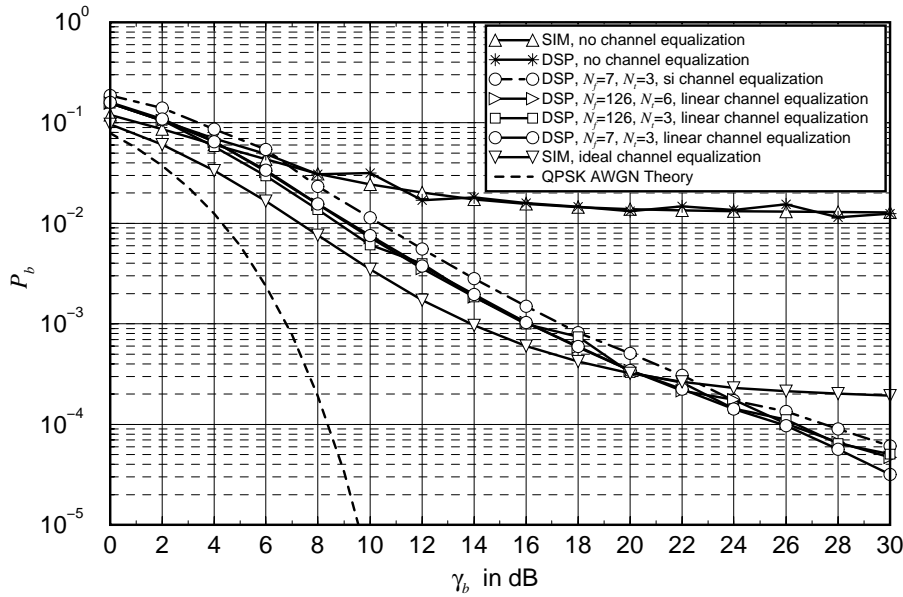


Figure 5.7: Average BER for OFDM QPSK with aeronautical taxi channel and different equalization settings

the taxi channel, compare Table 5.2. The frequency selectivity is very low, so that it would be sufficient to have one or two pilot symbols in direction of frequency to estimate the phase and amplitude distortions of all subcarriers in the corresponding OFDM symbol. The  $si(x)$  interpolation introduces additional noise due to its large passband gain, whereas the linear interpolation already suppresses the interpolated signal close to the passband edge and only has an approximately constant gain in  $\sim 20\%$  of the passband center, compared to  $\sim 80\%$  for the  $si(x)$  case with  $N_{tap} = 5$ , so that high frequency noise occurring with pilot oversampling is suppressed. The other results with linear interpolation for the cases with and without pilot oversampling show similar performances. The  $si(x)$  interpolation would not make sense for  $N_f = 126$  due to an insufficient number of available pilot taps. Since ICI is neglected with the WSSUS frequency domain channel model, there is no error floor in the simulation results with the DSP system which of course is not true for the system under real conditions.

Finally, the results for the **parking channel** are shown in Fig. 5.8. Since there is no LOS path present, demodulation of the QPSK symbols without equalization does not make sense. ICI is below  $91.7/3846 \approx 2.4\%$ . For comparison, the theoretical QPSK Rayleigh fading performance from [Pro95, Section 14-4-2] is depicted as well.

It becomes evident that already small violations of the sampling theorem,  $N_f = 42$  instead of  $N_f \leq 37$  and  $N_t = 24$  instead of  $N_t \leq 20$ , result in poor BER performance. For pilot symbol distances close to two times oversampling, i.e.  $N_f = 18, N_t = 8$ ,  $si(x)$  interpolation succeeds over linear interpolation. Further oversampling, i.e.  $N_f = 7, N_t = 3$ , again changes the statistics for the benefit of linear interpolation. A BER floor occurs for ideal equalization, using the time domain channel implementation, due to the remaining ICI. It shows that there is a mismatch of  $\sim 2 \dots 3$  dB between the theoretical Rayleigh / ideal equalization and the real equalization

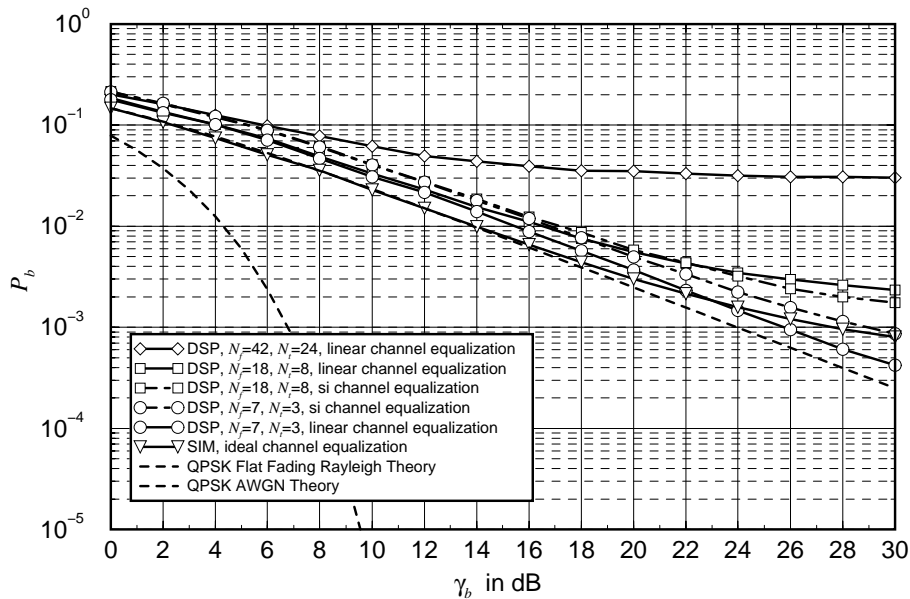


Figure 5.8: Average BER for OFDM QPSK with aeronautical parking channel and different equalization settings

with estimation and interpolation. This is related to a summation of additive noise terms in the real interpolation and equalization process, comparable to the loss that occurs from coherent to differential coherent demodulation with AWGN.

### 5.2.2 Results with Non-Linear Power-Amplifier

Today's transmitters, especially mobile ones, use solid-state power-amplifiers. These transmitters have the advantage that their *AM/PM-conversion* is negligible. This means that phase distortions due to varying input amplitudes are very small. On the other hand, *AM/AM-conversion* due to the limited amplifier output power has to be taken into account. AM/AM-conversion for solid-state amplifiers is described by three parameters, namely the small signal gain factor in the area where the input/output-relation can be considered linear, the saturation output value for the maximum output amplitude and the buckling characteristic parameter  $p$  of the curve when the output amplitude approaches its maximum [Rap92]. The resulting equation for an AM/AM-conversion with small signal gain equal to one and maximum saturation output amplitude equal to one is

$$g(A) = \frac{A}{(1 + (A^2)^p)^{\frac{1}{2p}}}, \quad (5.14)$$

where  $A$  is the input amplitude and  $g(A)$  is the corresponding output amplitude. The characteristic curve is dot-symmetric. A representative buckling parameter for solid state amplifiers is  $p = 2.6$ . The corresponding logarithmic input/output-characteristic is shown in Fig. 5.9.

It is obvious that a performance degradation of the digital link has to be expected if the output amplitude is within the non-linear area of the curve. That effect is investigated in the following.

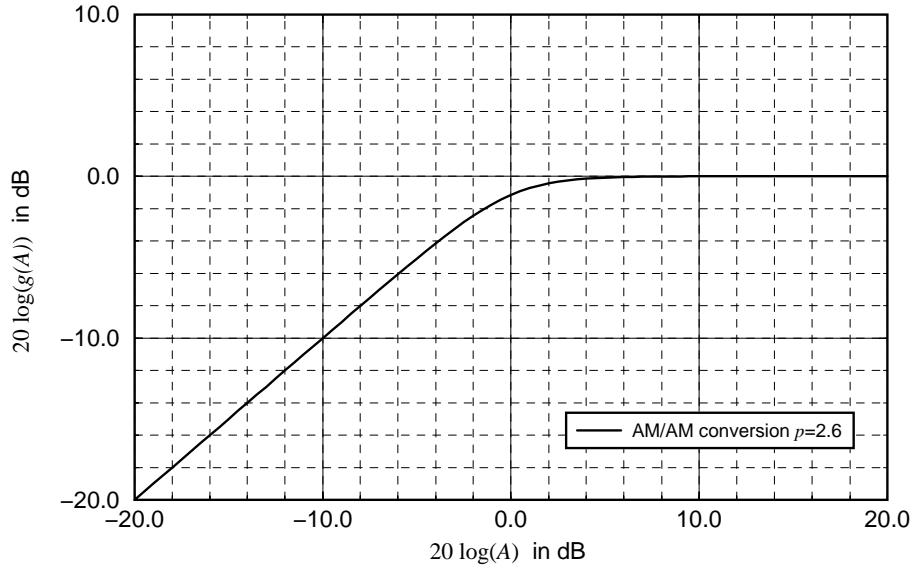


Figure 5.9: AM/AM-conversion of non-linear solid-state amplifier

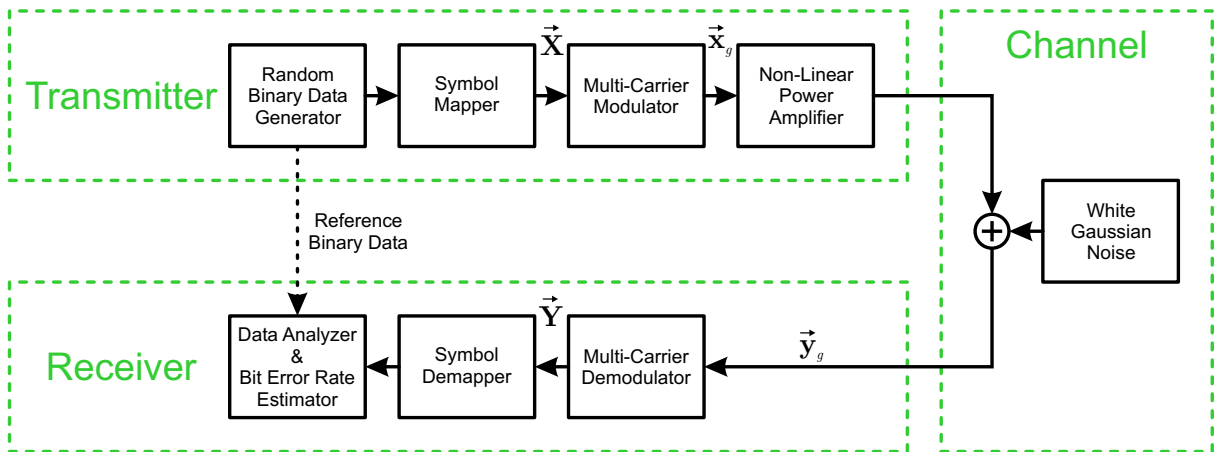


Figure 5.10: Simulator for OFDM transmission with non-linear amplifier

The average output power of the samples from the OFDM symbol time-domain vector  $\vec{x}_g$  is therefore normalized to one. As shown in Fig. 5.10, these samples pass through the non-linear power-amplifier and an additional AWGN channel, are received as the time-domain vector  $\vec{y}_g$  and analyzed. The so-called Input Back Off (IBO) of the amplifier can be adjusted. The IBO describes the average operation point below the maximum operation point in which the amplifier currently is used. For example, an IBO equal to 3 dB means, that the used average output power is only half of the theoretical maximum output power. The higher the IBO, the more the amplifier operates in its linear region, but also the more power is wasted resulting in technically more complex designs and physically larger amplifier dimensions.

Bit error rate performance results with different IBOs are given in Fig. 5.11. It can be seen that operation close to the maximum output power gives large performance degradation as already expected. This is explained by the large PAPR of OFDM signals. Without further special methods, like PAPR-reduction through coding [Oc100], an IBO of at least 3 dB should

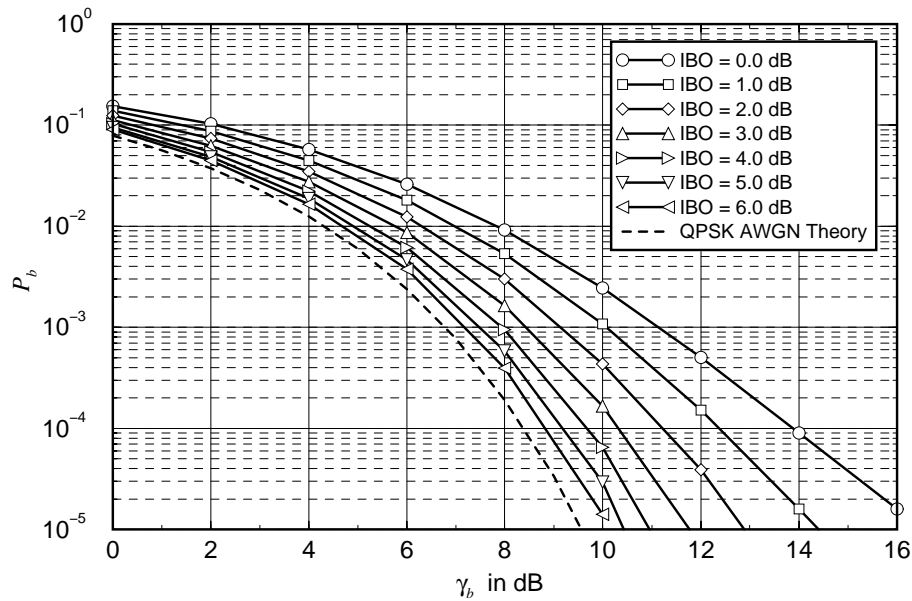


Figure 5.11: Average BER for OFDM QPSK with non-linear amplifier

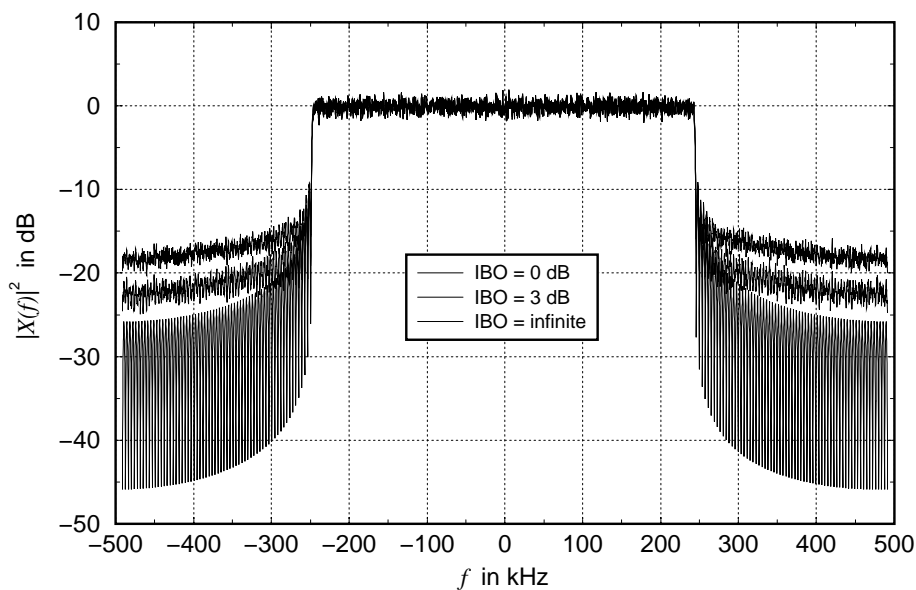


Figure 5.12: Average transmitter power spectrum for OFDM QPSK with non-linear amplifier

be envisaged to get an acceptable performance degradation for OFDM with M-PSK.

BER performance degradation is not the only drawback of non-linear amplifiers. Just as important is the resulting noise floor in the spectrum. Fig. 5.12 shows the noise floor for IBO=0 dB, IBO=3 dB and for the ideal transmitted OFDM spectrum (IBO= $\infty$  dB). It is observed that the noise floor on the borders is still about 5 dB higher for an IBO of 3 dB than in the ideal case.

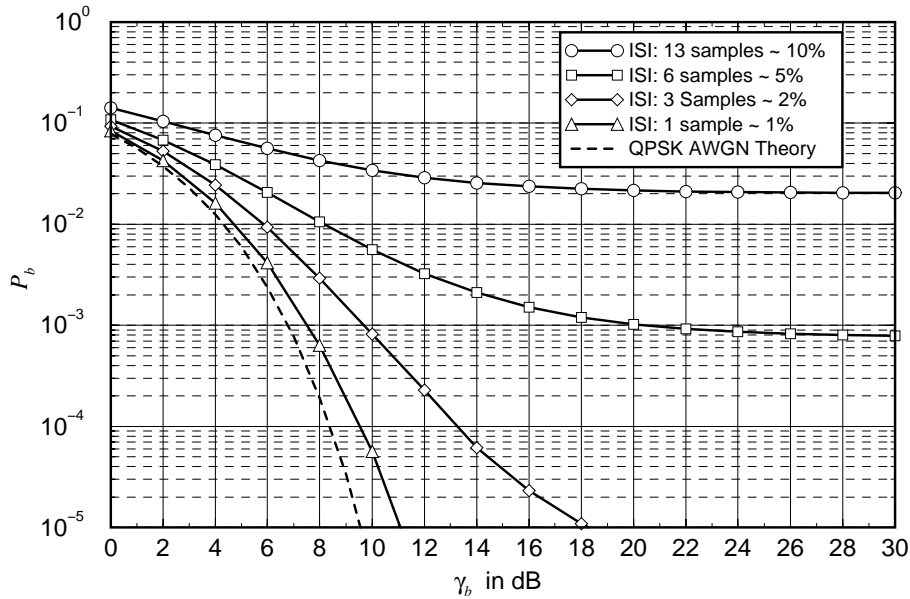


Figure 5.13: Average BER for OFDM QPSK with ISI due to frame/symbol timing offset

### 5.2.3 Results with Frame/Symbol Timing Synchronization Offset

In Fig. 5.13, the performance results for different OFDM frame/symbol timing offsets resulting in ISI, i.e. outside the valid guard interval, are displayed. The chosen offsets are integer multiples of the sampling time  $T_{sample}$ , thus avoiding any other interpolation effects between neighbouring samples. Linearly increasing phase shifts of the subcarriers are avoided internally.

It shows that ISI is extremely critical for the system performance. Even small offsets  $\Delta t/T_s < 2\%$  cause large degradations. Since ISI can't be circumvented by a higher SNR, an error floor remains. Therefore, timing offsets outside the guard interval should be prevented under all circumstances.

### 5.2.4 Results with Carrier Frequency Synchronization Offset

A similar evaluation is performed for carrier frequency synchronization offsets. This time  $\Delta f_c/F_s$  is considered. Corresponding results are shown in Fig. 5.14. As long as the offsets stay below 5%, the performance degradation is tolerable. Between 5% and 10%, a rapid increase of the degradation is observed. Offsets above 10% are intolerable.

This result is also interesting for OFDM transmission systems affected by echoes with Doppler shifts different to the Doppler shift of the LOS path. Considering the relative frequency offset and the attenuation between the echo and the LOS path, it can be assessed whether there will be a considerable performance degradation. Thus, it is possible to judge whether the discrepancy is tolerable or not.

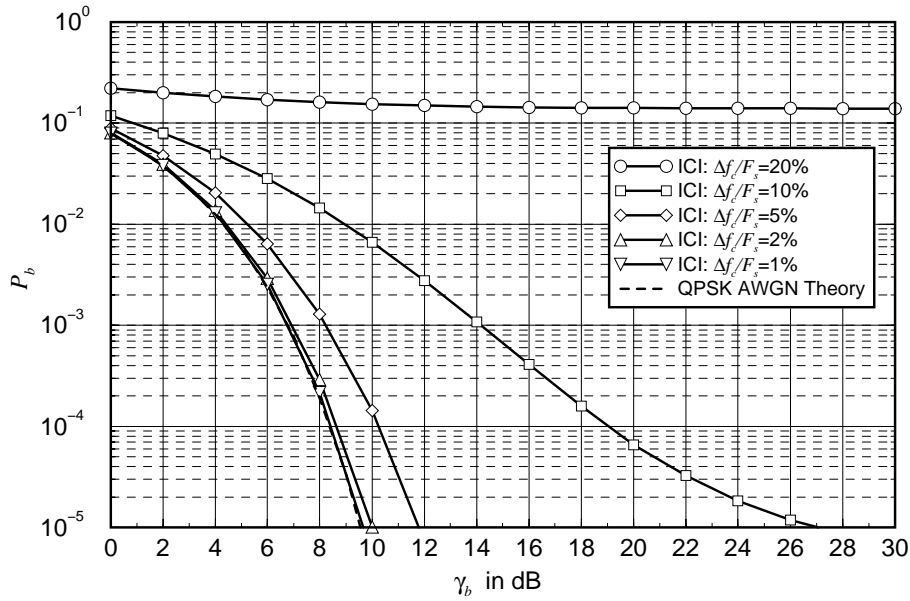


Figure 5.14: Average BER for OFDM QPSK with ICI due to carrier frequency offset

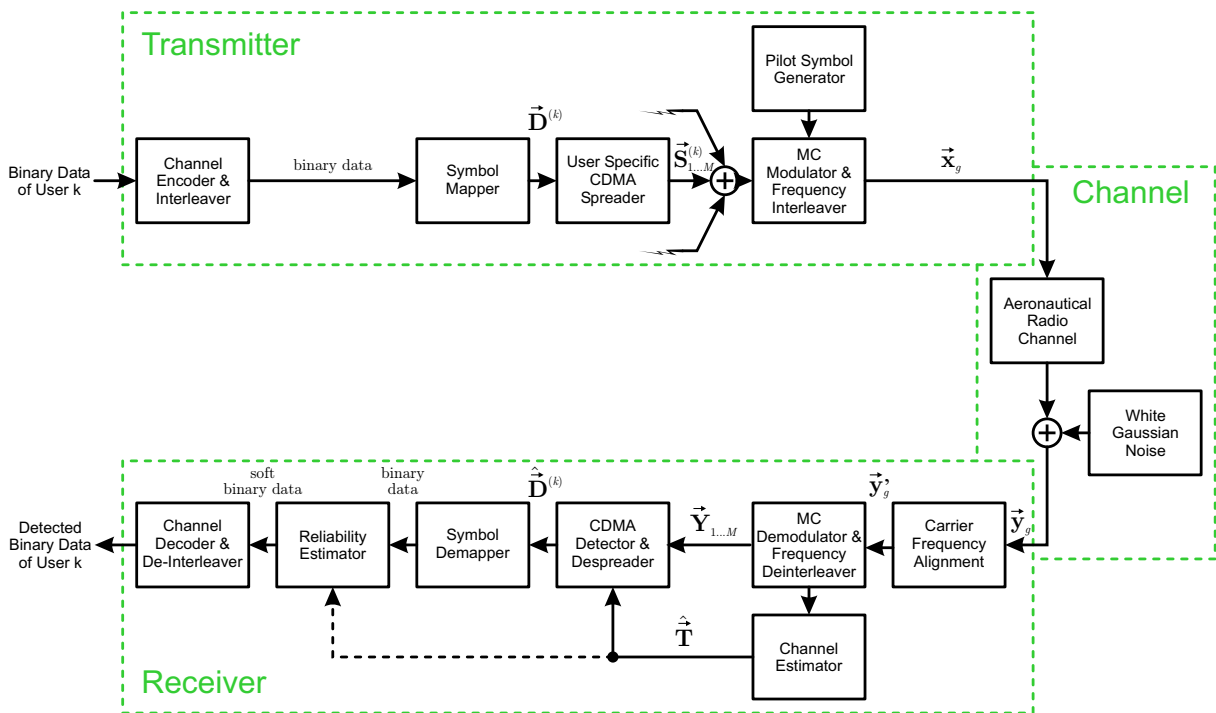


Figure 5.15: Simulator for coherent multi-user MC-CDMA OFDM transmission with aeronautical channel models

### 5.2.5 Results with Multi-User MC-CDMA

The introduction of spreading on subcarrier level changes the system from simple multi-carrier modulation to multi-carrier CDMA. The corresponding simulator for MC-CDMA is shown in Fig. 5.15. Since there is not just one user, but there are possibly several users accessing the transmission system simultaneously, the information of a certain user  $k$  is observed in the

following. The binary data is passed through a channel encoder and interleaver with rate  $R$ . The binary output of the channel encoder is mapped to the chosen modulation constellation, i.e. in this case QPSK (2 bit).  $M$  of these data symbols are combined in the data symbol vector  $\vec{\mathbf{D}}^{(k)}$ . Each data symbol is then spread with the user specific spreading vector  $\vec{\mathbf{C}}^{(k)}$ , resulting in  $M$  source vectors  $\vec{\mathbf{S}}_m^{(k)}$  each consisting of  $L$  elements. The source vectors of all users in the current group are summed up to the spread vectors  $\vec{\mathbf{S}}_m$ . In an additional stage, the  $Q$  groups are interleaved on subcarrier level with chip spreading distance  $D_{chip} = 28$  for  $L = 4$  and chip spreading distance  $D_{chip} = 14$  for  $L = 8$ , synchronization and pilot symbols are added with the proper spacings, i.e.  $N_f = 7, N_t = 3$ , the subcarriers are IFFT transformed to the time domain and the guard interval is added, resulting in the time domain vector  $\vec{\mathbf{x}}_g$ . The energy  $E_s$  of one data symbol  $D_m^{(k)}$  has to be distributed on  $L$  subcarriers resulting in the new energy per subcarrier  $E_s/L$ . To keep the average power per subcarrier constant for the spread subcarrier symbols and the pilot symbols, the pilot symbol energy  $E_{pilot}$  has to comply with

$$E_{pilot} = K_Q \cdot E_s/L, \quad (5.15)$$

for the case that there are currently  $K_Q = K/Q$  active users in each group, where  $K$  is the total number of active users in all groups and an integer multiple of  $Q$ .

After processing the signal with the WSSUS aeronautical channel model and adding WGN, the carrier frequency alignment, MC demodulation, channel estimation and equalization on the receiver side are the same as for coherent OFDM QPSK transmission, compare Section 5.2.1. Linear interpolation is used to obtain the estimates. For simplicity, Single-user Detection (SD) is applied for CDMA despreading. The equalized  $M$  received vectors  $\vec{\mathbf{Y}}_m$ , consisting of  $L$  elements each, are despread with the corresponding spreading vector  $\vec{\mathbf{C}}^{(k)}$  for the  $k$ th user by calculating the dot product, resulting in the estimated data symbol vector  $\hat{\vec{\mathbf{D}}}^{(k)}$  consisting of  $M$  elements. Each element is then QPSK demapped and provided with an additional reliability information to obtain soft binary input data for optimum channel decoding. Since the equalization process already offers intrinsic reliability information within the data symbols, these two steps are obsolete and the soft binary data is extracted with the method mentioned earlier in this chapter. The final detected binary data of the  $k$ th user is obtained after de-interleaving and channel decoding. The additional channel code and spreading have to be considered in the energy balance for the BER performance as follows

$$\begin{aligned} \gamma_b &= \gamma_c - \underbrace{10 \cdot \log(R) \text{ dB}}_{\text{channel code}} - \underbrace{10 \cdot \log(\log_2(M)) \text{ dB}}_{\text{MPSK modulation}} - \underbrace{10 \cdot \log(L \cdot 1/L) \text{ dB}}_{\text{spreading}} \\ &= \gamma_c - \underbrace{10 \cdot \log(R) \text{ dB}} - \underbrace{10 \cdot \log(\log_2(M)) \text{ dB}}. \end{aligned} \quad (5.16)$$

The energy used by the pilot symbols is again neglected.

Fig. 5.16 depicts performance results with different spreading lengths  $L = 4$  and  $L = 8$  for the aeronautical parking channel. Only one user is present in each of the  $Q$  user groups, i.e.  $K_Q = 1$ . In that case, MRC has to be used in the equalization process to obtain the best results due to optimum diversity combining, compare Section 4.2.3 and [Kai98]. The results for  $L = 4$

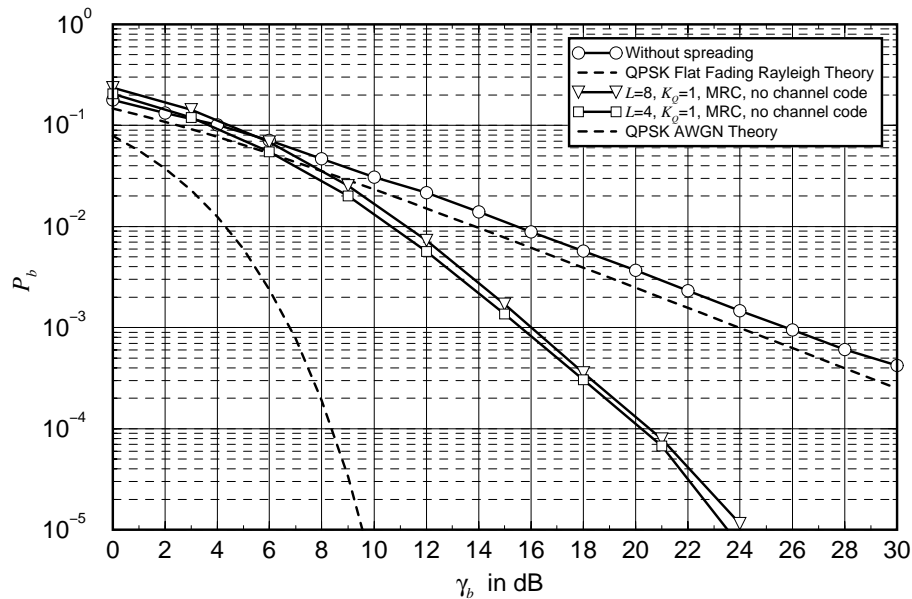


Figure 5.16: Average BER for OFDM QPSK MC-CDMA with different spreading lengths  $L$  in the aeronautical parking scenario

and  $L = 8$  are only varying slightly. This shows that the maximum diversity gain is already obtained for  $L = 4$  and no further improvements are possible within the current bandwidth. The results for  $L = 8$  are a little worse even though it should be the other way around. This effect can be related to the channel model; for  $L = 8$  twice as many parameter sets have to be calculated resulting in a variation of the statistics.

In the following a spreading length of  $L = 8$  is assumed. The system is filled with  $K_Q = 1, 2, 4, 8$  active users. For  $K_Q = 1, 2, 4$  MRC is used. The corresponding performance results are shown in Fig. 5.17. While for  $K_Q = 2$  the performance degradation compared to  $K_Q = 1$  is still small, a large performance degradation is observed for  $K_Q = 4$ . This is explained by the fact that MRC is only the optimum equalization method for one active user. The optimum equalization for several active users is MMSE equalization. Since this method requires the knowledge of  $\gamma_c$ , it is in most cases optimized for a desired operation point with fixed  $\gamma_c$  [Kai98]. A suboptimum method is ZF equalization, i.e. MMSE with  $\gamma_c \rightarrow \infty$ . Using ZF, the BER for  $K_Q = 4$  can be lowered to  $3.9 \cdot 10^{-4}$  at  $\gamma_b = 30.0$  dB. For the full system load, i.e.  $K_Q = 8$  active users, the results using ZF equalization are shown as well. With increasing SNR, the performance approaches the case without spreading. Using MMSE equalization even with a fixed  $\gamma_c$ , the BER can be lowered below this curve, thus justifying the use of spreading even for a fully loaded system.

### 5.2.6 Discussion of the Coherent Performance Results

Summing up the results for coherent modulation with coherent detection, it can be concluded that OFDM MC-CDMA is a very promising technique for digital aeronautical communication

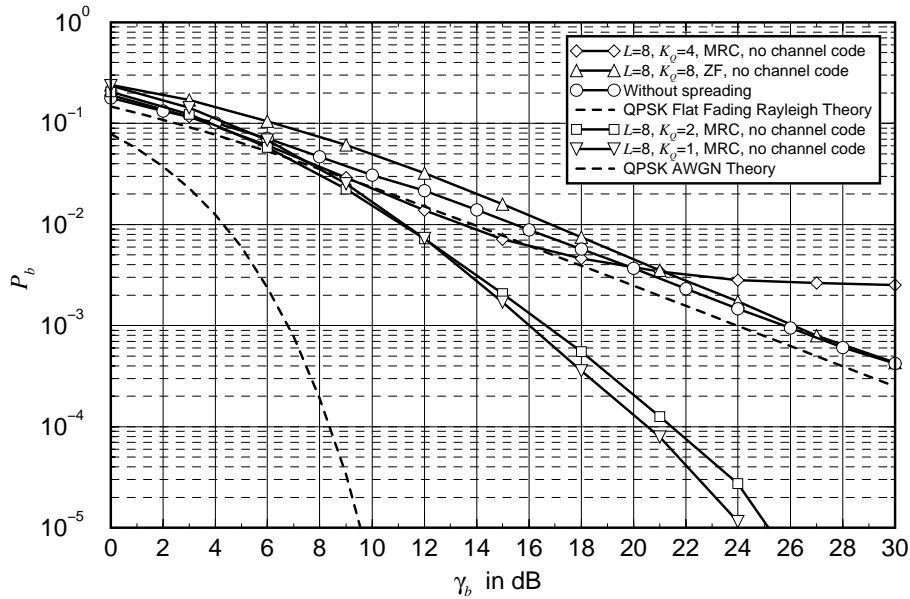


Figure 5.17: Average BER for OFDM QPSK MC-CDMA with spreading length  $L = 8$  and different numbers of active users  $K_Q$  in the aeronautical parking scenario

systems. Due to the special environmental conditions, i.e. a strong LOS path at high velocities, and conditions close to Rayleigh fading at low velocities, the investigated techniques are applicable. To decrease the chance of a BER degradation in the en-route and arrival scenarios, appropriate measures should be taken to detect the strong LOS path condition and disable the channel equalization under these conditions by only correcting the carrier frequency and average carrier phase offsets.

It has been shown that if only a limited number of pilot symbols is available or if the filter bandwidth of the interpolation process has been chosen too high,  $\text{si}(x)$  interpolation delivers very poor performance results. This is circumvented by using linear interpolation, since the center part of the corresponding filter function can be considered constant, delivering especially good results starting with two-times oversampling of the pilot symbols. Another advantage is that linear interpolation needs only two surrounding pilot symbols, thus also lowering the computational complexity. The performance can be further optimized by using power boosting of the pilot symbols compared to the data symbols, an issue that already has been included in the DVB-T standard [DVB99]. Power-boosted pilot symbols benefit from the fact that with increasing pilot symbol power, the influence of additive noise on the pilot symbols decreases, making the channel equalization less vulnerable to a wrong channel estimation. That way, the loss of 2...3 dB between the theoretical performance and the effective performance is decreased as well.

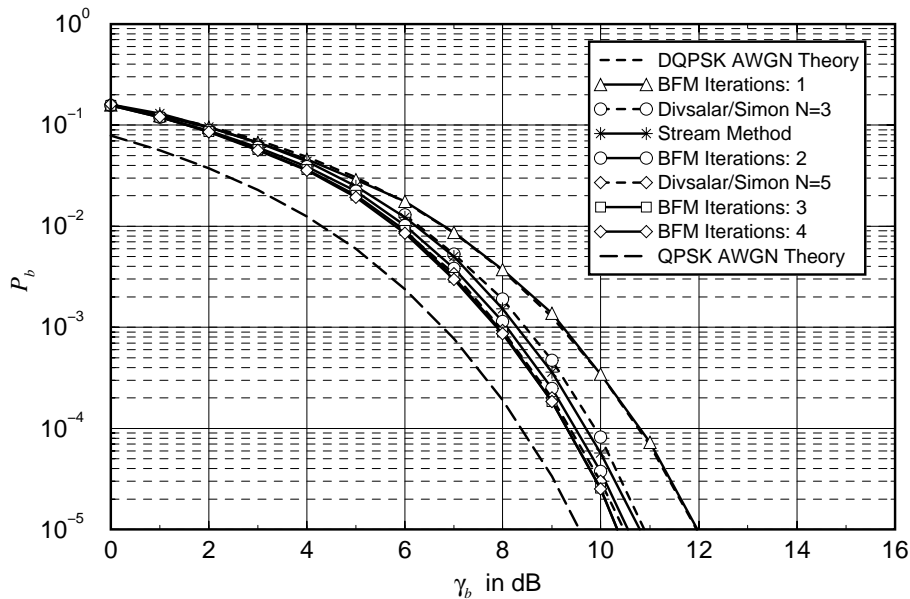


Figure 5.18: Average BER with 2D-DD for OFDM DQPSK with AWGN

## 5.3 Performance Analysis for Differential Coherent DQPSK

### 5.3.1 Results with AWGN Applying Two-Dimensional Differential Demodulation

The 2D-DD methods proposed in Section 4.4 to enhance the differential demodulation of differentially modulated signals are first verified for the AWGN case. In the following sections, 2D-DD is also investigated for received signals with different distortions. For DQPSK it can be evaluated from theoretical assumptions [PRR82] that

$$P_b \approx \frac{1}{2} \cdot P_E(4) \quad (5.17)$$

for the case that Gray-encoding has been used for the symbols of the constellation diagram. In Fig. 5.18, the results for 2D-DD with the brute force method for maximum iteration path depths  $\mathcal{N} = 1 \dots 4$  and the stream method are compared.

The performance results for  $\mathcal{N} = 1$ , i.e. standard DPSK demodulation, compare (4.36), comply with the DQPSK AWGN theory for One-Dimensional Differential Demodulation (1D-DD). For iteration path depths  $\mathcal{N} \geq 2$ , the required SNR can be significantly decreased. For example to achieve a BER of  $P_b = 10^{-4}$ , the SNR can be reduced by  $\sim 1.25$  dB already for an iteration path depth of  $\mathcal{N} = 2$ . Larger iteration path depths result in even larger gains. The number of alternative paths with length  $\mathcal{L} = 2$  is equal to 4, and for  $\mathcal{L} = 3$  is equal to 12. This means that for an iteration path depth of  $\mathcal{N} = 2$ , 4 alternative paths are investigated and that for  $\mathcal{N} = 3$ ,  $4 + 12 = 16$  alternative paths are investigated, and so on.

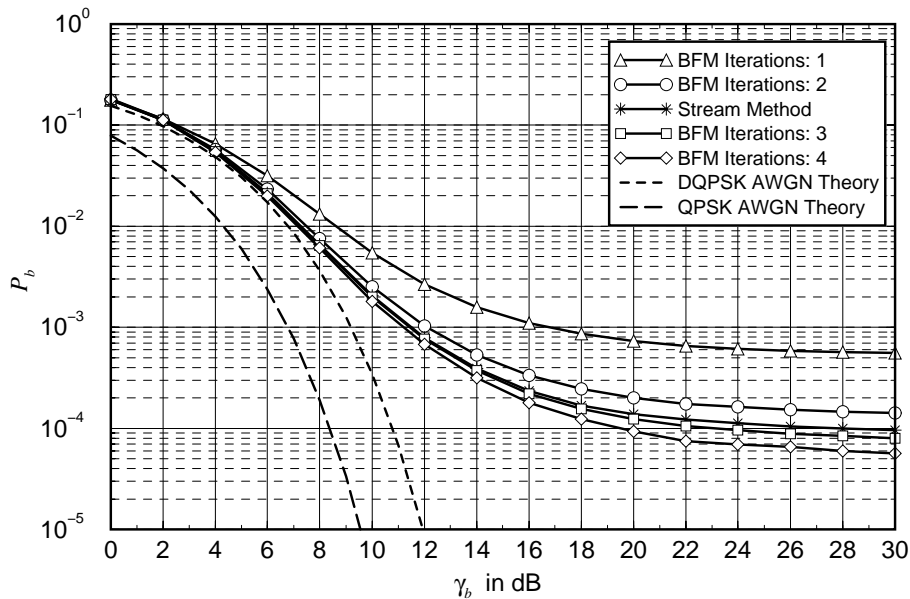


Figure 5.19: Average BER with 2D-DD for OFDM DQPSK with aeronautical en-route (ground-air) channel

The stream method does not perform as good as the brute force method here, since it does not evaluate all possible paths and neglects shorter paths that might give a more reliable result.

For comparison, the simulation results with multiple-symbol differential detection from [DiS90] are depicted as well. It shows that choosing a detour path with two steps, i.e.  $\mathcal{N} = 2$  for 2D-DD, is more advantageous than using the comparable observation interval of  $N = 3$  for multiple-symbol detection. The same applies for  $\mathcal{N} = 4$  and  $N = 5$ . Already  $\mathcal{N} = 3$  outperforms  $N = 5$ . It follows that analyzing multiple dimensions, if available, and treating each differential step independent from other differential steps has an edge over the detection algorithm proposed in [DiS90]. The 2D-DD algorithm furthermore makes it possible to eliminate bad paths during the search and thus reduces the overall computational complexity.

### 5.3.2 Results with Aeronautical Channel Models

In the next step, the suitability of 2D-DD for the aeronautical fading channel models is investigated. The simulation system is comparable to the one shown in Fig. 5.2, only this time no channel estimator and no frequency domain channel equalizer are used (grey blocks). Additionally, the symbol mapper now performs DQPSK modulation and the symbol demapper either performs 1D-DD or 2D-DD. The first scenario that is considered is the **en-route ground-air channel**. The results in Fig. 5.19 show that for standard 1D-DD (BFM,  $\mathcal{N} = 1$ ), an error floor remains. This error floor is reduced with 2D-DD by about a decade in the resulting BER. The required SNR for a BER of  $P_b = 10^{-3}$  is reduced by  $\sim 4.5$  dB for the brute force method with  $\mathcal{N} = 2$ , and by more than 5 dB for the stream method or the brute force method with  $\mathcal{N} \geq 3$ . Furthermore, compared to the AWGN-only 1D-DD case of Fig. 5.18, it is observed

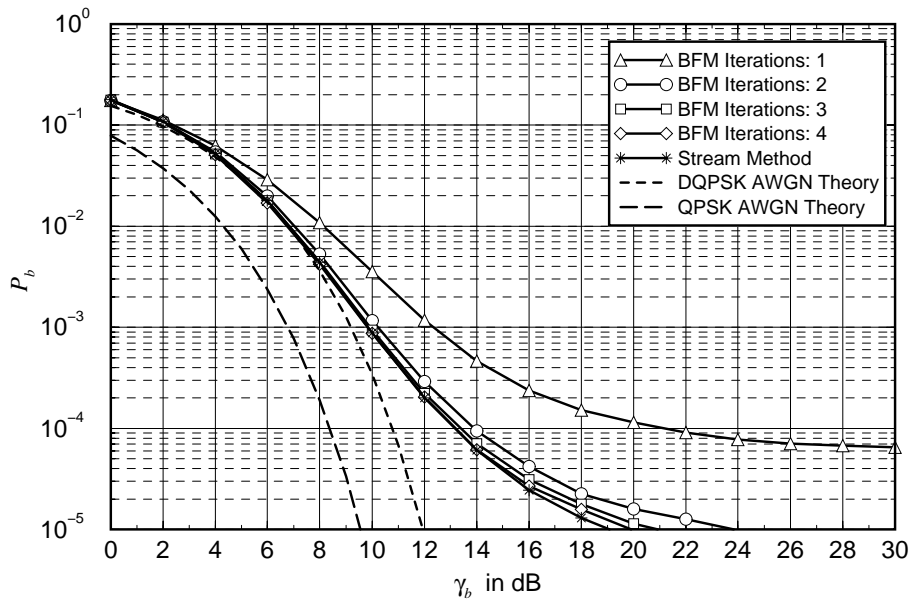


Figure 5.20: Average BER with 2D-DD for OFDM DQPSK with aeronautical arrival channel

that the stream method now performs better than the BFM with  $\mathcal{N} = 2$  and that for  $\mathcal{N} > 3$ , the error floor continues to decrease. Since there is no explicit channel estimation and therefore the chance to do a wrong channel equalization is missing, 2D-DD performs in this case better than coherent demodulation with equalization, compare Fig. 5.4.

The next scenario is the **arrival channel**. The corresponding performance results are shown in Fig. 5.20. Again 2D-DD decreases the remaining BER floor significantly by more than a decade. The required SNR at  $P_b = 10^{-3}$  is decreased by  $\sim 2$  dB. The performance improvement is already present with short iteration path depths of the brute force method. Using the stream method additionally improves the achievable gain compared to the depicted brute force methods with  $\mathcal{N} \leq 4$ . Since the stream method gives the best results for the arrival channel, a look is taken at the statistics of the chosen path length  $\mathcal{L}$  for the differential demodulation. For 1D-DD, the probability of choosing a path with length one is 100%. For the case that 2D-DD with the stream method is applied, the statistics change. Now the probability of choosing a path with length three is about the same as choosing a path with length one, i.e. both about 36%. For paths with length five, the probability goes down to 13% and for length seven to 6% and is further decreasing for longer paths as shown in Fig. 5.21. This means that about 91% of the chosen paths have a short length of 1, 3, 5 or 7 and the remaining 9% are distributed among path lengths with  $\mathcal{L} \geq 9$ . Limiting the maximum path iteration depth is reasonable in practical implementations to reduce the calculation complexity.

The results for the **taxi channel** are shown in Fig. 5.22. With the decreasing Rice-factor compared to the en-route and arrival scenarios, the correlations between the OFDM-symbols and between the subcarriers are reduced. This results in a high error floor for 1D-DD, since phase shifts between the OFDM-symbols increase the probability for a wrong symbol estimation. The same applies for 2D-DD with additional phase shifts between the subcarriers that degrade the

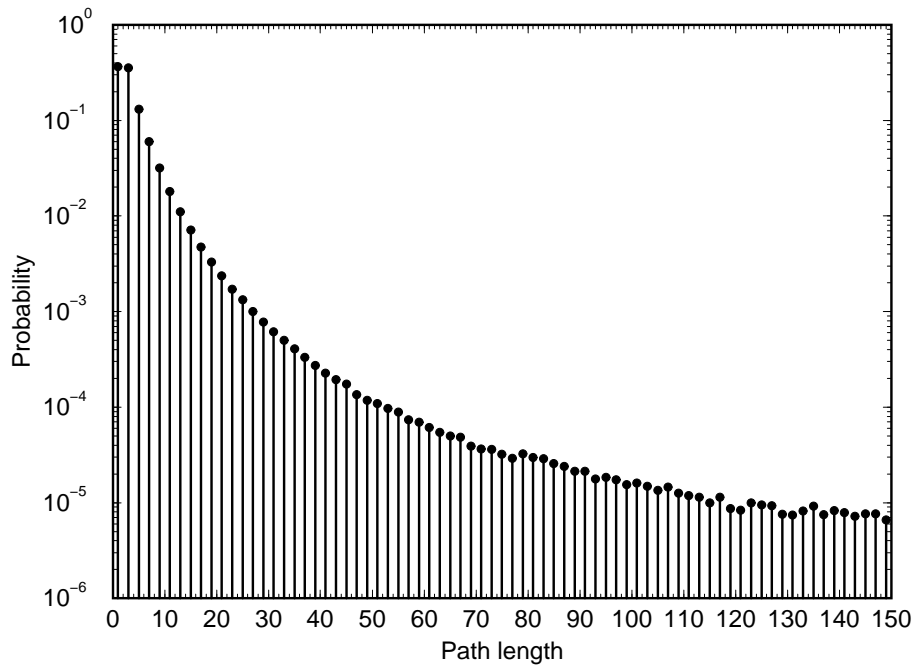


Figure 5.21: Statistical distribution of chosen stream method path length  $\mathcal{L}$  for aeronautical arrival channel at  $\gamma_b = 20$  dB

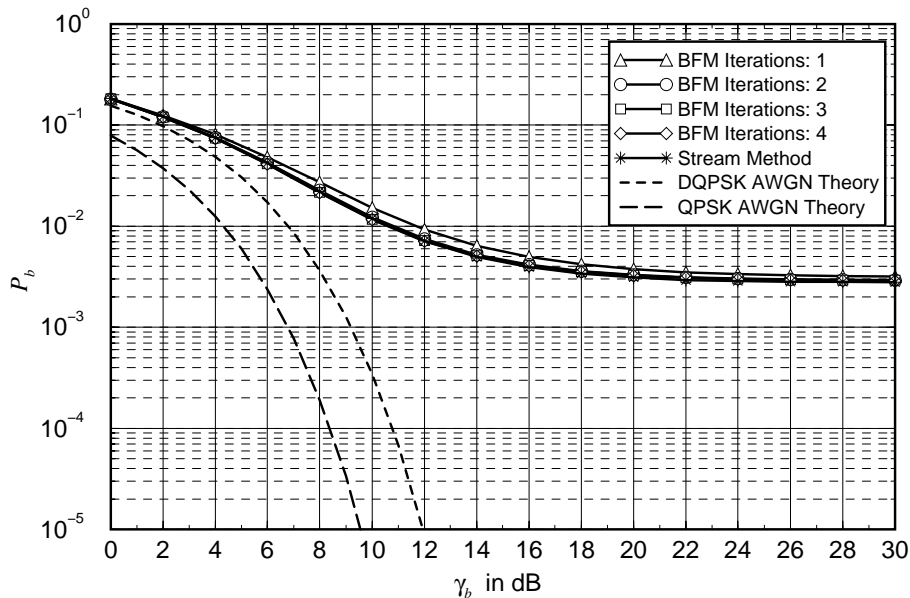


Figure 5.22: Average BER with 2D-DD for OFDM DQPSK with aeronautical taxi channel

performance of the algorithm. The stream method still gives the best performance results with an SNR gain of  $\sim 1$  dB at  $P_b = 10^{-2}$ . But since the error floor cannot be significantly lowered with the current algorithm, the gain cannot be considered as a true performance improvement.

Similar conclusions can be drawn for the **parking channel** performance results displayed in Fig. 5.23. This time the gain at  $P_b = 10^{-2}$  is  $\sim 1$  dB, but again a high error floor remains. For comparison, the theoretical DQPSK Rayleigh fading performance for high  $\gamma_b$  is depicted as

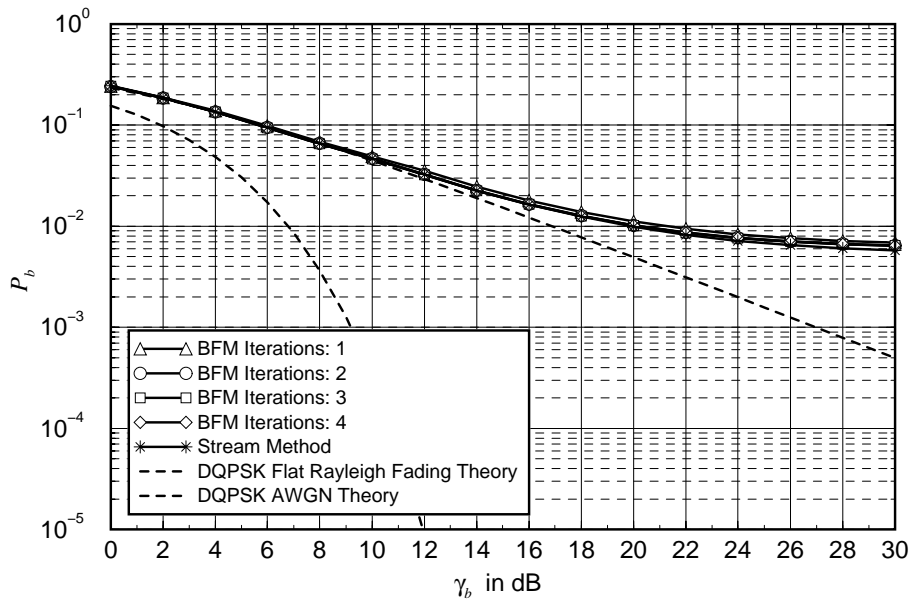


Figure 5.23: Average BER with 2D-DD for OFDM DQPSK with aeronautical parking channel well [Pro95, Section 14-4-2]. The remaining error floor again can be ascribed to ICI.

### 5.3.3 Results with Non-Linear Power-Amplifier

The previous sections have shown that the 2D-DD algorithm has an excellent performance in channel conditions as long as correlations between subcarrier-symbols are present. In the next sections it is evaluated whether the resulting BER can also benefit for signal conditions where distortions are applied in the transmitter or receiver respectively.

First, a look is taken at DQPSK-modulated signals with standard 1D-DD that are affected by a non-linear transmitter power-amplifier. The corresponding performance is depicted in Fig. 5.24 for different IBOs, compare Section 5.2.2. With respect to the results, an IBO of at least 3 dB should be considered for a tolerable performance degradation. Applying 2D-DD with the brute force method for an IBO of 3 dB, see Fig. 5.25, the performance at  $P_b = 10^{-4}$  can be improved by  $\sim 2$  dB, reducing the performance loss compared to the AWGN-only 1D-DD case to 0.7 dB.

### 5.3.4 Results with Frame/Symbol Timing Synchronization Offset

Fig. 5.26 shows performance degradations using 1D-DD caused by different receiver frame/symbol timing offsets  $\Delta t/T_s$ . Similar to the coherent case, compare Fig. 5.13, already small ISI below 2% results in a large performance degradation with a remaining error floor. Using 2D-DD BFM in conjunction with different timing offsets, the performance can be improved significantly. For  $\Delta t/T_s \approx 2\%$ , the BER floor is reduced to a fourth. For  $\Delta t/T_s \approx 1\%$ ,

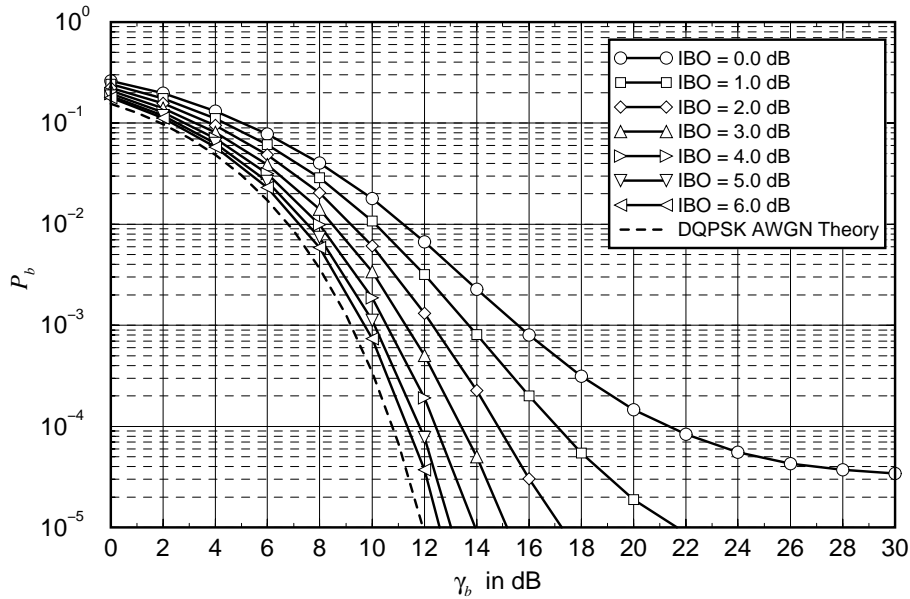


Figure 5.24: Average BER for OFDM DQPSK with non-linear amplifier

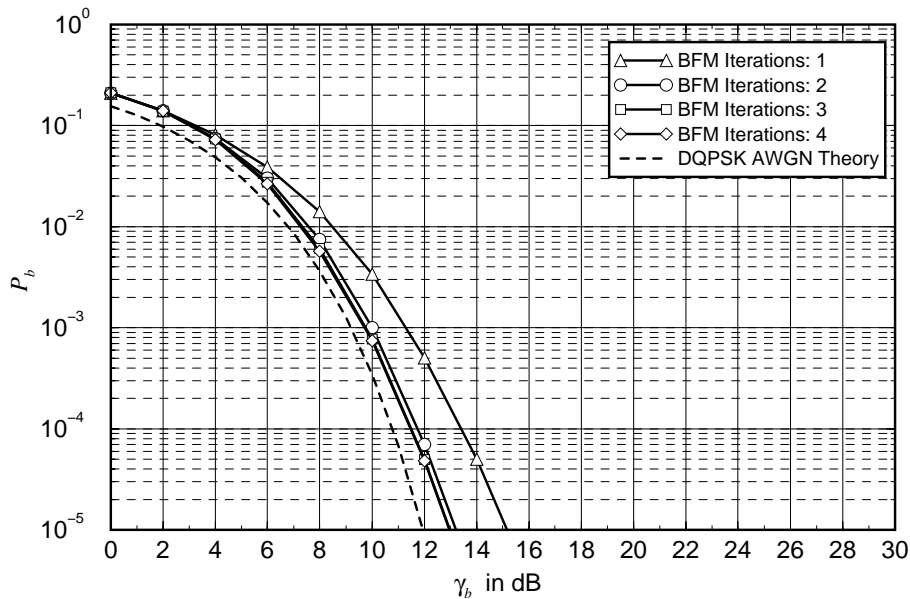


Figure 5.25: Average BER with 2D-DD for OFDM DQPSK with non-linear amplifier (IBO = 3.0 dB)

the required SNR at  $P_b = 10^{-4}$  is reduced by  $\sim 2.5$  dB, obtaining almost the performance of the AWGN-only 1D-DD case. The corresponding simulation results are depicted in Fig. 5.27.

### 5.3.5 Results with Carrier Frequency Synchronization Offset

The results for 1D-DD with a variety of carrier frequency offsets  $\Delta f_c/F_s$  are shown in Fig. 5.28. Comparing these results with the coherent ones in Fig. 5.14, it is evident that DQPSK demodulation has a better performance for high SNRs than QPSK demodulation. This effect is

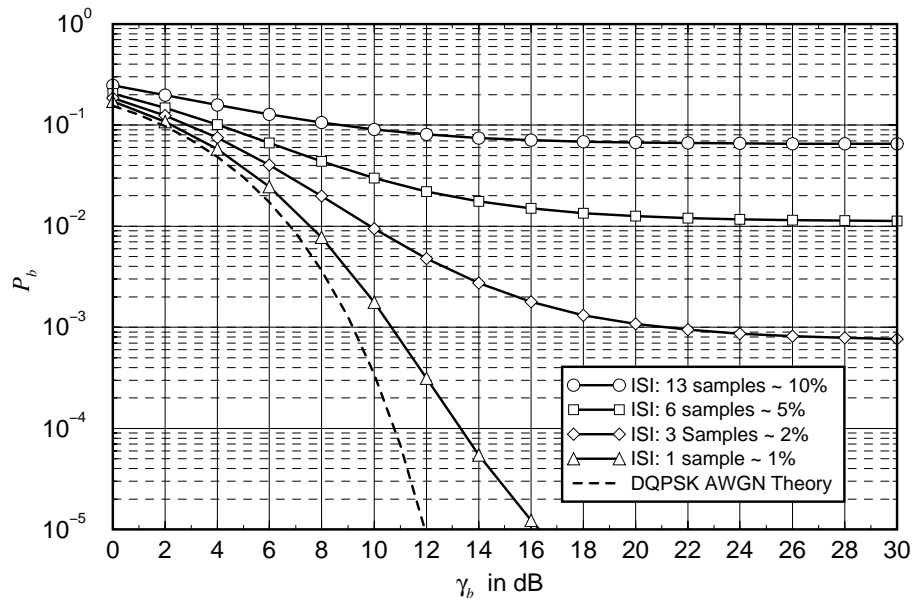


Figure 5.26: Average BER for OFDM DQPSK with ISI due to frame/symbol timing offset

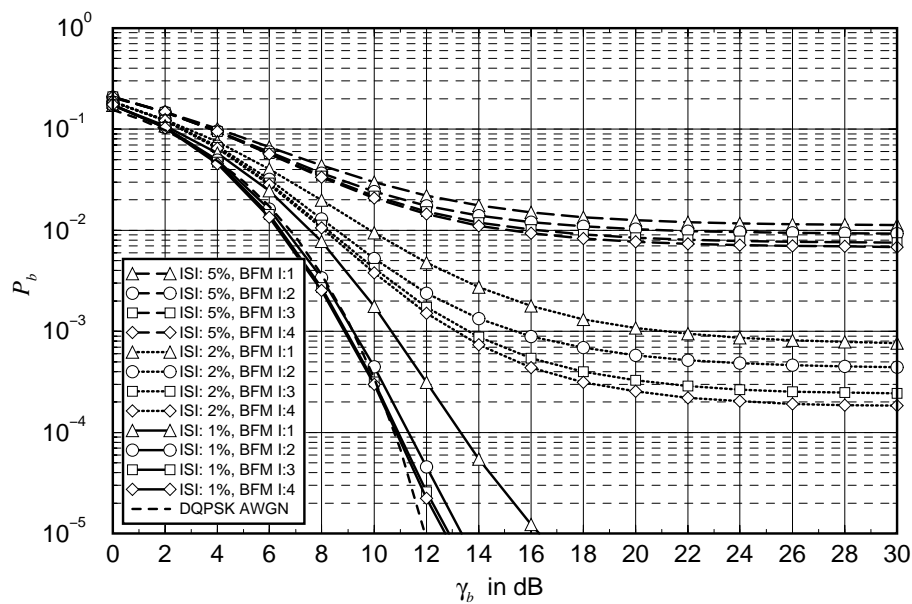


Figure 5.27: Average BER with 2D-DD for OFDM DQPSK with ISI due to frame/symbol timing offset

explained in a little more detail in the following.

Without loss of generality, it is assumed that for the coherent modulation a symbol with amplitude one and phase  $0^\circ$  is transmitted and that for the differential coherent modulation two symbols with amplitude one and phase  $0^\circ$  are transmitted which on the other hand again include the differential symbol with amplitude one and phase  $0^\circ$ . A neighbouring interfering subcarrier adds a signal with amplitude  $x$  smaller than one, i.e.  $x \in [0; 1]$ , and one of the four possible phase states  $0^\circ, 90^\circ, 180^\circ$  or  $-90^\circ$ . For the second symbol needed for differential demodulation, the interfering phase is assumed to be  $0^\circ$  without loss of generality. The received

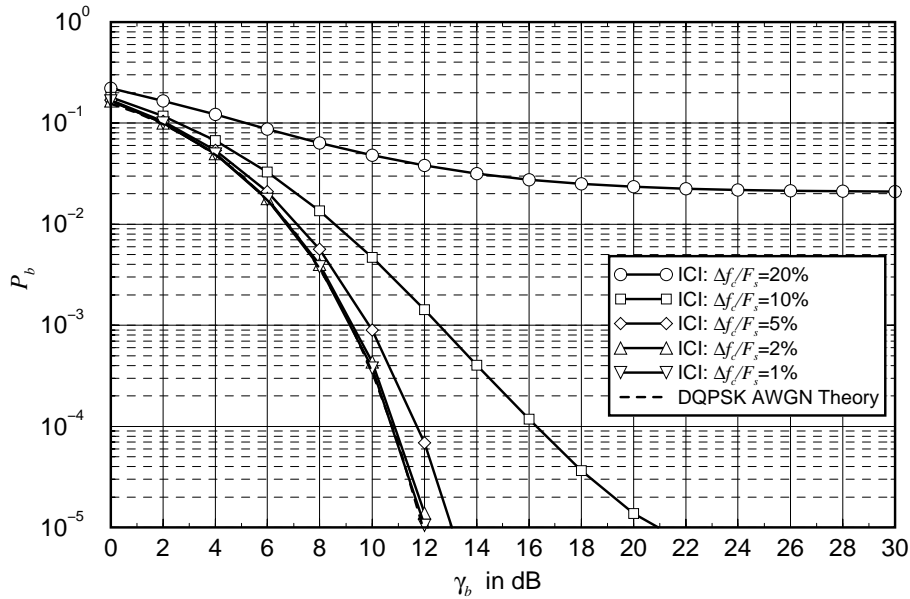


Figure 5.28: Average BER for OFDM DQPSK with ICI due to carrier frequency offset

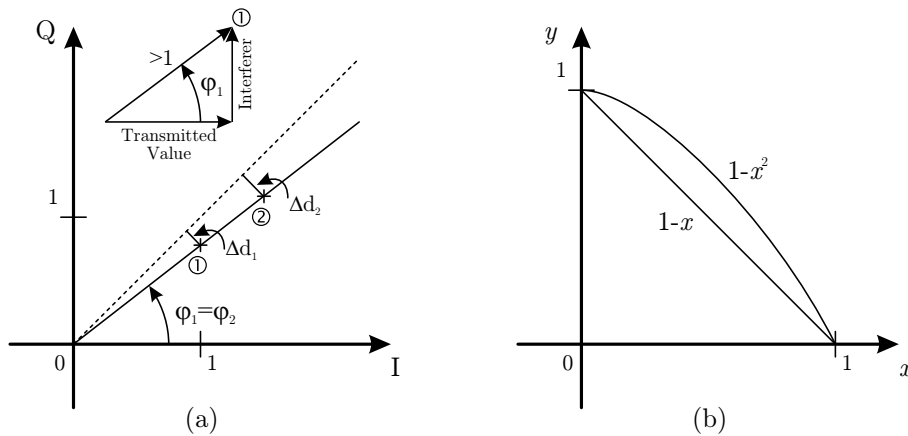


Figure 5.29: Benefits of OFDM DQPSK over OFDM QPSK for ICI-distorted demodulation

subcarrier symbols are first considered without any additional noise.

For the case that the interfering subcarrier has the same phase as the observed subcarrier, i.e.  $0^\circ$  for the symbol in the coherent case and for the first symbol in the differential coherent case, there is a constructive superpositioning of the interferer and the observed subcarrier and both, coherent and differential coherent demodulation, benefit from this condition.

If the interferer now has a phase shift of  $\pm 90^\circ$ , there is no direct conclusion possible. Therefore, a look at the difference between coherent and differential coherent demodulation is taken. In Fig. 5.29(a), the transmitted value with an interfering  $90^\circ$  subcarrier is shown. They sum up to the new vector (1) with phase  $\varphi_1$  that has an amplitude larger than one. The resulting distance to the  $45^\circ$  decision border of QPSK is  $\Delta d_1$  for the coherent case. In the differential coherent case this vector is multiplied with a second vector also having an amplitude larger than one and a phase of  $0^\circ$  due to constructive superpositioning of the second symbol and the

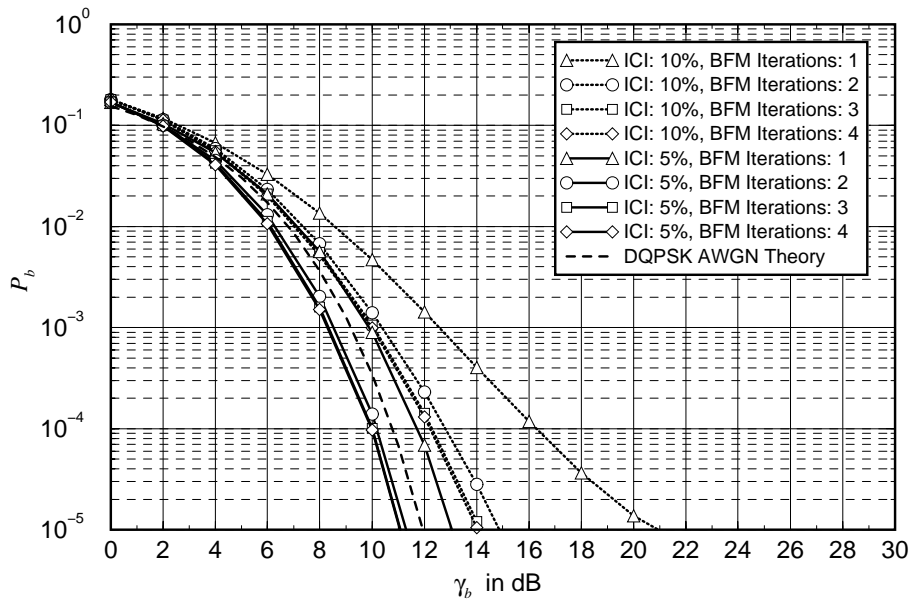


Figure 5.30: Average BER with 2D-DD for OFDM DQPSK with ICI due to carrier frequency offset

second interferer. The resulting phase of this vector (2) is also  $\varphi_2 = \varphi_1$ , but the amplitude is larger compared to the vector (1), resulting in a larger distance  $\Delta d_2$  to the decision border. With additive noise, the second vector is better protected due to its larger distance, thus giving DQPSK an edge over QPSK for the  $\pm 90^\circ$  case.

The last case is an interferer with  $180^\circ$  phase shift. In the coherent case, the interferer amplitude is subtracted from the observed amplitude resulting in  $(1 - x)$ . For the differential coherent case this amplitude has to be multiplied with the second symbol plus interferer ( $0^\circ$ ) resulting in the amplitude  $(1 - x) \cdot (1 + x) = 1 - x^2$ . Both amplitudes for different values of  $x$  are displayed in Fig. 5.29(b). It can be seen that the amplitude in the differential coherent case is always larger or equal to the amplitude in the coherent case. The result again is an edge of DQPSK over QPSK offering a better protection.

Using all possible interferer combinations for the first and second symbol in the differential coherent case delivers more solutions where it is not always possible to determine which of the coherent or differentially coherent demodulation techniques has an edge over the other one. Summarizing the results it can be concluded that in the presented one out of four options, coherent and differential coherent demodulation are affected in a similar constructive way. In the remaining three out of four options, differential coherent demodulation has an edge over coherent demodulation, thus explaining the performance gain of DQPSK compared to QPSK.

Applying 2D-DD further improves the performance, as can be seen in Fig. 5.30. For  $\Delta f_c/F_s = 10\%$ , the required SNR is reduced by  $\sim 4$  dB and for  $\Delta f_c/F_s = 5\%$ , the required SNR is reduced by  $\sim 1.75$  dB, both at  $P_b = 10^{-4}$ . For the latter case it is even possible to reduce the SNR below AWGN-only 1D-DD.

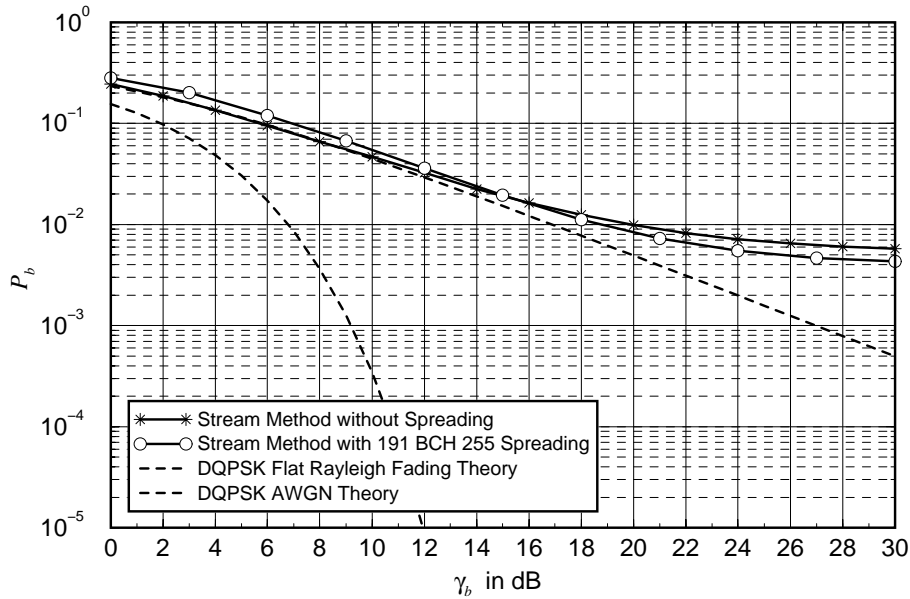


Figure 5.31: Average BER with 2D-DD for OFDM DQPSK with GF(2) BCH-code (255, 191) used for binary spreading with hard-decision decoding in the aeronautical parking scenario

### 5.3.6 Results with Coded CDMA System

Considering the differential MC-CDMA scheme of Fig. 4.8(a) with a (255, 191) BCH-code and additional 2D-DD stream method demodulation in the aeronautical parking channel, the results of Fig. 5.31 are obtained. The 255 spread bits are placed on the 256 bits of one OFDM symbol leaving one bit empty. Hard decision decoding is applied on the receiver side. Only a minor performance improvement compared to the case without spreading is observed. Using 2D-DD with soft output and more efficient codes with soft decision will considerably improve the results. But taking all reasonable code and user constellations into account would certainly go beyond the scope of this work.

### 5.3.7 Discussion of the Differential Coherent Performance Results and Two-Dimensional Differential Demodulation

Compared to coherently demodulated signals, the striking advantage of differential coherent demodulation is that it does not need an explicit channel estimation and equalization. The channel is implicitly estimated and equalized by the conjugate complex multiplication, compare (4.36), that removes the constant channel phase offsets between two received symbols for the estimated source symbol. Thus, the amount of reference symbols, comparable to the pilot symbols for coherent signals, is much lower or even can be avoided completely.

Even though differential coherent demodulation introduces additional noise, it has a direct edge over coherent demodulation in some cases, e.g. if ICI is present. It has an indirect edge since it avoids channel estimation and equalization and therefore reduces the complexity and

computational load. The obsolete channel estimation is an interesting quality for the data link from a mobile station to the base station. Since it is a difficult task to do an individual channel estimation for each transmitting mobile station, differential MC-CDMA with frequency interleaving possibly combined with TDMA is a promising option for this link.

Considering 2D-DD, it has been shown that applying 2D-DD, instead of 1D-DD, improves the BER performance in all conditions. Starting from the AWGN case, 2D-DD brings the differential coherent demodulation close to the theoretical coherent one which cannot be achieved due to channel estimation and equalization. It further significantly reduces the error floor in fading channels with a strong LOS path and is able to compensate non-linear effects from the transmitter power-amplifier. The influence of noise, introduced through mismatches in the synchronization algorithm, is reduced as well. Since 2D-DD can be used for existing as well as for new systems, it is an ideal extension for differential coherent demodulation. It can be further improved by introducing alternative path evaluation methods and/or removing the average phase offsets in frequency and time direction before the start of the algorithm.

## 5.4 Selection of System for Ground-Air and Air-Ground Link

### 5.4.1 Coherent Ground-Air Link

In accordance with the simulation results from Section 5.2, an OFDM frame structure for the DSP demonstrator system with the parameters shown in Table 5.3 is compiled.

The corresponding OFDM frame structure is shown in the upper part of Fig. 5.32. The first OFDM symbol, the so-called zero-symbol, is left empty. It is followed by the two synchronization symbols necessary for the Schmidl and Cox algorithm presented in Section 4.5.4.1. The remaining 25 OFDM symbols are reserved for the user data and pilot symbols. In all OFDM symbols the 0 Hz subcarrier, i.e.  $l' = 64$ , and subcarriers on both sides of the spectrum are not used, compare Section 3.2.3.2. Since MC-CDMA is to be used, user groups have to be composed each consisting of  $L = 8$  chips. These user groups are shown in the bottom part of Fig. 5.32. The chips of a group are each spaced  $D_{chip} = 14$  subcarriers apart from each other. With this configuration, a total number of  $Q = 11$  user groups is possible, provided that the remaining positions of the user group with the 0 Hz subcarrier are not used. To keep the structure as simple as possible, the pilot positions in OFDM symbols without pilot symbols are not used as well. Assuming that in the demonstrator system one user occupies all user groups with its spreading sequence, i.e.  $M = 11$ , a total of  $11 \cdot 25 \cdot 2 = 550$  raw data bits per user is available for an overall number of  $L = 8$  users.

Table 5.3: Coherent ground-air link demonstrator parameters

Bandwidth	$B = 492.307$ kHz
Carrier frequency	$f_c = 5.1465$ GHz
OFDM, inverse OFDM	128 point IFFT, 128 point FFT
Subcarrier spacing	$F_s = 3.85$ kHz
Guard interval	$T_g = 10.2$ $\mu$ s ( $\equiv 5$ samples)
OFDM symbol duration including guard interval	$T'_s = 270.2$ $\mu$ s
Number of OFDM symbols in OFDM frame	$N_s = 28$
OFDM frame duration	$T_{fr} = 7.56$ ms
Data symbol mapping	QPSK with Gray encoding
Spreading code	Walsh-Hadamard code
Spreading code length	$L = 8$
Channel estimation	2· 1-D FIR filter
Interpolation type	linear (2· 2 filter taps)
Pilot symbol distance in frequency	$N_f = 7$
Delay filter bandwidth	$\tau_{filter} = 37.1$ $\mu$ s
Pilot symbol distance in time	$N_t = 3$
Doppler filter bandwidth	$f_{D_{filter}} = 616.9$ Hz
Number of user groups per OFDM symbol	$Q = 11$
Maximum number of active users per group	$K_{Q_{max}} = 8$
Maximum number of active users per OFDM frame	$K_{max} = 88$
Raw bit rate per user	$6.6$ kbit/s $\leq R_b \leq 581.7$ kbit/s

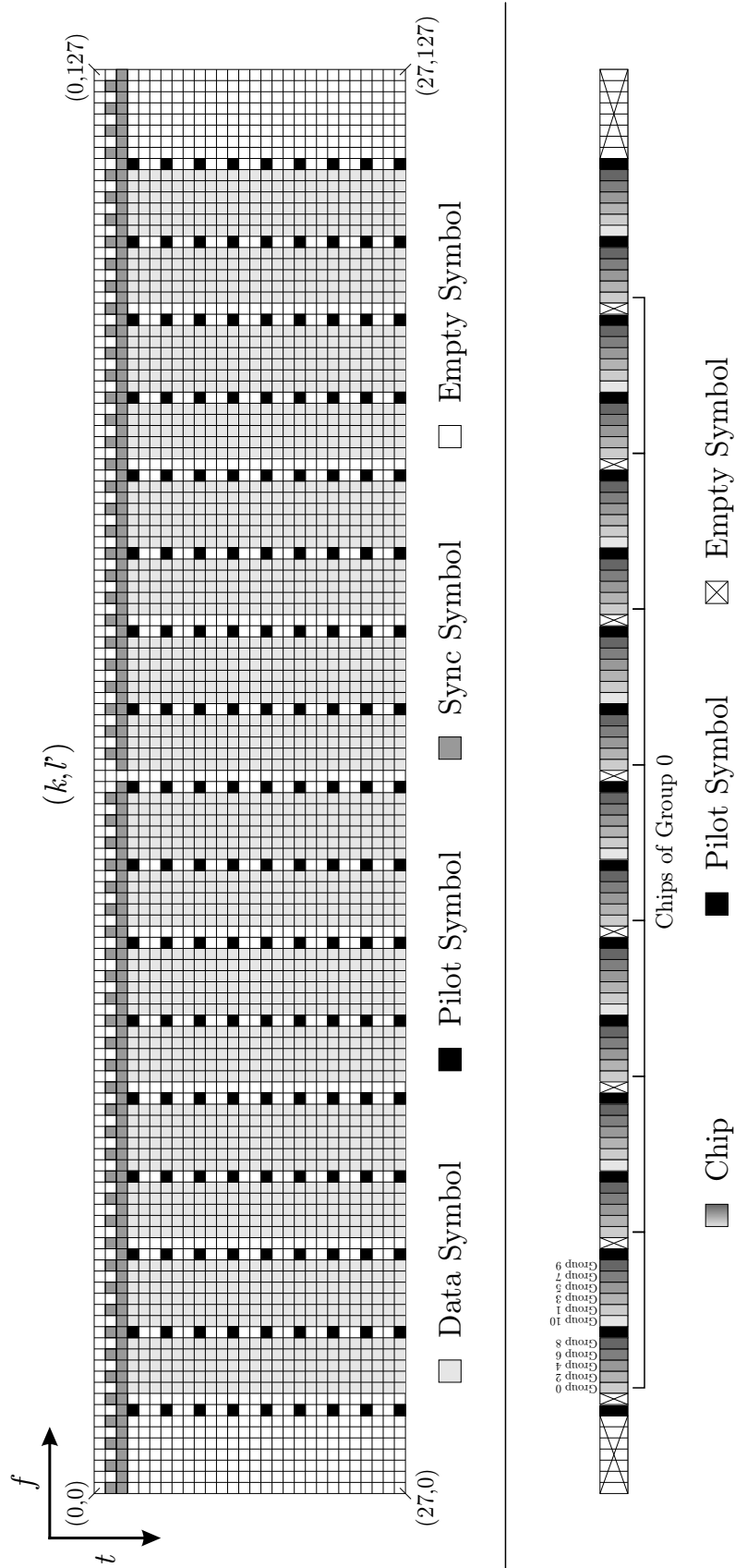


Figure 5.32: OFDM frame structure for coherent ground-air link demonstrator

### 5.4.2 Differential Coherent Air-Ground Link

In accordance with the simulation results from Section 5.3, an OFDM frame structure for the DSP demonstrator system with the parameters shown in Table 5.4 is compiled.

Table 5.4: Differential coherent air-ground link demonstrator parameters

Bandwidth	$B = 492.307$ kHz
Carrier frequency	$f_c = 5.1465$ GHz
OFDM, inverse OFDM	128 point IFFT, 128 point FFT
Subcarrier spacing	$F_s = 3.85$ kHz
Guard interval	$T_g = 10.2$ $\mu$ s ( $\equiv 5$ samples)
OFDM symbol duration including guard interval	$T'_s = 270.2$ $\mu$ s
Number of OFDM symbols in OFDM frame	$N_s = 28$
OFDM frame duration	$T_{fr} = 7.56$ ms
Data symbol mapping	DQPSK with Gray encoding
Number of reference OFDM symbols	1
Number of DQPSK symbols per OFDM symbol	112
Raw bit rate	$R_b = 710.7$ kbit/s

The corresponding OFDM frame structure is shown in Fig. 5.33. The zero- and synchronization OFDM symbols are followed by one OFDM reference symbol needed for the first differential modulation and demodulation step.

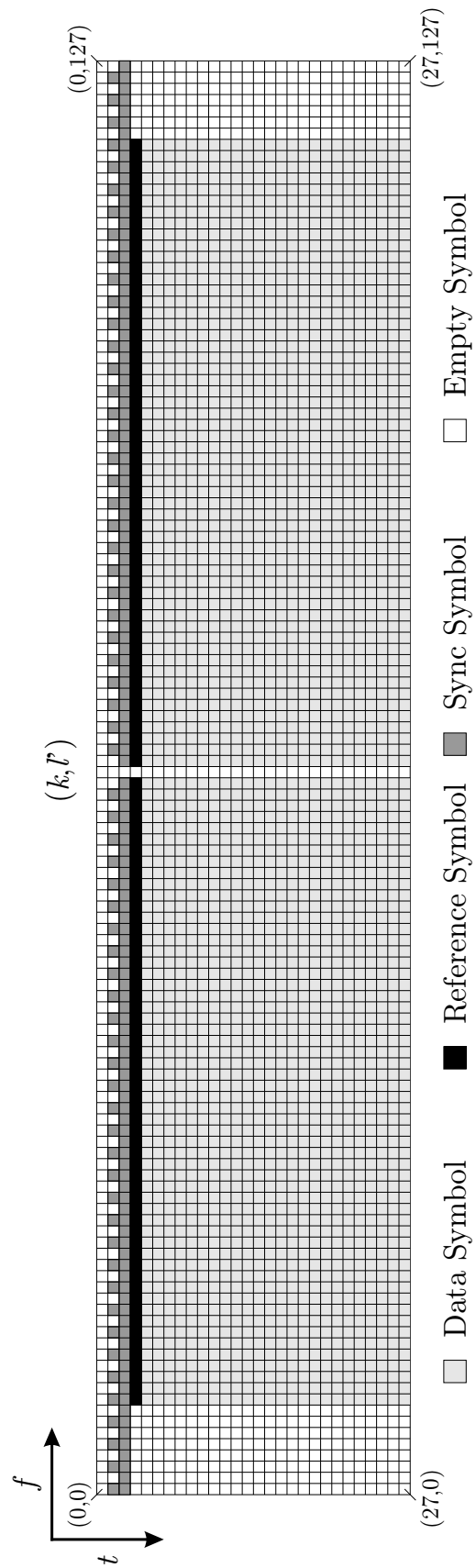


Figure 5.33: OFDM frame structure for differential coherent air-ground link demonstrator

# Chapter 6

## System Implementation

For implementing the OFDM system in DSP technology, one of the main objectives is to keep the system as flexible and adaptable as possible. This requirement is based on the need to be able to make changes at any time during the system design phase and keep the system transparent for programming purposes. Therefore, a development system is chosen for the transmitting and receiving unit that consists of several processors. Each processor can take care of a dedicated task in the communications system and reduce the programmers effort to be forced to write highly optimized routines. The focus is drawn on optimizing the algorithms and not the program structure.

### 6.1 Flexible and Adaptable Parameter Structure

Another benefit of a flexible and adaptable digital communications system parameter structure is the ability to create a Software-Defined Radio (SDR), where each parameter structure from a set of parameter structures can be tested individually in its hardware and software implementation, thus creating a system with accurately defined interfaces and ideal testability.

The parameter structures are stored in configuration files, where by changing one or several values in these files, the communications system functionality and/or purpose can be altered by a simple restart or recompilation of the communications system software.

#### 6.1.1 OFDM/TDMA Frame Parameters

The first step is to establish a parameter structure for the OFDM frame with an additional TDMA frame on top to increase the user capacity. The outline of such a TDMA frame is shown in Fig. 6.1. The TDMA frame with duration

$$T_{TDMA} = N_{fr} \cdot T_{fr} \quad (6.1)$$

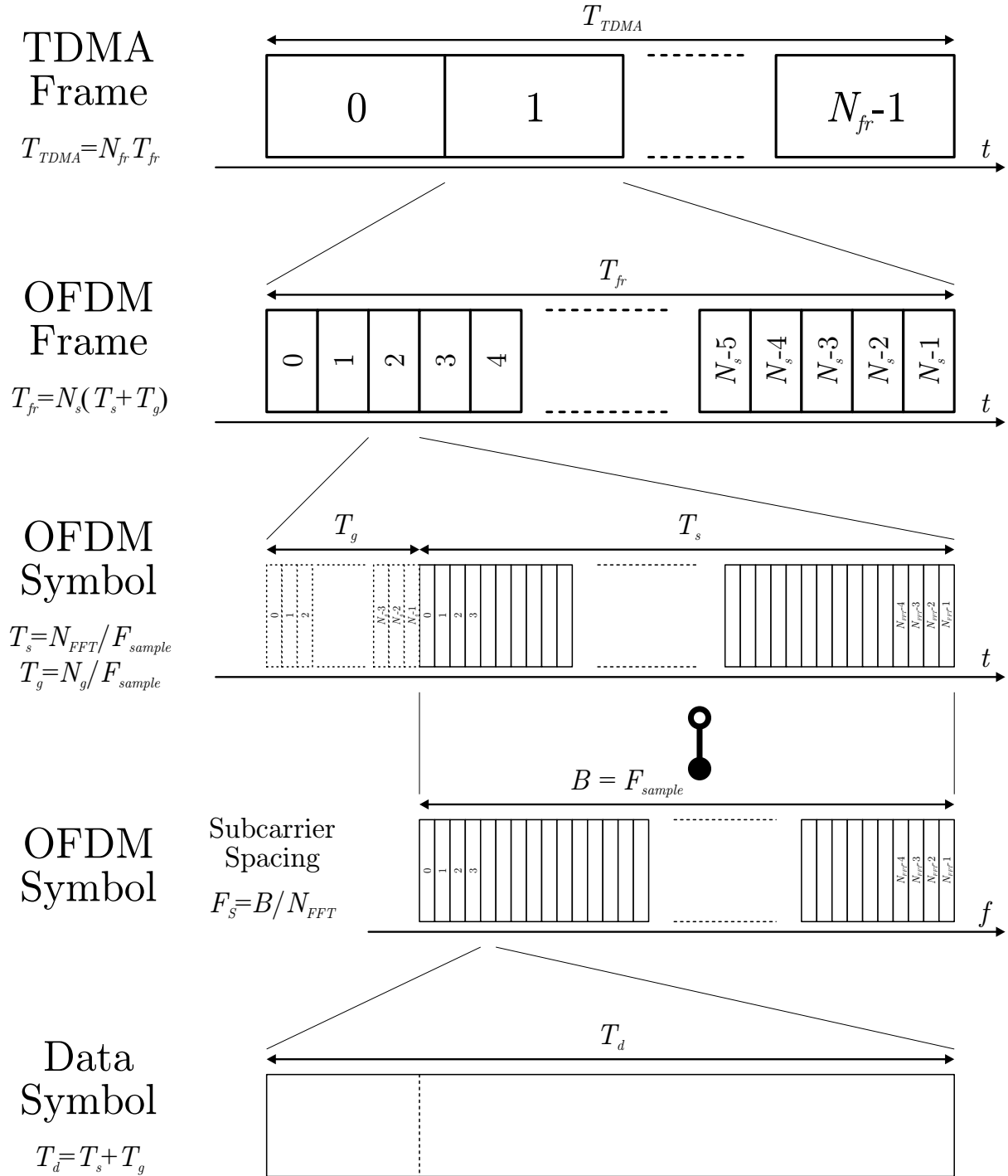


Figure 6.1: OFDM/TDMA frame structure

consists of  $N_{fr}$  slots. Each slot with duration

$$T_{fr} = N_s \cdot T'_s = N_s \cdot (T_s + T_g) \tag{6.2}$$

consists of an OFDM frame with  $N_s$  OFDM symbols. The duration of one OFDM symbol is

$$T'_s = (N_{FFT} + N_g) \cdot \frac{1}{F_{sample}}, \tag{6.3}$$

assuming that an IFFT/FFT with  $N_c = N_{FFT}$  is used for the multi-carrier modulation/demodulation. The effective bandwidth of the corresponding OFDM symbol frequency domain representation is

$$B = F_{sample} , \quad (6.4)$$

with a subcarrier spacing of

$$F_s = \frac{B}{N_{FFT}} = \frac{1}{T_s} \quad (6.5)$$

The resulting effective symbol rate for the data symbols in one subcarrier is

$$R_d = \frac{1}{T_d} = \frac{1}{T'_s} = \frac{B}{N_{FFT} + N_g} . \quad (6.6)$$

Further necessary parameters are the number of subcarriers that are used  $N'_c$ , including the 0 Hz subcarrier, and the first subcarrier that is used  $l'_{start}$ . For the example of Fig. 5.32 these values are  $N_g = 5$ ,  $N'_c = 113$  and  $l'_{start} = 7$ .

It can be concluded that by defining the parameter structure consisting of the elements

$$[N_{fr}, N_s, N_{FFT}, N_g, N'_c, l'_{start}, F_{sample}] \quad (6.7)$$

the OFDM/TDMA frame is completely defined.

Note that single-carrier and spread-spectrum modulation are included in this definition as well for the special case with  $N_{FFT} = 1$ ,  $N_g = 0$ ,  $N'_c = 1$  and  $l'_{start} = 0$ . For single-carrier modulation  $N_s$  has to be set to the length of one TDMA data burst and  $F_{sample} = F_{ov}$ . For spread-spectrum modulation  $N_s$  is equal to a multiple of  $L$  and  $F_{sample} = 1/T_{chip}$ .

### 6.1.2 Estimation and Equalization Parameters

For the case that coherent modulation with coherent detection is used, some additional parameters, already introduced in previous chapters, have to be defined for the estimation, interpolation and equalization process. They are by name the pilot distances in direction of frequency  $N_f$  and time  $N_t$ , the number of used filter taps for interpolation  $N_{tap}$  and the interpolation type, e.g. linear or si. If different pilot symbol values should be used in all pilot symbol positions, it is necessary to define a list of  $N_{pilot}$  complex I/Q values  $\vec{X}_{pilot}$ .

The resulting parameter structure consists of the elements

$$[N_f, N_t, N_{tap}, \{\text{linear, si}\}, \vec{X}_{pilot}] . \quad (6.8)$$

For the example system the values are  $N_f = 7$ ,  $N_t = 3$ ,  $N_{tap} = 5$ , *linear* and all pilot symbols are equal, i.e.  $X_{pilot} = (\text{constant}, 0.0)$ .

### 6.1.3 Synchronization Parameters

The synchronization symbol parameters need to be defined as well. Each of the  $N_{sync}$  synchronization symbols consist of  $N_c$  complex I/Q values  $\vec{\mathbf{X}}_{sync}$ . The positions  $k_{sync}$  of each synchronization symbol are also specified.

The resulting parameter structure consists of the elements

$$\left[ N_{sync}, \vec{\mathbf{X}}_{sync,0}, \dots, \vec{\mathbf{X}}_{sync,(N_{sync}-1)}, k_{sync,0}, \dots, k_{sync,(N_{sync}-1)} \right]. \quad (6.9)$$

For the example system the values are  $N_{sync} = 2$ ,  $k_{sync,0} = 1$  and  $k_{sync,1} = 2$ .

### 6.1.4 MC-CDMA Parameters

The coherent MC-CDMA parameters are treated as follows. The spreading code length  $L$  is linked with the spreading chip distance  $D_{chip}$ . Furthermore, the number of spreading groups  $M \cdot Q$  and the first carrier for each spreading group  $l'_{start,mq}$  needs to be defined, resulting in the implementation of the simple parameter structure shown in the bottom part of Fig. 5.32 with the elements

$$\left[ L, D_{chip}, M \cdot Q, l'_{start,0}, \dots, l'_{start,(M \cdot Q - 1)} \right]. \quad (6.10)$$

The values for the example system are  $L = 8$ ,  $D_{chip} = 14$ ,  $M \cdot Q = 11$  and  $l'_{start,0}, \dots, l'_{start,10} = (9, 16, 10, 17, 11, 18, 12, 19, 13, 20, 15)$ .

An even more sophisticated solution is obtained by indexing each position in the OFDM frame from  $0 \dots (N_s \cdot N_{FFT} - 1)$  despite of indexing only the positions within the OFDM symbol. That way, not only additional groups in OFDM symbols without pilot symbols can be defined, but also the chip positions of one group can be adapted individually for a more beneficial frame allocation.

### 6.1.5 Digital Programmable Filters

So far, only parameter structures for the software part of a communications system have been defined, but there are additional components in the signal path after the D/A-conversion on the transmitter side and in front of A/D-conversion on the receiver side that need to be considered as well. One group of these components are filters for the lowpass area.

If a SDR should be capable to not only transmit one signal with a specific bandwidth  $B$ , it is necessary to adapt the sampling frequency  $F_{sample}$  as well as the corresponding lowpass filters. Recent integrated filter circuits often offer the possibility to adjust the filter characteristic with a minimum of external components, e.g. only one additional resistor, over a wide range of frequencies [LTC98]. This offers the possibility to adjust the desired filter frequency with a network of different resistors that can be digitally switched. Even more sophisticated solutions

already have an IEEE 1149.1 JTAG serial port interface that offers the possibility of In-System Programming (ISP) and configuration of several filters/components with only one serial bus [LAT00]. The drawback of the ISP analog circuit is that the filter is only of 5th order, whereas the resistor-adjustable filter has 10th order.

### 6.1.6 RF Components

The higher the frequency gets in the signal path, i.e. in the IF and RF area, the more complex an adjustable system gets. If different carrier frequencies  $f_c$  are about to be used in the SDR and the bandwidth  $B$  of the different configurations are not too different, it is possible to use the same Intermediate Frequency (IF) area, e.g. 70 MHz, with the same filtering and amplifying components. SDRs with different Radio Frequency (RF) areas are highly difficult to implement due to the critical restrictions on the Power Amplifier (PA), filters, antennas or the Automatic Gain Control (AGC). SDRs with such structures will in most cases need to have separate implementations for the RF part.

### 6.1.7 Protocol Interface Structure

The connection of components from layers above the data link and physical layer needs to be considered as well. Declarations have to be done about the number of virtual channels and the number of bits in each packet per channel available to the protocol layers. In the example of Fig. 5.32, the number of virtual channels is equal to  $L = 8$  and the number of bits for each channel is equal to  $(N_s - 3) \cdot 11 \cdot 2 = 550$ , assuming that a virtual channel uses all spreading groups. It is the task of the protocol structure to multiplex one or several of the virtual channels to user or broadcast channels in correspondence with the required bit rates.

Even though most components can be defined by parameter sets as shown above, it remains an open question how fast a software-defined radio really can be switched from one configuration into another one. Example C-code header-files for a SDR MC-CDMA system, like used in the DSP demonstrator, are shown in Appendix D.

## 6.2 DSP-System

### 6.2.1 TARMAC ADL Demonstrator System Structure

Besides the aim to have a flexible and adaptable OFDM system for research activities, the demonstrator system is designed for the Taxi And Ramp Management And Control (TARMAC) project at the German Aerospace Center (DLR).

The air traffic on and around airports will continuously increase in the next years and will possibly be doubled in 2015. Since especially the airports have been identified as a bottleneck in air traffic handling, it is necessary to increase the efficiency and thus the throughput in the air and on the ground to meet the capacity requirements of the future. The project TARMAC is the DLR's contribution to the Advanced Surface Movement Guidance and Control System (A-SMGCS) and not only incorporates the communication link between the ground system and aircrafts or other vehicles, but also a sensor and planning system for improved situation awareness and traffic handling.

Existing aeronautical communications systems like the Global Positioning and Communication (GP&C) system are not capable to handle the additional communication load needed for an efficient A-SMGCS operation. Therefore, the development and implementation of a new Advanced Data Link (ADL) for operation within the airport and its surrounding area is necessary. The final system should be capable of handling at least 100 connected users simultaneously with a bit rate of 128 kbit/s per user. The demonstrator implementation has a restricted throughput, whereas the physical conditions implied on the system by the transmission channel remain the same.

The outline of the TARMAC ADL DSP demonstrator communications system is shown in Fig. 6.2. Due to a restricted hardware complexity, only the ground-air link is implemented in DSP hardware in the demonstrator system. This is sufficient for testing the OFDM transmission with different configurations and estimating the BER performance in different environmental conditions. The components of the ground-air link are as follows:

- A SUN UNIX host workstation on the transmitter and receiver side with the DSP C-Compiler and the necessary programs and drivers for downloading the built applications to the DSP system.
- An SBUS to VME-bus set of interface cards in the workstations and the VME-racks for program and data exchange.
- Two DSP processor cards with a total of four Texas Instruments TMS320C40 floating point processors [TMS96] and a dual-channel 16-bit D/A-converter board on the transmitter side.
- Two DSP processor cards with a total of six TMS320C40 floating point processors and an eight-channel 12-bit A/D-converter board on the receiver side.
- The necessary hardware for mixing the lowpass I/Q-signal to and from the 5 GHz RF band with a 70 MHz IF band. This hardware includes lowpass filtering, 70 MHz modulation/demodulation, 5 GHz modulation/demodulation, several bandpass filtering stages, power amplification, automatic gain control and the transmitter and receiver antennas.

The transmitter is mounted in a fixed position on the ground, whereas the receiver can be installed in a test vehicle or aircraft. Since the TARMAC project also includes an interactive pilot

airborne display, a reverse air-ground link and a corresponding protocol and interface structure is necessary. The information on the reverse link is limited to operational acknowledges from the pilot and technical acknowledges for the protocol. Therefore, the existing GP&C aeronautical VHF modem is used for this link [GPC97]. The transmitter-side workstation is used as the Ground Data Router (GDR) to forward the information that is to be transmitted to the ADL DSP system and receive operational and technical acknowledges from the GP&C modem, where the technical acknowledges are forwarded to the ADL Protocol (ADLP) in the DSP system. The receiver side workstation is used as the On-board Data Router (ODR) that gets the received information and the technical acknowledges of the ADLP from the DSP system and forwards the technical acknowledges to the GP&C modem. The implemented ADLP is based on the Radio Link Protocol (RLP), where a maximum block of length  $200 \cdot 63 = 12600$  data bits can be transmitted. Each 200 bit packet has its own acknowledge and if no acknowledge has been received after a certain period, the corresponding packet is retransmitted for a configurable number of times.

The GDR gets the information, that is to be transmitted via the ADL, from the ground system via a Common Object Request Broker Architecture (CORBA) Event Channel (CEC) on a TCP/IP connection and splits it in suitable blocks for the ADLP. On the receiver side, the information is reassembled and forwarded on another CEC to the airborne pilot display system. Operational acknowledges from the airborne system are forwarded through the chain ODR-GP&C-GDR to the ground system with two more CECs.

## 6.2.2 Multiprocessor System Structure

Each of the TMS320C40 processors has its own memory and is located on a carrier board with VME-bus and JTAG interfaces. Communication and data exchange between processors is done by using one of the six processor's COMM ports. The wiring between the processors, processor boards and the connection to the D/A-converter and host system for the transmitter system is shown in Fig. 6.3. The two DSP carrier boards are Loughborough Sound Images (LSI) DBV42's [LSI94]. The D/A-board is a LSI DB212B [LSI95b].

A similar structure applies for the receiver system. This time the additional Pentland VGX A/D-converter is connected [PEN98] and the six processors require the use of a different DSP carrier board, i.e. LSI DBV44 [LSI95a]. For display purposes on an oscilloscope, a DB212B D/A-converter is also connected. The whole receiver DSP system is shown in Fig. 6.4.

The different operations necessary in an OFDM system, like for example FFT/IFFT transformation or channel estimation with equalization, can be divided into different tasks. These tasks are then distributed on the different processors to obtain an equal load sharing between the processors. For this purpose it is necessary that the different tasks exchange data via the COMM ports. Hand-programming of the processor communication, distributing the tasks on the different processors and starting all tasks simultaneously is a difficult operation. Therefore,

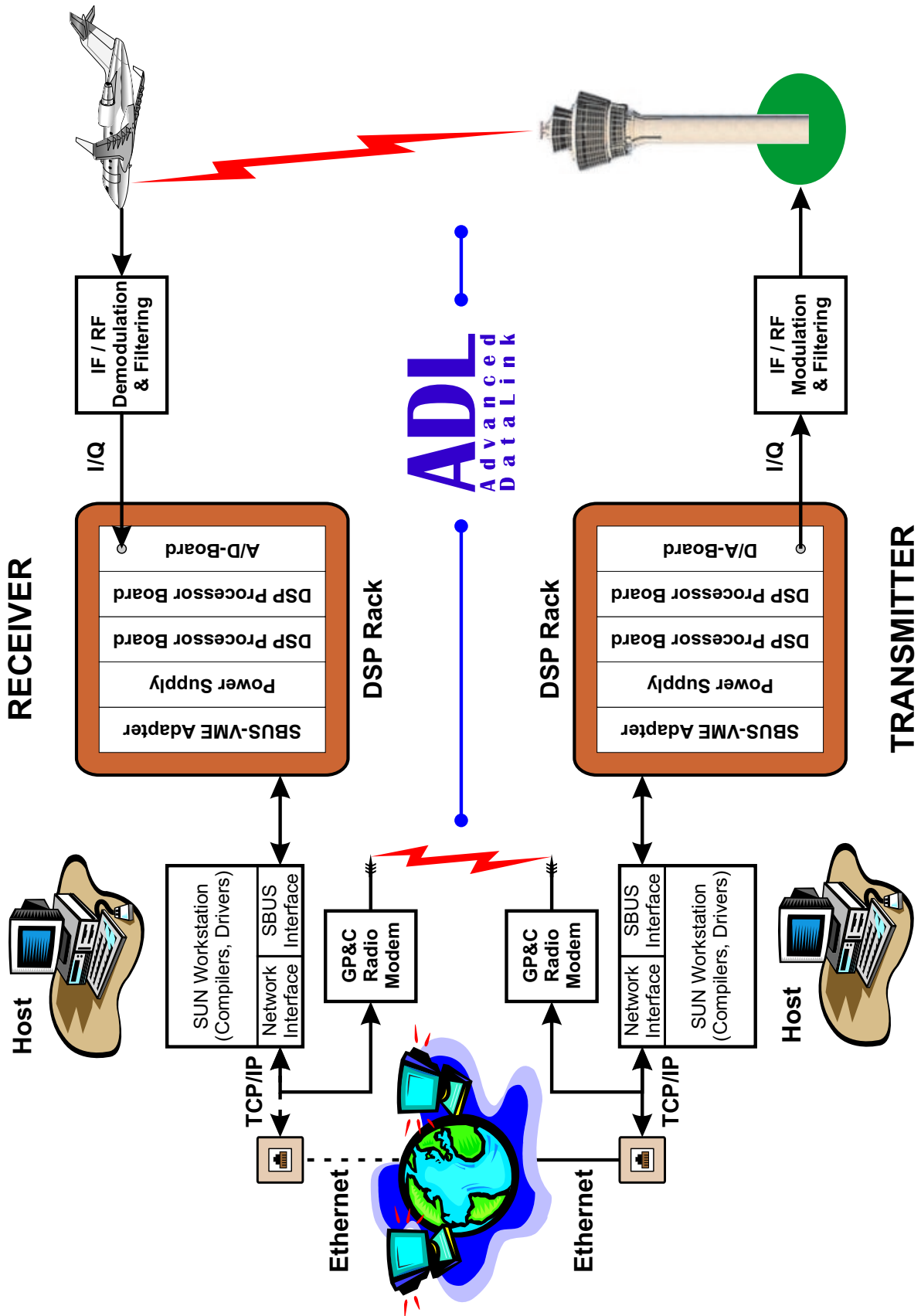


Figure 6.2: TARMAC ADL demonstrator communications system structure

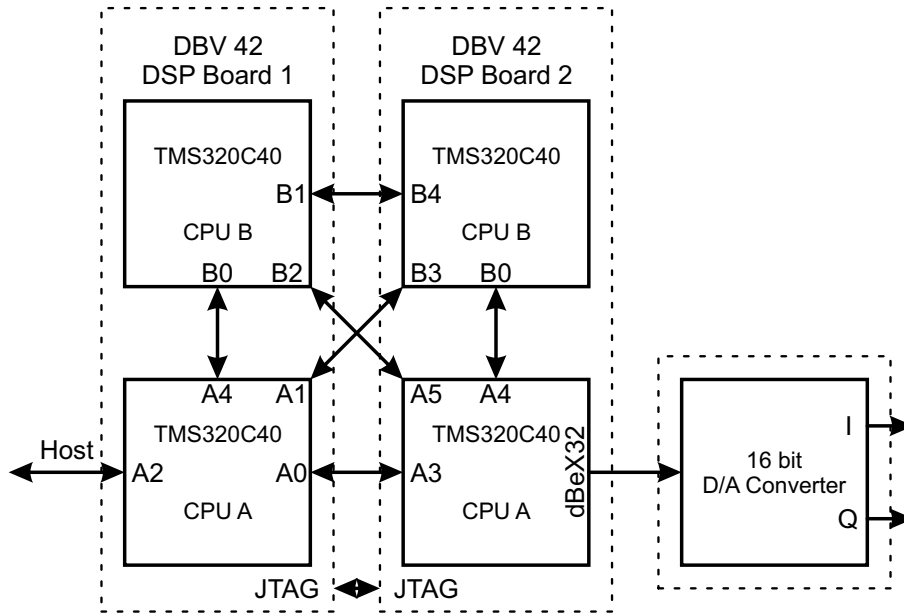


Figure 6.3: Transmitter DSP system structure

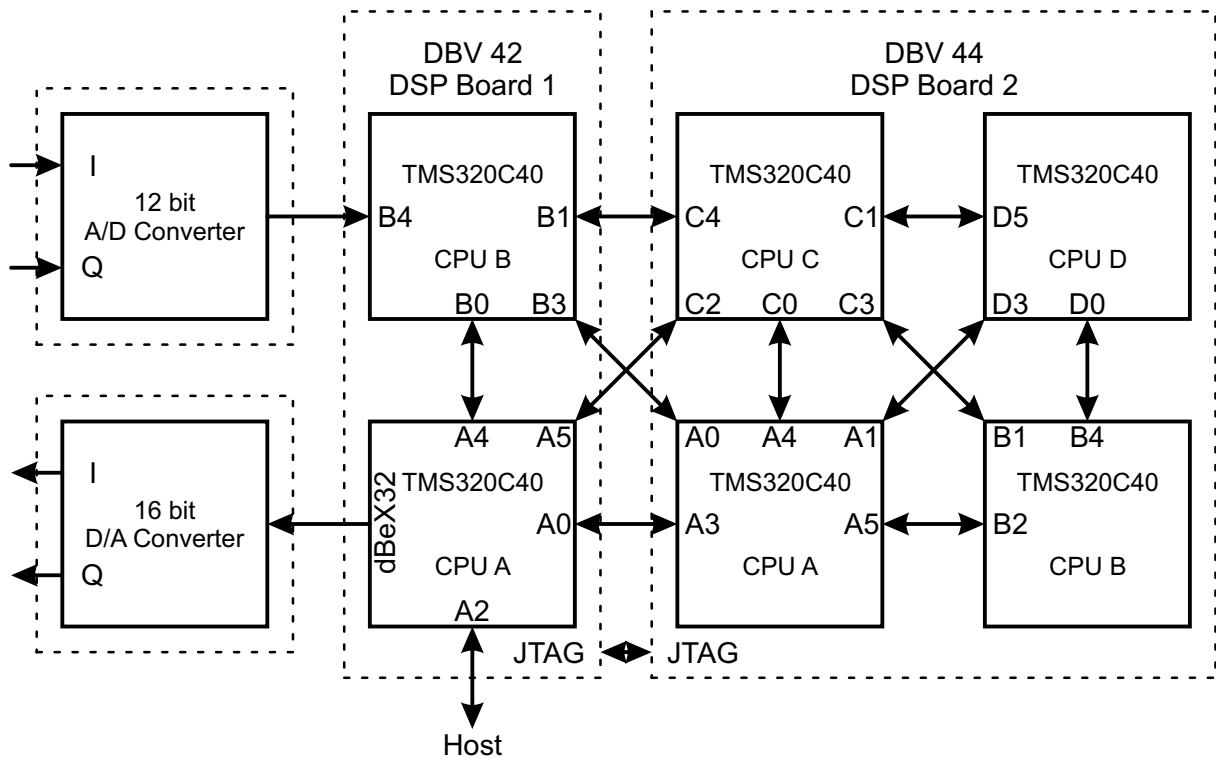


Figure 6.4: Receiver DSP system structure

the special 3L Parallel C-compiler is used which offers some add-ons to the standard C-compiler that handle these jobs [3LL]. It is possible to specify the wiring between the processors, to place one or several tasks on one processor and to download and run an application consisting of several tasks on several processors onto the DSP system. Terminal output and file input/output on the host system is possible, too. The whole application is run in a sort of real-time operating

system using an OSI layer model for internal communication and data exchange.

The overall processor and task layout for the ADL OFDM demonstrator system is shown in Fig. 6.5. Solid boxes in the upper and lower part indicate the use of one processor, whereas dotted boxes indicate several tasks on one processor. The transmitter DSP system is divided as follows:

- The *sun driver gdr* and *adlp gdr* tasks contain the ADLP and the interface to the GDR for one user.
- The *ofdm mc-cdma generator* contains the OFDM frame generation with a definable number of pseudo users that can be added for testing purposes. Additionally, the pilot symbols and synchronization symbols are appended to the frame.
- The *ofdm ifft* contains appropriate carrier reordering as mentioned in Section 3.2.3 and IFFT transformation of the OFDM subcarriers.
- The *ofdm driver* adds the guard interval and has some additional features for TDMA mode operation. It sets up and communicates with the D/A-board via a 32-bit interface.

Between the transmitter and the receiver, influences from the transmitter and receiver LP/IF/RF hardware and the transmission channel itself have to be taken into account. The receiver DSP system, using the modified Schmidl and Cox synchronization algorithm from Sections 4.5.4.1 and 4.5.5 with oversampling and offset-free metric averaging, is divided as follows:

- The *ofdm sync 1* task gets the received samples from the A/D-converter. The A/D-board is set up via the VME-bus, whereas the data is transferred via a faster COMM-port. Furthermore, this task finds the optimum OFDM symbol/frame timing.
- In the *ofdm sync 2* task, the fractional carrier frequency offset of the two synchronization symbols is corrected and they are FFT-transformed. The integer part of the frequency offset is found and, together with the fractional part, is forwarded to the *ofdm frc correction* and *ofdm int correction* tasks respectively.
- The *ofdm frc correction* task performs the fractional carrier frequency offset correction for all remaining OFDM symbols of the frame in software.
- The *ofdm fft sync* task transforms the corrected values back to the frequency domain with an FFT.
- The *ofdm int correction* task finally does a cyclic shift of the subcarriers to correct the integer frequency offset.
- Channel estimation and equalization with selectable parameters, i.e. si/linear-interpolation and MRC/ZF-equalization, is implemented in the *ofdm estimation* task.

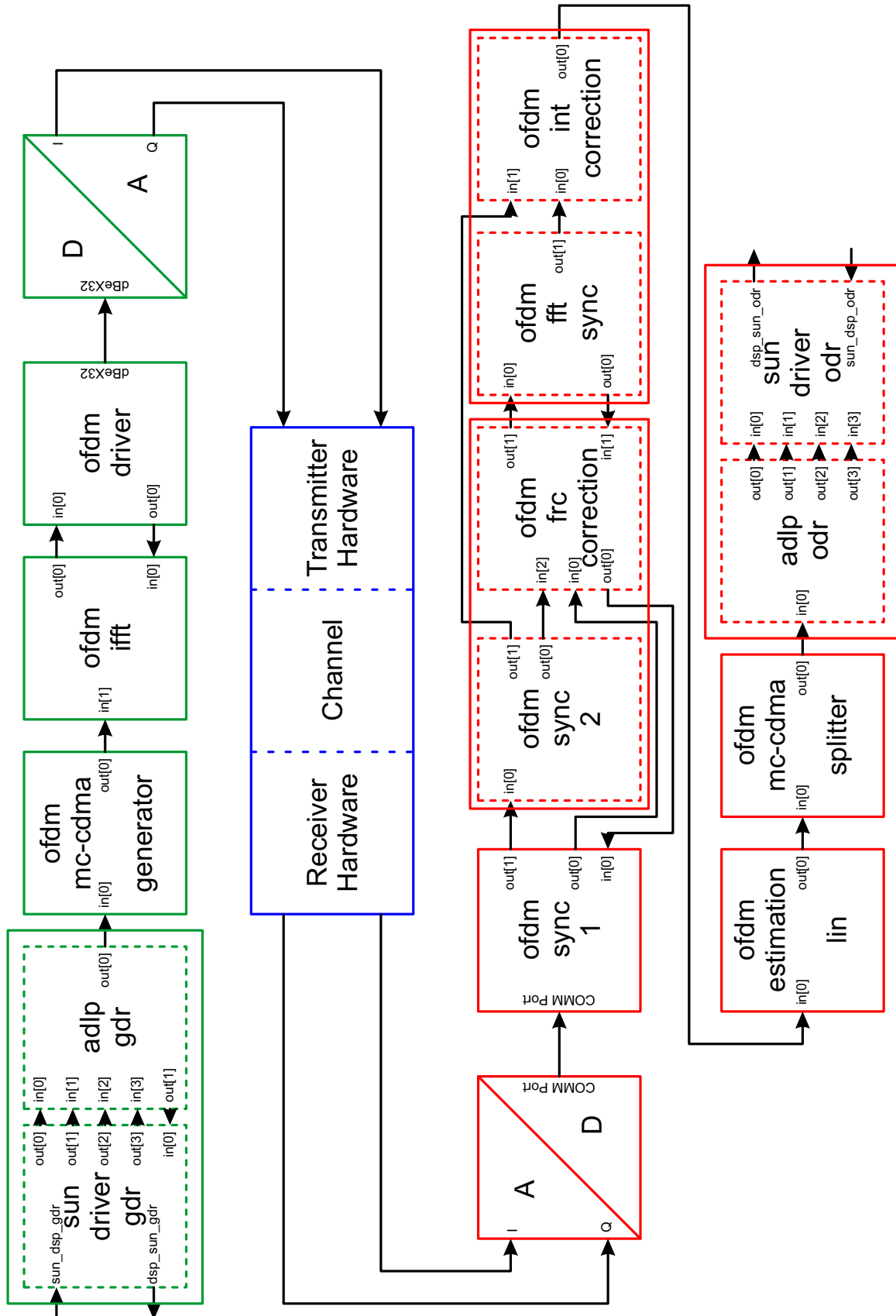


Figure 6.5: Tasks and processor layout for OFDM ADL demonstrator system

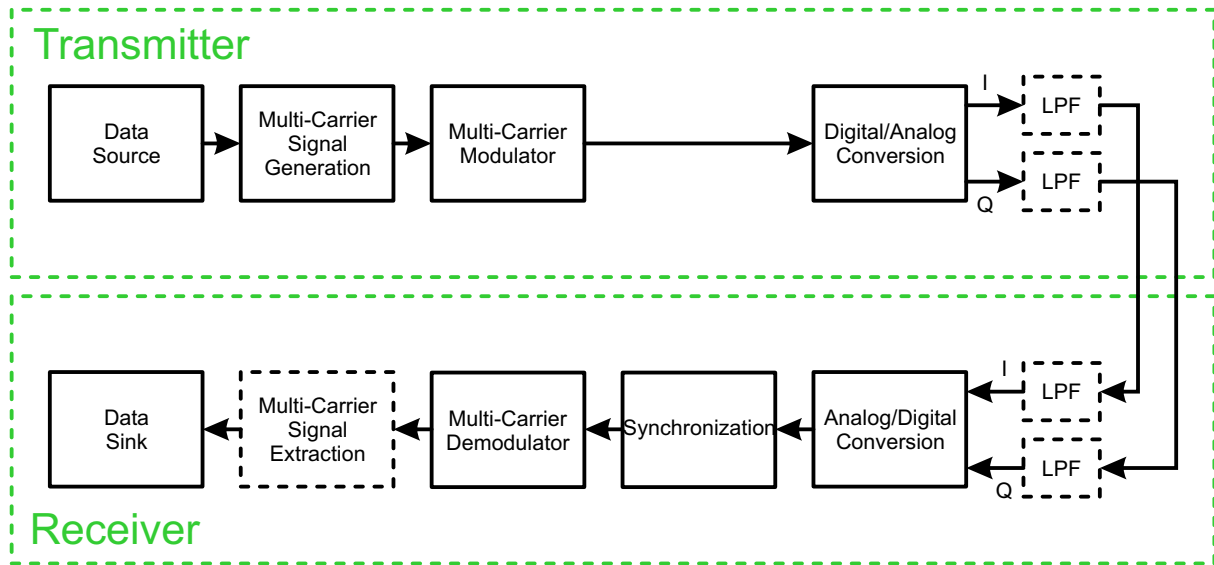


Figure 6.6: OFDM demonstrator set-up for lowpass area test

- The *ofdm mc-cdma splitter* task despreads and extracts the binary data stream.
- The *adlp odr* and *sun driver odr* tasks include the receiver side implementation of the ADLP protocol and interface to the ODR for one user.

The binary data stream interface for one user between the ADLP and the MC-CDMA generator/splitter is defined to be  $240 + 6 = 246$  bit, including six zero-stuffing tail-bits. This is related to a possible channel encoder/decoder that can be included in the MC-CDMA generator/splitter tasks or in separate external tasks if a high computational load is involved in the encoding/decoding process. The necessary code is expected to be a memory six terminated convolutional code with rate  $R = 1/2$ . The resulting number of codeword bits is  $2 \cdot 246 = 492$  bit. Using only the spreading groups  $0 \dots 9$  from the coherent demonstrator frame in Fig. 5.32, which offer  $10 \cdot 2 = 20$  bit per spreading sequence, the total number of  $25 \cdot 10 \cdot 2 = 500$  bit for each spreading sequence is available in the OFDM frame. Herewith, the number of data symbols per user and OFDM symbol is chosen to be  $M = 10$  and the number of user groups per OFDM symbol is chosen to be  $Q = 1$ . Comparing the available 500 bit to the used 492 bit, the last 4 groups in the last OFDM symbol of each frame remain unused in the demonstrator system for coherent MC-CDMA.

### 6.2.3 I/Q Lowpass Area Adaptation

In the following, aspects and difficulties that occur during the implementation of the OFDM hardware part, starting from D/A- and A/D-conversion, are investigated. First, a look is taken at the lowpass I/Q-area adaption. The system structure used for these investigations is shown in Fig. 6.6.

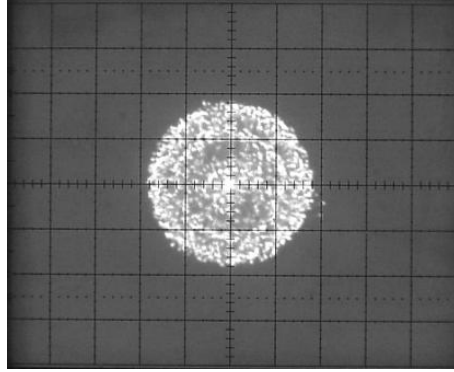


Figure 6.7: I/Q-constellation of received OFDM signal with inaccurate timing synchronization

Starting with a binary data source, a consecutive number of OFDM frames is generated in the MC signal generator. These frames could either contain MC-CDMA modulated or DQPSK modulated information, compare Fig. 5.32 and Fig. 5.33. The corresponding OFDM symbols are then IFFT-transformed to the time domain in the MC modulator and the guard interval is added. Optional LowPass Filters (LPFs) and  $50 \Omega$  line driving stages after the D/A-conversion can be included before the I/Q-signals are passed on to the receiver side with optional LPFs and A/D-conversion. In the aforementioned synchronization stage, the guard intervals are removed and the OFDM frames are timing and carrier frequency synchronized. The time domain representations of the OFDM symbols are then forwarded to the MC demodulator for FFT transformation.

Considering the fact that BER performances are to be evaluated or the system is to be tested with the ADLP, the next stage is MC-CDMA or DQPSK signal extraction followed by a binary data sink. Alternatively, the signal extraction and binary data sink can be replaced with special purpose visualization tasks that offer the possibility to look at the I/Q-constellation diagram or amplitude and phase distributions of the received subcarriers with the help of a D/A-converter and an oscilloscope.

### 6.2.3.1 Synchronization

The effects that are to be considered first, are timing synchronization offsets resulting in ISI. No LPFs are used at the moment. The effects of a mismatch in the OFDM symbol/frame timing on the subcarrier I/Q-constellations are shown in Fig. 6.7. All subcarriers of several OFDM frames are multiplexed on the oscilloscope, where the I-part is the horizontal axis and the Q-part is the vertical axis. The higher the ISI, the more the constellation looks like random noise.

With accurate timing at the end of the guard interval, the constellation diagram of the subcarriers looks like the one shown in Fig. 6.8, where DQPSK has been used. The eight positions instead of four result from a  $\pi/4$  shift for each differential modulation step by using the constellation of Fig. 5.1. The two constellation positions closer to the center are synchronization

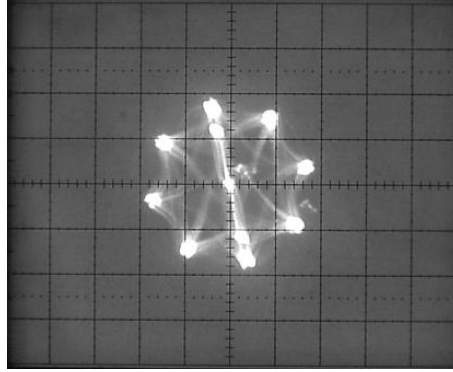


Figure 6.8: I/Q-constellation of received OFDM signal with accurate timing synchronization using DQPSK-modulated subcarriers

symbols, where the amplitude has been chosen lower than the amplitude of the data symbols for testing purposes.

Additionally, the maximum carrier frequency shift  $\Delta f_{c_{max}}$  from one OFDM frame to the next OFDM frame using the maximum Doppler rate from (5.2) and the OFDM frame duration from (6.2) and Tables 5.3/5.4 is

$$\Delta f_{c_{max}} = T_{fr} \cdot f'_{D_{max}} = -24.4 \text{ Hz} . \quad (6.11)$$

This is less than 1% of the subcarrier spacing  $F_s$ . Using the results of Fig. 5.14 and Fig. 5.28, it can be concluded that this offset has a minor influence on the system performance, so that it only has to be ensured that the carrier frequency offset estimation and correction is working for each OFDM frame without supplementary alignments within the frame. Since carrier frequency offsets are not possible in the lowpass area, carrier frequency synchronization is considered ideal for the lowpass area adaption, i.e. it is disabled.

### 6.2.3.2 Transmitter/Receiver Filter

In the next step, the influence of transmitter and receiver LPFs is investigated. For comparison, a look is taken at the system without additional filtering first. The corresponding spectrum for coherent MC-CDMA with one active user is shown in Fig. 6.9. It has been generated by using an I/Q-modulator for the 70 MHz IF band. The displayed frequency span is 2.5 MHz, so that the desired spectrum is approximately in the two center columns of the spectrum analysis. The continuing spectra on both sides are images of the original spectrum, compare Fig. 3.4(c)+(d). It is also possible to identify the unused subcarriers on both sides of the desired spectrum and their images.

Even more important are the amplitude  $a$  and phase  $\varphi$  distributions of the received subcarriers after FFT transformation. They are displayed in Fig. 6.10(a). Note that instead of the amplitude  $a$ , the squared amplitude  $a^2$  is shown. Again OFDM symbols of several OFDM frames are displayed. Constructive adding of the desired spectrum and its images, induced by the

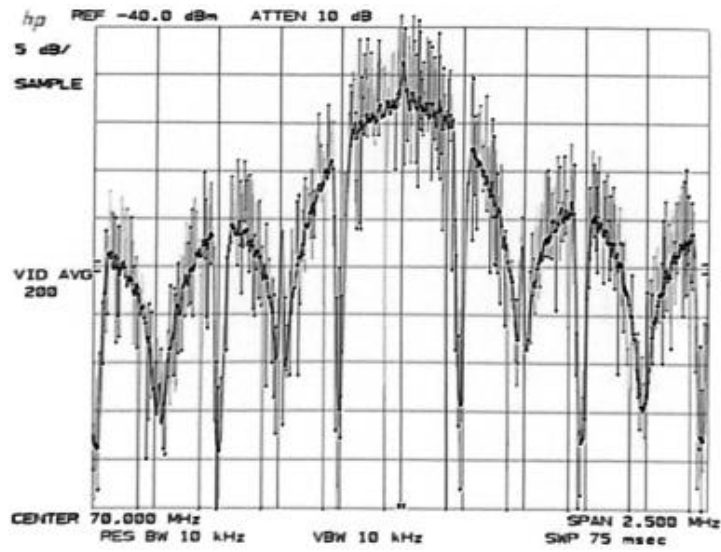
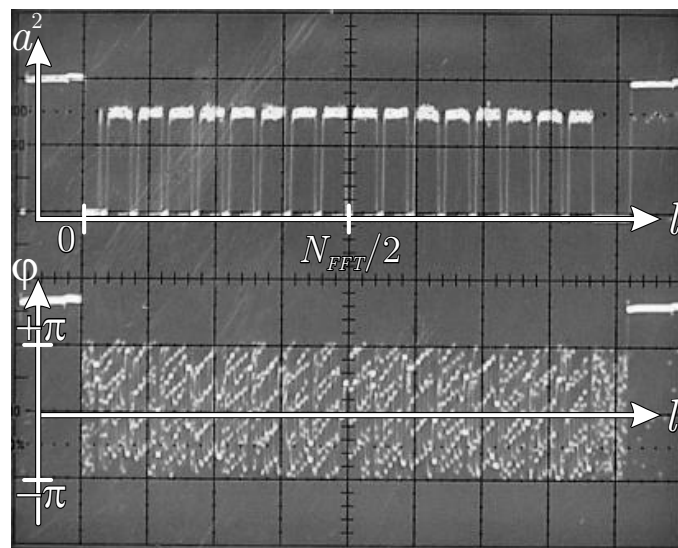
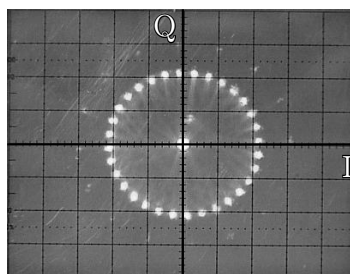


Figure 6.9: MC-CDMA demonstrator subcarrier spectrum without filtering



(a)



(b)

Figure 6.10: MC-CDMA demonstrator received subcarrier squared amplitudes and phases (a) and I/Q-constellation (b) without filtering and no equalization

D/A-conversion, leads to an equal amplitude distribution on all subcarriers. The increasing phase shift with increasing subcarrier index is related to the fact that in the excess-delay-free case, the ideal timing point is estimated in the center of the guard interval leading to a cyclic shift of the samples in the time domain, i.e. an increasing phase shift in the frequency domain.

Fig. 6.10(b) displays the corresponding I/Q-constellation. It is observed that all received symbols are located on a circle with only minimum variations in amplitude. The I/Q-positions outside the main circle are from the first synchronization symbol.

**Elliptic 5th Order Lowpass Filter - Fixed** The situation changes as soon as lowpass filtering, currently only on the transmitter side, is introduced. To avoid high frequency oscillation on the edges of the rectangular D/A-pulses, the connection between the D/A-outputs and the filter inputs has to be compensated with a simple RC lowpass element. The resulting spectrum, using the Linear Technology 500 kHz elliptic 5th order lowpass filter LTC 1560 [LTC97], is shown in Fig. 6.11. Looking at the received subcarriers squared amplitude and phase distributions in Fig. 6.12(a), only a minor amplitude loss is observed in the center of the subcarrier spectrum. The I/Q-constellation diagram of Fig. 6.12(b) shows no palpable loss. Nevertheless, the occupied bandwidth of approximately 1 MHz is still too inefficient compared to the real signal bandwidth.

**Root Raised Cosine 10th Order Lowpass Filter - Resistor Adjustable** Further reduction of the filter bandwidth by using the resistor-tunable Linear Technology Root Raised Cosine (RRC) 10th order lowpass filter LTC 1569 [LTC98] with a set cutoff frequency of  $f_g = 251$  kHz leads to the transmitted spectrum of Fig. 6.13. The frequency span of the analysis plot is reduced to 1 MHz with the desired spectrum now being in approximately the five central columns. Some small parts of the images close to the desired spectrum remain, whereas all other images are missing. Due to the cutoff frequency being close to the maximum used subcarrier frequency of  $\sim 219$  kHz, the subcarriers close to the edges of the desired spectrum are also attenuated. This becomes more obvious by looking at the squared amplitude distribution of the received subcarriers in Fig. 6.14(a). Furthermore, frequency-dependent amplitude variations on subcarrier level are observed. These variations are related to a mismatch of the filter bandwidths in the I- and Q-channel of the LPFs. Depending on the fact whether the data symbol contains information in the I- and/or Q-channel, the received subcarrier amplitude varies, which is an unwanted effect that has to be compensated by aligning the LPF bandwidths. In the constellation diagram of Fig. 6.14(b) the symbols have strong amplitude variations and no longer can be considered to be located on a circle. These variations are not desired since they signify that the subcarriers are unequally protected against noise on the channel and cause problems for coherent MC-CDMA, since the orthogonality of the spreading sequences is partially lost. If only PSK or DPSK symbols are transmitted on the subcarriers, the unequal protection remains, but since the information is in the phase alone, adequate results still will be obtainable.

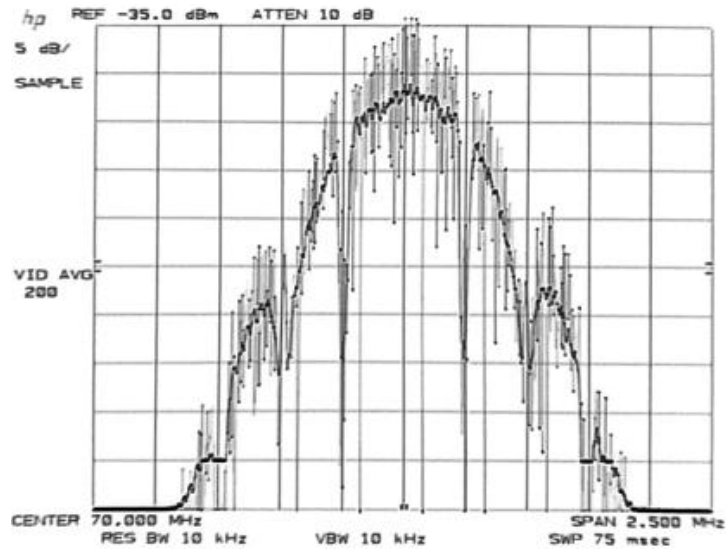
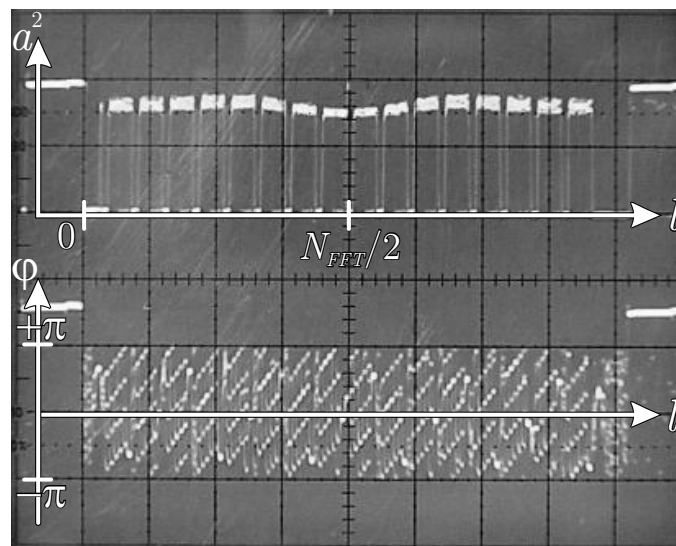
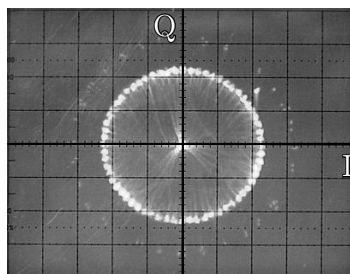


Figure 6.11: MC-CDMA demonstrator subcarrier spectrum with  $f_g = 500$  kHz elliptic 5th order LP filter



(a)



(b)

Figure 6.12: MC-CDMA demonstrator received subcarrier squared amplitudes and phases (a) and I/Q-constellation (b) with  $f_g = 500$  kHz elliptic 5th order LP filter and no equalization

**Subcarrier Amplitude  $\text{si}(x)$  Pre-compensation** In the following, it is attempted to get rid of the unequal protection and amplitude variations by pre-compensation of the subcarriers in the MC-modulator of the transmitter. In Section 3.2.3.3, a method has been introduced to compensate the  $\text{si}(x)$  spectral shaping due to the rectangular pulses of the D/A-converter. This is implemented first. The resulting transmitted spectrum is shown in Fig. 6.15. Each subcarrier is amplified with its corresponding real-valued factor so that the edges of the desired spectrum are boosted. It has to be noted though, that the remains of the undesired images are boosted, too. The change in the subcarrier amplitudes is palpable in Fig. 6.16(a) and the distribution of the symbols in the I/Q-diagram of Fig. 6.16(b), where the variance of the circle has decreased.

**Channel Estimation, Interpolation and Equalization** In the coherent MC-CDMA system it is essential that the absolute phase and amplitude of each subcarrier is restored. The multiplexed pilot symbols are used now to estimate and equalize the phase shifts caused by the ISI-free timing offset. First, linear interpolation with MRC equalization is applied to the received subcarriers of Fig. 6.16. The results are shown in Fig. 6.17. It is observed that large amplitude incursions occur in between the pilot symbols at the positions in which the channel is estimated. This behaviour is explained by Fig. 6.18. If a large phase difference occurs between the pilot symbols, due to an increasing phase shift of the subcarriers, the linear interpolation between two pilot symbols (1) and (2) comes close to the zero crossing point and the amplitudes of the data subcarrier positions collapse. The four QPSK constellation positions in Fig. 6.17(b) are clearly visible after the channel equalization, but have a large variance. The symbols that are located on the positive I-axis are the equalized pilot symbols. With two-times pilot symbol oversampling and without additional phase rotations, a maximum phase shift of  $\pm 90^\circ$  in between pilot symbols is guaranteed, so that linear interpolation will cause no unacceptable amplitude incursions.

The situation changes when  $\text{si}(x)$  interpolation is used. Now the shortening of the  $\text{si}(x)$ -function leads to overdriven subcarrier amplitudes as displayed in Fig. 6.19. The variance of the constellation positions decreases in that case.

**Subcarrier Amplitude Pre-compensation Using Estimated Amplitudes** The preceding evaluations have shown that the subcarrier amplitudes are sensitive to filtering and interpolation distortions. Amplitude distortions beside the interpolation effects are only partially improved by  $\text{si}(x)$  pre-compensation.

It is now investigated whether a more sophisticated amplitude pre-compensation scheme, using estimation of the received subcarrier amplitudes, can further improve the situation. For this purpose, the in-system programmable analog 5th order lowpass filtering circuit ispPAC80 is applied [LAT00], which is configured to implement 5th order elliptic lowpass filtering with a cutoff frequency of  $f_g = 241$  kHz. Elliptic filtering is chosen since the attenuation of this filter type in the stopband is much steeper compared to Bessel, Butterworth or Chebychev filtering.

Instead of MC-CDMA, simple OFDM QPSK is used on all subcarriers for visualization and estimation purposes. The resulting spectrum is shown in Fig. 6.20 with the corresponding received subcarrier amplitudes, phases and I/Q-constellation, given in Fig. 6.21. Phase bending on both ends of the subcarrier spectrum due to the chosen filter type is visible in Fig. 6.21(a).

Using  $\text{si}(x)$  subcarrier pre-compensation almost solves the unequal amplitude distribution as can be concluded from Fig. 6.22 and Fig. 6.23. Only the subcarriers close to both ends of the spectrum are overdriven. This could be avoided by further reducing the cutoff frequency, but that on the other hand would result in undesirable increased phase bending. Again amplitude variations, this time frequency-independent, are observed on subcarrier level in Fig. 6.23(a). They are related to a DC amplifier-gain mismatch in the I- and Q-channel that has to be compensated as well.

By measuring and averaging the received subcarrier amplitudes, it is possible to calculate an individually optimized pre-compensation factor for each subcarrier. This is done below for the received subcarrier amplitudes of Fig. 6.21(a). The new resulting spectrum is displayed in Fig. 6.24 with its receiver side amplitude and phase distributions, see Fig. 6.25(a). The amplitude variance of the constellation circle in Fig. 6.25(b) is reduced.

Further optimization of the filter bandwidth, correction of DC-offsets and DC-gain mismatches and introduction of LPFs on the transmitter and receiver side leads to the following chosen parameters: The filter type is chosen to be an elliptical 5th order LPF with a cutoff frequency of  $f_g = 248$  kHz, a passband frequency of 222 kHz with a passband ripple of  $-0.06$  dB and a stopband frequency of 327 kHz with a stopband attenuation of  $-39$  dB. That is the best that can be achieved with the available programmable filter.

The subcarrier amplitude compensation is done by a pre-compensation of the D/A-converter and transmitter filter in the MC modulator and by a post-compensation of the receiver filter in the MC demodulator. Therefore, the estimation process for the subcarrier amplitudes is done in two steps. First, only the transmitter LPFs are connected and the amplitude pre-compensation factors are estimated. Then, the receiver filters are connected as well and the post-compensation factors are estimated with already activated pre-compensation. The resulting transmitter spectrum is shown in Fig. 6.26. The corresponding squared amplitudes and phases are depicted in Fig. 6.27(a). Phase bending occurs now in the transmitter and receiver filters and is therefore clearly visible. The increased amplitude noise close to the filter edges is circumvented, since these subcarriers are not used for the data transmission anyway. The constellation circle of Fig. 6.27(b) is almost perfect.

It has to be noted that subcarrier compensation of course also can be performed with complex-valued correction factors, so that phase distortions can be compensated as well. But this technique increases the computational load from two multiplications to four multiplications and two additions per subcarrier value and should only be applied if phase bending is unacceptable.

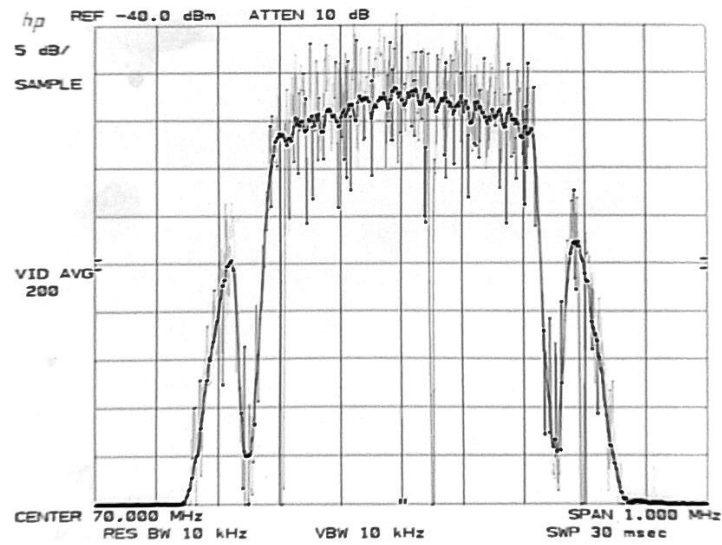
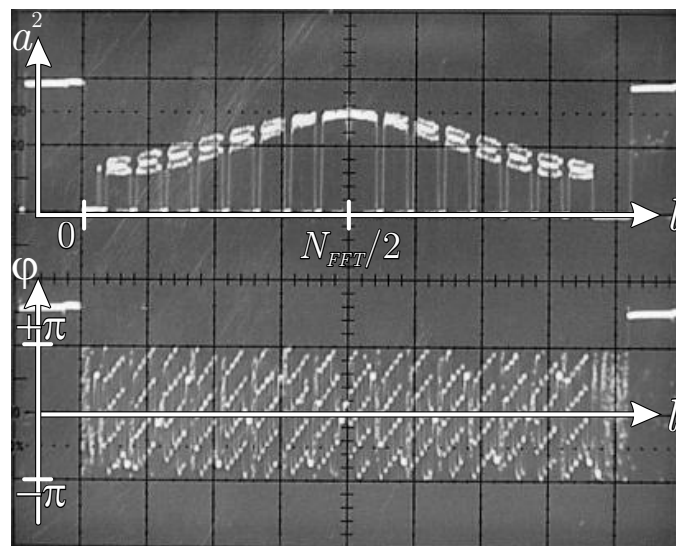
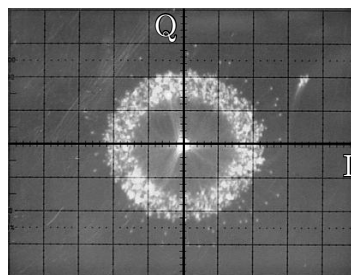


Figure 6.13: MC-CDMA demonstrator subcarrier spectrum with  $f_g = 251$  kHz RRC linear phase 10th order LP filter



(a)



(b)

Figure 6.14: MC-CDMA demonstrator received subcarrier squared amplitudes and phases (a) and I/Q-constellation (b) with  $f_g = 251$  kHz RRC linear phase 10th order LP filter and no equalization

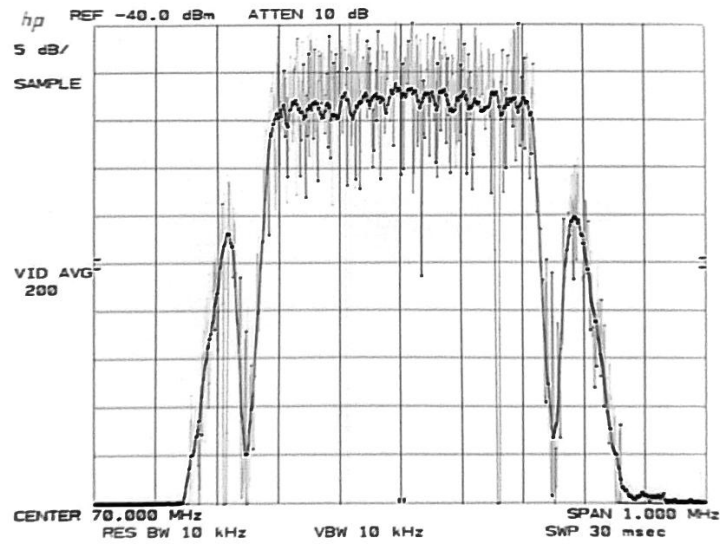
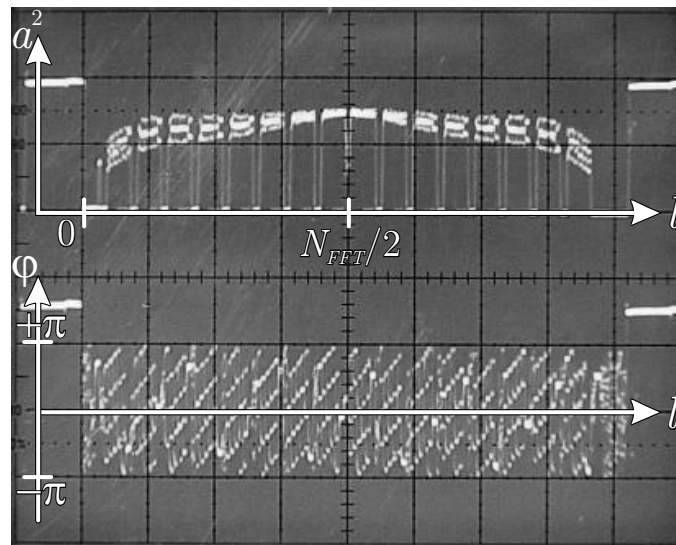
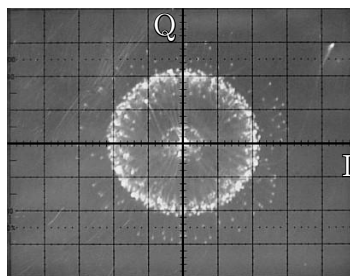


Figure 6.15: MC-CDMA demonstrator subcarrier spectrum with  $\text{si}(x)$  D/A-pulse pre-compensation and  $f_g = 251$  kHz RRC linear phase 10th order LP filter

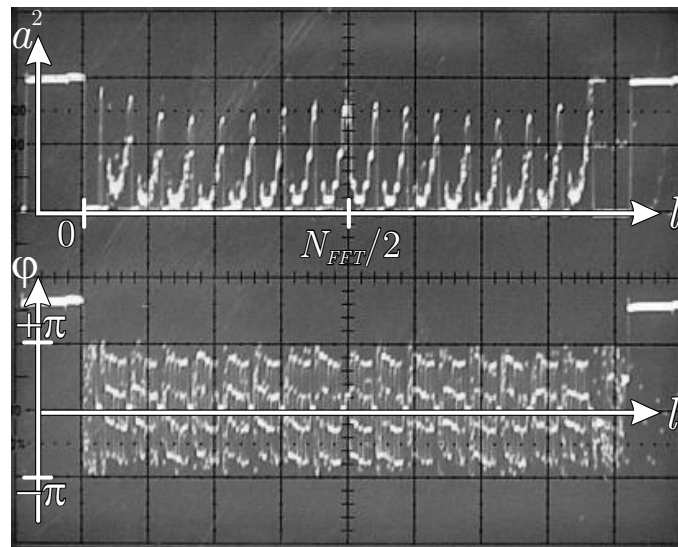


(a)

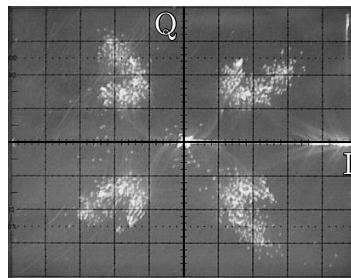


(b)

Figure 6.16: MC-CDMA demonstrator received subcarrier squared amplitudes and phases (a) and I/Q-constellation (b) with  $\text{si}(x)$  D/A-pulse pre-compensation,  $f_g = 251$  kHz RRC linear phase 10th order LP filter and no equalization



(a)



(b)

Figure 6.17: MC-CDMA demonstrator received subcarrier squared amplitudes and phases (a) and I/Q-constellation (b) with  $\text{si}(x)$  D/A-pulse pre-compensation,  $f_g = 251$  kHz RRC linear phase 10th order LP filter and with linear MRC equalization

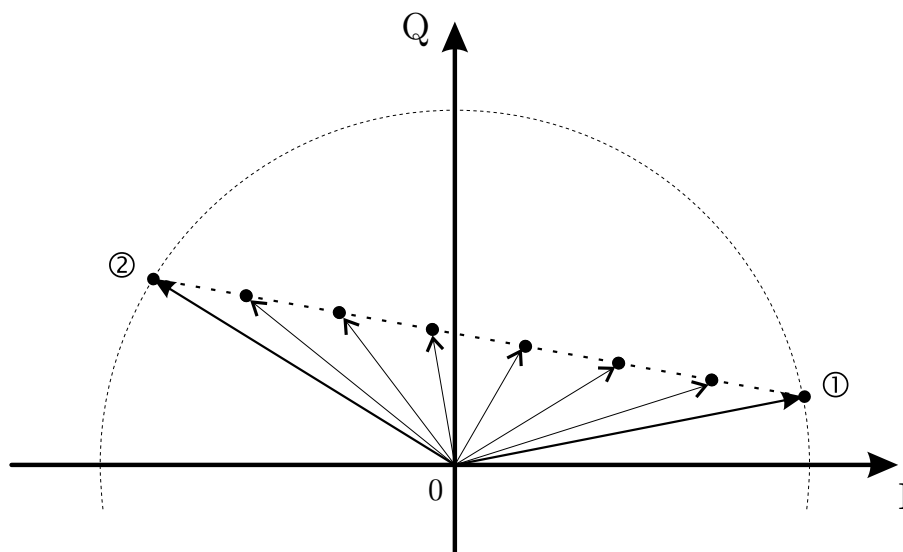
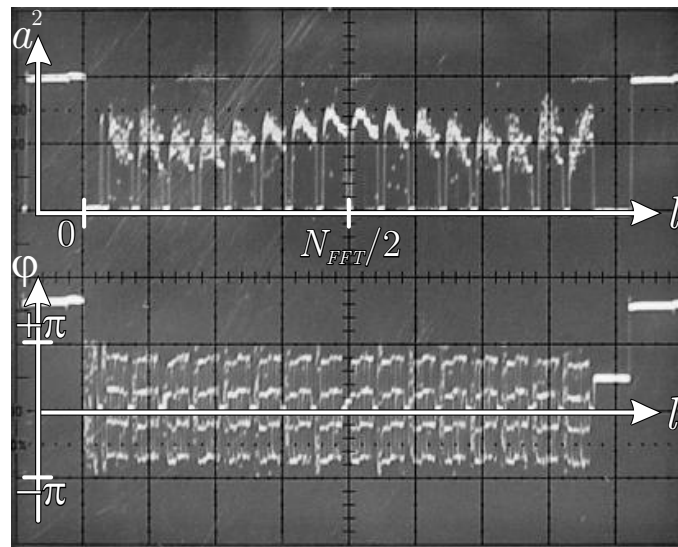
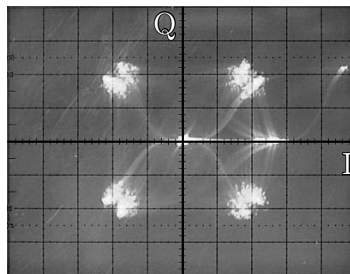


Figure 6.18: Amplitude incursions using linear interpolation due to large phase differences between pilot symbols



(a)



(b)

Figure 6.19: MC-CDMA demonstrator received subcarrier squared amplitudes and phases (a) and I/Q-constellation (b) with  $\text{si}(x)$  D/A-pulse pre-compensation,  $f_g = 251$  kHz RRC linear phase 10th order LP filter and with  $\text{si}(x)$  MRC equalization

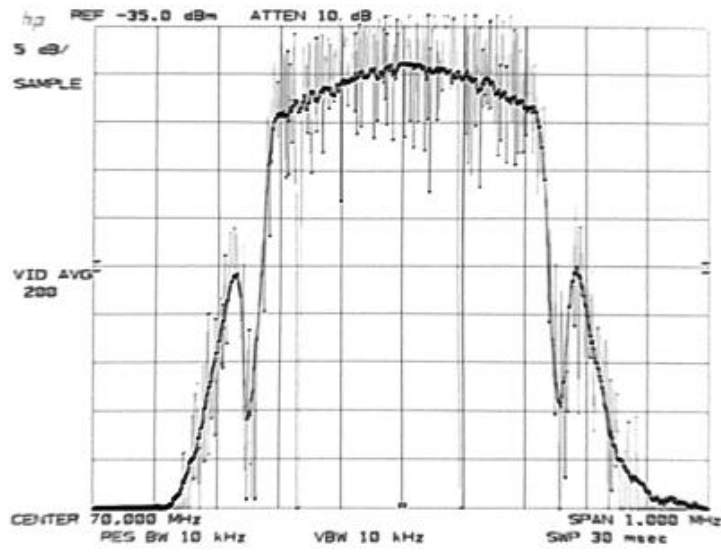
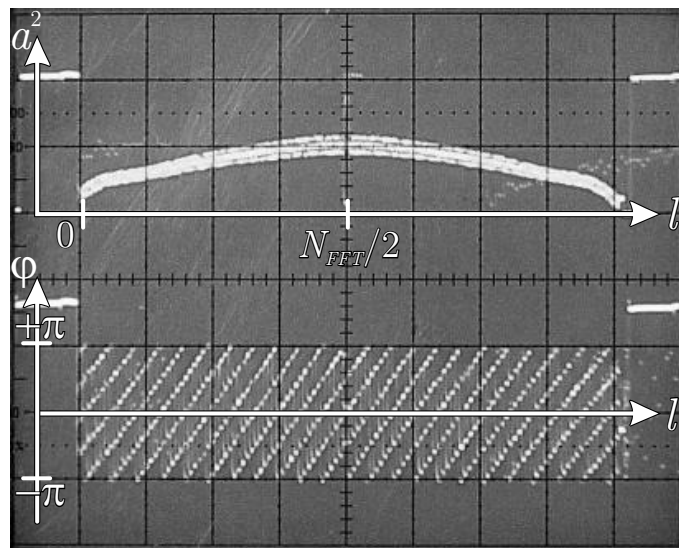
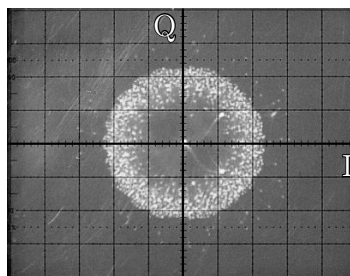


Figure 6.20: OFDM QPSK demonstrator subcarrier spectrum with  $f_g = 241$  kHz elliptic 5th order LP filter



(a)



(b)

Figure 6.21: OFDM QPSK demonstrator received subcarrier squared amplitudes and phases (a) and I/Q-constellation (b) with  $f_g = 241$  kHz elliptic 5th order LP filter and no equalization

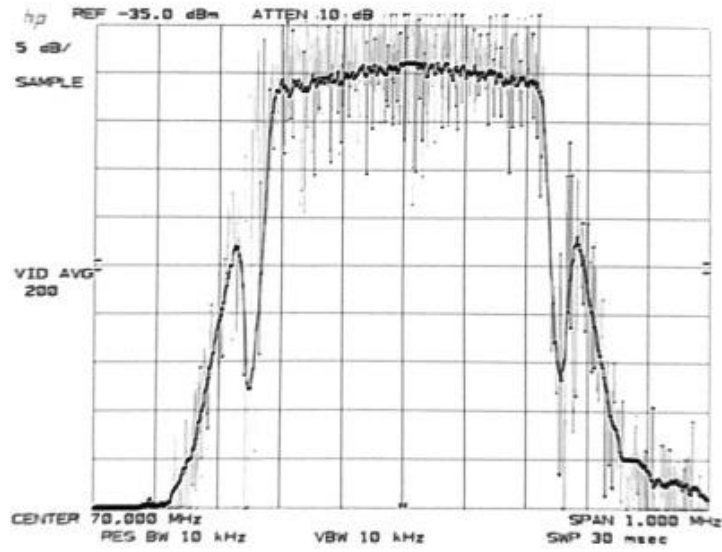
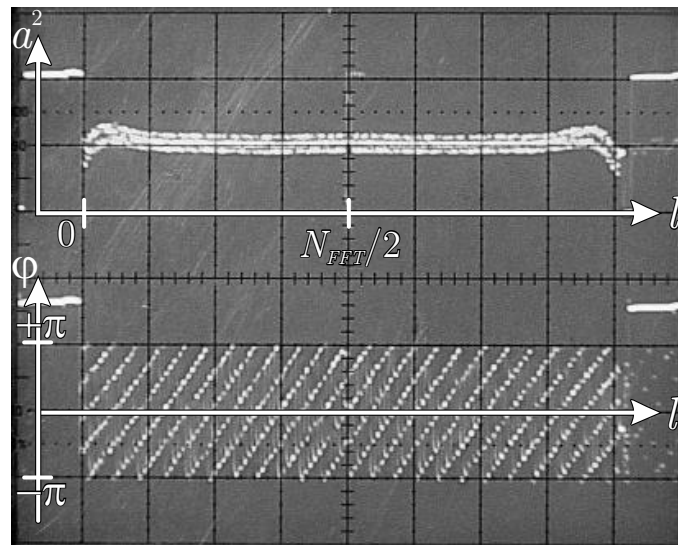
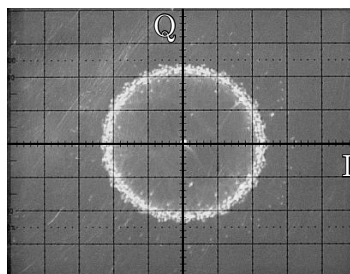


Figure 6.22: OFDM QPSK demonstrator subcarrier spectrum with  $\text{si}(x)$  D/A-pulse pre-compensation and  $f_g = 241$  kHz elliptic 5th order LP filter



(a)



(b)

Figure 6.23: OFDM QPSK demonstrator received subcarrier squared amplitudes and phases (a) and I/Q-constellation (b) with  $\text{si}(x)$  D/A-pulse pre-compensation,  $f_g = 241$  kHz elliptic 5th order LP filter and no equalization

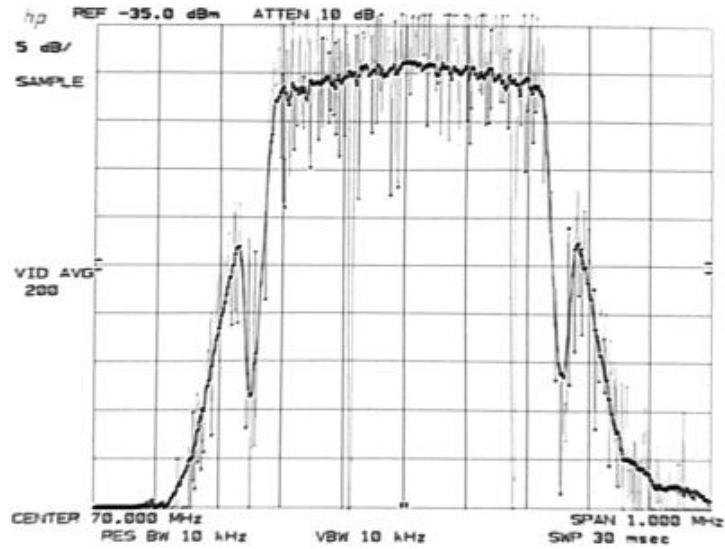
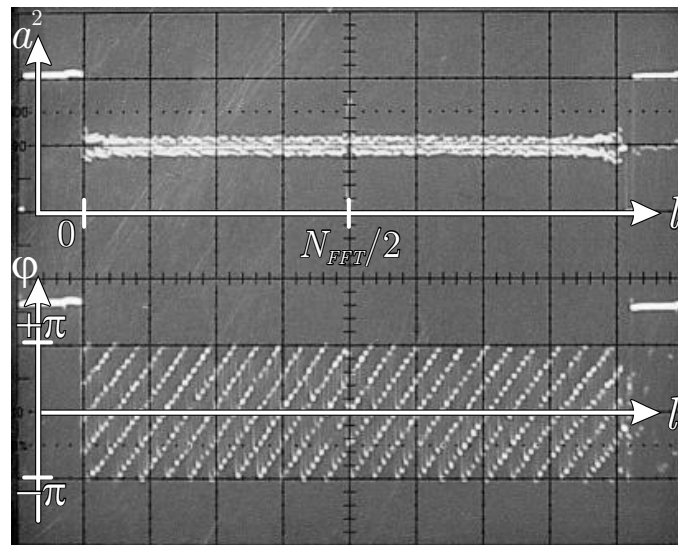
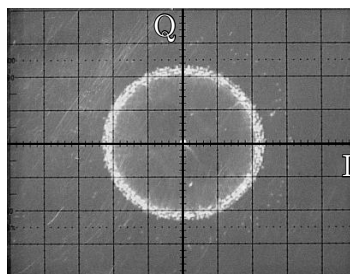


Figure 6.24: OFDM QPSK demonstrator subcarrier spectrum with estimated subcarrier amplitude pre-compensation and  $f_g = 241$  kHz elliptic 5th order LP filter



(a)



(b)

Figure 6.25: OFDM QPSK demonstrator received subcarrier squared amplitudes and phases (a) and I/Q-constellation (b) with estimated subcarrier amplitude pre-compensation,  $f_g = 241$  kHz elliptic 5th order LP filter and no equalization

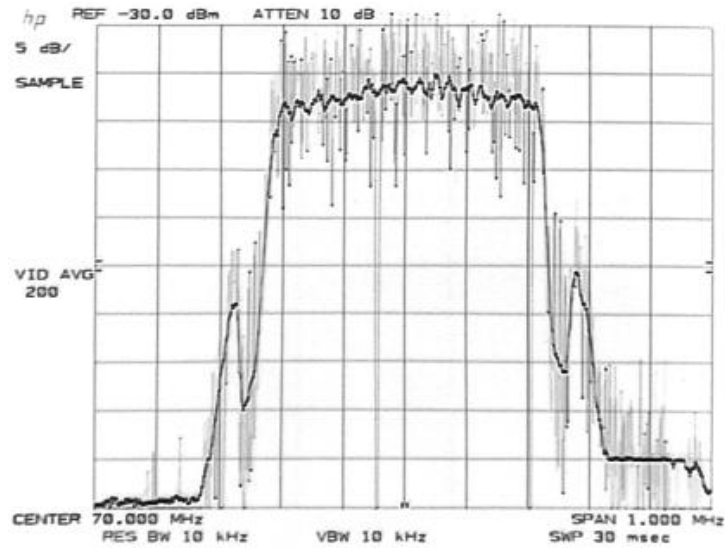
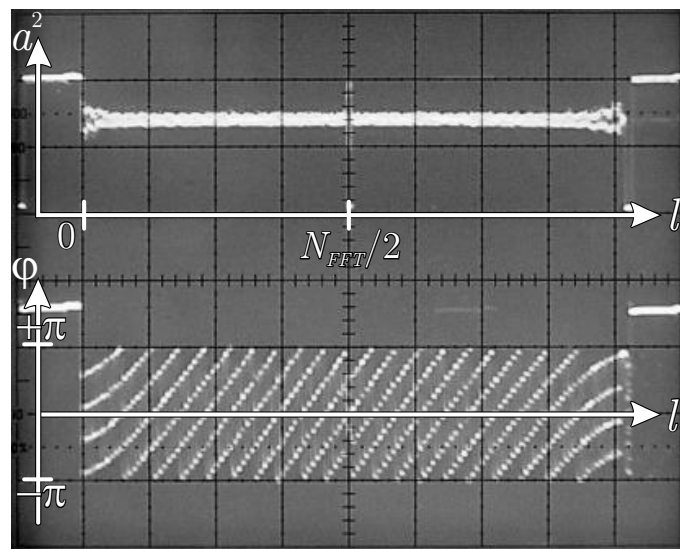
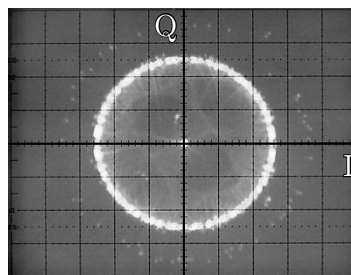


Figure 6.26: OFDM MC-CDMA demonstrator subcarrier spectrum with estimated subcarrier amplitude compensation on transmitter and receiver side with  $f_g = 248$  kHz elliptic 5th order LP filters



(a)



(b)

Figure 6.27: OFDM QPSK demonstrator received subcarrier squared amplitudes and phases (a) and I/Q-constellation (b) with estimated subcarrier amplitude compensation on transmitter and receiver side,  $f_g = 248$  kHz elliptic 5th order LP filters and no equalization

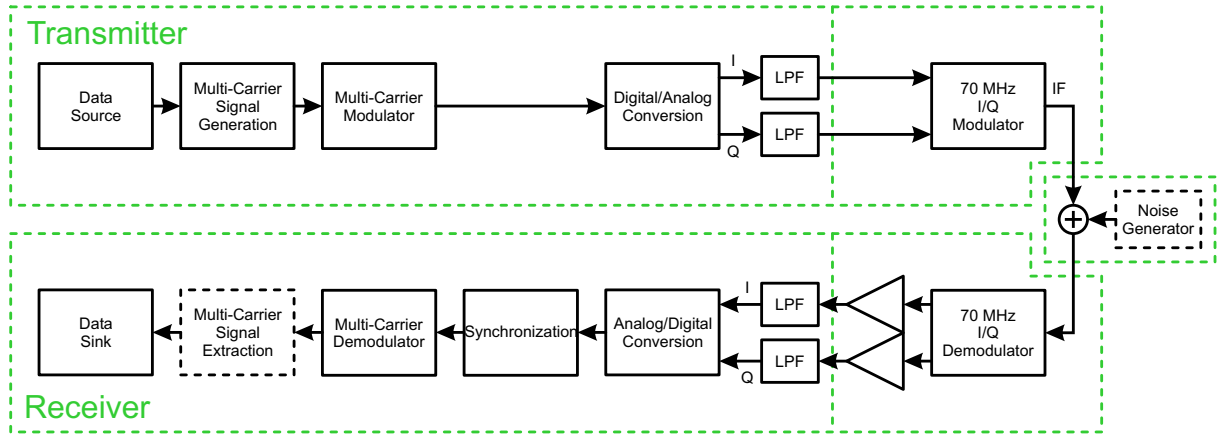


Figure 6.28: OFDM demonstrator set-up for intermediate frequency area test

## 6.2.4 IF Area Analysis

In the next step, the IF part of the transmitter and receiver is introduced. The chosen IF carrier frequency is 70 MHz. The I/Q-modulator and the I/Q-demodulator with additional amplifying stages are connected as shown in Fig. 6.28. The amplifying stages are necessary since the applied I/Q-demodulator is not built for MC communications and thus has to operate 20 dB below its regular operating point to get a linear output. An IF band noise generator can be connected to determine the BER performance of the implemented system.

### 6.2.4.1 Subcarrier Pre-Compensation

First, a look is taken at the received subcarriers without additional compensation, i.e. only LP compensation. The corresponding subcarrier squared amplitudes and phases and the I/Q-constellation are depicted in Fig. 6.29. It can be seen that the I/Q-modulator and I/Q-demodulator have a strong influence on the subcarrier amplitudes.

The occurring mismatch due to the transmitter LPFs, I/Q-modulator and I/Q-demodulator is pre-compensated in the transmitter, whereas the receiver LPFs mismatch is post-compensated in the receiver by applying a similar two-step IF subcarrier estimation procedure as mentioned above for the LP area. The resulting transmitter MC-CDMA spectrum is shown in Fig. 6.30. It is observed that the transmitted spectrum is now almost flat across the desired bandwidth. Looking at the received subcarrier amplitudes and phases in Fig. 6.31(a), it can be seen that the average subcarrier amplitudes are equal, but the noise floor has increased and thus the constellation circle of Fig. 6.31(b) widens slightly.

### 6.2.4.2 Performance Analysis

To be able to determine the average BER  $P_b$  compared to the SNR per bit  $\gamma_b$  in the implemented system, some additional measurements and calculations are necessary.

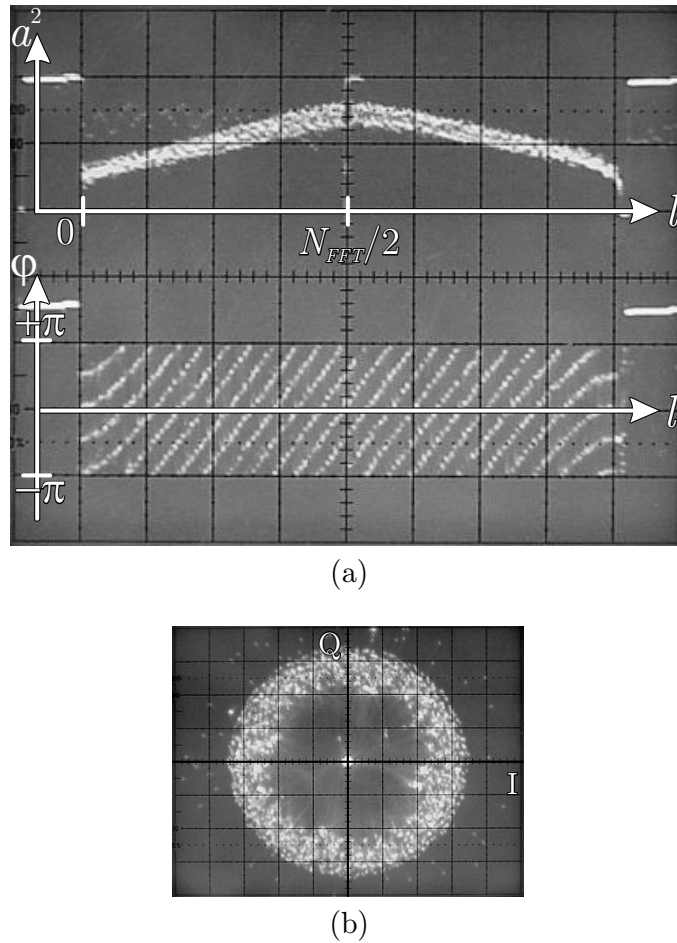


Figure 6.29: OFDM QPSK demonstrator received IF subcarrier squared amplitudes and phases (a) and I/Q-constellation (b) with estimated subcarrier amplitude LP compensation,  $f_g = 248$  kHz elliptic 5th order LP filters and no equalization

The average received signal power  $C$  [dBW] without added noise is determined with a power meter. The added noise with power density  $N_0$  [dBWs] is determined with the spectrum analyzer noise level mode by applying the set noise level and getting the noise floor readout [dBW] normalized to 1 Hz bandwidth  $\Rightarrow$ [dBW/1Hz=dBWs]. The final  $\gamma_b$  is calculated by

$$\gamma_b = \frac{C}{N_0} \cdot \frac{T_{fr}}{N_{bit}},$$

$$\gamma_b \text{ [dB]} = C \text{ [dBW]} - N_0 \text{ [dBWs]} + \left(10 \cdot \log \left( \frac{T_{fr}}{N_{bit}} \right)\right) \text{ [dBs]}, \quad (6.12)$$

where  $N_{bit}$  is the number of information bits transmitted per OFDM frame. This energy balance takes into account the energy needed for the synchronization, pilot and/or reference symbols. If not otherwise noted, synchronization of the receiver is done as follows: The ideal OFDM frame/symbol timing is estimated and thus freerunning, whereas carrier frequency synchronization is disabled, i.e.  $\widehat{\Delta f_c} = 0$  and the sampling clocks of the transmitter and receiver are coupled, i.e.  $\Delta f_{clk} = 0$ .

The results for **DQPSK modulated subcarriers**, see frame structure in Fig. 5.33, are pre-

sented first. In Fig. 6.32, BER performances, using the  $f_g = 241$  kHz LPFs, are shown. The topmost curve was obtained without correcting the DC offsets and DC gain mismatches, see Fig. 6.25, and without the additional IF part compensation. The next curve has already DC compensation, followed by the third curve that additionally has IF part compensation.

It is obvious that correcting DC mismatches has an important influence on the achievable performance and avoids an increased error floor. The performance is improved by  $\sim 2$  dB at  $P_b = 10^{-3}$ . Appropriate compensation of the subcarriers gives an additional gain due to equal error protection. The remaining loss compared to the DQPSK theory curve is related to the energy consuming synchronization and reference OFDM symbols,  $\sim 0.55$  dB, and the unavoidable implementation loss,  $\sim 0.45$  dB at  $P_b = 10^{-3}$ . For comparison, a curve using a  $R = 1/2$  repetition code with soft-decision is also shown. This code only gives a minor improvement and thus is not considered any more in the following. More effective block or convolutional codes have to be applied in an operational system.

From now on, the optimized LPFs with  $f_g = 248$  kHz are used. The new filter parameters show no visible improvement of the BER performance, see Fig. 6.33. On the other hand, implementing 2D-DD with the brute force method and maximum iteration path depth  $\mathcal{N} = 2$  gives a considerable improvement of the BER, compare with Fig. 5.18. Even with synchronization and reference symbols, the performance of the DQPSK AWGN theory is achievable.

The results for **MC-CDMA modulated subcarriers**, see frame structure in Fig. 5.32, are presented next. Only the first ten spreading groups are occupied. The BER performances of Fig. 6.34 for  $K_Q = 1$  and  $K_Q = 8$  active users again were performed with and without additional IF part compensation.

It shows that the IF part compensation has, due to the spreading, only a minor influence on the performance. Note that performance results for  $K_Q = 8$  active users are better, since they share the energy needed for the synchronization and pilot symbols which is kept constant here. Besides the implementation loss and the loss due to the energy that is consumed for the pilot and synchronization symbols,  $\sim 0.8$  dB, an additional loss of  $2 \dots 3$  dB is observed compared to the theoretical QPSK AWGN curve. It is related to the channel estimation and equalization process that introduces additional noise in the system and thus degrades the performance.

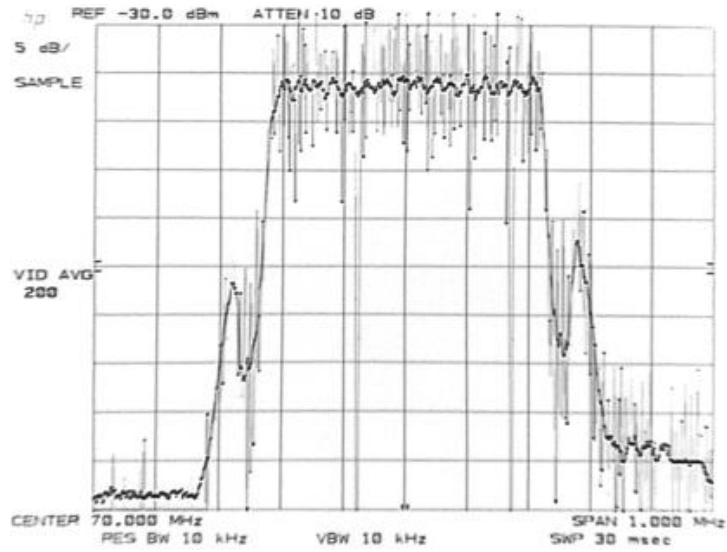
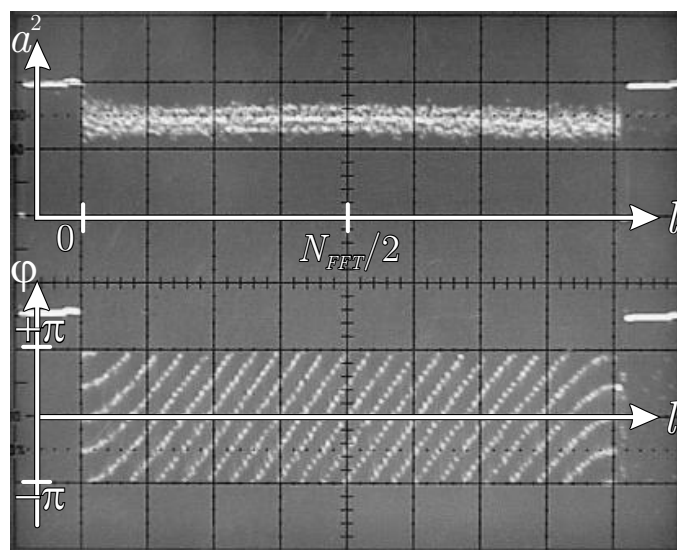
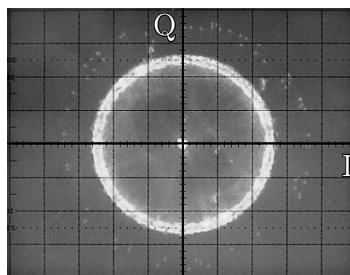


Figure 6.30: MC-CDMA demonstrator subcarrier spectrum with estimated subcarrier IF amplitude compensation on transmitter and receiver side with  $f_g = 248$  kHz elliptic 5th order LP filters



(a)



(b)

Figure 6.31: OFDM QPSK demonstrator received IF subcarrier squared amplitudes and phases (a) and I/Q-constellation (b) with estimated subcarrier amplitude IF compensation,  $f_g = 248$  kHz elliptic 5th order LP filters and no equalization

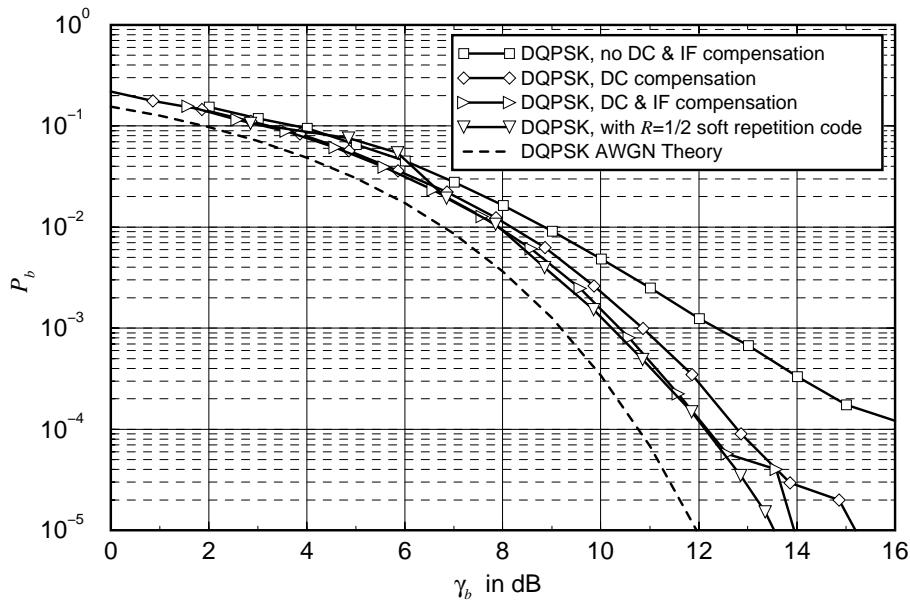


Figure 6.32: Average BER for OFDM DQPSK with wired transmission in IF band and different compensation conditions; symbol/frame timing synchronization freerunning; carrier frequency synchronization disabled; sampling rates coupled

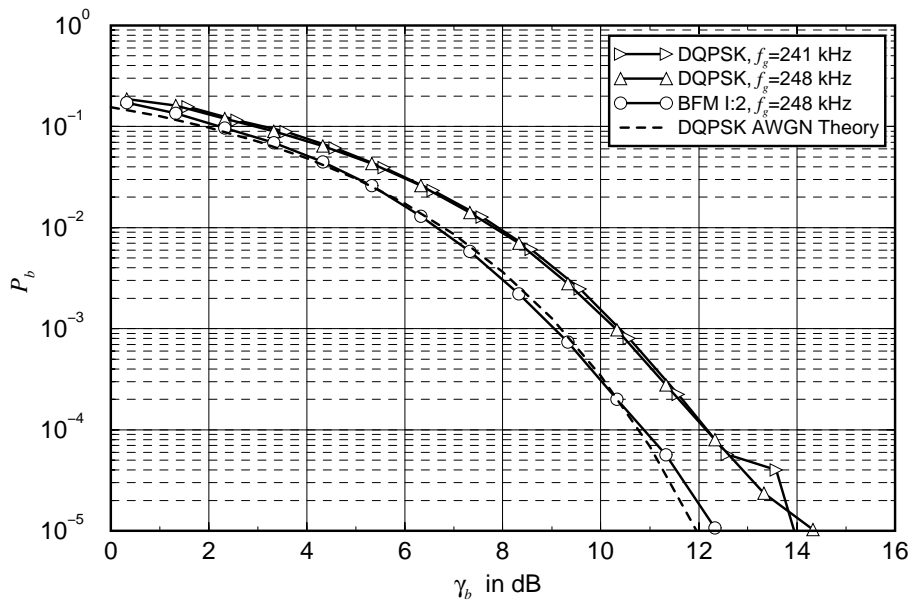


Figure 6.33: Average BER with 2D-DD for OFDM DQPSK with wired transmission in IF band and different filter bandwidths; symbol/frame timing synchronization freerunning; carrier frequency synchronization disabled; sampling rates coupled

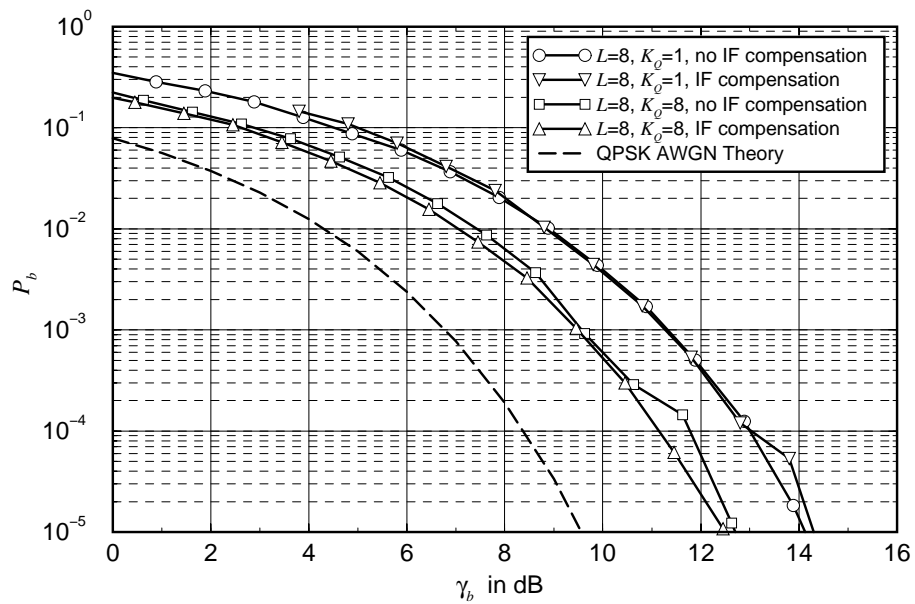


Figure 6.34: Average BER for OFDM QPSK MC-CDMA with wired transmission in IF band, linear ZF channel equalization and different compensation conditions; symbol/frame timing synchronization freerunning; carrier frequency synchronization disabled; sampling rates coupled

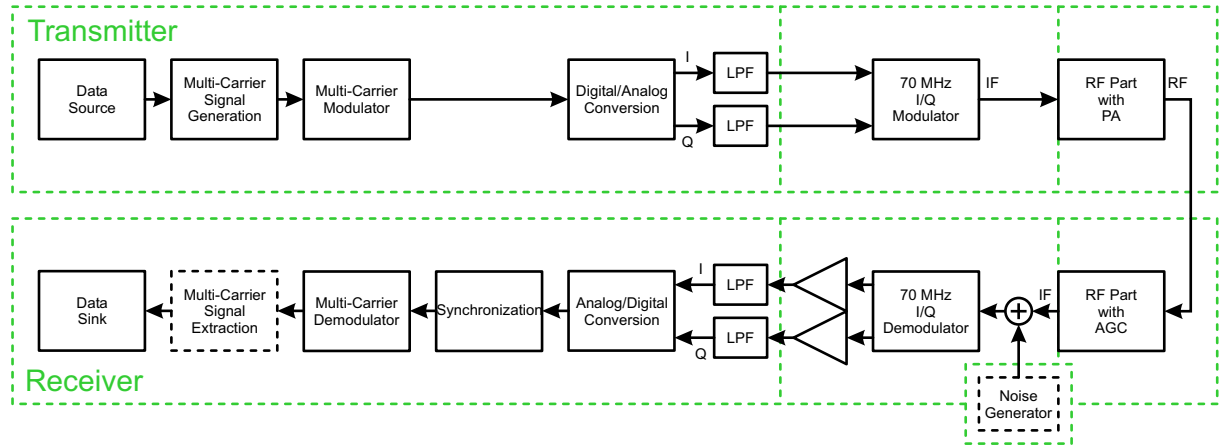


Figure 6.35: OFDM demonstrator set-up for radio frequency area test

## 6.2.5 RF Area Analysis

In the final step, the Radio Frequency (RF) part is connected to the system. The corresponding demonstrator laboratory set-up, consisting of a wired connection without antennas, is shown in Fig. 6.35.

The transmitter RF part basically consists of a BandPass Filter (BPF) with 2.5 MHz bandwidth for the IF band and a mixer that converts the signal up to the 5.1465 GHz area with a local oscillator followed by another 2.5 MHz BPF. A subsequent Power Amplifier (PA) delivers up to 15 W output power and is connected to a further BPF to suppress possible spectrum images due to non-linear effects. The signal is finally sent to the antenna, or in this case a connecting cable.

On the receiver side the signal from the antenna, or respectively from the connecting cable, is filtered with a BPF and then amplified with a Low Noise Amplifier (LNA) followed by the mixer necessary for the downconversion to the 70 MHz IF band. After another BPF, the signal is amplified with an Automatic Gain Control (AGC) that has a slope time of 100 ms. A final BPF removes distortions from the signal and forwards it to the 70 MHz I/Q-demodulator.

For BER performance analysis, the IF band noise generator can be inserted between the RF part output and the I/Q-demodulator input. In the transmitter as well as in the receiver, additional isolators, for protecting the circuit from possible signal reflections, attenuators, for signal conditioning, and 10 dB power splitters, for signal monitoring, are integrated.

### 6.2.5.1 Subcarrier Pre-Compensation

Since the applied BPFs have due to the licensed frequency spectrum a much larger bandwidth than the transmitted demonstrator signal, no further impact, considering spectral shaping, is expected from the RF part. This is proved in the following. Fig. 6.36 shows the received MC-CDMA subcarrier amplitudes and phases with connected RF part and only estimated IF part

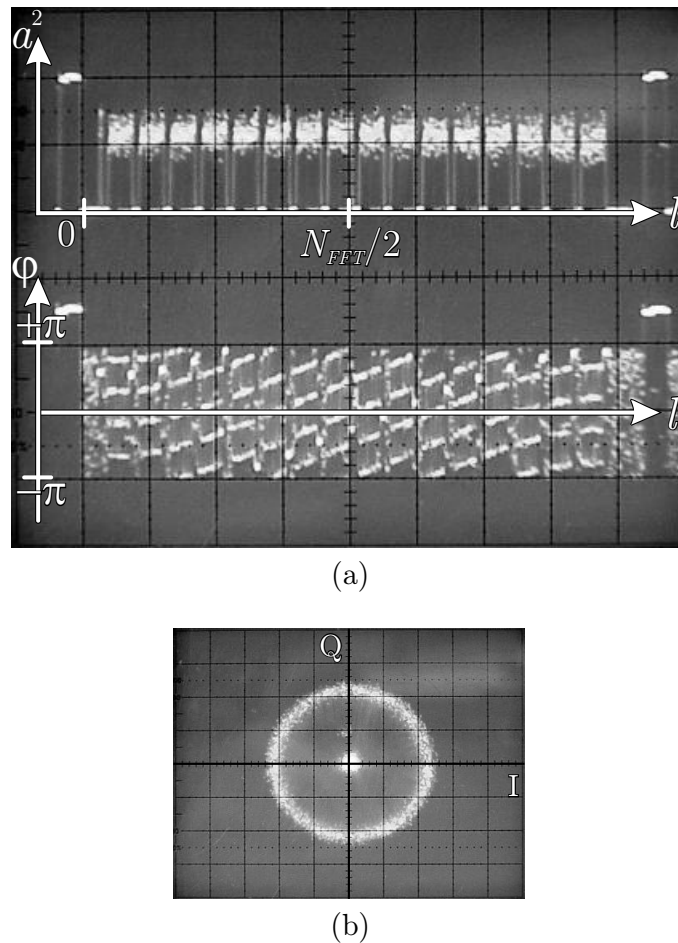


Figure 6.36: MC-CDMA ( $K_Q = 1$ , full power) demonstrator received RF subcarrier squared amplitudes and phases (a) and I/Q-constellation (b) with estimated subcarrier amplitude IF compensation,  $f_g = 248$  kHz elliptic 5th order LP filters and no equalization

compensation from Section 6.2.4.1. Note that only one user is active per group, i.e.  $K_Q = 1$ , and uses the same power per subcarrier as the pilot symbols. As can be seen from Fig. 6.36(a), the subcarrier amplitudes remain approximately the same on all subcarriers. Due to an increased noise level, the variance in the constellation diagram of Fig. 6.36(b) has increased.

After estimating and applying the real RF part pre- and post-compensation values, the transmitted MC-CDMA spectrum is shown in Fig. 6.37. The distribution of the amplitudes and the constellation variation in Fig. 6.38 improve slightly.

Since coherent MC-CDMA is applied, the channel of the received signal needs to be estimated and equalized. The result, using channel estimation with linear interpolation and ZF equalization, is shown in Fig. 6.39. It is evident that the pilot symbols have been forced to an equal amplitude, i.e. 1.0, and an equal phase, i.e.  $0^\circ$ . The four possible QPSK phases are clearly visible in the positions of the valid data symbols.

If up to eight users are transmitting with their individual spreading sequences and the average power per subcarrier should be the same as for the pilot symbols, each user must only use  $1/8$

of the pilot symbol power. This is assumed in the following. Fig. 6.40 shows the equalized constellation diagrams for  $K_Q = 1$ ,  $K_Q = 2$ ,  $K_Q = 5$  and  $K_Q = 8$  active users per group. Due to superpositioning of the individual QPSK symbols from the users, the subcarrier constellation diagrams vary, where constellation positions close to the outside margin are less likely than to the center. Note that transmitting no signal on one of the subcarriers is a valid constellation position for transmissions with an even number of active users, and that eight of these constellation positions are used to extract the corresponding data symbol for one user. The equalized pilot symbols on the positive I-axis can be seen, too.

For the wired RF connection, of course not the full PA power is needed. With a further reduction of the PA power, the currently present noise can be lowered.

### 6.2.5.2 Performance Analysis

In the performance analysis, **DQPSK modulated subcarriers** are considered first. As expected, with freerunning transmitter and receiver sampling clocks and freerunning carrier frequency synchronization, the system performance compared to the theory is degraded the most, see Fig. 6.41. For the case that only the sampling clocks are running free and the carrier frequency synchronization is disabled, due to a sufficient accuracy of the IF and RF oscillators, the performance remains about the same. With additionally coupled sampling clocks, the performance with only IF compensation compared to RF compensation are about the same within the measurement accuracy. For comparison, the IF band performance from Fig. 6.33 is shown as well. It is derived that the RF part produces an additional implementation loss of  $\sim 1.3$  dB at  $P_b = 10^{-3}$ .

In the next step, 2D-DD is considered. The cases with and without freerunning sampling clocks and carrier frequency synchronization are considered in Fig. 6.42. 2D-DD improves the performance in both cases by  $\sim 1.2$  dB at  $P_b = 10^{-3}$ , keeping the remaining implementation loss compared to the common DQPSK theory below  $\sim 1.3$  dB.

Now, the performance of **coherent MC-CDMA** is evaluated. Fig. 6.43 shows the results with  $K_Q = 1$  and  $K_Q = 8$  active users per group. Since again for  $K_Q = 1$ , the whole synchronization and pilot symbol energy has to be provided, the performance in that case is worse than for  $K_Q = 8$ . Differences between the results for using the correct RF compensation values in spite of applying the IF compensation values are within the measurement accuracy bounds. The additional implementation loss compared to the IF band that can be derived from Fig. 6.43 is  $\sim 1.5$  dB at  $P_b = 10^{-3}$ .

Until now, the transmitter and receiver sampling clocks were coupled and carrier frequency synchronization was disabled. This is changed in the results of Fig. 6.44. A similar behaviour as for the DQPSK performance in Fig. 6.41 is observed. With independent sampling clocks and freerunning carrier frequency synchronization, the performance degrades slightly.

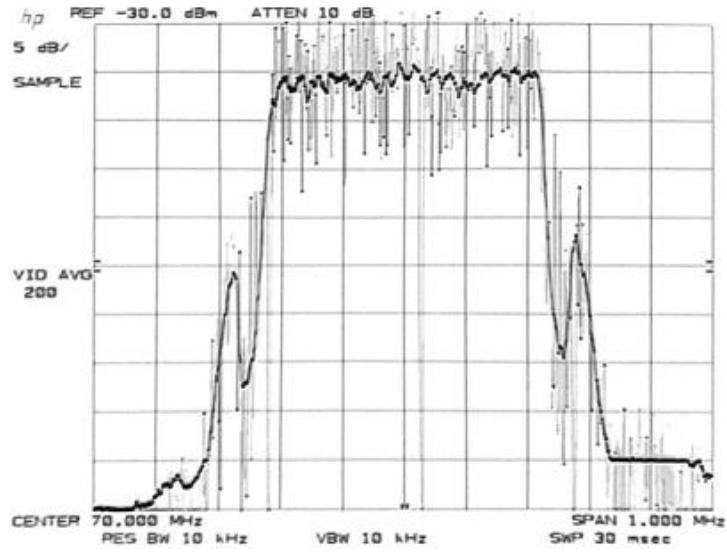
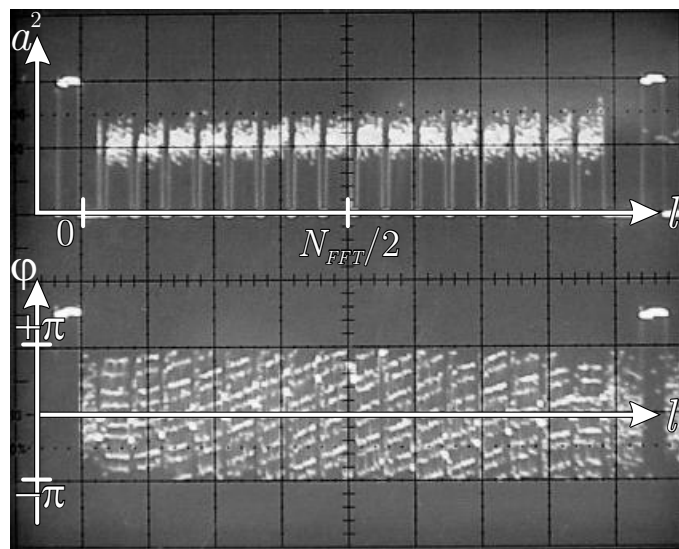
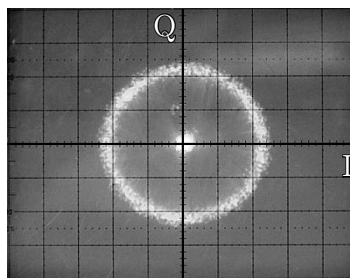


Figure 6.37: MC-CDMA demonstrator subcarrier spectrum with estimated subcarrier RF amplitude compensation on transmitter and receiver side with  $f_g = 248$  kHz elliptic 5th order LP filters



(a)



(b)

Figure 6.38: MC-CDMA ( $K_Q = 1$ , full power) demonstrator received RF subcarrier squared amplitudes and phases (a) and I/Q-constellation (b) with estimated subcarrier amplitude RF compensation,  $f_g = 248$  kHz elliptic 5th order LP filters and no equalization

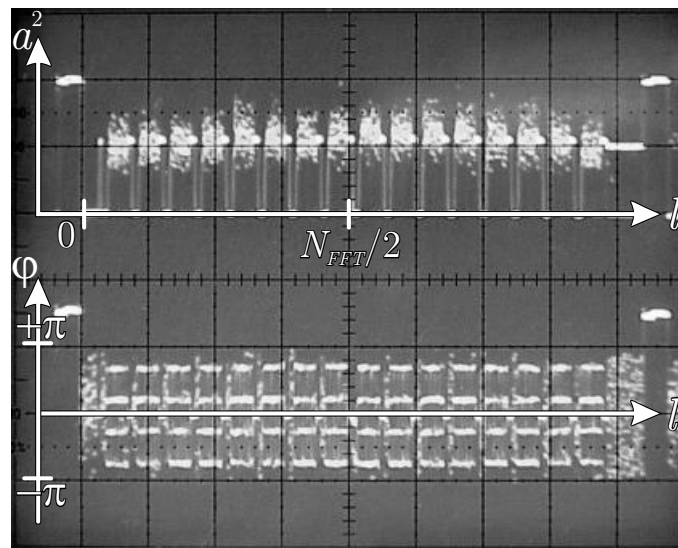


Figure 6.39: MC-CDMA ( $K_Q = 1$ , full power) demonstrator received RF subcarrier squared amplitudes and phases with estimated subcarrier amplitude RF compensation,  $f_g = 248$  kHz elliptic 5th order LP filters and linear interpolated ZF equalization

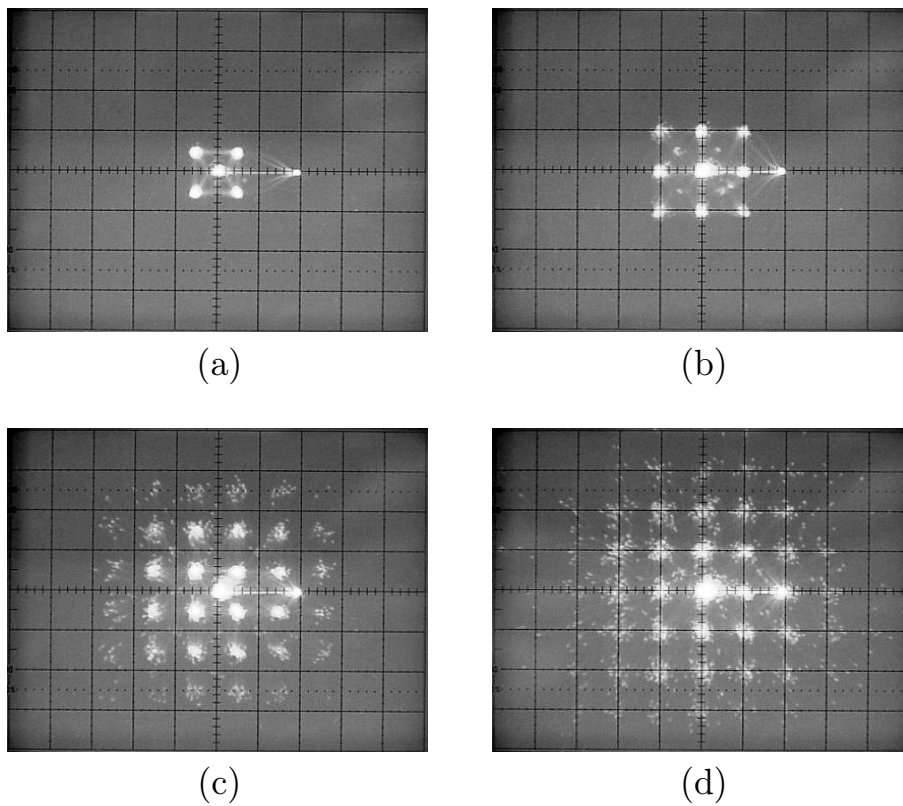


Figure 6.40: Received RF MC-CDMA subcarrier constellation diagrams for spreading code length  $L = 8$  and  $K_Q = 1$  (a),  $K_Q = 2$  (b),  $K_Q = 5$  (c) and  $K_Q = 8$  (d) active users per user group

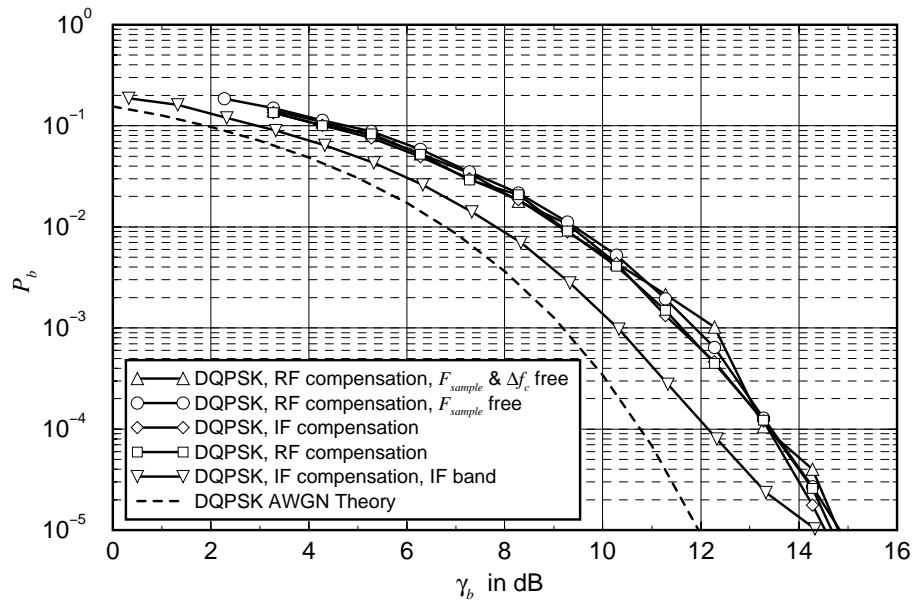


Figure 6.41: Average BER for OFDM DQPSK with wired transmission in RF band and different compensation and synchronization conditions; symbol/frame timing synchronization freerunning

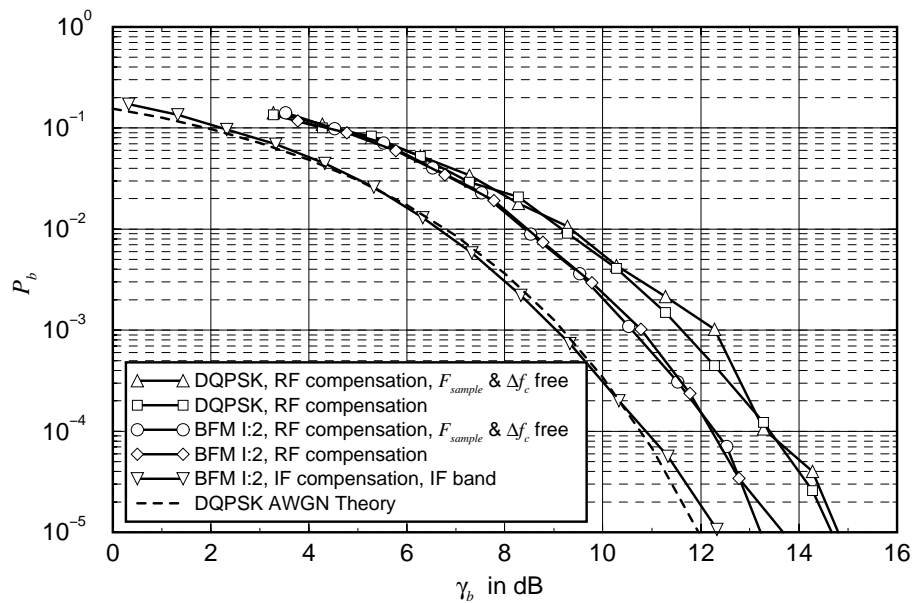


Figure 6.42: Average BER with 2D-DD for OFDM DQPSK with wired transmission in RF band and different synchronization conditions; symbol/frame timing synchronization freerunning

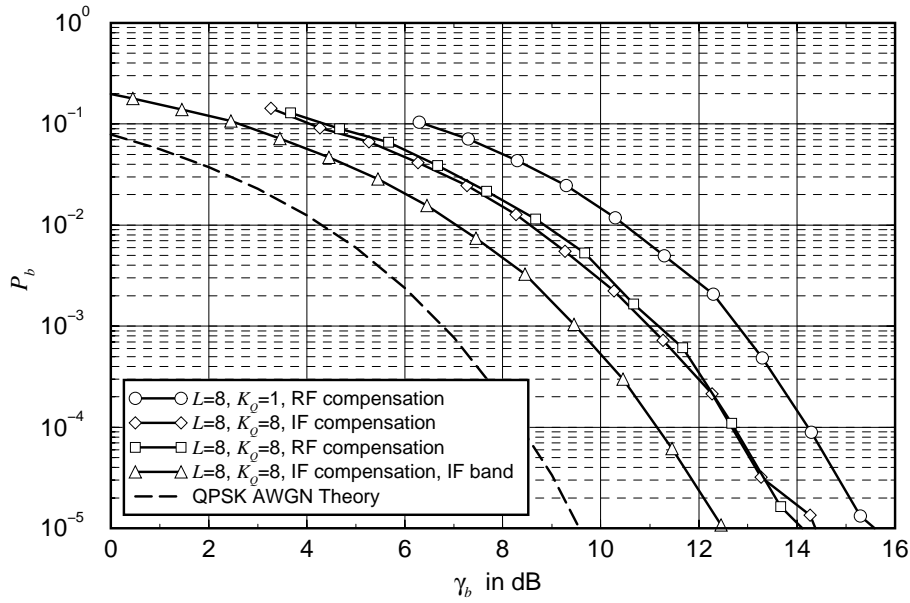


Figure 6.43: Average BER for OFDM QPSK MC-CDMA with wired transmission in RF band, linear ZF channel equalization and different compensation conditions; symbol/frame timing synchronization freerunning; carrier frequency synchronization disabled; sampling rates coupled

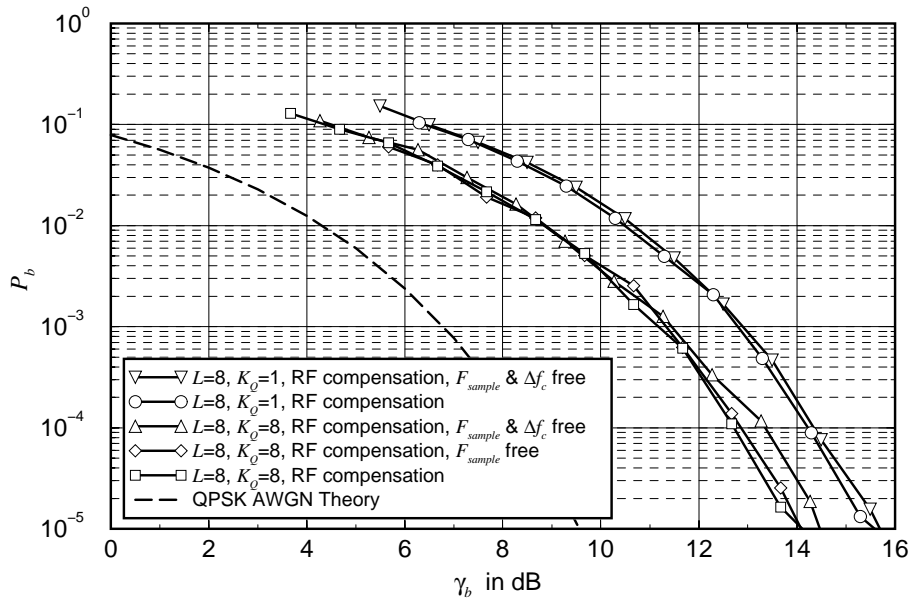


Figure 6.44: Average BER for OFDM QPSK MC-CDMA with wired transmission in RF band, linear ZF channel equalization and different synchronization conditions; symbol/frame timing synchronization freerunning

## 6.2.6 Conclusions for the DSP-System Implementation

Table 6.1 summarizes the possible sources of error in a practical hardware implementation that have been observed during the DSP system evaluation process. Impacts on the signal and possible countermeasures are given.

Table 6.1: Errors, their impact on the signal and countermeasures

Error source	Impact	Countermeasure
DC-offset	0 Hz subcarrier unusable	Do not use 0 Hz subcarrier
Gain mismatch between I- and Q-channel	Varying amplitudes on subcarrier-level; frequency-independent	Balance I- and Q-gain in transmitter and receiver
Lowpass filter bandwidth mismatch between I- and Q-channel	Varying amplitudes on subcarrier-level; increasing with frequency	Line-up lowpass filter bandwidths in I- and Q-channel
Distortions due to filters, I/Q-modulator, I/Q-demodulator, other hardware parts	Frequency-dependent attenuation and phase rotation of the subcarriers	Pre- and post-compensation of the subcarriers in the transmitter and receiver

Some of the distortions can be circumvented by using state-of-the-art digital up- and down-converters instead of the analog filters and I/Q-modulator/demodulator. Unfortunately these converters were not available yet at the time when the practical demonstrator system implementation started.

Even though the results in Section 6.2.5.2 suggest that 2D-DD DQPSK and coherent MC-CDMA have comparable performances, the degrading effects of fading channels are stronger in the DQPSK case. Nevertheless, it has been shown that with accurate compensation, the implementation loss for MC-CDMA can be lowered to  $\sim 5.2$  dB (including the loss through channel estimation of  $\sim 2 \dots 3$  dB) and for DQPSK to  $\sim 2.2$  dB; both excluding the energy needed for pilot, reference and synchronization symbols which give an additional degradation. Applying 2D-DD with  $\mathcal{N} = 2$  further reduces the implementation loss for DQPSK to  $\sim 1.1$  dB. All values consider a BER of  $P_b = 10^{-3}$ .

The wireless transmission channel in conjunction with the transmitter and receiver antennas imposes further noise to the signal.

First tests with a mobile van, in which the receiver equipment has been installed, have shown that the 2D-DD technique as well as the MC-CDMA technique are working in a real-world environment. Tests in the near future, including not only installations in the van, but also in a test aircraft, will have to prove the suitability in critical fading environments. The theoretical

link budget will have to face the real-world conditions and the necessary transmitter power for an operational range of up to 60 . . . 100 km is going to be derived.

# Chapter 7

## Summary

The purpose of the present work has been the design, evaluation and implementation of a multi-carrier transmission system for aeronautical communications in the vicinity of an airport. In this final chapter, the carried out work and the obtained results for the aeronautical communications system are summarized.

The concept of the aeronautical communications system is divided into several individual parts. Starting from the transmission channel scenarios and the selected OFDM modulation technique, other components like CDMA multiplexing and subcarrier compensation have been added resulting from simulation and practical implementation aspects.

A **novel aeronautical channel model** has been presented that is based on the statistical identities of the underlying *Doppler and delay power spectra*. Distinguishable *scenarios for the case that the aircraft is en-route, arriving, taxiing or parking* have been identified. These scenarios deliver a small area characterization of the aeronautical channel that is used to determine the performance of the investigated data link in the different conditions. Typical and worst case parameter sets based on published measurement results and empirical data have been derived. In conjunction with the *WSSUS channel model*, it has been shown that these parameter sets can be used for a *simulation of the aeronautical channel in the time and frequency domain* in a digital signal processing system. This can be done without imposing any simplifications, even for a system with discrete time and/or frequency samples.

Since CDMA is used in this work, a **comparison of the FDMA, TDMA and CDMA techniques** with respect to the distribution of time, bandwidth and applied power has been presented. The advantages of applying these techniques in **single-carrier, spread spectrum and multi-carrier modulation** have been discussed. Furthermore, the **influence of practical D/A-conversion** on these modulation schemes has been investigated. It has been found that multi-carrier modulation offers the best flexibility with respect to the fact that the number of active users can be exchanged for the available bandwidth per user. In conjunction with a D/A-converter, it has been shown that *supplementary subcarriers are necessary for a practical filter design* and that the subcarriers are unequally protected against distortions on the trans-

mission channel. Different methods have been discussed to keep the filtering process as simple as possible, *offer an equal protection of the subcarriers on the channel* and possibly *compensate other frequency-dependent distortions* that affect the subcarriers.

Multi-carrier modulation offers the possibility for a coherent or differential coherent modulation of the subcarriers. In the **coherent case**, additional pilot symbols are necessary to estimate and equalize the channel. The estimation process necessitates interpolation of the pilot symbols in the positions of the data symbols. **The different  $\text{si}(x)$ , linear, rectangular and spline interpolation techniques have been investigated with respect to their implementation complexity, computational load, number of available pilot symbols, phase shifts of the interpolation filter function and the in-band/out-of-band filter noise.** It has been found that if an excessive number of pilot symbols with respect to the sampling theorem is available, linear interpolation is the best option, since it only requires two neighbouring pilot symbols for the interpolation and additionally keeps the interpolation noise low.

For the case that **differential modulation** is applied, the Walsh-Hadamard CDMA technique used for coherent modulation cannot be applied due to the possible erasure of certain subcarriers. Therefore, a proposal has been made to **apply CDMA by using block codes on data level**. This technique offers the advantage that additional error protection, besides the use of the code for spreading, is possible.

Furthermore, a **novel two-dimensional algorithm for differential demodulation** has been introduced. Since this algorithm is applied in the receiver alone without changing the transmitter, it can be applied to existing standards, like for example DAB, as well as to new standards. It has been proved in theory, that *by choosing a detour path for demodulation, rather than the direct path, the reliability of the decision for a certain demodulated bit sequence is improved*. A **criteria, based on the minimum phase error**, has been introduced for choosing the right path. In addition to that, a **brute force and a stream method** have been presented **for the path evaluation** that take into account the transmission channel characteristics to restrain the investigation of unnecessary paths.

Coherent and differential coherent modulation both require accurate synchronization. Therefore, first the different **synchronization issues**, namely *OFDM frame/symbol synchronization, carrier frequency synchronization* and *sampling rate synchronization*, have been identified; followed by a presentation of the *effects of synchronization mismatches* on the signal-to-noise ratio of the subcarriers. The synchronization algorithms that are most commonly referred to in literature have been presented and the Schmidl & Cox algorithm has been chosen for the DSP demonstrator system, since it requires only two OFDM symbols to achieve timing, carrier frequency and sampling rate synchronization. Furthermore, it also offers the possibility to estimate the SNR which is of interest for MMSE algorithms that require this knowledge. **Proposals for the improvement of two drawbacks of the Schmidl & Cox algorithm** have been worked out. One deals with the fact that *oversampling on the receiver side* considerably improves the performance by investigating two sets of samples and then choosing the most promising. The other considers a *change in the transmitted synchronization sequence* to

accurately determine the end of the guard interval in the receiver. This is done by halving the number of subcarriers in the synchronization symbols and instead of transmitting two full symbols transmitting four half-symbols.

Based on the physical channel conditions, that have been worked out earlier in this work, a **set of system parameters** has been chosen for the simulation and DSP demonstrator system. This includes step by step instructions how to generate the system parameters, since some of them depend on each other.

Both the performance of the coherent QPSK and the differential coherent DQPSK system have been evaluated. The **results for QPSK** can be summarized as follows:

- The system performs well in all aeronautical channel conditions.
- The strong LOS path in the en-route and arrival scenario guarantees a safe operation even for large distances outside the airport area.
- A degradation of the BER performance between 2...3 dB has to be expected due to equalization with an estimated channel.
- Disabling the channel equalization in conditions with a strong LOS path, i.e. only correcting the carrier frequency offset and the mean phase offset if possible, can further reduce the BER floor.
- Using MC-CDMA with Walsh-Hadamard sequences further improves the BER performance, especially in the critical taxiing and parking conditions with a weak or no LOS path.
- Due to the limited number of pilot symbols available for channel estimation,  $\text{si}(x)$  interpolation delivers poor results since in theory the filter taps and the filter function have to be infinite.
- Linear-interpolated equalization delivers good results for the case that at least two-times oversampling for the pilot symbols is applied. It furthermore reduces the computational complexity, since only two neighbouring pilot symbols are needed for the interpolation.
- Non-linear (transmitter power amplifier) effects and synchronization mismatches are critical for the system performance and have to be circumvented by all means.

In addition to this, the **DQPSK results** can be summarized in a similar way:

- DQPSK has an edge over QPSK, since it requires no explicit channel equalization and is therefore an interesting candidate for the reverse link from mobile stations to the base station; the drawback of this is a loss of 2...3 dB in the theoretical AWGN BER performance of DQPSK compared to QPSK.

- The performance degradation is further increased by higher BER floors in the aeronautical channel conditions.
- In contrast to this, DQPSK performs better than QPSK for the case that ICI is present.
- If block codes are used for spreading on data level, differential coherent modulation can use CDMA as well.
- The introduction of two-dimensional differential demodulation is able to improve the BER performance in all investigated conditions.
- For the AWGN case, 2D-DD brings differential coherent demodulation close to the theoretical coherent demodulation.
- The error floor in aeronautical fading channel conditions with a strong LOS path is significantly reduced with 2D-DD.
- Degrading non-linear amplifier effects, as well as degrading effects through noise introduced by synchronization mismatches are lowered by applying 2D-DD.

Using the obtained results, the **parameter sets for a coherent ground-air and a differential coherent air-ground link DSP demonstrator**, both based on a 128 point IFFT/FFT, have been proposed.

To keep the **experimental multi-processor DSP demonstrator system** as *flexible and adaptable* as possible to user needs, **parameter structures for a software-defined radio** have been established. These structures, which are based on C-code header-files for the DSP demonstrator, make it possible to change the functionality of the whole OFDM system by changing only a few values in the according parameter structures.

The purpose of the demonstrator system is to have a ground-air link available for the DLR project TARMAC that contributes to an Advanced Surface Movement Guidance and Control System (A-SMGCS) in the surrounding area of an airport. Furthermore, it offers the possibility to **investigate 2D-DD, MC-CDMA and the influence of transmitter and receiver hardware in a real-world environment**. The *considered Tx/Rx hardware* in this work included *amplifiers, filters, I/Q-modulators and I/Q-demodulators*. It showed that accurate tuning and compensation is necessary to obtain the optimum performance results. Already small mismatches cause intolerably high degradation and increased BER floors. The *implementation loss compared to the theoretical performance* has been evaluated and it showed that QPSK has a loss of  $\sim 3.5$  dB, whereas DQPSK has only a loss of  $\sim 1.8$  dB since it requires no noise-influenced channel estimation and equalization. The implementation loss for DQPSK is further reduced to  $\sim 0.8$  dB by applying 2D-DD. All mentioned implementation losses exclude the energy needed for the synchronization, pilot and reference symbols, which is  $\sim 0.8$  dB for QPSK and  $\sim 0.55$  dB for DQPSK.

The results of this work can serve as a reference and an incentive for further studies in the area of (aeronautical) mobile communications and related topics:

- The presented channel model can serve as a standard for the investigation of aeronautical communications links. A standardized channel model will make results of different studies easier to compare.
- The aspects obtained from the implementation are also useful for the the realization of other digital data links.
- The novel topic of coding, MA and 2D-DD has been established for differentially modulated MC systems which are of special interest for the uplink.
- Similar channel conditions, like the ones presented here, can be expected for fourth generation (4G) mobile communications systems. With the obtained performance results, it can be concluded that MC modulation is a promising candidate for 4G systems as well.

# Appendix A

## Maximum Doppler Rate Derivation

For the case that an aircraft flies over a ground station, the maximum Doppler rate is derived as follows. From the current Doppler shift in (2.19)

$$f_D(t) = f_{D_{max}} \cdot \frac{d(t)}{\sqrt{d^2(t) + h^2}} \quad (\text{A.1})$$

with the Tx-Rx distance above ground in (2.20)

$$d(t) = d_0 - vt, \quad (\text{A.2})$$

the current Doppler rate  $f'_D(t)$  is calculated

$$f'_D(t) = \frac{df_D(t)}{dt} = -f_{D_{max}} \cdot \left( \frac{v}{\sqrt{(vt)^2 + h^2}} - \frac{v^3 t^2}{(\sqrt{(vt)^2 + h^2})^3} \right) = -f_{D_{max}} \frac{v h^2}{(\sqrt{(vt)^2 + h^2})^3}, \quad (\text{A.3})$$

where  $d_0 = 0$  is assumed without loss of generality. This function has the only minimum, i.e.  $f''_D(t) = 0$ ,  $f'''_D(t) > 0$ , at  $t = 0$ , so that the Doppler rate with the maximum absolute value

$$f'_{D_{max}} = f'_D(t)|_{t=0} = -f_{D_{max}} \cdot \frac{v}{h} = -f_c \cdot \frac{v^2}{c \cdot h} \quad (\text{A.4})$$

is obtained using  $f_{D_{max}} = f_c \cdot v/c$ .

# Appendix B

## Shortened $\text{si}(x)$ -Function Spectrum

The normalized shortened  $\text{si}(x)$ -function

$$w_{N_{tap}}(x) = \begin{cases} \text{si}(\pi x) & |x| < \frac{N_{tap}}{2} \\ 0 & \text{otherwise} \end{cases}, \quad (\text{B.1})$$

is obtained by multiplying a  $\text{si}(x)$ -function (4.6) with a rectangular function  $\text{rect}(x)$  (3.4) as follows

$$w_{N_{tap}}(x) = \text{si}(\pi x) \cdot \text{rect}\left(\frac{x}{N_{tap}}\right). \quad (\text{B.2})$$

The spectrum representation of this equation is expressed by

$$W_{N_{tap}}(y) = \text{rect}(y) * (N_{tap} \cdot \text{si}(\pi y N_{tap})) \quad (\text{B.3})$$

Resolving the convolution delivers

$$\begin{aligned} W_{N_{tap}}(y) &= \int_{-\infty}^{\infty} \text{rect}(y-z) \cdot N_{tap} \cdot \text{si}(\pi z N_{tap}) dz \\ &= N_{tap} \int_{y-1/2}^{y+1/2} \text{si}(\pi z N_{tap}) dz. \end{aligned} \quad (\text{B.4})$$

Substituting  $\xi = z\pi N_{tap}$ , thus  $dz = 1/(\pi N_{tap}) d\xi$ , and applying the integral sine from (4.19) finally results in

$$\begin{aligned} W_{N_{tap}}(y) &= \frac{1}{\pi} \int_{(y-1/2)\pi N_{tap}}^{(y+1/2)\pi N_{tap}} \text{si}(\xi) d\xi \\ &= \frac{1}{\pi} \left[ \text{Si}\left(\left(y + \frac{1}{2}\right)\pi N_{tap}\right) - \text{Si}\left(\left(y - \frac{1}{2}\right)\pi N_{tap}\right) \right]. \end{aligned} \quad (\text{B.5})$$

$w_{N_{tap},f_D}(t)$ ,  $W_{N_{tap},f_D}(f_D)$  are obtained by substituting  $x = t/(N_t T'_s)$  and  $w_{N_{tap},\tau}(f)$ ,  $W_{N_{tap},\tau}(\tau)$  are obtained by substituting  $x = f/(N_f F_s)$  and applying  $\mathcal{F}\{w(kx)\} = 1/|k| \cdot W(y/k)$ .

# Appendix C

## Linear Interpolation Function Spectrum

The normalized linear interpolation function

$$d(x) = \begin{cases} 1 - |x| & |x| < 1 \\ 0 & \text{otherwise} \end{cases}, \quad (\text{C.1})$$

is derived by a convolution of two rectangular pulses  $\text{rect}(x)$  as follows

$$d(x) = \text{rect}(x) * \text{rect}(x). \quad (\text{C.2})$$

The according spectrum representation results from

$$D(y) = \text{si}(\pi y) \cdot \text{si}(\pi y) = [\text{si}(\pi y)]^2. \quad (\text{C.3})$$

$w_{N_{tap},f_D}(t)$ ,  $W_{N_{tap},f_D}(f_D)$  are obtained by substituting  $x = t/(N_t T'_s)$  and  $w_{N_{tap},\tau}(f)$ ,  $W_{N_{tap},\tau}(\tau)$  are obtained by substituting  $x = f/(N_f F_s)$  and applying  $\mathcal{F}\{d(kx)\} = 1/|k| \cdot D(y/k)$ .

# Appendix D

## Example Files for a SDR MC-CDMA Parameter Structure

The following two C-code header-files illustrate the use of a flexible and adaptable user parameter structure for a SDR MC-CDMA system. The main header-file `ofdm_parameters.h` contains information about the TDMA/OFDM frame structure, subcarrier compensation values, synchronization symbols, synchronization mode, channel estimation/equalization and the applied modulation scheme.

```
#include <dspvec.h>                /* complexf used in this header file */

#define OFDM_PARAMETERS             /* This shows the tasks that the OFDM parameters
                                   have been set. */

#define N_FRAMES                   8    /* Number of OFDM frames per TDMA frame */
#define TDMA_MODE                  2    /* Specify TDMA operation mode */
                                       /* 0 = Only first OFDM frame is filled;
                                       other OFDM frames are transmitted empty
                                       1 = Each OFDM frame is filled with
                                       the same information sequence
                                       2 = Each OFDM frame is filled with
                                       its individual information sequence */

#define N_SYMB                     28   /* Number of OFDM symbols per OFDM frame (incl. zero symbol) */
#define N_SYNC                     2    /* Number of synchronization symbols */
#define OFDM_ZERO_SYMB             0    /* Define position of zero symbol in OFDM frame */
#define N_FFT                      128  /* Number of IFFT/FFT symbols (min. 128) */
#define LOG2_N_FFT                  7    /* The base-2 logarithm of N_FFT */
#define N_GUARD                     5    /* Number of symbols for guard interval [20;256[ */
#define OFDM_ZERO_VAL              0    /* DAC Value if OFDM zero symbol is sent */
#define OFDM_EMPTY_VAL             0    /* DAC Value if empty OFDM symbol is sent */
#define N_C_USED                    113  /* Number of used carriers */
#define FIRST_PILOT                 7    /* Define subcarrier position of first pilot symbol */
#define N_F                          7    /* Distance of pilot symbols in frequency direction */
#define N_P_USED_F                  5    /* # of nearest Pilots to use in Int-r */
#define N_T                          3    /* Distance of pilot symbols in time direction */
```

```

#define N_P_USED_T      5      /* # of nearest Pilots to use in Int-r*/

#define MAG_IFFT_CORRECTION /* Set this define to correct the subcarriers
                             with the inverse estimated magnitude in
                             float magCorValuesIFFT[N_FFT] */

#define MAG_FFT_CORRECTION /* Set this define to correct the subcarriers
                             with the inverse estimated magnitude in
                             float magCorValuesFFT[N_FFT] */

#ifndef MAG_COR_VALUES
#define MAG_COR_VALUES
#include "../MAG_CORR_VALUES/magCorValues_isp80_ID5477_IQmoddemod_RF_IFFT.c"
#include "../MAG_CORR_VALUES/magCorValues_isp80_ID5477_IQmoddemod_RF_FFT.c"
#endif

#define N_INFORMATION  240    /* number of information bits */
#define N_TAIL          6     /* tail bits for channel coding */

#define PSK_SCALE       175.0 /* Scaling factor for BPSK, QPSK and 8-PSK symbols */
#define PILOT_SCALE     175.0 /* amplitude scale for pilot symbols */
#define SYNC_SCALE      175.0 /* amplitude scale for synchronization symbols */
#define QPSK            /* define modulation {BPSK, QPSK, QAM16} */
#ifdef QPSK
/* defines for QPSK */
#define MOD_NAME        "QPSK" /* define name for hardcopy */
#define D1_SCALE        43.8   /* amplitude scale for modulation 1U 7P (8 active users) */
#define N_MOD_STATES   4       /* Number of states per symbol */
#define N_MOD_BITS     2       /* Number of bits representing those states */
#ifndef MODULATION_SYMBOLS
#define MODULATION_SYMBOLS
const complexf ModSymbol[N_MOD_STATES] = {{D1_SCALE, D1_SCALE}, {D1_SCALE,-D1_SCALE},
{-D1_SCALE, D1_SCALE}, {-D1_SCALE, -D1_SCALE}};
#endif
#endif

#define FREQ_SYNC_MODE  1     /* CarrierFrequencyOffset correction Modes */
/* 0 = Hardware correction
   1 = Software correction */

#define RX_OVERSAMPLING 1     /* OverSampling Modes */
/* 0 = without oversampling
   1 = with oversampling (2 times) */

#define ZERO_FORCING_EST 1    /* ZeroForcing Modes in the Channel Estimation */
/* 0 = without ZeroForcing (MRC)
   1 = with ZeroForcing (ZF) */

#ifndef SYNC_SYMBOLS
#define SYNC_SYMBOLS
#include "/software/local/dspsystem/ofdm_sync_sequences/ofdm_sync_seq128.h"
/* const complexf syncSymb1[128], const complexf syncSymb2[128] */
#endif

#define SAMP_FREQ       492307 /* OFDM sampling frequency for D/A- and A/D-conversion */

```

In the second header-file `mc_cdma_parameters.h`, the parameters for the MC-CDMA structure are described, including the number of users to generate, the channel encoder code rate, the spreading length, the spreading chip distance, the spreading sequences and the assignment of the spreading sequences to the individual users.

```
#ifndef MC_CDMA_PARAMETERS
#define MC_CDMA_PARAMETERS      /* Indicates that MC_CDMA_PARAMETERS has been set */
#include "ofdm_parameters.h"    /* For N_INFORMATION, N_TAIL */

#define N_USER_G                1      /* Number of users to generate {0 - max. users} */
#define N_USER_P                7      /* Number of interfering pseudo users in generator */

#define N_USER_S                1      /* Number of users to split {0 - max. users} */

#define N_GROUPS                10     /* Number of usergroups */

#define N_INFO_BITS              (N_INFORMATION+N_TAIL) /* Number of input info bits */
#define N_CODE_BITS              (2*N_INFO_BITS)      /* Info bits after channel coding;
                                                    must be an even number */

#if ((N_CODE_BITS % 2) != 0)
#error "Error: N_CODE_BITS has to be an even number!"
#endif

#define L_SPREADING              8      /* Length of spreading code */
#define SPREAD_DISTANCE          14     /* Distance of channels with same spreading code
                                        within a group */

struct vc_struct
{
    unsigned Group;
    unsigned Sequence;
    void *pNext;
};

struct pseudouser_properties
{
    int group;
    int sequence;
};

/* Specify user (-1 means no user) for each virtual channel in generator
   (= physical channel * spreading sequence) */
const int ChannelsGenerator[L_SPREADING][N_GROUPS] = \
/* group : */
/*  0  1  2  3  4  5  6  7  8  9  /  spreading sequence*/
/* -----*/
{{ 0,  0,  0,  0,  0,  0,  0,  0,  0,  0}, /* 0      */
 { -1, -1, -1, -1, -1, -1, -1, -1, -1, -1}, /* 1      */
 { -1, -1, -1, -1, -1, -1, -1, -1, -1, -1}, /* 2      */
 { -1, -1, -1, -1, -1, -1, -1, -1, -1, -1}, /* 3      */
 { -1, -1, -1, -1, -1, -1, -1, -1, -1, -1}, /* 4      */
```

```

    { -1, -1, -1, -1, -1, -1, -1, -1, -1, -1}, /* 5 */
    { -1, -1, -1, -1, -1, -1, -1, -1, -1, -1}, /* 6 */
    { -1, -1, -1, -1, -1, -1, -1, -1, -1, -1}}; /* 7 */

/* Specify user (-1 means no user) for each virtual channel in splitter
   (= physical channel * spreading sequence) */
const int ChannelsSplitter[L_SPREADING][N_GROUPS] = \
/* group : */
/* 0 1 2 3 4 5 6 7 8 9 / spreading sequence*/
/* -----*/
{ { 0, 0, 0, 0, 0, 0, 0, 0, 0, 0}, /* 0 */
  { -1, -1, -1, -1, -1, -1, -1, -1, -1, -1}, /* 1 */
  { -1, -1, -1, -1, -1, -1, -1, -1, -1, -1}, /* 2 */
  { -1, -1, -1, -1, -1, -1, -1, -1, -1, -1}, /* 3 */
  { -1, -1, -1, -1, -1, -1, -1, -1, -1, -1}, /* 4 */
  { -1, -1, -1, -1, -1, -1, -1, -1, -1, -1}, /* 5 */
  { -1, -1, -1, -1, -1, -1, -1, -1, -1, -1}, /* 6 */
  { -1, -1, -1, -1, -1, -1, -1, -1, -1, -1}}; /* 7 */

/* Specify group [0 - (N_GROUPS-1), -1] (-1 means all) and
   spreading sequence [0 - (L_SPREADING-1)] for each pseudo user */
const struct pseudouser_properties UsersPseudo[N_USER_P] = \
  {{-1, 1}, {-1, 2}, {-1, 3}, {-1, 4}, {-1, 5}, {-1, 6}, {-1, 7}};

/* Specify carrier to start with for each group */
const unsigned StartCarrier[N_GROUPS] = \
  {9, 16, 10, 17, 11, 18, 12, 19, 13, 20};

/* Specify spreading sequences - use Walsh-Hadamard sequences */
const complexf SpreadSequence[L_SPREADING][L_SPREADING]= \
{{{+1.0,0.0},{-1.0,0.0},{+1.0,0.0},{-1.0,0.0},{-1.0,0.0},{+1.0,0.0},{-1.0,0.0},{+1.0,0.0}},
 {{+1.0,0.0},{+1.0,0.0},{-1.0,0.0},{-1.0,0.0},{-1.0,0.0},{-1.0,0.0},{+1.0,0.0},{+1.0,0.0}},
 {{+1.0,0.0},{-1.0,0.0},{-1.0,0.0},{+1.0,0.0},{-1.0,0.0},{+1.0,0.0},{+1.0,0.0},{-1.0,0.0}},
 {{+1.0,0.0},{+1.0,0.0},{+1.0,0.0},{+1.0,0.0},{-1.0,0.0},{-1.0,0.0},{-1.0,0.0},{-1.0,0.0}},
 {{+1.0,0.0},{-1.0,0.0},{+1.0,0.0},{-1.0,0.0},{+1.0,0.0},{-1.0,0.0},{+1.0,0.0},{-1.0,0.0}},
 {{+1.0,0.0},{+1.0,0.0},{-1.0,0.0},{-1.0,0.0},{+1.0,0.0},{+1.0,0.0},{-1.0,0.0},{-1.0,0.0}},
 {{+1.0,0.0},{-1.0,0.0},{-1.0,0.0},{+1.0,0.0},{+1.0,0.0},{-1.0,0.0},{-1.0,0.0},{+1.0,0.0}},
 {{+1.0,0.0},{+1.0,0.0},{+1.0,0.0},{+1.0,0.0},{+1.0,0.0},{+1.0,0.0},{+1.0,0.0},{+1.0,0.0}}};

```

# Notations

## Symbols

$a$	amplitude of line of sight path
$B$	bandwidth
$B_s$	subcarrier bandwidth
$\mathcal{B}(g)$	correlation metric for integer part carrier frequency offset
$c$	speed of light
$c^2$	variance of the diffuse scattered multipath components
$c_i$	random or pseudo-random spreading chip values
$C$	average received signal power
$\vec{C}^{(l)}$	$l$ th spreading code vector
$C_i^{(l)}$	$i$ th element of $l$ th spreading code vector
$\mathcal{C}$	set of complex numbers
$d$	distance
$\Delta d$	detour distance
$D_{chip}$	distance of spreading code chips for MC-CDMA
$D_{k,l}$	data/source symbol at $l$ th subcarrier in $k$ th OFDM symbol
$D^{(k)}$	data symbol of $k$ th user
$D_m^{(k)}$	$m$ th data symbol of $k$ th user
$\vec{D}$	data/source symbol vector
$E\{.\}$	expectation
$E_b$	energy per bit
$E_{pilot}$	energy per pilot symbol
$E_s$	energy per modulation symbol; not spread
$f$	frequency
$\Delta f$	frequency difference
$\vec{f}$	subcarrier frequency vector
$f_l$	$l$ th element of subcarrier frequency vector
$f_c$	carrier frequency
$\Delta f_c$	carrier frequency offset
$(\Delta f_c)_{frac}$	fractional part of carrier frequency offset

$(\Delta f_c)_{int}$	integer part of carrier frequency offset
$\Delta f_{clk}$	sampling rate offset
$f_g$	lowpass filter cutoff frequency
$f_D$	Doppler frequency
$f_{D_{filter}}$	maximum Doppler frequency permitted for filter design
$f_{D_{LOS}}$	Doppler shift of line of sight path
$f_{D_{max}}$	maximum Doppler frequency
$f'_{D_{max}}$	maximum Doppler rate
$f_{D_n}$	Doppler frequency of $n$ -th echo
$F_d$	data symbol rate
$F_{ov}$	oversampling rate
$F_s$	subcarrier spacing
$F_{sample}$	sampling rate
$\mathcal{F}\{.\}$	Fourier transform
$g$	index for integer frequency offset synchronization
$\mathbf{G}$	frequency domain equalization matrix
$G_{k,l}$	equalization value for $l$ th subcarrier in $k$ th OFDM symbol
$G_{SS}$	spread spectrum spreading gain
$h$	altitude of aircraft above ground
$h(\tau, t)$	time-variant channel weight function
$h_0(\tau_A, t)$	time-variant channel impulse response
$H(f, f_D)$	Doppler-variant channel transfer function
$i$	(tap) index
$j$	$\sqrt{-1}$
$k$	discrete-time index
$k_{pilot}$	discrete positions of pilots in time direction
$K$	number of active users
$K_{max}$	maximum number of active users
$K_Q$	number of active users in each user group
$K_{Q_{max}}$	maximum number of active users in each user group
$K_{Rice}$	Rice factor
$l$	discrete-frequency index
$l_{pilot}$	discrete positions of pilots in frequency direction
$l'_{start}$	position of first used subcarrier
$l'_{start,q}$	subcarrier position of the first chip from the $q$ th group
$\log(.)$	logarithm with base 10
$L$	spreading code length
$L_-$	number of taps in negative direction of time
$L_+$	number of taps in positive direction of time
$\mathcal{L}$	current iteration path length
$M$	number of data symbols per user and OFDM symbol

$\mathcal{M}(d)$	frame timing metric for synchronization
$\text{nint}(\cdot)$	nearest integer value
$N$	noise power
$\vec{N}$	noise vector
$N_l$	$l$ th element of noise vector
$N_{bit}$	number of transmitted information bits per OFDM frame
$N_c$	number of subcarriers
$N'_c$	number of used subcarriers
$N_f$	distance of pilot symbols in frequency direction
$N_{fr}$	number of time slots per TDMA frame
$N_g$	number of guard samples
$N_s$	number of OFDM symbols per OFDM frame
$N_t$	distance of pilot symbols in time direction
$N_{tap}$	number of filter taps / pilot symbols for equalization
$N_{FFT}$	number of FFT/IFFT subcarriers
$N_0$	noise power density
$\mathcal{N}$	maximum iteration path depth
$p(\cdot)$	probability density function
$P_b$	average BER
$P_s(\tau, f_D)$	two-dimensional delay-Doppler power spectrum
$P_{subcarrier}$	subcarrier power
$P_{ICI}$	intersubcarrier interference power
$P_{R_x}$	received power
$P_{T_x}$	transmitted power
$\mathcal{P}(d)$	timing/carrier offset vector sum for synchronization
$Q$	number of user groups per OFDM symbol
$R$	code rate
$R_b$	bit rate
$R_d$	data symbol rate
$\mathcal{R}$	set of real numbers
$\mathcal{R}(d)$	received energy for synchronization
$\text{si}(x)$	$\sin(x)/x$
$S(\tau, f_D)$	delay-Doppler function
$\text{Si}(x)$	integral sine
$\vec{S}$	spread vector containing the information of up to $L$ users
$S_l$	$l$ th element of spread vector
$\vec{S}_{m,q}$	spread vector for $m$ th data symbols of users in $q$ th group
$S_{l,m,q}$	$l$ th element of spread vector for $m$ th data symbols of users in $q$ th group
$\vec{S}^{(k)}$	source vector for data symbol of $k$ th user
$S_l^{(k)}$	$l$ th element of source vector for data symbol of $k$ th user
$\vec{S}_m^{(k)}$	source vector for $m$ th data symbol of $k$ th user

$S_{l,m}^{(k)}$	$l$ th element of source vector for $m$ th data symbol of $k$ th user
$\mathcal{S}(\theta)$	energy term for synchronization
$t$	time
$\Delta t$	time difference
$\mathbf{T}$	channel transfer function matrix
$T_{k,l}$	channel transfer function value for $l$ th subcarrier in $k$ th OFDM symbol
$\vec{\mathbf{T}}$	channel transfer function vector
$T_l$	$l$ th element of channel transfer function vector
$T(f, t)$	time-variant channel transfer function
$T_{chip}$	chip duration
$T_d$	data symbol duration
$T_{fr}$	OFDM frame duration
$T_g$	duration of guard interval
$T_{ov}$	duration of oversampling sample
$T_s$	OFDM symbol duration without guard interval
$T'_s$	OFDM symbol duration with guard interval
$T_{sample}$	sample duration
$T_{TDMA}$	TDMA frame duration
$T_0$	equivalent noise temperature
$u_n$	random, uniformly distributed variable between 0 and 1
$v$	velocity
$\Delta v$	relative velocity
$v_{min}$	minimum velocity
$v_{max}$	maximum velocity
$V_l$	element of complex-valued PN sequence on $l$ th subcarrier
$x(t)$	transmitted signal
$\vec{\mathbf{x}}$	time domain representation of transmitted vector
$x_k$	$k$ th element of discrete time transmission signal or vector $\vec{\mathbf{x}}$
$\vec{\mathbf{x}}_g$	time domain representation of transmitted vector including guard interval
$\mathbf{X}$	matrix frequency domain representation of transmitted OFDM frame
$X_{k,l}$	transmitted value for $l$ th subcarrier in $k$ th OFDM symbol
$\vec{\mathbf{X}}$	frequency domain representation of transmitted vector
$X_l$	$l$ th element of discrete frequency transmission vector $\vec{\mathbf{X}}$
$\vec{\mathbf{y}}$	time domain representation of received vector
$y_k$	$k$ th element of discrete time reception signal or vector $\vec{\mathbf{y}}$
$\vec{\mathbf{y}}_g$	time domain representation of received vector including guard interval
$\mathbf{Y}$	matrix frequency domain representation of received OFDM frame
$Y_{k,l}$	received value for $l$ th subcarrier in $k$ th OFDM symbol
$\vec{\mathbf{Y}}$	frequency domain representation of received vector
$Y_l$	$l$ th element of discrete frequency reception vector $\vec{\mathbf{Y}}$

$\alpha$	roll-off factor
$\beta$	beamwidth
$\delta(t)$	Dirac delta function
$\gamma_b$	average SNR per bit at the input of the data detector
$\gamma_c$	average SNR per subcarrier at the input of the data detector
$\gamma(\theta)$	weighted correlation magnitude
$\lambda$	wavelength
$\phi(t)$	autocorrelation function
$\rho$	correlation coefficient
$\tau$	delay
$\tau_A$	excitation instance
$\tau_{filter}$	maximum delay permitted for filter design
$\tau_{max}$	maximum delay
$\tau_{slope}$	slope time for exponentially decreasing delay
$\tau_n$	delay of $n$ th echo
$\theta$	index for start of guard interval synchronization
$\theta_n$	phase of $n$ th echo
$\varphi_{a_L}$	lowest angle of arrival for received signal
$\varphi_{a_H}$	highest angle of arrival for received signal
$\Delta\varphi_l$	phase rotation of $l$ -th subcarrier compared to reference
$(.) * (.)$	convolution
$(.)^{(k)}$	value of $k$ th user
$(.)^T$	transposition of a vector or matrix
$(.)^{-1}$	inversion
$(.)^*$	complex conjugation
$ \cdot $	absolute value
$\angle(\cdot)$	angle of complex value
$\widehat{(\cdot)}$	estimated value
$[x]$	physical unit of $x$
$\lfloor x \rfloor$	largest integer smaller or equal to $x$
$\lceil x \rceil$	smallest integer larger or equal to $x$
$\infty$	infinity

## Abbreviations

ACF	Auto Correlation Function
A/D	Analog-to-Digital
ADL	Advanced Data Link
ADLP	Advanced Data Link Protocol
AGC	Automatic Gain Control
AM	Amplitude Modulation
A-SMGCS	Advanced Surface Movement Guidance and Control System
AWGN	Additive White Gaussian Noise
BER	Bit Error Rate
BFM	Brute Force Method
BPF	BandPass Filter
BPSK	Binary Phase Shift Keying
CCF	Cross Correlation Function
CDMA	Code Division Multiple Access
CEC	CORBA Event Channel
CORBA	Common Object Request Broker Architecture
COST	European Cooperation in the Field of Scientific and Technical Research
CW	Continuous Wave
D/A	Digital-to-Analog
DAB	Digital Audio Broadcasting
DAPSK	Differential Amplitude and Phase Shift Keying
DC	Direct Current
DFT	Discrete Fourier Transform
DLR	German Aerospace Center
DPSK	Differential Phase Shift Keying
DQPSK	Differential Quadrature Phase Shift Keying
DSP	Digital Signal Processing
DS-SS-CDMA	Direct Sequence Spread Spectrum Code Division Multiple Access
DVB	Digital Video Broadcasting
e.g.	for example
EGC	Equal Gain Combining
FDMA	Frequency Division Multiple Access
FFT	Fast Fourier Transform
FIR	Finite Impulse Response
FM	Frequency Modulation
GDR	Ground Data Router
GF	Galois Field
GHz	Giga Hertz
GO	Geometrical Optics

GP&C	Global Positioning and Communication
GSM	Global System for Mobile communications
Hz	Hertz
i.e.	that is
IBO	Input Back Off
ICI	IntersubCarrier Interference
IDFT	Inverse Discrete Fourier Transform
IEEE	The Institute of Electrical and Electronics Engineers
IF	Intermediate Frequency
IFFT	Inverse Fast Fourier Transform
IP	Internet Protocol
I/Q	In-phase/Quadrature
ISI	InterSymbol Interference
ISINR	In-band-Signal to In-band-Noise Ratio
ISONR	In-band-Signal to Out-of-band-Noise Ratio
ISP	In-System Programmable
JD	Joint Detection
JTAG	Standard Test Access Port and Boundary-Scan Architecture
LLR	Log-Likelihood Ratio
LNA	Low Noise Amplifier
LOS	Line Of Sight
LP	LowPass
LPF	LowPass Filter
MA	Multiple Access
MAI	Multiple Access Interference
MC	Multi-Carrier
MC-CDMA	Multi-Carrier Code Division Multiple Access
MF	Matched Filter
MHz	Mega Hertz
ML	Maximum Likelihood
MLE	Maximum Likelihood Estimation
MLS	Microwave Landing System
MLSE	Maximum Likelihood Sequence Estimation
MMSE	Minimum Mean Square Error
MRC	Maximum Ratio Combining
ODR	On-board Data Router
OFDM	Orthogonal Frequency Division Multiplexing
OSI	Open System Interconnection
PA	Power Amplifier
PAPR	Peak-to-Average Power Ratio
pdf	Probability Density Function

PN	Pseudo Noise
PSK	Phase Shift Keying
QAM	Quadrature Amplitude Modulation
QPSK	Quadrature Phase Shift Keying
RC	Resistor Capacitor
RF	Radio Frequency
RLP	Radio Link Protocol
RRC	Root Raised Cosine
RS	Reed-Solomon
Rx	Receiver
SC	Single-Carrier
SD	Single-user Detection
SDR	Software-Defined Radio
SNR	Signal-to-Noise Ratio
SS	Spread Spectrum
TARMAC	Taxi And Ramp Management And Control
TCP	Transport Control Protocol
TDMA	Time Division Multiple Access
Tx	Transmitter
UHF	Ultra High Frequency (300-3000 MHz)
UMTS	Universal Mobile Telecommunications System
UTD	Uniform Theory of Diffraction
VDL	VHF Data Link
VHF	Very High Frequency (30-300 MHz)
VME	VERSAmodule Eurocard
WGN	White Gaussian Noise
WSSUS	Wide Sense Stationary Uncorrelated Scattering
ZF	Zero-Forcing
1-D	One-Dimensional
1D-DD	One-Dimensional Differential Demodulation
2-D	Two-Dimensional
2D-DD	Two-Dimensional Differential Demodulation

# Bibliography

- [3LL] 3L, *C4x Parallel C User Guide*, V 2.0.4, Edinburgh, Scotland: 3L Limited, July 1995.
- [AdS95] F. Adachi and M. Sawahashi, "Decision feedback differential phase detection of M-ary DPSK signals," *IEEE Transactions on Vehicular Technology*, vol. 44, no. 2, pp. 203-210, May 1995.
- [BeB98] T.R. Beale and M.A. Boytim, *Digital Phase-Lock Loop Network*. United States Patent Nr. 5,790,615, August 4, 1998.
- [Bel63] P.A. Bello, "Characterization of randomly time-variant linear channels," *IEEE Transactions on Communication Systems*, vol. CS-11, pp. 360-393, December 1963.
- [Bel73] P.A. Bello, "Aeronautical channel characterization," *IEEE Transactions on Communications*, vol. COM-21, no. 5, pp. 548-563, May 1973.
- [Cha97] B. Chateau, B. Roturier, B. Souny, P. Combes and H. Chevalier, "Modelling of multipath and ducting effects in VHF propagation channel for aeronautical mobiles," *Aeronautical Mobile Communications Panel*, document AMCP/WG-D/7-WP/27, Madrid, Spain, April 1997.
- [Cla68] R.H. Clarke, "A statistical theory of mobile-radio reception," *Bell Systems Technical Journal*, vol. 47, pp. 957-1000, July-August 1968.
- [CIM94] F. Classen and H. Meyr, "Frequency synchronization algorithms for OFDM systems suitable for communication over frequency selective fading channels," in *Proceedings IEEE Vehicular Technology Conference 1994 (VTC'94)*, pp. 1655-1659, 1994.
- [COS88] COST 207, *Digital Land Mobile Radio Communications*. Final Report, Luxembourg: Office for Official Publications of the European Communities, September 1988.
- [DAB95] ETSI ETS 300 401, *Radio Broadcasting Systems; Digital Audio Broadcasting (DAB) to mobile, portable and fixed receivers*. European Standard (Telecommunications series), Valbonne, France, February 1995.
- [DDR01] P. Delhaise, B. Desperier and B. Roturier, *VDL Mode 2 Physical layer validation report*. EATMP Reference Number COM-5-11-0501, EUROCONTROL, April 2001.

- [DiS90] D. Divsalar and M.K. Simon, "Multiple-symbol differential detection of MPSK," *IEEE Transactions on Communications*, vol. 38, no. 3, pp. 300-308, March 1990.
- [DVB99] ETSI EN 300 744, *Digital Video Broadcasting (DVB); Framing structure, channel coding and modulation for digital terrestrial television*. European Standard (Telecommunications series), Valbonne, France, July 1999.
- [Dye97] G. Dyer and T.G. Gilbert, "Channel sounding measurements in the VHF A/G radio communications channel," *Aeronautical Mobile Communications Panel*, document AMCP/WG-D/8-WP/19, Oberpfaffenhofen, Germany, December 1997.
- [Eln92] S.M. Elnoubi, "A simplified stochastic model for the aeronautical mobile radio channel," in *Proceedings IEEE Vehicular Technology Conference*, pp. 960-963, 1992.
- [FaP93] K. Fazel and L. Papke, "On the performance of convolutionally-coded CDMA/OFDM for mobile communication system," in *Proceedings IEEE International Symposium on Personal, Indoor and Mobile Radio Communications (PIMRC'93)*, Yokohama, Japan, pp. 468-472, September 1993.
- [GAA94] J.J. Gledhill, S.V. Anikhindi and P.A. Avon, *Reception of Orthogonal Frequency Division Multiplexed Signals*. United States Patent Nr. 5,345,440, September 6, 1994.
- [Gan72] M.J. Gans, "A power-spectral theory of propagation in the mobile-radio environment," *IEEE Transactions on Vehicular Technology*, vol. VT-21, no. 1, pp. 27-38, February 1972.
- [Gol67] R. Gold, "Optimal binary sequences for spread-spectrum multiplexing," *IEEE Transactions on Information Theory*, vol. IT-13, no. 4, pp. 619-621, October 1967.
- [GPC97] GP&C Sweden AB, *GP&C R3, Transponder R3 - User Guide and Reference Manual*. Solna, Sweden, December 1997.
- [Hay86] S. Haykin, *Adaptive Filter Theory*. Englewood Cliffs, NJ: Prentice-Hall, 1986.
- [HHL99] E. Haas, P. Höher, H. Lang and U.-C. Fiebig, *Future VHF Architecture Implementation Study; WP 5000: Physical Layer; Final Report*. EUROCONTROL, June 1999.
- [HKR97] P. Hoehner, S. Kaiser and P. Robertson, "Two-dimensional pilot-symbol-aided channel estimation by Wiener-filtering," in *Proceedings IEEE ICASSP'97*, Munich, Germany, pp. 1845-1848, April 1997.
- [HIP00] ETSI TS 101 475, *Broadband Radio Access Networks (BRAN); HIPERLAN Type 2; Physical (PHY) layer*. European Standard (Telecommunications series), Valbonne, France, November 2000.

- [Hoe92] P. Hoeher, "A statistical discrete-time model for the WSSUS multipath channel," *IEEE Transactions on Vehicular Technology*, vol. 41, no. 4, pp. 461-468, November 1992.
- [HoL99] P. Hoeher and J. Lodge, "'Turbo DPSK': Iterative differential PSK demodulation and channel decoding," *IEEE Transactions on Communications*, vol. 47, no. 6, pp. 837-843, June 1999.
- [Hub96] J.B. Huber, "Systemtheoretische Grundlagen der Modellierung von Mobilfunkkanälen," in *Proceedings Kurs 5 der Ferienakademie 1996: Mehrfachzugriffsverfahren für Mobilkommunikationssysteme*, Sarntal, Südtirol, pp. 1-40, September 1996.
- [HuM99] J. Huber and S. Müller-Weinfurtner, *Burst Carrier Frequency Synchronization and Iterative Frequency-Domain Frame Synchronization for OFDM*. International Application Published under the Patent Cooperation Treaty (PCT) Nr. WO 99/65180, December 16, 1999.
- [Jak74] W.C. Jakes, Ed., *Microwave Mobile Communications*. New York: Wiley, 1974.
- [Kai98] S. Kaiser, "Multi-Carrier CDMA Mobile Radio Systems - Analysis and Optimization of Detection, Decoding, and Channel Estimation," *VDI Fortschrittberichte*, Reihe 10, Nr. 531, Düsseldorf, Germany: VDI-Verlag GmbH, January 1998.
- [LAT00] Lattice Semiconductor, *Datasheet ispPAC 80, In-System Programmable Analog Circuit*. Hillsboro, Oregon: Lattice Semiconductor Corporation, March 2000.
- [LaW98] E. Langberg and J.-D. Wang, *System and Method Producing Improved Frame Synchronization in a Digital Communication System*. United States Patent Nr. 5,748,686, May 5, 1998.
- [LSI94] Loughborough Sound Images, *DBV42 TIM-40 Carrier Board Technical Reference Manual*, V 1.00, Loughborough, England: Loughborough Sound Images Limited, March 1994.
- [LSI95a] Loughborough Sound Images, *DBV44 TMS320C4x VME Board Technical Reference Manual*, V 1.04, Loughborough, England: Loughborough Sound Images Limited, November 1995.
- [LSI95b] Loughborough Sound Images, *DB212B Dual-Channel ADC and DAC Board User Manual*, V 1.14, Loughborough, England: Loughborough Sound Images Limited, October 1995.
- [LTC97] Linear Technology, *Datasheet LTC 1560-1, 1MHz/500kHz Continuous Time, Low Noise, Lowpass Elliptic Filter*. Milpitas, CA: Linear Technology Corporation, 1997.

- [LTC98] Linear Technology, *Datasheet LTC 1569-7, Linear Phase, DC Accurate, Tunable, 10th Order Lowpass Filter*. Milpitas, CA: Linear Technology Corporation, 1998.
- [MeD97] U. Mengali and A.N. D'Andrea, *Synchronization Techniques for Digital Receivers*. New York: Plenum Press, 1997.
- [Moo94] P.H. Moose, "A technique for orthogonal frequency division multiplexing frequency offset correction," *IEEE Transactions on Communications*, vol. 42, no. 10, pp. 2908-2913, October 1994.
- [MZB00] H. Zinn, M. Zeng and V.K. Bhargava, "On timing offset estimation for OFDM systems," *IEEE Communications Letters*, vol. 4, no. 7, pp. 242-244, July 2000.
- [Neu87] A. Neul and J. Hagenauer, "Propagation measurements for the aeronautical satellite channel," in *Proceedings IEEE Vehicular Technology Conference 1987 (VTC'87)*, pp. 90-97, 1987.
- [NoS99] Nomura and Shinagawa-ku, *Frame synchronisation in a DAB receiver*. European Patent Application Nr. EP 0 980 157 A2, August 6, 1999.
- [OeI00] H. Ochiai and H. Imai, "MDPSK-OFDM with highly power-efficient block codes for frequency-selective fading channels," *IEEE Transactions on Vehicular Technology*, vol. 49, no. 1, pp. 74-82, January 2000.
- [Pai73] J. Painter, S.C. Gupta and L.R. Wilson, "Multipath modeling for aeronautical communications," *IEEE Transactions on Communications*, vol. COM-21, no. 5, pp. 658-662, May 1973.
- [Pap91] A. Papoulis, *Probability, Random Variables, and Stochastic Processes*. 3rd edition, New York: McGraw-Hill, 1991.
- [PEN98] Pentland, *Operating Manual VGD3 - 8 Channel, 3 MSPS, 12 Bit ADC Daughterboard for VGX*. Revision 01D, Livingston, Scotland: Pentland Systems Ltd, October 1998.
- [PoM95] T. Pollet and M. Moeneclaey, "Synchronizability of OFDM signals," in *Proceedings IEEE GLOBECOM'95*, Singapore, pp. 2054-2058, November 1995.
- [Pro95] J.G. Proakis, *Digital Communications*. 3rd edition, New York: McGraw-Hill, 1995.
- [PRR82] R.F. Pawula, S.O. Rice and J.H. Roberts, "Distribution of the phase angle between two vectors perturbed by Gaussian noise," *IEEE Transactions on Communications*, vol. COM-30, no. 8, pp. 1828-1841, August 1982.
- [Rap92] C. Rapp, "Analyse der nichtlinearen Verzerrungen modulierter Digitalsignale - Vergleich codierter und uncodierter Modulationsverfahren und Methoden der Kompensation durch Vorverzerrung," *VDI Fortschrittberichte*, Reihe 10, Nr. 195, Düsseldorf, Germany: VDI-Verlag GmbH, 1992.

- [RTC93] RTCA, "Signal-in-space minimum aviation system performance standards for advanced VHF digital data communications including compatibility with digital voice techniques," *Radio Technical Commission for Aeronautics*, RTCA paper no. 26-93/SC172-68, January 1993.
- [Rob97] P. Robertson, "Close-to-optimal one-shot frequency synchronization for OFDM using pilot carriers," in *Proceedings CTMC at IEEE GLOBECOM'97*, Phoenix, Arizona, pp. 97-102, November 1997.
- [RoB97] H. Rohling and K. Brüninghaus, "High rate OFDM-modem with quasi-coherent DAPSK," in *Proceedings IEEE Vehicular Technology Conference 1997 (VTC'97)*, Phoenix, Arizona, pp. 2055-2059, May 1997.
- [Rot97] B. Roturier and B. Chateau, "Experimental and theoretical field strength evaluation on VHF channel for aeronautical mobiles," *Aeronautical Mobile Communications Panel*, document AMCP/WG-D/7-WP/58, Madrid, Spain, April 1997.
- [SBB95] M. Sandell, J.-J. van de Beek and P.O. Börjesson, "Timing and frequency synchronization in OFDM systems using the cyclic prefix," in *Proceedings 1995 International Symposium on Synchronization*, Essen, Germany, pp. 16-19, December 14/15, 1995.
- [ScC97] T.M. Schmidl and D.C. Cox, "Robust frequency and timing synchronization for OFDM," *IEEE Transactions on Communications*, vol. 45, no. 12, pp. 1613-1621, December 1995.
- [ScC98] T.M. Schmidl and D.C. Cox, *Timing and Frequency Synchronization of OFDM Signals*. United States Patent Nr. 5,732,113, March 24, 1998.
- [Sch92] E. Schrüfer, *Signalverarbeitung - Numerische Verarbeitung digitaler Signale*. 2te Auflage, München, Germany: Hanser, 1992.
- [ShC83] S. Lin and D.J. Costello Jr., *Error Control Coding: Fundamentals and Applications*. Englewood Cliffs, NJ: Prentice-Hall, 1983.
- [Sti71] J.J. Stiffler, *Theory of Synchronous Communication*. Englewood Cliffs, NJ: Prentice-Hall, 1971.
- [SYP00] H.-K. Song, Y.-H. You, J.-H. Paik and Y.-S. Cho, "Frequency-offset synchronization and channel estimation for OFDM-based transmission," *IEEE Communications Letters*, vol. 4, no. 3, pp. 95-97, March 2000.
- [TLZ00] U. Tureli, H. Liu and M.D. Zoltowski, "OFDM blind carrier offset estimation ESPRIT," *IEEE Transactions on Communications*, vol. 48, no. 9, pp. 1459-1461, September 2000.
- [TMS96] Texas Instruments, *TMS320C4x User's Guide*. Dallas, Texas: Texas Instruments Incorporated, 1996.

- [ToK98] L. Tomba and W.A. Krzymien, "On the use of chip-level differential encoding for the uplink of MC-CDMA systems," in *Proceedings IEEE Vehicular Technology Conference 1998 (VTC'98)*, Ottawa, Canada, pp. 958-962, May 1998.
- [TsS99] Tsuruoka and Shinagawa-ku, *Carrier synchronisation for DAB reception*. European Patent Application Nr. EP 0 939 528 A2, February 25, 1999.
- [WaL93] W.D. Warner and C. Leung, "OFDM/FM frame synchronization for mobile radio data communication," *IEEE Transactions on Vehicular Technology*, vol. 42, no. 3, pp. 302-313, August 1993.
- [WaL95] C.S. Leung and W.D. Warner, *Method and Apparatus for Frame Synchronization in Mobile OFDM Data Communication*. United States Patent Nr. 5,444,697, August 22, 1995.
- [Wei71] S.B. Weinstein and P.M. Ebert, "Data transmission by frequency-division multiplexing using the discrete fourier transform," *IEEE Transactions on Communications*, vol. COM-19, no. 5, pp. 628-634, October 1971.
- [WeS95] L. Wei and C. Schlegel, "Synchronization requirements for multi-user OFDM on satellite mobile and two-path Rayleigh fading channels," *IEEE Transactions on Communications*, vol. 43, no. 2/3/4, pp. 887-895, February/March/April 1995.
- [Wol94] S. Wolfram, *Mathematica - Ein System für Mathematik auf dem Computer*. Zweite Auflage, Wolfram Research Inc., München, Germany: Addison-Wesley Verlag GmbH, 1994.
- [YLF93] N. Yee, J.-P. Linnartz and G. Fettweis, "Multi-carrier CDMA in indoor wireless radio networks," in *Proceedings IEEE International Symposium on Personal, Indoor and Mobile Radio Communications (PIMRC'93)*, Yokohama, Japan, pp. 109-113, September 1993.

# Publications

E. Haas, "Untersuchung und Simulation des Physical Layer eines D8PSK-modulierten TDMA-Systems," in *Proceedings Workshop Kommunikationstechnik*, Technische Universität Hamburg-Harburg, Germany, September 1997.

E. Haas, "Improvement of the BER-performance of a discriminator receiver through the implementation of a non-linear decision," in *Proceedings 9. Joint Conference on Communications and Coding 1998*, Courmayeur, Italy, January 1998.

E. Haas, "Improvement of the BER-performance of a discriminator receiver through the implementation of a non-linear decision," *Kleinheubacher Tagung 1998*, Kleinheubach, Germany, September 1998.

E. Haas, P. Höher, H. Lang and U.-C. Fiebig, *Future VHF Architecture Implementation Study; WP 5000: Physical Layer; Final Report*. EUROCONTROL, June 1999.

E. Haas, "Performance improvement of a discriminator receiver through the implementation of a non-linear decision," *IEEE Communications Letters*, vol. 3, no. 6, pp. 166-168, June 1999.

E. Haas, "A novel non-linear decision algorithm for simple receiver structures," in *Proceedings Third Workshop for Communications Technology*, Schloss Reisenburg, Germany, July 1999.

E. Haas and S. Kaiser, "Two-dimensional differential demodulation of OFDM frames," *Multi-Carrier Spread-Spectrum and Related Topics*, K. Fazel and S. Kaiser (Eds.), Boston: Kluwer Academic Publishers, ISBN 0-7923-7740-0, pp. 125-132, December 1999.

P. Höher and E. Haas, "Aeronautical channel modeling at VHF-band," in *Proceedings IEEE Vehicular Technology Conference (VTC'99 - Fall)*, Amsterdam, The Netherlands, pp. 1961-1966, September 1999.

E. Haas and S. Kaiser, "Analysis of two-dimensional differential demodulation for OFDM," in *Proceedings 5th International OFDM-Workshop in Hamburg*, Hamburg, Germany, paper no. 16, September 2000.

E. Haas and S. Kaiser, "Analysis of two-dimensional differential demodulation for OFDM," in *Proceedings IEEE Global Telecommunications Conference (GLOBECOM 2000)*, San Francisco, USA, pp. 751-755, November/December 2000.

- E. Haas and S. Kaiser, *Differentielle Demodulation in zwei oder mehr Dimensionen*. European Patent Application Nr. EP 1 085 741 A2, March 2001.
- E. Haas and M. Schnell, "Development of an advanced airport data link," in *Proceedings Deutscher Luft- und Raumfahrtkongress 2001*, Hamburg, Germany, September 2001.
- E. Haas and M. Schnell, "Development and implementation of an advanced airport data link," *Multi-Carrier Spread-Spectrum and Related Topics*, K. Fazel and S. Kaiser (Eds.), Boston: Kluwer Academic Publishers, ISBN 0-7923-7653-6, pp. 85-95, 2002.
- E. Haas, "Aeronautical channel modelling," *IEEE Transactions on Vehicular Technology*, vol. 51, no. 2, pp. 254-264, March 2002.
- E. Haas, H. Lang and M. Schnell, "Development and implementation of an advanced airport data link based on multi-carrier communications," *Proceedings IEEE 7th International Symposium on Spread Spectrum Techniques and Applications (ISSSTA 2002)*, Prague, Czech Republic, September 2002.
- E. Haas, H. Lang and M. Schnell, "Development and implementation of an advanced airport data link based on multi-carrier communications," *European Transactions on Telecommunications: 3rd Special Issue on Multi-Carrier-Spread-Spectrum*, vol. 13, no. 5, September/October 2002.
- E. Haas and M. Schnell, "Analysis of compensation methods for OFDM implementation effects," *Proceedings IEEE 5th International Symposium on Wireless Personal Multimedia Communications (WPMC 2002)*, Honolulu, Hawaii, pp. 1000-1004, October 2002.
- E. Haas and S. Kaiser, "Two-dimensional differential demodulation for OFDM," *IEEE Transactions on Communications*, accepted to be published.